Technische Universiteit Delft

Non-Modal Growth Induced by Discrete Roughness Elements in a Swept Wing Boundary Layer

Modelling & Diagnostics

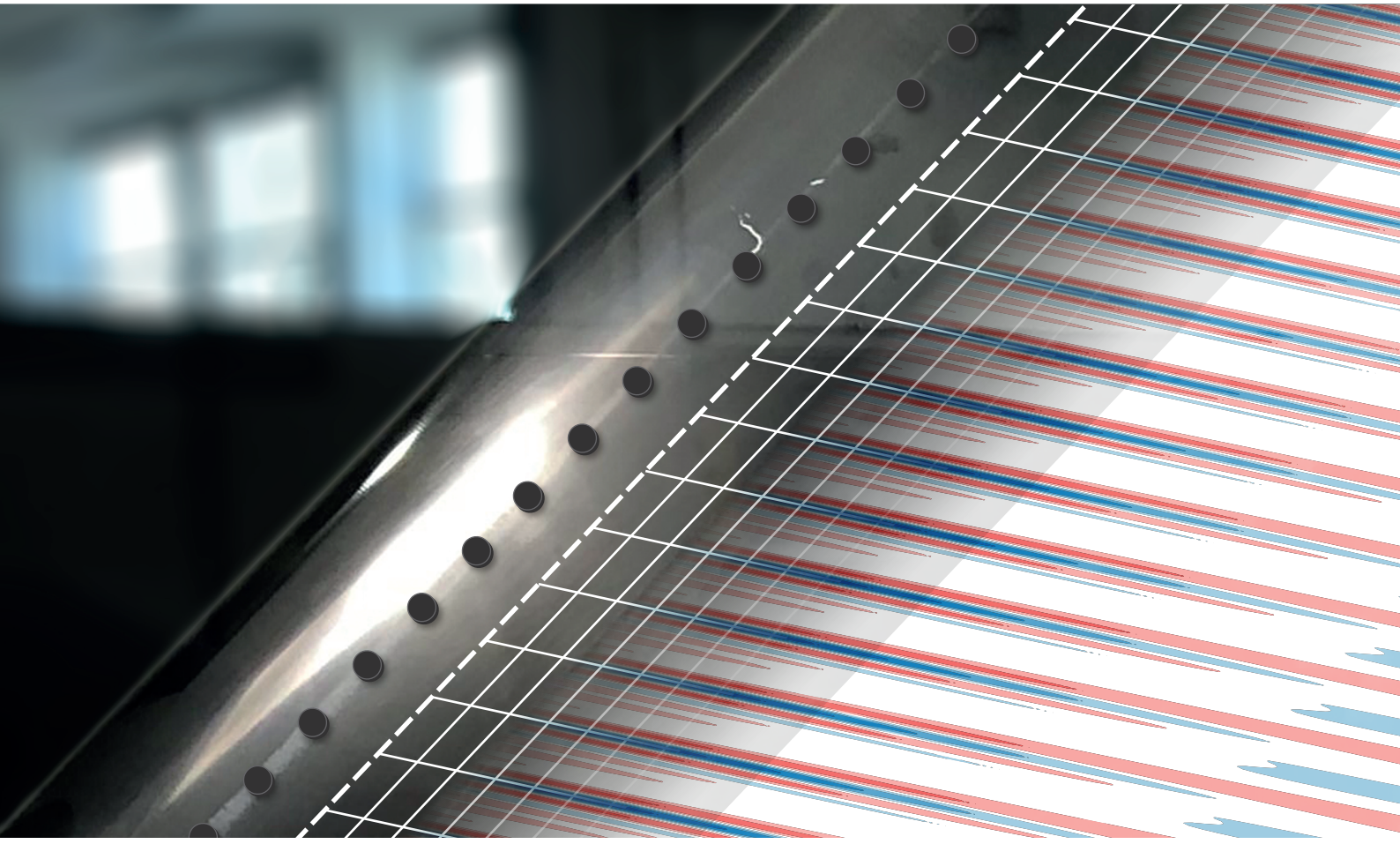

Aaron Duane Sequeira

TU Delft

Non-Modal Growth Induced by Discrete Roughness Elements in a Swept Wing Boundary Layer

Modelling & Diagnostics

by

Aaron Duane Sequeira

to obtain the degree of Master of Science
at the Delft University of Technology,
to be defended publicly on Friday, 23rd December, 2022 at 11:00 AM.

Student number:	5258766	
Project duration:	20th September, 2021 – 23rd December, 2022	
Thesis committee:	Dr. M. Kotsonis,	Associate Professor, TU Delft
	Dr. W.J. Baars,	Assistant Professor, TU Delft
	Dr. S.J. Hulshoff,	Assistant Professor, TU Delft
	Ir. G. Zoppini,	PhD Candidate, TU Delft
	Ir. S.H.J. Westerbeek,	PhD Candidate, TU Delft

Cover: Close-up photograph of the TU Delft M3J swept wing model, taken by the author. A numerical grid and DRE wake flowfield is overlayed.
An electronic version of this thesis is available at http://repository.tudelft.nl/.

TU Delft

Preface

These last two years spent pursuing my MSc. degree have been quite unorthodox, to say the least. Starting out in the midst of a global pandemic, where I thought I would forget how to ever socialize again, I was left feeling quite ambiguous about the direction in which my second year would take me. However, that was quickly put to ease when I started working on this very document laid out before you, now at the end of which I can say that I would not have had it any other way. This work encompasses a year's worth of research in the field of aerodynamics, a journey that was primarily undertaken by yours truly, but would not have been possible without the support of too many people to name in this short space.

First and foremost, I would like to expresses my sincerest gratitude to my supervisory team, Marios, Giulia and Sven. A year ago, I approached Marios hoping to have the chance to learn a little something about boundary layer transition, a phenomenon that had piqued my curiosity at the time. Little did I know that in my time working at the low-speed lab, this ounce of curiosity would turn into passion. Not just for the aerodynamics involved, but also for the scientific method. Our discussions were always engaging and my ideas always met with enthusiasm. I have gained so much from our time working together, and for that I will always be grateful. To Giulia, thank you for everything. From patiently dealing with all my questions to surviving those long hours in the wind tunnel, I don't think I can express how grateful I am for your support. I have learned so much about boundary layers, roughness and transition from you, and what it feels like to be an experimentalist. For that, Grazie! Was it not for you Sven, I think I would have never survived the mathematics of fluid stability. Thank you for all our discussions, for asking me hard questions, and for the lively lunches. It's truly amazing to see real-world predictive tools be formulated out of abstract concepts. I would also like to extended my gratitude to Jordi, for organizing those meetings on transient growth and giving me the chance to discuss my findings. They truly helped shape part of this work, and deepened my understanding of this complex topic. A big thank you to all my other colleagues at the LSL; Alberto, Kaisheng, Theo, Marina and Srijit, for the discussions, outings, and support whenever I needed it! Special thanks to Emiel and Stefan, for their invaluable support during the weeks of the experimental campaign.

The time I've spent in Delft would've felt absolutely hollow if not for the wonderful people that I've met along the way. To my closest friends here, the AeroMIT boys, Brian, Ullas and Bhanu, thank you. We've come a long way from building those RC planes in that dingy workshop five years ago. Thank you for all the weekend shenanigans, cycling trips, beer tasting, never-ending laughs and all those memorable moments, both in and out of Delft. It has truly felt like home away from home. I also want to shout out to Kiran, the former German and now French branch of AeroMIT. Thank you for making those memorable trips to Delft, one of which subconsciously pushed me to start this thesis. I want to thank the Delft "Study Circle", Aniruddha (Jape), Jahnavi and Nikhil, for all our studious and not-so-studious escapades. My experiences with studying aerodynamics in Delft were made so much better because of you. Thank you Lucas (and Bhanu), for all the fun conversations, dinners and good memories at César Franckstraat, and to all my friends out of Delft who have always been around. And to you Soumya, thank you. Thank you for always reminding me, through thick and thin, to never lose hope, and that my best is enough.

Lastly, but never ever least, I dedicate this work to my parents, Melville and Michele, and my brother Joshua. Six years ago, I told you that my dream was to work with aircraft, and you did not hesitate to support me through and through. Through your love, hard work and sacrifices, I have done more than I could have possibly imagined those six years ago. You have enabled me to see the world, meet the people I never thought I would meet, and experience the best of what my field has to offer. Every page of this document is as much yours as it is mine. Thank you.

Aaron Duane Sequeira
Delft, December 2022

Abstract

Laminar-to-turbulent boundary layer transition on the wings and stabilizers of aircraft leads to a large increase in the skin-friction drag they experience during flight. This has motivated prolific research into understanding and delaying the transition process, in an effort to improve the economic and ecological impact of air travel. The swept wing poses a particular challenge to this, as the transition scenario in flight is typically governed by the growth and breakdown of stationary crossflow instabilities (CFI). These are destabilized by flow conditions that would suppress instabilities on straight wings, such as Tollmien–Schlichting waves, complicating the use of laminar flow control techniques. Previous research has shown stationary CFI to be highly receptive to surface roughness, with the use of discrete roughness elements (DRE) having emerged as a forcing/control strategy. However, the mechanisms behind which DRE condition the onset of CFI in a swept wing boundary layer are still a topic of ongoing investigations.

The research presented in this Master thesis aims to further characterize the relation between the DRE forcing configuration and the onset of swept wing boundary layer instabilities, through an investigation of its wake flowfield. The DRE wake has previously been observed to be highly non-modal in nature, limiting the use of modal linear stability theory in predicting stationary disturbance evolution in the element vicinity. To address this, a linear, non-modal, parabolized stability framework is derived, capable of simulating transient growth within the DRE wake region. The numerical framework is initialized with experimental DRE wake data from a previous study, for a DRE array of critical forcing height. The predicted stability characteristics qualitatively agree with experiment, with the numerical solver successfully evolving the stationary DRE wake structure into stationary CFI downstream of the array. However, a quantitative match with experiment could not be attained. The results were also noted to be sensitive to the choice of initial conditions, as well as to the numerical discretization.

In addition to the stationary numerical simulations, hot-wire anemometry measurements are conducted at the TU Delft low turbulence wind tunnel, providing a first-time experimental characterization of the evolution of unsteady disturbances in the DRE wake for a swept wing boundary layer. Regions of high fluctuation intensity are observed to be localized around the top and sides of each element in the DRE array, with their spectral characteristics associated to circular cylinder shedding. For a critical DRE forcing, the evolution of the wake flow is largely governed by the stationary structures, although unsteady disturbance energy is observed to undergo a brief period of transient energy amplification. A super-critical DRE forcing introduces strongly tonal fluctuations into the DRE wake, whose amplification is enhanced by interaction between the stationary structures. The high fluctuation levels are sustained and grow to non-linear amplitudes, inhibiting the relaxation of steady disturbance energy. This leads to rapid, local turbulent breakdown in the vicinity of the elements.

Contents

List of Figures

List of Tables

Nomenclature

Acronyms

LFC	-	Laminar Flow Control
BL	-	Boundary Layer
CFI	-	Crossflow Instability
TS	-	Tollmein-Schilchting
ASU	-	Arizona State University
DRE	-	Discrete Roughness Elements
LST	-	Linear Stability Theory
DNS	-	Direct Numerical Simulations
PSE	-	Parabolized Stability Equations
LPSE	-	Linear Parabolized Stability Equations
NPSE	-	Non-Linear Parabolized Stability Equations
RIT	-	Roughness-Induced Transition
NS	-	Navier-Stokes
BLE	-	Boundary Layer Equations
NLF	-	Natural Laminar Flow
PDE	-	Partial Differential Equation
OS	-	Orr-Sommerfeld
DLR	-	Deutsches Zentrum für Luft-und Raumfahrt
TAMU	-	Texas A&M University
PIV	-	Particle Image Velocimetry
HWA	-	Hot-Wire Anemometry
FSC	-	Falkner-Skan-Cooke
SLST	-	Secondary Linear Stability Theory
KH	-	Kelvin Helmholtz
POD	-	Proper Orthogonal Decomposition
UFD	-	Upstream Flow Deformation
IR	-	Infrared
HSV	-	Horseshoe Vortex
PTV	-	Particle Tracking Velocimetry
FS	-	Falkner-Skan
ODE	-	Ordinary Differential Equation
BC	-	Boundary Conditions
NmPSE	-	Non-Modal Parabolized Stability Equations (NmPSE)
PSDM	-	Pseudo-Spectral Differentiation Matrices
ILST	-	Incompressible Local Stability Theory
HLNS	-	Harmonic Linearised Navier Stokes
LTT	-	Low Turbulence Tunnel
CTA	-	Constant Temperature Anemometer
FFT	-	Fast Fourier Transform
PCHIP	-	Piecewise Cubic Hermite Interpolating Polynomials

Symbols

Physical Paramters

Re	-	Reynolds Number
μ	-	Dynamic Viscosity
ρ	-	Density
ν	-	Kinematic Viscosity
p	-	Static Pressure
t	-	Time
τ_{wall}	-	Wall Shear Stress
c_f	-	Skin-Friction Coefficient
c_p	-	Pressure Coefficient
δ_{99}	-	Boundary Layer thickness
δ^*	-	Displacement thickness
δ_θ	-	Momentum thickness
E	-	Kinetic Energy

Geometric Paramters

(X, Y, Z)	-	Wind Tunnel Coordinate System
(x, y, z)	-	Wing/Flat Plate Coordinate System
d_D	-	Roughness Diameter
k_D	-	Roughness Height
λ	-	Spanwise Wavelength
Λ	-	Sweep Angle

Velocity Components

Q	-	Velocity Magnitude
(U, V, W)	-	Baseflow Velocity Components
(u', v', w')	-	Disturbance Velocity Components
$(\tilde{u}, \tilde{v}, \tilde{w})$	-	Disturbance Shape Functions

Stability Parameters

α	-	Streamwise Wavenumber
β	-	Spanwise Wavenumber
ω	-	Angular Frequency
θ	-	Shape Function Phase
Θ	-	Distrubance Phase Fuction
N	-	N-factor

1

Introduction

1.1. Background & Motivation

The number of aircraft in the sky has exhibited rapid growth overall since the early 2000s, owing to the increased accessibility to air travel and its consequent high demand [83]. Carbon dioxide emissions by airlines have reportedly increased by 32% from 2013 to 2018 [41], and are expected to continue growing up to 2050. This has driven research into sustainable aviation, with collaborative advances towards the improved fuel-efficiency and ecological impact of aircraft [114]. One aspect of this is the reduction of the parasitic drag experienced by an aircraft's wings and stabilizers, particularly its skin-friction component, which comprises nearly 50% of the total drag budget [4]. Laminar flow control (LFC) techniques aim to mitigate the onset of the turbulent boundary layer (BL) that is present on most commercial aircraft in operation today, by delaying the laminar-to-turbulent transition process. This promotes larger regions of laminar flow and its inherently lower skin-friction drag penalty.

High-subsonic and transonic commercial aircraft are typically designed with swept wing configurations to increase their critical Mach numbers, postponing shock formation and its accompanying drag divergence. Despite the large advantage these types of wings offer, the airflow over a swept airfoil is inherently three-dimensional, characterised by the presence of a crossflow velocity component within the viscous BL [101, 109]. This complicates the transition process as the BL becomes receptive to an additional instability mechanism: the crossflow instability (CFI) [70, 5, 101, 109]. In regions of favourable pressure gradient, the travelling Tollmien-Schilchting (TS) waves [104] that typically lead to transition in the unswept scenario are damped. The inflected crossflow velocity profile instead conditions the growth of stationary and travelling crossflow waves [28, 10]. In a low turbulence environment such as that of free-flight, the stationary crossflow waves assume the role of the dominant BL instability [28, 10, 88]. These take the form of streamwise vortices that strongly distort the BL mean-flow, leading to an earlier onset of non-linearities and turbulent breakdown as compared to the unswept scenario.

Experiments by Müller & Bippes [80] demonstrated that transition caused by these stationary vortices is highly susceptible to surface roughness. Irregularities that arise from the manufacturing process in the form of panels, rivets, paint etc. are ubiquitous on aircraft wings and fall into this category. This has led to over thirty years of research dedicated to understanding how naturally occurring surface roughness and various types of artificial roughness influence the onset of CFI, and thus transition on swept wings.

Initial efforts into characterizing roughness-receptivity on swept wings were primarily experimental, with Radeztsky et. al [88] testing a range of roughness configurations. They noted that transition was significantly affected by natural surface roughness, by controlling the surface finishing of their model. Additionally, their use of an isolated 3-D roughness element that did not cause immediate turbulent breakdown revealed a coupling between the amplitude and spectrum of the observed CFI and the element height and diameter. Follow-up experiments at the Arizona State University (ASU) [92] attempted to control the CFI spectrum through the use of an array of periodically spaced, discrete roughness elements (DRE). This led to the development of spanwise uniform transition fronts, different to those produced by natural surface roughness. By setting the inter-element spacing equal to the most amplified crossflow mode predicted by linear stability theory (LST), they observed strong growth and

non-linear amplitude saturation of the forced mode and its harmonics. Further configurations with varying forcing wavelengths showed that only the fundamental CFI mode and its super-harmonics were introduced into the boundary layer, i.e. there was no evidence of wavelength doubling.

The use of DRE became a popular strategy in the decades that followed, both in the study of CFI and transition prediction methods for swept wings. The ability to artificially introduce an instability mode into the BL, as well as to improve the spanwise uniformity of the transitional flow, strengthens the comparisons between experimental and numerical works to be drawn. The growth of CFI has been characterized through Direct Numerical Simulations (DNS) [12, 127, 121, 62] as well as through Parabolized Stability Equations (PSE) (linear (LPSE) and non-linear (NPSE)) [48, 46, 122]. These numerical investigations are in good agreement with experimental findings. However, receptivity continues to pose a challenge in fully modelling crossflow-induced transition. Parallel-flow solvers are seen to suffer from an over-prediction of receptivity amplitudes, as highlighted by Saric et. al [101]. Studies by Tempelmann et. al [122] use an adjoint-based PSE framework to estimate the amplitudes of CFI generated by roughness, albeit being valid only for small roughness heights and limited by the assumptions inherent to the PSE.

DRE have also been investigated as a passive LFC technique. Numerous studies by Saric and colleagues [100, 99, 102] attempt to use a DRE configuration that does not contain the most amplified CFI mode or any of its harmonics. The excitation of a less-unstable, sub-critical mode (i.e. shorter wavelength mode) inhibits the growth of the most unstable one and delays transition to downstream of its natural, unforced location. A more recent work by Zoppini et. al [135] uses a series of DRE arrays in chordwise succession to induce and overlap crossflow waves such that they destructively interfere, reducing their amplitude and postponing the onset of non-linear breakdown. Despite the effectiveness of these methods in most scenarios, they remain limited in their application due to sensitivity to environmental conditions and an incomplete understanding of the receptivity process. This further highlights a need for a detailing of the initial stages of roughness-induced CFI development.

Zoppini et. al [139] conducted an experimental study on the effect of the DRE height and location on swept-wing transition caused by stationary CFI, supplemented by NPSE simulations. Their estimation of initial instability amplitudes suggests that the near-element flow topology is crucial in relating the external forcing configuration (i.e. DRE geometry) to modal CFI development. Comprehensive DNS studies by Kurz & Kloker [62], Brynjell & Rahkola [14] reveal the intricate features pertinent to the near-element flowfield. They report a low-speed wake aft of each roughness element, accompanied by a horseshoe vortex system. This vortical flow induces a series of low and high speed streaks, similar to those observed in experiments with roughness in 2-D boundary layers [34, 61, 62]. Recent experimental work on resolving the DRE wake-flow [136] confirm these DNS findings and highlight non-modal growth [104, 120, 68] as a mechanism in CFI receptivity to DRE.

While significant advances have been made in understanding the complex flow topology in the vicinity of DRE, the process through which they condition the onset of instability in swept wings is still not fully understood. State-of-the-art numerical tools such as the PSE suffer from limitations in their mathematical framework that do not allow for non-modal growth to be analysed. The current study is an effort to resolve these discrepancies and provide alternative methods to modelling the stationary perturbation fields generated by DRE. A first time detailed description of unsteady DRE-wake disturbances in 3-D boundary layers is also offered, in an effort to fully characterize the receptivity process. The findings of this work will provide for a better understanding of how roughness conditions CFI, possible driving the development of more accurate predictive models or more effective LFC techniques.

The remainder of this chapter aims to detail historical work, as well as the latest literature on swept wing boundary layers, crossflow instabilities and roughness-induced transition (RIT). Section 1.2 provides the reader with a brief introduction to boundary layers, with an emphasis on those pertinent to swept wings. This is followed by a discussion on boundary layer transition, stability theory and the features of the crossflow instability (Section 1.3). A comprehensive review of research on roughness elements in 3-D boundary layers is conducted in Section 1.4, encompassing experimental and numerical efforts to understand receptivity. Section 1.5 details non-modal growth, highlights advancements in numerical methods used for its prediction, and emphasizes connections to DRE receptivity in swept wing boundary layers. Finally, Sections 1.6 and 1.7 identify gaps in the literature discussed and define the main research questions and objective of this work.

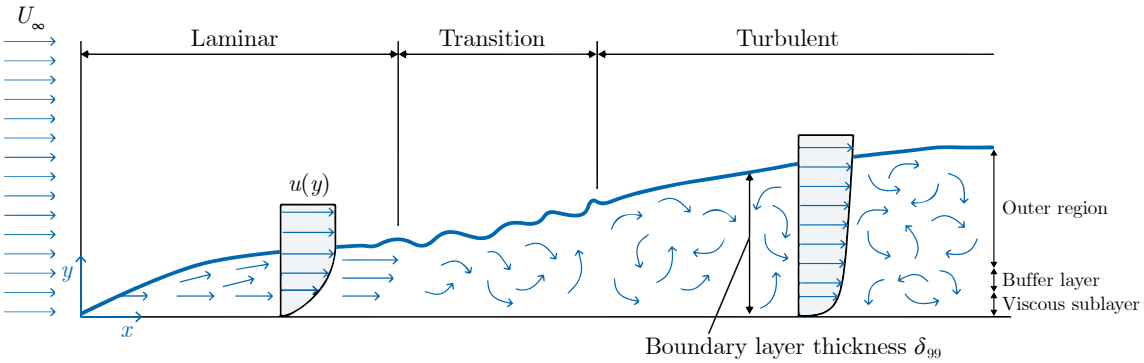

Figure 1.1: A schematic of the development and transition of a boundary layer.

1.2. The Viscous Boundary Layer

A full mathematical description of the dynamics of fluid flow is given by the famous Navier-Stokes (NS) equations. However their complex, highly non-linear nature makes both analytical and numerical analysis extremely challenging. In his 1904 paper [87] Ludwig Prandtl proposed a simplification of these equations for high Reynolds number (Re), wall-bounded flows, splitting the flowfield into two regions: the outer inviscid region, where classical potential flow solutions are valid, and the boundary layer region, where the effects of viscosity are significant. This allowed for the NS equations to be reduced into the Boundary Layer Equations (BLE), valid in a thin fluid layer adjacent to the wall, and enabled an analysis of such flowfields without needing to solve the full NS equations.

Physically, the BL represents the region of fluid close to a wall where the velocity relative to the wall goes to zero. This is due to the no-slip condition, where viscous forces locally act to retard fluid particles. The variation of velocity from zero at the wall to its freestream magnitude is represented by the BL velocity profile, with streamwise, wall-normal and spanwise components. The demarcation between freestream and BL flow is rather ambiguous in definition as the velocity profiles asymptotically converge to the freestream as one moves away from the wall. Typically, the physical extent of the BL has been taken to be the height above the wall at which the streamwise profile attains 99% its freestream magnitude U_∞, denoted as δ_{99}.

An important quantity in the analysis of boundary layers is the gradient of the velocity profile at the wall. This can be related to the shear stress exerted by the fluid on the wall, through its dynamic viscosity μ, and consequently the coefficient of skin-friction c_f:

$$\tau_{\text{wall}} = \mu \left.\frac{\partial u}{\partial y}\right|_{y=0} , \tag{1.1a}$$

$$c_f = \frac{\tau_{\text{wall}}}{\frac{1}{2}\rho U_\infty^2} . \tag{1.1b}$$

As a laminar boundary layer develops, it experiences the onset and growth of instabilities and inevitably breaks down into chaotic, turbulent BL flow. The process through which these instabilities are introduced, amplify and break down is referred to as *boundary layer transition*, visualized in Figure 1.1. The ordered nature of laminar flow sees viscous diffusion as the primary mechanism for wall-normal momentum transport in the BL. In contrast, a turbulent BL features additional transport through velocity fluctuations, encouraging the mixing of high and low momentum fluid regions [134]. These fluctuations sweep higher-momentum fluid toward the wall, leading to *fuller* velocity profiles and thus, stronger wall-normal velocity gradients. The direct implication of this is an increase in the wall shear stress and skin-friction (through equation 1.1) for a turbulent BL, as compared to laminar one.

The static pressure distribution, p, around a body is a significant factor that influences BL development. Favourable streamwise pressure gradients ($\partial p/\partial x < 0$) lead to accelerated fluid flow, subsequently leading to increased streamwise momentum within the BL. The opposite is true for adverse pressure gradients ($\partial p/\partial x > 0$) i.e. decelerated flow. The fluid particles within the boundary layer instead suffer a loss in kinetic energy. For strong adverse pressure gradients, the already low-momentum fluid close to the wall is unable to overcome the increasing pressure and stagnates, causing a detachment of the BL from the surface [75]. This process of *boundary layer separation* is accompanied by a

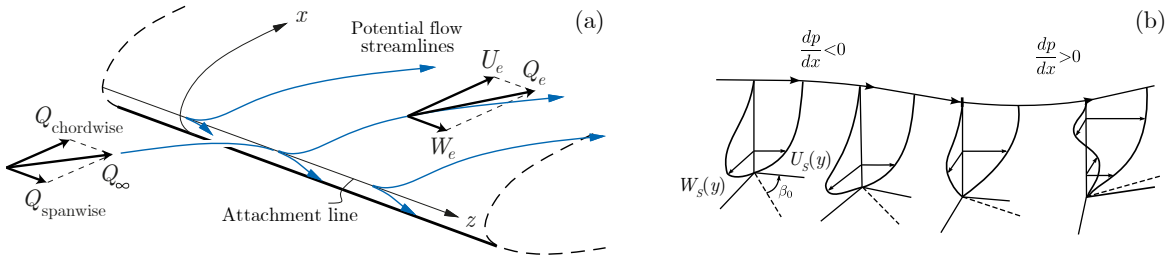

Figure 1.2: (a) Schematic of the inviscid streamlines at the leading edge of a swept airfoil, adapted from Drela [31], and (b) 3-D boundary layer profiles at various chordwise stations, from Lucas [68]. The angle between wall and potential streamlines is denoted by β_0.

low-pressure, low-velocity region of reversed flow. For aircraft in high-lift configurations, this causes a detrimental increase in the pressure drag experienced. It is for this reason that turbulent boundary layers can be preferred in specific industrial applications, as their higher momentum content enables greater resistance to separation. However, for example, an aircraft wing in cruise conditions would benefit more from the reduced skin-friction drag that a laminar BL offers. as flying with a turbulent BL leads to increased energy consumption, costs, and pollution.

Swept Wing Boundary Layer

While the dynamics of the BL over straight aircraft wings can typically be approximated by 2-D flat-plate flow, the swept wing features a fundamental difference: its inherent three-dimensionality. For the case of an *infinite* swept airfoil the incoming freestream velocity can be decomposed into a chordwise component, orthogonal to the leading edge, and a spanwise component, parallel to the leading edge. The analysis of an infinite airfoil implies spanwise invariance i.e. flow quantities are independent of the spanwise coordinate. This further implies that the pressure distribution over a swept airfoil only varies in the chordwise direction. Combined with an invariant spanwise velocity, this leads to curved inviscid streamlines over the wing, as depicted in Figure 1.2a.

The streamline curvature subjects the external fluid particles to centrifugal acceleration, which is balanced by the chordwise pressure gradient. However, the effects of viscosity within the boundary layer lead to a reduction in the magnitude of the velocity. This creates an imbalance between the pressure and centrifugal forces in the BL and causes a secondary movement of fluid particles in a direction orthogonal to the inviscid streamlines [101, 109]. The result is the generation of a crossflow velocity profile in accelerated (or decelerated) swept boundary layers (Figure 1.2b). While the BL now features three velocity components, it remains spanwise invariant and is locally only *quasi three-dimensional*, allowing for a simplification in its analysis.

The crossflow velocity profile is constrained by the no-slip condition at the wall and the freestream matching condition outside the BL, where it must also tend to zero. This leads to it attaining its maximum at some point within the boundary layer, resulting in a point of inflection in the velocity profile. An important result from inviscid LST is that the presence of an inflection point allows for the existence of *inviscid* instability modes, manifesting in a 3-D BL as co-rotating vortices closely aligned with the external streamlines [104, 101]. The viscous TS instability is suppressed in regions of accelerated flow while, in contrast, the crossflow velocity profile is strengthened. This in turn enables stronger amplification of CFI, complicating the use of natural laminar flow (NLF) airfoils in tackling transition on swept wings.

1.3. Stability of 3-D Boundary Layers

1.3.1. Transition Pathways

Transition to turbulence occurs through the amplification of perturbations to a laminar basic state of the fluid. The amplification is due to destabilizing mechanisms inherent to this basic state, either inviscid or viscous in nature as previously discussed. The disturbances are introduced into the fluid through a process known as receptivity, where environmental conditions (such as freestream vorticity, or surface roughness) are translated into disturbances within the laminar basic state [76, 70]. The process through which these disturbances are amplified can take multiple forms, depending on their initial amplitude and

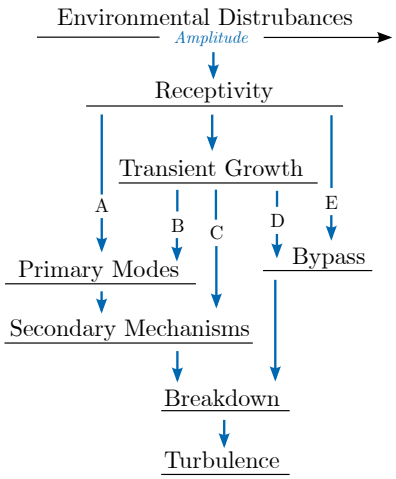

Figure 1.3: The various pathways to turbulence, described by Morkovin et. al [77]. Figure adapted from Lucas [68].

shape when introduced into the BL. Reshotko & Tumin [94], Schmid & Henningson [104] discuss these pathways to transition for wall-bounded shear flows. In most scenarios, the initial growth of disturbances is well predicted by modal linear stability theory, where disturbance amplitudes are assumed to be sufficiently small. However, some flow scenarios exhibit strong initial amplification of disturbances, bypassing the linear growth regime. For this reason, Morkovin [76] labelled this scenario *bypass transition*, where disturbances were amplified despite the prediction of stable, decaying eigenmodes by LST. The consensus on the mechanisms behind this form of transition is the presence of transient growth, a short-scale phenomena that leads to the rapid growth of instability [93, 104]. Mathematically, this is associated to the superposition of non-orthogonal eigenmodes where individually decaying modes can have a vectorial sum that exhibits growth [104]. The onset of either modal amplification or bypass transition is heavily dependent on the external disturbance level, with Morkovin et. al [77] proposing a series of routes through which disturbances are amplified.

- Path A is the traditional transition scenario, and occurs for low-amplitude external disturbance levels. Here, disturbances introduced into the BL undergo exponential amplification and include TS waves, crossflow vortices and Görtler instabilities. In CFI-dominated transition, the primary modes amplify and saturate at amplitudes of approximately 20% of the local freestream velocity [28, 92, 101], where the secondary instability manifests over a modulated baseflow and breakdown into turbulence is imminent. The gap between the onset of disturbances through receptivity and the development of non-linear, secondary instability is much larger than that between the onset of the secondary instability and breakdown. It is for these scenarios that LST has been able to sufficiently predict transition for flows with large linear-amplification regimes, through empirical correlations such as the e^N-method [126, 115].
- As external disturbance levels increase, transient growth takes part in the receptivity process. Here in path B, non-modal mechanisms leads to an initial growth (or decay) of disturbances that further downstream attain a modal nature, being exponentially amplified. This has been investigated numerically in 3-D boundary layers by Tempelmann et. al [120] and Kurz & Kloker [62] who show that non-modal streaks naturally feed into the modal CFI, and also observed in experiments by Zoppini et. al [139, 136]. Given its significant role in determining the initial conditions for modal instability onset, a study of this pathway forms part of the scope of this work.
- Path C represents a scenario where the external disturbance levels are high enough so that modal growth is overridden by transient amplification. In 2-D boundary layers Klebanoff et. al [57] have shown that high freestream turbulence levels induce streamwise vortices into the BL that grow non-modally. These vortices modulate the baseflow, generating regions of high shear and leading to the early onset of secondary instability mechanisms.
- Similar to path C, path D represents a scenario where transient growth is the dominant growth mechanism. However, unlike in path C where transition is caused by the secondary instability

that results from a BL modulated by streaks, a full spectrum of disturbances is now initiated by non-modal growth [68]. This was observed in 2-D boundary layers by Ergin & White [34] and in a swept wing BL by Zoppini et. al [136] where both works use an array of high-amplitude DRE to trigger this pathway. A strong amplification of the steady velocity streaks is seen followed by the onset of turbulent wedges. Ergin & White [34] also report the rapid amplification of high-frequency, unsteady disturbances and detail their interaction with the steady velocity streaks in leading to transition.

- With path E there exists no regime of linear amplification. The large external disturbance levels lead to a direct breakdown of the BL into turbulence with a questionable notion of laminarity and transition [68].

Paths A-C are the most relevant transition scenarios for the low-disturbance environments experienced by aircraft in flight. As both modal and non-modal growth pertinent to these scenarios is initially linear in nature, the following sections discuss the state-of-the-art in LST and its use in the study of CFI in swept wing boundary layers.

1.3.2. Modal Analysis

The Navier-Stokes equations form the mathematical basis for stability analysis of fluid flows. They are a non-linear, coupled system of partial differential equations (PDE) derived from conservation laws for mass and momentum. For low-speed aerodynamic boundary layer flows the effects of temperature are irrelevant and incompressibility may be assumed, along with Newtonian-fluid behaviour for the action of viscous stresses. This leads to a simplification of the governing equations, which in dimensional form are written as:

$$\boldsymbol{\nabla} \cdot \mathbf{q} = 0 \,, \tag{1.2a}$$

$$\frac{\partial \mathbf{q}}{\partial t} + (\mathbf{q} \cdot \boldsymbol{\nabla})\mathbf{q} = -\frac{1}{\rho}\boldsymbol{\nabla} p + \nu \nabla^2 \mathbf{q} \,, \tag{1.2b}$$

where $\mathbf{q}$ is the velocity vector $(u, v, w)^T$ in the Cartesian coordinate system, p is the static pressure and $\nu = \mu/\rho$ is the kinematic viscosity. The operator $\boldsymbol{\nabla}$ for three-dimensional, Cartesian vector fields is defined as $(\frac{\partial}{\partial x}, \frac{\partial}{\partial y}, \frac{\partial}{\partial z})^T$.

The crux of fluid stability analysis is the decomposition of the flowfield into a baseflow ($\mathbf{Q}$) and a disturbance field ($\mathbf{q}'$) [104]. The baseflow is computed as a laminar solution to the steady NS equations and is the known reference state upon which the disturbance field, also a solution of the NS equations, acts:

$$\mathbf{q}(x, y, z, t) = \mathbf{Q}(x, y, z) + \mathbf{q}'(x, y, z, t) \,, \tag{1.3}$$

where is noted that the baseflow is time-independent. A similar decomposition is also carried out for the pressure, such that it may be separated into its baseflow (P)[1] and disturbance (p') components. Upon substitution into the NS equations and subtraction of the governing equations for the baseflow[2], the non-linear disturbance equations are obtained. These equations describe the evolution of the velocity and pressure disturbances under the action of the baseflow:

$$\boldsymbol{\nabla} \cdot \mathbf{q}' = 0 \,, \tag{1.4a}$$

$$\frac{\partial \mathbf{q}'}{\partial t} + (\mathbf{Q} \cdot \boldsymbol{\nabla})\mathbf{q}' + (\mathbf{q}' \cdot \boldsymbol{\nabla})\mathbf{Q} + (\mathbf{q}' \cdot \boldsymbol{\nabla})\mathbf{q}' = -\frac{1}{\rho}\boldsymbol{\nabla} p' + \nu \nabla^2 \mathbf{q}' \,. \tag{1.4b}$$

The equations 1.4 retain the mathematical complexity of the full NS equations and are simplified further based on the type of analysis employed. Linear methods make the assumption of an infinitesimal disturbance field such that $\mathbf{q}' \ll \mathbf{Q}$ and $p' \ll P$. This allows for a linearisation of the disturbance equations through an order of magnitude analysis, neglecting the higher-order, multiplicative, non-linear terms. Henningson [47] shows through an integration of equation 1.4 that the main mechanisms for total disturbance energy growth are contained within its linear terms, and that the instantaneous total energy growth rates are independent of disturbance amplitude[3]. Thus the evolution of sufficiently small, finite-amplitude disturbances can be analysed through the linearised disturbance equations.

[1] In this context, P denotes the static pressure of the baseflow, contrary to it being used denote the total pressure.
[2] The subtraction of the governing equations for the baseflow is a valid operation, as it is a solution to the NS equations.
[3] The reader is referred to Henningson [47] and Schmid & Henningson [104] for a full derivation of these statements.

Parallel Flows & Local Stability

The parallel flow assumption implies that the baseflow is only dependent on the wall-normal coordinate and that the vertical velocity V is equal to zero i.e. $\mathbf{Q} = (U(y), 0, W(y))^T$. The streamwise and spanwise baseflow derivatives can then be eliminated from the linearised disturbance equations. The implication of this is that the flow stability characteristics are determined locally, at each spatial or temporal station, independent of the flow quantities at neighbouring locations. Neglecting the wall-normal velocity in the baseflow also suggests that the boundary layer does not grow spatially, as this would violate the parallel flow assumption.

The Fourier ansatz is introduced for the disturbance quantities; they exhibit wave-like behaviour in the streamwise and spanwise directions, and have shape functions that are only dependent on the wall-normal coordinate. This is equivalent to analysing the linearised disturbance equations in Fourier space. The disturbance velocities (and pressure) may thus be expressed in the form of complex exponentials:

$$\mathbf{q}'(x, y, z, t) = \tilde{\mathbf{q}}(y) e^{i(\alpha x + \beta z - \omega t)} \ , \tag{1.5}$$

where α and β are spatial wavenumbers and ω is the angular frequency. Inserting this ansatz into the linearised disturbance equations for 3-D parallel flows and re-arranging to eliminate the disturbance pressure leads to the classical, fourth-order[4] Orr-Sommerfeld (OS) equation [82, 117] and the inhomogeneous Squire equation [118]:

$$\left[(-i\omega + i\alpha U + i\beta W)\left(\frac{\mathrm{d}^2}{\mathrm{d}y^2} - (\alpha^2+\beta^2)\right) - \left(i\alpha\frac{\mathrm{d}^2 U}{\mathrm{d}y^2} + i\beta\frac{\mathrm{d}^2 W}{\mathrm{d}y^2}\right) - \frac{1}{\mathrm{Re}}\left(\frac{\mathrm{d}^2}{\mathrm{d}y^2} - (\alpha^2+\beta^2)\right)^2\right]\tilde{v} = 0 \ , \tag{1.6a}$$

$$\left[(-i\omega + i\alpha U + i\beta W) - \frac{1}{\mathrm{Re}}\left(\frac{\mathrm{d}^2}{\mathrm{d}y^2} - (\alpha^2+\beta^2)\right)\right]\tilde{\eta} = \left[i\alpha\frac{\mathrm{d}W}{\mathrm{d}y} - i\beta\frac{\mathrm{d}U}{\mathrm{d}y}\right]\tilde{v} \ , \tag{1.6b}$$

where $\tilde{v}$ and $\tilde{\eta}$ are the wall-normal velocity and vorticity shape functions respectively. The wall-normal vorticity is representative of the streamwise and spanwise disturbances through:

$$\tilde{\eta}(y) = i\beta\tilde{u}(y) - i\alpha\tilde{w}(y) \ . \tag{1.7}$$

The equations of 1.6 constitute an eigenvalue problem for the disturbance quantities and can be analysed through two related frameworks: the temporal approach and the spatial approach. With the former, the spatial wavenumbers α and β are assumed real and are prescribed quantities while the angular frequency ω constitutes the complex eigenvalue in the generalized problem. Similarly, in the spatial approach, ω is assumed real while the eigenvalue problem is solved for the complex spatial wavenumbers and their corresponding shape functions. The two approaches are related through Gaster's transformation [39], however the spatial approach is more frequently used in the analysis of BL flows and is employed in the current work. This is done as BL flows develop spatially, and instabilities such as stationary CFI are more appropriately analysed within the spatial framework[5]. In either case, the growth rate of a disturbance is determined through the imaginary components of the eigenvalue spectrum $(-\alpha_i, -\beta_i, -\omega_i)$. In the 3-D, spanwise-invariant, spatial framework, ω is real and $\beta_i = 0$[6], and so growth is contained solely within α_i. An infinitesimal perturbation is locally stable if $\alpha_i > 0$, neutral if $\alpha_i = 0$ and unstable for $\alpha_i < 0$.

The stability of parallel flows is governed by the existence of eigenmodes with $\alpha_i < 0$. The isoline representing $\alpha_i = 0$ can be used to demarcate the spatial boundary between unstable and stable regions for a series of eigenmodes, the so-called neutral stability curve. This is presented in Figure 1.4 for CFI in a swept BL. The interior of the neutral curve represents the region of instability, where disturbances in the wavenumber range bounded by it are amplified. The amplitude growth of disturbances between two streamwise stations, x_0 and x, can be computed through an integration of their corresponding α_i

[4] The equations are fourth-order in the wavenumber α.

[5] The wavenumbers ω and β are typically known a priori for CFI analyses and α is solved for.

[6] The assumption that $\beta_i = 0$ was introduced by Mack [71] for an infinite swept airfoil but is not necessarily verified for general 3-D flows. The reader is referred to Arnal [3] for a discussion on solutions to this problem.

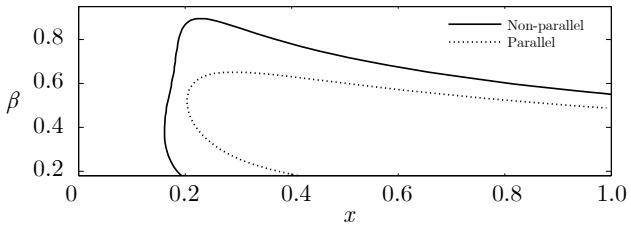

Figure 1.4: The neutral stability curves for CFI on an accelerated, swept boundary layer. Figure reproduced from Tempelmann et. al [120].

along horizontal lines in the stability diagram:

$$\frac{1}{A}\frac{\mathrm{d}A}{\mathrm{d}x} = -\alpha_i \ , \tag{1.8a}$$

$$\ln\left(\frac{A}{A_0}\right) = N = -\int_{x_0}^{x} \alpha_i(\xi,\beta,\omega)\mathrm{d}\xi \ , \tag{1.8b}$$

where A and A_0 are the amplitudes at x and x_0 respectively, and N is the N-factor. Traditional transition prediction methods such as e^N [115, 126] prescribe transition to occur when the most amplified wave exponentially grows to 7-10 times its initial amplitude i.e. its N-factor increases to a magnitude of 7-10, an empirical threshold that depends heavily on environmental conditions and the onset of non-linearities[7].

Effects of Non-Parallelism

Simen [113], Bertolotti et. al [7], Herbert [48] propose an alternative spatial analysis method that accounts for non-parallelism in flows such as a developing BL. Here, the Fourier ansatz used to derive the Orr-Sommerfeld system is modified to allow for a mild dependency of the shape function and wavenumber α on the streamwise coordinate.

$$\mathbf{q}'(x,y,z,t) = \tilde{\mathbf{q}}(x,y)e^{i\Theta(x,z,t)} \ , \tag{1.9a}$$

$$\Theta(x,z,t) = \int_{x_0}^{x} \alpha_i(\xi)\mathrm{d}\xi + \beta z - \omega t \ , \tag{1.9b}$$

where $\tilde{\mathbf{q}}(x,y)$ is a slowly-varying shape function and $\Theta(x,z,t)$ is the oscillatory phase function. The integration of α in the streamwise direction allows for the flow historicity to be accounted for. On introducing the modified ansatz into the linearised disturbance equations and retaining the streamwise derivatives of the baseflow, one obtains an elliptic set of PDE for the disturbance velocities and pressure. Through the slow-varying assumption, an order of magnitude analysis may be carried out to eliminate higher-order derivatives of $\tilde{\mathbf{q}}$ and α such that the governing equations are made parabolic[8] [7, 48]. The resulting system constitutes an initial-boundary value problem for the spatial evolution of modal disturbances, known as the Linear Parabolized Stability Equations, and can be solved through a marching technique.

The streamwise dependence of both the shape function and phase function introduces ambiguity into the PSE, in the sense that disturbance growth and oscillation may be captured by either part of the ansatz. In order to resolve this and maintain slow variation of the shape function, a normalization condition is introduced (see Herbert[48]) where residual streamwise growth and oscillation in the shape function are redirected into the complex exponent $\alpha(x)$ in the phase function:

$$\int_0^\infty \tilde{\mathbf{q}}^H \frac{\partial \tilde{\mathbf{q}}}{\partial x}\mathrm{d}y = 0 \ , \tag{1.10}$$

where $\tilde{\mathbf{q}}^H$ is the complex conjugate transpose of $\tilde{\mathbf{q}}$. This condition is enforced at each marching station and minimizes the growth and phase change present in $\tilde{\mathbf{q}}$. The integral in equation 1.10 also eliminates

[7] Arnal [3] and Reed [91] show that linear methods fall short in correlating crossflow-dominated transition.

[8] However, it is to be noted the pressure gradient term in the equations, $\frac{\partial p}{\partial x}$, is a source of residual ellipticity. Thus, the equations are not fully parabolic [66].

the wall normal dependency of α and implies that the kinetic energy of the shape function varies minimally between stations.

Tempelmann et. al [120] highlight differences between the neutral stability curves obtained using local and non-local analyses (Figure 1.4) although the authors note the mild sensitivity of the PSE-predicted neutral curve to its position of initialization. The PSE have also been extended to account for non-linear interactions between modes and the baseflow, making them a popular tool for the analysis of CFI in swept wing boundary layers [46] due to the presence of a large laminar extent of non-linear saturation [28, 92, 101]. The inclusion of non-linear terms in the governing equations is out of the scope of this work, as the focus is mainly on transition path B in Figure 1.3, where these terms do not play role.

Modal Instabilities on Swept Wings

The swept wing BL is host to four modal instability mechanisms that can lead to laminar-turbulent transition, based on geometrical features and freestream conditions [9, 101, 99].

The first is the familiar Tollmien-Schlichting instability, that takes the form of viscous, streamwise, travelling waves within the BL. First observed experimentally by Schubauer & Skramstad [107], TS waves are associated to natural transition in 2-D boundary layers, growing exponentially until they reach an amplitude of 1% of the local freestream velocity. A secondary instability then develops which induces various vortical structures that lead to the onset of turbulence. Highly susceptible to the external pressure gradient, TS waves are damped in accelerated BL flows and typically occur aft of the mid-chord in swept wings where the adverse pressure gradient leads to their rapid amplification [128, 120, 99].

Görtler [43] observed the existence of spatially growing, longitudinal vortices with spanwise periodicity in laminar boundary layers over concave walls. The instability mechanism was found to be inviscid in nature [89], and caused due to an imbalance between centrifugal forces and the wall-normal pressure gradient within the BL. The counter-rotating Görtler vortices manifest in regions of concave curvature, such as the trailing edge of reflex airfoils, and can lead to transition through secondary instabilities arising from a distortion of the mean velocity profile. They have a limited influence on the transition process downstream of the leading edge of swept wings, as the convex curvature present acts to stabilize these vortices[9].

The third source of instability on a swept wing can be due to its attachment line, which is represented by the locus of points of maximum pressure at its leading edge. Unlike in a 2-D airfoil, the flow at the leading edge of a swept wing does not fully stagnate and features a spanwise freestream velocity component, parallel to the leading edge. This can lead to a developing boundary layer along the attachment line that supports the amplification of viscous, modal instabilities that lead to transition similarly to those in 2-D flat-plate flows [44, 68]. Alternatively, the attachment line can convect turbulent structures created at a wing-fuselage junction along the span, contaminating the leading edge BL and resulting in early transition [90, 9]. Pfenninger [84] developed a criterion based on a Reynolds number, $\mathrm{Re}_{\mathrm{AL}}$, associated to the attachment line, where flow configurations with values of $\mathrm{Re}_{\mathrm{AL}}$ lower than 250 led to a damping of convected turbulent spots. Saric et. al [99] suggest that an appropriate selection of wing sweep and leading edge design such that $\mathrm{Re}_{\mathrm{AL}}$ is sub-critical is sufficient to eliminate attachment line contamination for a broad range of flow conditions.

Finally, the prevalent instability mechanism in accelerated, swept BL flows is the crossflow instability, introduced in Section 1.2. Due to its relevance in the current work, it will be discussed separately in the following section.

1.3.3. The Crossflow Instability

Receptivity & Mode Selection

Crossflow instabilities are initiated by the inflectional nature of the crossflow velocity profile [70], as discussed in Section 1.2. LST predicts that unstable modes manifest as either stationary ($\omega = 0$) or travelling ($\omega \neq 0$) waves, although their introduction into the BL is significantly dependant on environmental conditions, through receptivity [101].

Extensive experimentation was carried out by Bippes, Müller and co-workers at the Deutsches Zentrum für Luft-und Raumfahrt (DLR) [80, 28, 10] on mode selection in swept boundary layers. They

[9] For a full review of the Görtler instability, the reader is referred to Saric [103].

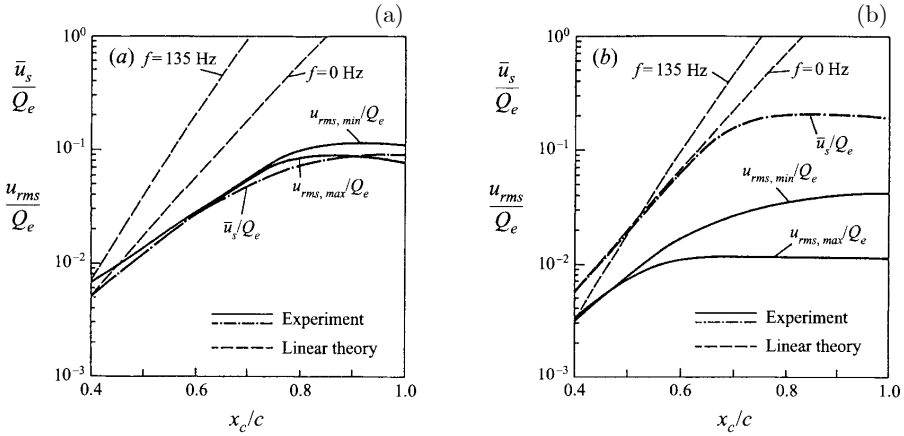

Figure 1.5: Spatial growth of stationary ($\bar{u}_s$) and travelling (u_{rms}) CFI for two freestream turbulence intensity levels (a) $T_u = 0.15\%$ (b) $T_u = 0.08\%$. From Dehyle & Bippes [28].

identified the dominant contributors in the transition process for a variety of environmental disturbance levels. Specifically, Müller [79] experimentally studied the BL on a swept flat-plate for two levels of freestream turbulence intensity T_u (Figure 1.5). For the higher level ($T_u = 0.15\%$) he observed that both stationary and travelling modes were excited within the BL and exhibited almost equal growth, in contrast to analyses with LST which predicted higher growth rates for travelling modes. On lowering T_u to 0.08%, the stationary modes were seen to be more amplified than travelling modes, saturating at much larger amplitudes. Dehyle & Bippes [28] conduct follow up experiments on a swept flat-plate and studied the effect of varying surface roughness in combination with freestream turbulence levels. They indicate that the stationary CFI are highly sensitive to surface roughness, increasing in amplitude with rougher configurations and undergoing earlier non-linear amplitude saturation. For a constant T_u and in the roughness range considered, the travelling modes were seen to be fairly insensitive to the roughness level and transition was dominated by the stationary modes. Moderately varying T_u only affected transition indirectly, attenuating the growth of the stationary vortices. It was only above turbulence levels of 0.2% that the travelling modes were initiated to sufficiently high amplitudes such that they dominated the transition process. A further increase in T_u was then seen to accelerate transition. Bippes [10] later emphasized that transition in low-disturbance environments was primarily due to the growth of the stationary CFI, initiated by surface roughness, while travelling modes only become relevant for higher freestream turbulence levels.

The role of low-intensity freestream fluctuations ($T_u < 0.2\%$) on crossflow-dominated transition was investigated by Downs & White [29] at the Texas A&M University (TAMU) through the use of turbulence screens, along with the effect of surface roughness. Their findings confirm the hypothesis by Bippes [10] that stationary modes are initiated by surface roughness, while turbulence levels mostly provide the initial conditions for the onset of travelling modes. Initial stationary disturbance amplitude was observed to be largely unaffected by freestream turbulence levels less than 0.19%, while the initial amplitudes of travelling modes were noted to be sensitive to both T_u as well as surface roughness. An attenuation of the stationary disturbance saturation amplitude was reported for increasing T_u, coinciding with observations by Dehyle & Bippes [28]. Nonetheless, transition was still seen to be dominated by stationary CFI for the T_u range tested, although enhanced turbulence levels advanced the location of transition.

Primary & Secondary Instabilities

As stationary CFI are the initiators of swept BL transition in the low T_u environments characteristic of free-flight, a detailing of the mechanisms through which they are introduced into BL, amplify, and break down becomes of interest.

Stability Experiments conducted at the Arizona State University (ASU) by Reibert et. al [92] attempted to characterize the development of stationary CFI over a 45° swept wing model, through a series of hot-wire scans characterizing the BL velocity fields. They make use of a full-span array of 6 μm high DRE, spaced at 12 mm, to trigger the onset of the most unstable stationary CFI mode. The resulting spanwise uniformity of the disturbance field allowed for an isolated crossflow vortex to be

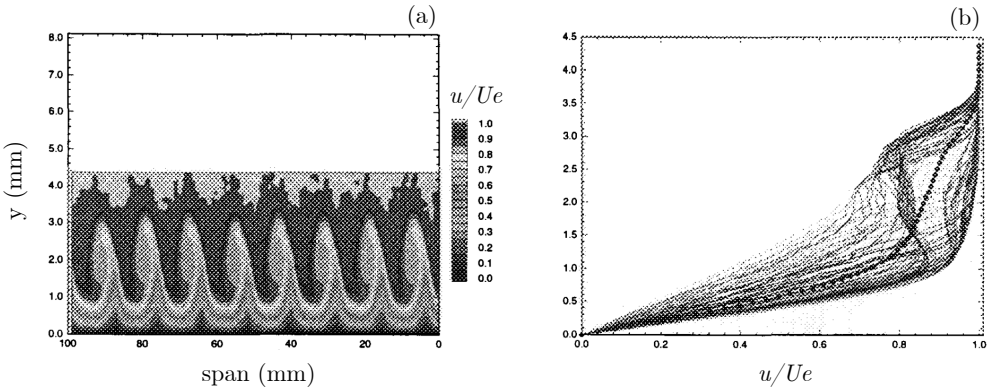

Figure 1.6: (a) Streamwise velocity contours obtained using hot-wire anemometry, depicting a BL modulated by stationary CFI initiated with a 12 mm spaced DRE array. (b) Spanwise array of BL velocity profiles corresponding to the velocity field in the left figure. Dots indicate the spanwise-averaged velocity profile. Figure reproduced from Reibert et. al [92].

analysed and meaningful comparisons with numerical predictions to be drawn. The crossflow vortex produced regions of upwelling and downwelling fluid, transporting low-momentum fluid away from the wall and high-momentum fluid toward it. For a sufficiently strong vortex, this leads to a distortion of the mean-flow and apparent rollover of low-momentum fluid, as seen in (Figure 1.6a). This distorted basic state features a series of spanwise accelerated, decelerated and doubly-inflected velocity profiles ((Figure 1.6b)) that lead to the onset of a secondary instability [59]. The spanwise spectral content of the stationary CFI is obtained through a Fourier analysis, and amplitudes of the dominant mode (with wavelength λ_1) and its first two harmonics (with smaller wavelengths λ_2 and λ_3) are computed through integration of the spectral peaks at each chordwise location. The first harmonic, λ_2, is seen to be measurable as λ_1 undergoes non-linear amplitude saturation, which occurs well before the location of transition. The experimental observations agree excellently with NPSE simulations conducted by Haynes & Reed [45] for the primary stationary mode. It is also noted that LPSE solutions qualitatively predict the initial CFI growth, indicating that non-linear effects initially weak.

Further simulations by Haynes & Reed [46] used an NPSE accounting for streamline curvature, still correlating well with the measurements by Reibert et. al [92]. In particular, the NPSE solution highlighted that the CFI development is sensitive to curvature effects, hence its inclusion in the NPSE is required for the numerical results to adequately match experiment. Additionally, convex surfaces were seen to have a stabilizing effect on the stationary CFI modes.

Serpieri & Kotsonis [111] carried out detailed spatial measurements of the stationary CFI evolution on a 45° swept wing model through highly-resolved, tomographic Particle Image Velocimetry (PIV), at the Delft University of Technology. Similarly to previous experimental work on stationary CFI, the most unstable stationary mode was forced through the use of an array of 9 mm spaced DRE, 10 μm in height. An overview of the disturbance field is obtained through fluorescent oil visualization (Figure 1.7) where uniformly spaced streaks were observed close to the transition front. These develop with a spanwise periodicity corresponding to the DRE forcing wavelength and are indicative of the non-linear, mean-flow deformation associated to the stationary CFI. The streaks were also observed to be slightly inclined with respect to the inviscid streamline, in agreement with LST predictions. The use of tomographic PIV enabled the measurement of all three velocity components within a 3-D measurement domain, characterizing the stationary CFI as a series of co-rotating vortices. The disturbance velocity component aligned with the vortex axis was noted to be nearly two orders of magnitude larger than the in-plane components. In spite of this relatively weak in-plane motion, it was seen to be effective in redistributing BL momentum, distorting the mean-flow and leading to the earlier onset of non-linearities in CFI-dominated transition (Figure 1.8a).

The mean-flow distorted by the stationary CFI becomes susceptible to unsteady secondary instabilities, superimposed on the stationary (primary) modes. Poll [85] first reported the existence of high-frequency fluctuations over stationary CFI in experiments with the BL on a swept cylinder. Kohama et. al [59] reported similar findings in a swept wing BL with transition caused by the stationary crossflow modes.

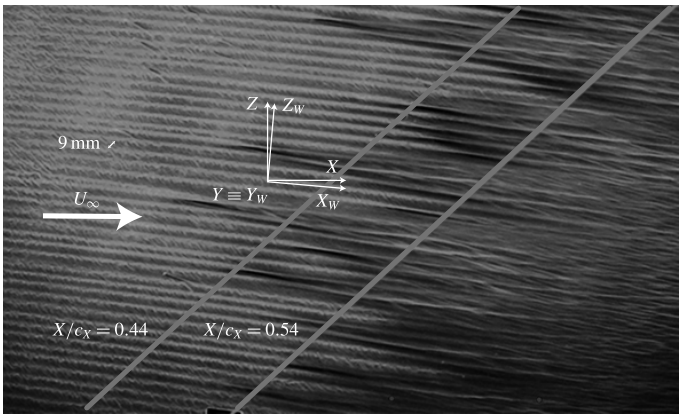

Figure 1.7: Fluorescent oil visualisation of CFI development and transition over a swept wing. Flow comes from the right. Bright streaks represent the imprint of the crossflow vortices (high-shear regions) on the wing surface, with the 9 mm spacing corresponding to the most amplified crossflow mode. The grey lines represent the approximate upstream and downstream bounds of the transition region. Figure reproduced from Serpieri & Kotsonis [111].

Numerical studies by Malik et. al [73] determined the evolution of primary CFI modes using NPSE simulations, and used a 2-D temporal eigenvalue framework to analyse the secondary instabilities on the ASU experimental configurations [92]. With an assumption that the secondary instabilities are of a convective nature, they used Gaster's transformation [39] to track its modes' spatial evolution. The results show good agreement with experimental findings. They presented a classification of the secondary instability into two main modes: type I and type II. The first is localised around the outer upwelling region of the primary CFI and is related to a spanwise gradient in the streamwise velocity component, for which it is commonly labelled as the $z-$mode. The type I instability is characterized by higher energy content and lower frequencies. The second mode, type II, is related to the wall-normal shear in the streamwise velocity (and hence known as the $y-$mode) and is located on top of the primary vortices. The type II modes features higher frequencies and lower energy, with respect to the type I modes. An estimation for the location of transition was made based on the amplification of secondary instabilities, and correlates well with transition measurements by Reibert et. al [92].

Further numerical research into the secondary CFI was conducted by various authors through DNS of swept boundary layers [50, 127, 12]. Högberg and Henningson studied the secondary instability in a swept Falkner-Skan-Cooke (FSC) BL, applying steady forcing of the primary modes and the use of volume body forcing to randomly excite the secondary instability. They identified the existence of a third instability mode, labelled type III, when the unsteady excitation was applied at upstream locations. These modes are located at the bottom of the primary CFI structure, within its inner-upwelling region, and are characterized by low frequencies. By shifting the volume forcing to more downstream locations, close to primary mode saturation, the high-frequency type I modes are triggered. These exhibit much larger growth rates when compared to the type III instability. Wasserman & Kloker [127] visualized the type I secondary instability as a sequence of convected, co-rotating helicoidal structures that exist on top of the outer-upwelling region of the primary stationary vortices. Their DNS study also confirmed the convective nature of the secondary instabilities, as hypothesized in previous theoretical work [52, 58]. In another study [128], they investigated instability evolution in the presence of pressure gradient changeover and detailed interactions between CFI and destabilized TS waves. A study conducted by Bonfigli & Kloker [12] uses DNS in combination with secondary linear stability theory (SLST) [73, 58] to investigate the secondary instabilities. The two techniques show good agreement in the extracted eigenfunctions and growth rates when their baseflows are tuned to match each other. The type I and type III instabilities are captured in both methods, however only SLST can predict the amplification of the type II mode. No destabilization of the type III instability is reported for solely stationary or travelling primary modes, which is expected as the type III instability is generated by the interaction between them [50]. The authors also identified the nature of the type I and type II modes to be of the Kelvin-Helmholtz (KH) type.

A first detailed experimental investigation regarding secondary CFI was carried out by White & Saric [132] at the ASU unsteady wind tunnel, on their 45° swept wing model. They employed hot-wire anemometry (HWA) to temporally resolve the velocity fluctuations of the secondary instabilities, under

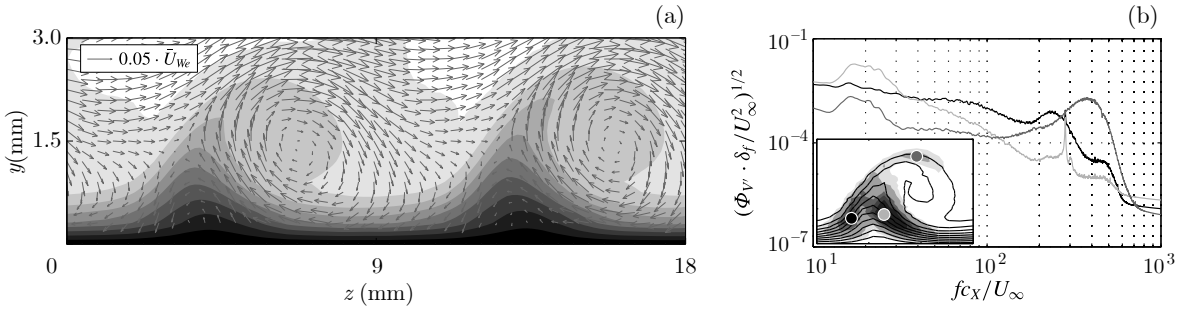

Figure 1.8: Chordwise slices of the stationary crossflow vortices (a) Time-averaged streamwise velocity contours (10 levels, from 0 to 1) with vectors representing the in-plane velocity components. (b) Non-dimensionalized spectra of the velocity fluctuations at secondary instability locations indicated by correspondingly coloured markers in the inset figure: light grey - type III, dark grey - type II, black - type I. Inset: Time-average velocity field (black lines) and velocity fluctuation field (greyscale contours). Figure reproduced from Serpieri & Kotsonis [111].

forcing through a DRE array at a freestream Reynolds number of Re$= 2.4 \times 10^6$. The type I and type II modes were identified, with their appearance and explosive growth documented as the cause of turbulent breakdown. The effect of varying Re, freestream turbulence, and acoustic forcing on the development of the secondary instability was also investigated. Forcing at a DRE wavelength lower than the most unstable primary mode (sub-critical) led to increased energy within the type I mode, while the type II mode was seen to dominate for super-critical forcing.

The study conducted by Serpieri & Kotsonis [111] also provides a dedicated experimental description of the secondary instabilities through bandpass-filtered hot-wire scans of the unsteady velocity field. All three secondary instability modes are characterized with their pertinent characteristics (Figure 1.8b), and compare well with previous experimental and numerical observations [50, 127, 12, 132]. Proper Orthogonal Decomposition (POD) of the velocity fields obtained using tomographic PIV was carried out in order to examine the spatial organisation of the secondary instability. The higher energy pair of POD modes is associated to the type III instability that arises from stationary-travelling primary mode interaction [50, 12] while the lower energy pair corresponds to the high-frequency type I mode. The most energetic POD mode identified presents structures aligned with the spanwise shear, and is attributed to a low-frequency oscillation of the stationary crossflow vortices. While the exact source of the oscillatory behaviour could not be determined, the high energy of the associated POD mode was amounted to a mean-flow distortion induced by this oscillation.

1.4. Roughness-Induced Transition on Swept Wings

The experiments conducted by Bippes & colleagues [80, 28, 10], discussed in Section 1.3.3, show that the receptivity and development of stationary CFI in swept BL flows is highly sensitive to surface roughness. Numerous studies have thus been dedicated to understanding the role of various types of roughness in conditioning CFI, broadly categorized into 2-D and 3-D elements. The former includes spanwise-uniform excrescences such as backward and forward facing steps [95], while the latter may be further sub-categorized into isolated [88, 60, 138], discrete [92, 100, 62, 139] and distributed (random) roughness elements [19, 30, 32, 112].

1.4.1. Crossflow Instabilities and Surface Roughness

Initial investigations of the effect of naturally-occurring surface roughness on swept wing BL transition were carried out experimentally by Radeztsky et. al [88]. The experiments were conducted on the 45° swept NLF(2)-0415 airfoil in a region of favourable pressure gradient, where transition is dominated by the crossflow instability. Naphthalene visualization of the flow over a rough painted (3.3 μm rms) surface finish revealed a jagged, highly local transition front composed of merging turbulent wedges, whose local characteristics were fixed in the spanwise coordinate. Using a hand-polished (0.1 μm rms) surface finish instead dramatically shifted the transition front downstream, although it remained topologically similar to the painted case. An isolated cylindrical element 6 μm in height was placed on top of the polished surface, close to the neutral point of the most unstable stationary mode, leading to the formation of a distinct turbulent wedge upstream of the natural transition front. This indicated that one of the

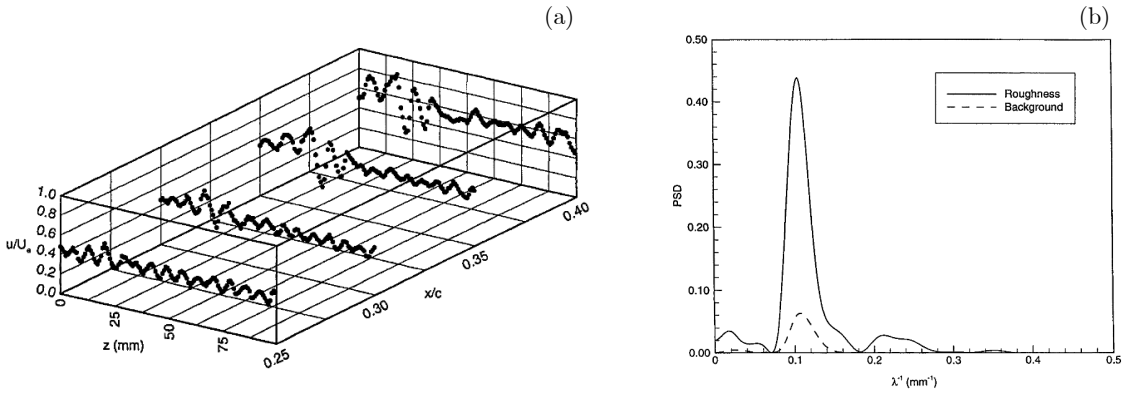

Figure 1.9: (a) Spanwise hot-wire scans showing streamwise vortex growth at a constant wall-normal distance for an isolated roughness element of height 6 μm. (b) Spanwise power spectrum of streamwise velocity from a hot-wire scan. Reproduced from Radeztsky et. al [88].

main results with roughness receptivity was a modification the initial amplitudes of the stationary CFI. Accordingly, transition occurred at lower N-factors as compared to a clean case. The spanwise hot-wire scans were also subjected to spatial spectral analysis, in order to correlate the roughness forcing to the emergence and development of the dominant crossflow mode (Figure 1.9). Additionally, transition was found to be unaffected by acoustic disturbances implying that receptivity to freestream fluctuations [80, 28] is due to turbulence levels.

These findings were further explored in the non-linear CFI saturation experiments undertaken by Reibert and colleagues [92] at the ASU, on a 45° swept airfoil (Section 1.3.3). Although the wing was polished to a low background roughness level (0.25 μm rms), the BL spectral content was seen to feature multiple CFI modes developing simultaneously, dominating the transition process. In an effort to increase the uniformity of the flow-field, an array of micron-size, cylindrical DRE was introduced with a spacing equal to the wavelength of the primary stationary CFI mode following Radeztsky et. al [88]. This was seen to concentrate the spectral energy into a single monochromatic mode, λ_1. The growth of the λ_2 and λ_3 harmonics was also measured, although no larger wavelength modes were detected. Setting the DRE spacing to $3\lambda_1$ generated the corresponding fundamental stationary mode, although significant disturbance energy was now contained within the λ_2, λ_3 and λ_4 harmonics due to non-linear interactions. Once more, there was no evidence of subharmonic modes i.e. no wavelength doubling.

Saric et. al [100] capitalized on this to develop a LFC technique applicable to CFI-dominated boundary layers. This is defined as *sub-critical* forcing, utilizing a 6 μm DRE array with a spanwise spacing two-thirds that of the most amplified CFI mode. The experimental setup used in this study was identical to that of Reibert et. al [92]. Naphthalene flow visualization shows that the transition front is delayed to approximately 80% chord, past the pressure minimum and the location of the natural transition front. In order to gain a more quantitative description of this process, spanwise hot-wire scans were acquired within the BL at various chord locations. The flowfield was seen to initially be dominated by CFI corresponding to the $\lambda_{2/3}$ forcing. These vortices exhibited amplitude growth up to $x/c = 0.5$ before undergoing saturation and strong decay, accompanied by a "washing-out" of the $\lambda_{2/3}$ structures. At locations beyond $x/c = 0.6$, the CFI spectrum is dominated by broadband energy distributed in the longer wavelengths. It was concluded that the sub-critically[10] forced 8 mm mode inhibited the growth of the more unstable 9 mm and 12 mm modes up to the point of its decay. Broadband disturbances initiated by natural roughness present on the model were then amplified and eventually led to transition.

The sub-critical DRE concept has been thoroughly investigated in subsequent studies by Saric and colleagues, involving variable roughness actuators [131] and a series of flight tests [99, 102], and has also been generalized into the numerical upstream flow deformation (UFD) technique [127, 74]. Here, sub-critical "control" modes are introduced into the BL to stabilize the naturally most amplified modes. However, the recent in-flight measurements by Saric et. al [102] highlight the high environmental sensitivity of DRE in practical applications; the sub-critical forcing resulted in significantly increased laminar flow on the swept wing model for only one in thirty flights. It was suggested that a more complete

[10] In the context of passive flow control using DRE, "sub-critical" refers to a forcing DRE wavelength less than the most unstable crossflow mode predicted by LST.

understanding of the CFI receptivity process was required, through DNS and lower-Re wind tunnel experiments, to fully characterize the effect of the roughness configuration and freestream turbulence on transition in this scenario.

1.4.2. Receptivity to Critical DRE

Early work on roughness-receptivity in swept boundary layers includes studies by Crouch [26], Ng & Crouch [81], Choudhari [21], who developed a parallel-flow framework to analyse receptivity within a Falkner-Skan-Cooke BL. The method was employed to model the DRE arrays used in the ASU experiments by Reibert et. al [92] and receptivity predictions seem to compare generally well with experiment. However, receptivity is over-predicted for forcing wavelengths longer than the most unstable primary stationary mode, possibly due to non-linear effects. Subsequent studies [8, 23] have shown that non-parallelism and curvature play a significant role in amplitude-based transition prediction for CFI. Collis & Lele [23] solve the steady NS equations for a swept, parabolic forebody and use this solution as the basic state for linearised receptivity computations including surface roughness. They find that receptivity for the most unstable CFI mode is under-predicted by nearly 77% when non-parallelism is neglected, with this error being maximum for roughness located near the first neutral point. As such, it becomes important for numerical methods used in the study of CFI receptivity to DRE to include non-parallel effects.

The swept wing configuration from the flight-test experiments by Carpenter et. al [18] and Saric et. al [102] was investigated numerically using DNS and the NPSE, in a study by Rizzetta et. al [96]. The leading-edge region of the experimental wing was approximated by a swept parabolic cylinder, over which three DRE array types were simulated: cylindrical, square and parabolic bump. The resulting flowfields were characterized using contours of the disturbance kinetic energy, which show the development of steady CFI aft of the roughness elements. Spanwise spectral analysis of the DNS fields was carried out at a location downstream of the roughness elements where modal behaviour is identified, and reveals that the initial spectral content is highly dependent on the roughness shape. Furthermore, the initial modal amplitudes at this location are seen to scale non-linearly with roughness heights ranged between 10 μm to 30 μm. These amplitudes are fed into an NPSE solver as initial conditions and used to compute CFI growth on two DNS baseflows: the clean parabolic cylinder and the experimental wing. The NPSE-computed stability for both cases is seen to agree well with DNS predictions for the cylindrical elements, although the NPSE and DNS results present a better downstream match when they share an identical baseflow.

Tempelmann et. al [122] at the KTH Royal Institute also conducted DNS of a swept wing boundary layer subject to forcing by DRE of various height, spacing, and chordwise placement. The geometrical configuration investigated was identical to the model used in wind tunnel experiments at the ASU [92, 100, 88]. The study was an effort to implement a roughness-receptivity model into the PSE framework using direct/adjoint optimization. Non-homogenous wall boundary conditions for the disturbance velocity was used to simulate the effect of surface roughness which is only valid for low-amplitude configurations i.e. for element heights less than 10% of the local displacement thickness [122]. The wind tunnel tests conducted by Reibert et. al [92] were in agreement with this condition and were hence used as additional validation for the proposed PSE receptivity model. Preliminary computations of disturbance amplitude evolution of the primary stationary CFI mode using the PSE/Adjoint-PSE method show excellent correspondence with DNS results, and are robust to the PSE initialization location. However, disturbance amplitudes were predicted to be 40% that of the experimental ones, possibly due to residual distributed surface roughness. This hypothesis was tested numerically by introducing a wavy wall upstream of the DREs to simulate natural roughness. The disturbance amplitudes were seen to be effectively receptive to the presence of this natural roughness. However, given its inherently random nature in an experimental framework, it was determined to be unlikely that it leads to a seemingly uniform discrepancy in the modal amplitudes. The authors concluded that the inability of the PSE-based receptivity model to match the ASU experiments [92] was most likely due to uncertainties in the location and size of the DREs on the wind tunnel model.

An experimental investigation into the effect of DRE height and chordwise location on CFI-dominated transition in a swept wing BL was performed by Zoppini et. al [139], at the Delft University of Technology. A set-up similar to Serpieri & Kotsonis [111] was used with cylindrical DRE arrays spaced at 8 mm, according to the most amplified crossflow mode predicted by LST. The authors characterize the roughness configuration through two scaling parameters; the ratio of the element height to the local BL

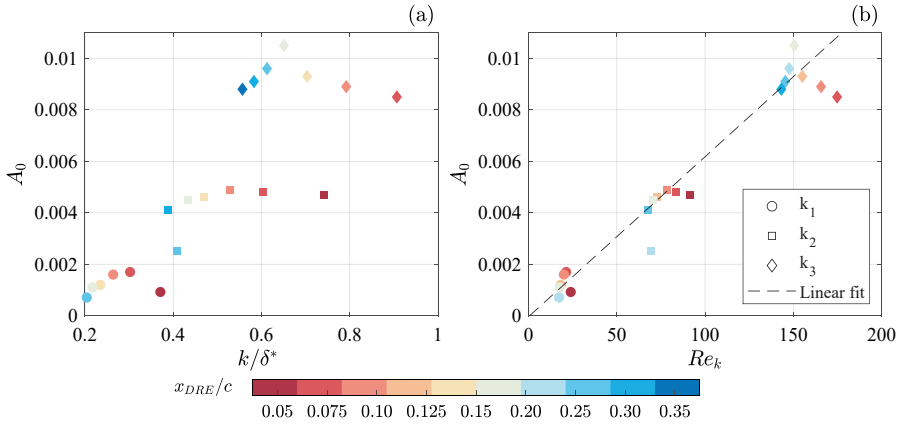

Figure 1.10: Initial instability amplitude (A_0) estimations obtained by matching NPSE simulations with experimental measurements, plotted against (a) k/δ^* (b) Re_k. Dashed line is a linear fit of the A_0 estimated data. The element heights k_1, k_2 and k_3 are 0.1 mm, 0.2 mm and 0.3 mm respectively and the colormap corresponds to the chordwise DRE location. Figure reproduced from Zoppini et. al [139].

displacement thickness (k/δ^*) [106, 122], and the roughness Reynolds number $Re_k = \frac{k \times |\mathbf{u}(k)|}{\nu}$ [42, 92, 62] where $|\mathbf{u}(k)|$ is the local BL velocity at the roughness height. Through infrared (IR) thermography measurements, a variation of these parameters was correlated with the location of the transition front, revealing a monotonic dependence on the forcing configuration. Higher amplitude roughness elements initiated stronger stationary CFI that advanced transition, while moving the arrays downstream postponed it. The experiments were complemented with NPSE simulations, from which the initial modal amplitude is estimated by matching the downstream amplitudes to that of the experiment. While the overall influence of the DRE on the initial CFI amplitudes is sufficiently captured through these estimations, inconsistencies with regard to a universal scaling law remain. However Re_k was seen to be more representative of modifications to the DRE amplitude, highlighting the importance of including the local BL momentum as opposed to using the purely geometrical k/δ^*. This is shown in Figure 1.10. Additionally, the flowfield in the direct vicinity of the elements is investigated using planar PIV. A momentum deficit region surrounded by higher-speed flow is identified behind each element, evolving into a high and low speed alternating pattern further downstream, as typical of stationary CFI dominated BLs. An estimation of the disturbance amplitudes through spectral analysis of the DRE wake suggested non-modal mechanisms affected the development of the near-element flow region, although this hypothesis could not be confirmed due to limited spatial resolution of the experimental measurements. Furthermore, it was seen that the wake is mostly influenced by blockage caused by the elements, rather than being affected by the local flow stability characteristics. Thus, the link between the physical DRE and the initial modal instability amplitudes is contained within the dynamics of the near-element flowfield, the study of which is key in understanding these intermediate steps in the receptivity process.

1.4.3. Near-Element Flow Features

Research into DRE wakes in swept boundary layers is limited due to the small scales and multiple parameters involved, and has primarily been through the use of DNS [14, 62]. However there exists a large body of work, both numerical and experimental, dedicated to understanding DRE wake behaviour in 2-D boundary layers [34, 61, 37, 20]. A majority of these studies characterize the downstream effect of the DRE array on the BL through the roughness Reynolds number Re_k. Forcing configurations that trigger transition to turbulence in the vicinity of the DRE array are considered *super-critical*, while those that lead to the onset of modal instability are termed *critical*. This allows for a bypass transition limit based on Re_k to be approximately defined, where a changeover in the dominant transitional mechanism is evident.

Stationary Flow Topology

DNS investigations by Brynjell & Rahkola [14] and Kurz & Kloker [62] provide and in-depth numerical characterization of the near-element flow topology for an array of cylindrical DRE. Their studies indicate the presence of a recirculation region and a horseshoe vortex (HSV) system that develop around each

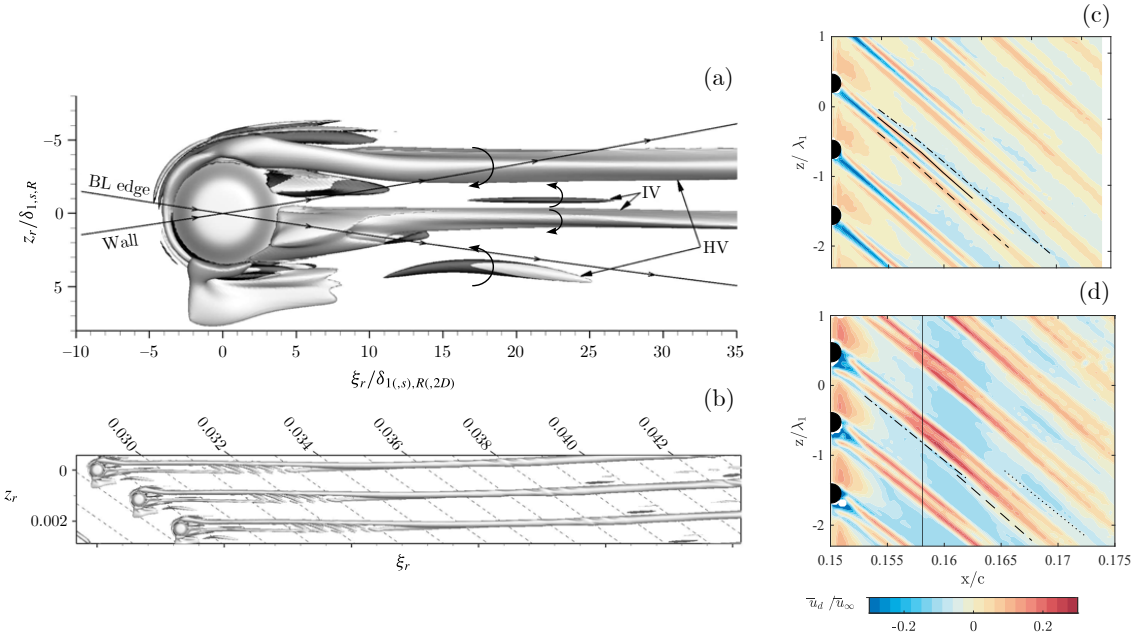

Figure 1.11: (a, b): Vorticity iso-surfaces ($\lambda - 2$ criterion) in the vicinity of the roughness element, from DNS by Kurz & Kloker [62]. The vorticity iso-surfaces are coloured according its sign. (a) HSV system developing around the roughness element in a swept BL. (b) Evolution of the DRE wake structures into stationary CFI further downstream for critical DRE amplitudes. (c, d): 3-D dual pulse PTV measurements of streamwise disturbance velocity in the DRE wake, from Zoppini et. al [139]. (c) Disturbance velocity contours corresponding to a critical DRE amplitude. Inner (—) and outer (- - -) high-speed streaks, and outer (-.-) low-speed streak. (d) Disturbance velocity contours corresponding to a super-critical DRE amplitude. High-speed streaks are stronger and merge downstream of the elements (black vertical line).

element in a DRE array. The horseshoe vortex system consists of two pairs of counter-rotating HSV legs: an outer pair generated upstream of the element possibly due to the roll-up of streamwise BL vorticity, and an inner pair that originates aft of the element within its re-circulation region. The inner HSV legs are likely induced by the outer HSV legs through the lift-up mechanism[11] [63] by re-distribution of momentum within the boundary layer. While the flow features in the vicinity of an element are similar for both 2-D and 3-D boundary layers, the presence of the crossflow velocity component in the 3-D scenario leads to significant differences in the downstream flowfield topology. The symmetry of the re-circulation region and HSV system typical of 2-D BL flows is lost in 3-D, where the preferred sense of rotation is dictated by the crossflow velocity component. Structures co-rotating with the crossflow are sustained while those that are counter-rotating are damped [62], leading to the retention of only one HSV leg within each of the two HSV pairs. For a critical Re_k, the sustained HSV legs are amplified and evolve into a stationary CFI further downstream. This is depicted in Figure 1.11. A super-critical forcing leads to a stronger re-circulation region aft of each element, amplifying unsteady disturbances initiated by element shedding to non-linear levels and leading to the development of turbulent wedges in the elements vicinity [14, 62].

The steady near-element features were experimentally described by Zoppini et. al [136], whose findings are in good agreement with previous DNS investigations [14, 62]. They conducted DRE wake measurements for critical and super-critical forcing configurations using tomographic particle tracking velocimetry (PTV). Contours of the streamwise velocity disturbances presented in Figure 1.11 show streaky structures forming in the vicinity of the element as a result of the developing HSV system. Both low- and high-speed streaks identified in the DRE wake first amplify before decaying further downstream. Spectral analysis is used to infer the BL content, allowing for an estimation of amplitude evolution of the individual spanwise Fourier modes. The total disturbance energy aft of the elements remains nearly constant, while that associated to the dominant CFI mode is seen to rapidly decay in this region. On the contrary, the first three harmonics of the dominant mode follow an opposing trend, first exhibiting algebraic growth followed by exponential decay. The individual Fourier mode

[11] The details of which are elaborated on in Section 1.5.2.

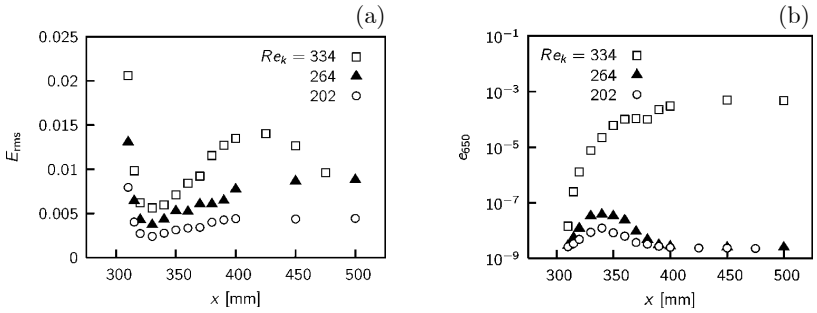

Figure 1.12: Streamwise evolution of disturbance energy aft of a DRE array in a Blasius boundary layer, for varying Re_k. (a) Steady disturbance energy evolution. (b) Unsteady energy contained in a frequency band centred around 650 Hz. Figure from Ergin & White [34].

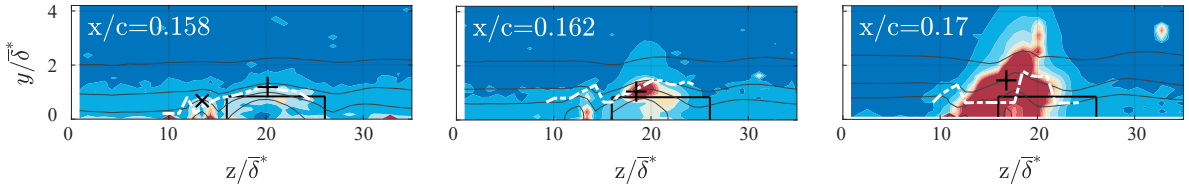

Figure 1.13: The wake of an isolated roughness element in a swept wing BL. Standard deviation contours of velocity acquired within $y-z$ planes using HWA are shown. Mean velocity isolines plotted every 20% of the freestream velocity. White dashed line indicates the wall-normal location of the BL velocity profile inflection points across the element wake. Maximum fluctuation locations on the top (+) and side (X) of the element are indicated. Figure reproduced from Zoppini et. al [138].

behaviour indicates the presence of non-modal mechanisms in the near-element flow region. Specifically, a comparison of the experimental energy with a model defined by White et. al [133] clearly indicates that transient growth is the dominant mechanism in the near-element flowfield. For critical DRE amplitudes, the streaks evolve into CFI downstream whose initial amplitudes are conditioned by the non-modal processes occurring in the DRE wake. The super-critical case features stronger high-speed streaks that merge shortly downstream of the elements location [62, 136]. This behaviour is strongly comparable to the flowfield pertaining to isolated roughness elements in 2-D and 3-D boundary layers [56, 61, 138]. The streaks merging is associated to the enhancement of the unsteadiness pertaining to the DRE wake region, eventually leading to the onset of turbulent wedges. The amplification of these unsteady disturbances plays a vital role in driving turbulent breakdown, however, a full characterization of their behaviour was not possible due to the lacking temporal resolution of the PTV measurements.

Unsteady Disturbances

While there exists no specific work detailing the spectrum of unsteady instabilities initiated by DREs in swept wing boundary layers, numerous investigations characterize their behavior in flat-plate boundary layers. Ergin & White [34] investigate DRE-induced velocity streaks in 2-D Blasius flow, using spanwise hot-wire scans. They estimate the disturbance energy corresponding to the stationary streaks, as well as the spatially-integrated unsteady energy contained within frequency bands centred around 650 Hz and 1300 Hz. Two competing mechanisms are identified: the rapid relaxation of the steady disturbance energy in the baseflow, and the growth of unsteady fluctuation energy (Figure 1.12). Specifically, for a critical forcing, the stationary streaks developing in the element wake stabilize before the unsteady disturbances grow to non-linear amplitudes. This leads to a stable baseflow in which the unsteady fluctuations decay without causing transition. However, for super-critical cases, the stronger element wakes and shear-layers lead to an explosive growth of unsteady fluctuations. This is coupled with a longer streamwise extent of the unstable baseflow, allowing for non-linear effects to set in and rapidly trigger turbulent breakdown. Furthermore, the authors postulate that the mechanism behind unsteady DRE-wake disturbances is of the KH-type, as opposed to hairpin vortices. This is drawn from the correlation between the spatial organisation of the unsteady fluctuations and local inflection points in the wall-normal and spanwise velocity profiles, as well as the dependence of unsteady disturbance growth on the Reynolds number.

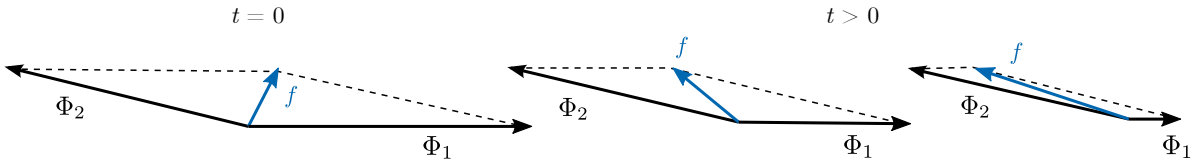

Figure 1.14: An illustration of transient growth using non-orthogonal basis vectors. The vector f is the sum of the eigenvectors Φ_1 and Φ_2, and strongly increases in length while both Φ_1 and Φ_2 decrease, albeit at different rates. Figure adapted from Schmid & Henningson [104].

A recent study by Zoppini et. al [138] involves the characterization of a high-amplitude isolated roughness element in a swept wing BL, through hot-wire measurements. The stationary flow features observed include the high and low-speed streaks developing in the element vicinity, comparably to previous numerical and experimental observations with roughness arrays [14, 62, 136]. The near-element flowfield is influenced by the presence of the crossflow velocity profile and loses its symmetry as it develops downstream. An analysis of the unsteady HWA velocity signals shows regions of high fluctuation intensity located on the top and sides of the element, corresponding to inflection points in the velocity profiles (Figure 1.13). In the element vicinity these fluctuations are seen to exhibit tonal behaviour, peak Strouhal numbers corresponding to the shedding ranges identified by Klebanoff et. al (0.18 - 0.25) [56]. The intensity of the frequency peaks is also seen to monotonically increase with Re_k. The unsteady disturbance spectrum attains a broadband nature further downstream, as the regions of high fluctuation intensity coalesce into a turbulent wedge.

The non-modal nature of disturbances in DRE wakes has been well established through these investigations, however, the large body of work on CFI and DRE has been developed within a modal framework i.e. exponential growth of unstable eigensolutions to the linear stability problem. The following section aims to detail the physics behind non-modally growing disturbances, in order to elucidate the correlation between the flow topology identified aft of DRE and the onset of primary stationary CFI.

1.5. Non-Modal Growth

LST has traditionally been used to identify the critical parameters for which infinitesimal perturbations are amplified in the baseflow, such as the Reynolds number. For values of Re lower than the critical value, all eigenmodes are predicted to be damped and the flow is considered stable. There however exist certain shear flows for which modal LST fails to explain experimental observations. In plane Poisueille flow, the critical Reynolds number according to eigenvalue predictions is well known to be 5772 [104] although transition can also be observed at Reynolds numbers as low as 1000. Similar findings exist for laminar Couette flow, which undergoes transition to turbulence despite being predicted to be unconditionally unstable by linear theory. These anomalies in experimental settings have long been associated to non-linearities not represented by LST. However, as discussed in Section 1.3.2, Henningson [47] shows that the growth mechanisms in the non-linear disturbance equations are contained exclusively within its linear terms. The non-linear terms are conservative in nature and act only to redistribute disturbance energy. It was thus concluded that a non-modal linear mechanism, independent of the presence of unstable eigenmodes, is responsible for disturbance growth in flow scenarios that are stable according to modal LST solutions.

1.5.1. Non-Normal Operators

Schmid & Henningson [104] study a model problem using the OS/Squire system (equation 1.6) for the evolution of a disturbance in a viscous fluid. They showed that while the eigenmodes of the system are stable and exponentially decay, a solution to the initial value-problem can exhibit algebraic amplification for short distances or times. This is possible when the associated set of eigenfunctions are non-orthogonal to each other, being solutions of a *non-normal* operator [125, 124]. Even if the individual, non-orthogonal eigenmodes undergo exponential decay, their superposition can exhibit an initial, transient growth before exponentially decaying according to the largest eigenfunction component. This is illustrated vectorially in Figure 1.14.

The non-normality of the linearised NS operator for small perturbations ($\mathcal{L}$) has been discussed by

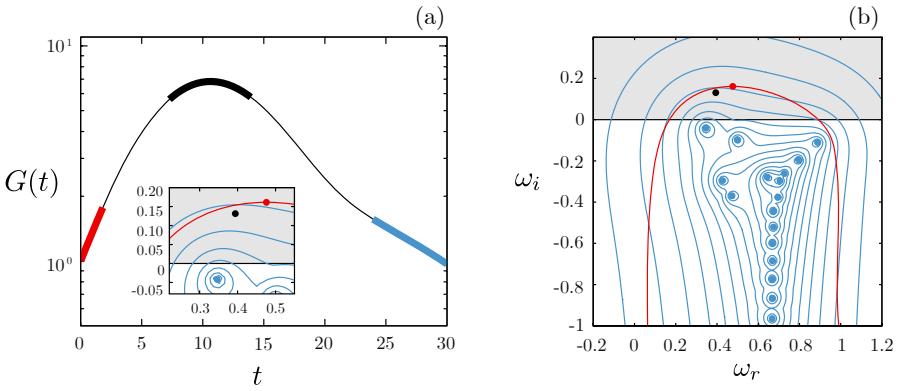

Figure 1.15: Transient disturbance energy growth in plane Poisueille flow for Re=1000 and $\alpha = 1$, reproduced from Schmid [105]. (a) Temporal evolution of normalised disturbance energy G(t). Coloured lines illustrate the connection between the spectral variables presented in (b) and the temporal energy growth. (b) Spectral characteristics of the stability operator. Blue dots are the discrete eigenvalues. The red line and red dot indicate the numerical range and numerical abscissa respectively. The $\epsilon-$pseudospectrum is represented by contours of the resolvent norm (blue lines), and the black dot marks the location of the Kriess constant.

Trefethen [125, 124], Schmid & Henningson [104] and Schmid [105] among others. They consider the temporal initial value problem and find that the maximum disturbance energy growth rate for very short times ($t = 0^+$) is given by the largest eigenvalue ($\lambda_{\max}$) of $(\mathcal{L} + \mathcal{L}^*)$, where $\mathcal{L}^*$ is the adjoint operator. This eigenvalue is known as the *numerical abscissa* and coincides with the maximum real part of the numerical range of $(\mathcal{L}+\mathcal{L}^*)$. A positive $\lambda_{\max}$ indicates that the numerical range extends into the unstable part of the complex $\omega-$plane and that transient growth can be expected for short times. Trefethen [125, 124] introduces the $\epsilon-$pseudospectrum of an operator $\mathcal{A}$ to measure the sensitivity of its eigenvalues to perturbations, with non-normal operators featuring highly sensitive eigenvalues. The resolvent norm of the operator ($\left\|(zI - \mathcal{A})^{-1}\right\|$), where $z \in \mathbb{C}$, is used to define the $\epsilon-$pseudospectrum as the parametrised set in the complex plane where:

$$\left\|(zI - \mathcal{A})^{-1}\right\| \geq 1/\epsilon \tag{1.11}$$

For $\epsilon = 0$, the spectrum of the operator $\mathcal{A}$ is retrieved[12], while $\epsilon-$pseudospectra contours for $\epsilon > 0$ are bounded by the curve where the resolvent norm is equal to ϵ^{-1}. A lower bound for the maximum attainable transient growth in time can be estimated through measuring the extent of the resolvent norm curves into the unstable domain, represented by the Kreiss constant κ [123]. An analysis of transient growth in plane Poisueille flow for Re= 1000 is presented by Schmid [105] and is depicted in Figure 1.15. The blue dots represent the eigenvalues of the operator and indicate modal stability for $t \gg 0$. The red line representing the numerical range is seen to extend into the unstable region of the $\omega-$plane indicating that transient growth can occur for short times. The maximum initial growth rate is dictated by the numerical abscissa (red dot). The location of the Kreiss constant is marked by the black dot in the $\epsilon-$pseudospectrum curves (blue lines), corresponding to the energy amplification peak for intermediate times.

1.5.2. Transient Growth Mechanisms

The spectral analysis of non-normal operators details the extent to which they may be able to support non-modal growth. However, the physical mechanisms behind which disturbances may be transiently amplified are not immediately revealed.

Early experimental work into transient growth in BL flows was by presented Ellingsen & Palm [33], who observed that low-amplitude, longitudinal vortices grow linearly in time when introduced into a 2-D BL. The vortices lead to the formation of a series of spanwise-alternating low and high velocity streaks that elongate in the streamwise direction. Landahl [63] proposed a physical explanation for the formation of these streaks: the wall-normal and spanwise disturbance velocities associated with the longitudinal vortices interact with the BL shear, causing a redistribution of streamwise momentum.

[12] As per the definition of the eigenvalue spectrum, $|\mathcal{A} - \lambda I| = 0$. A bounded inverse of $(zI - \mathcal{A})^{-1}$ thus does not exist, and the resolvent norm is infinite.

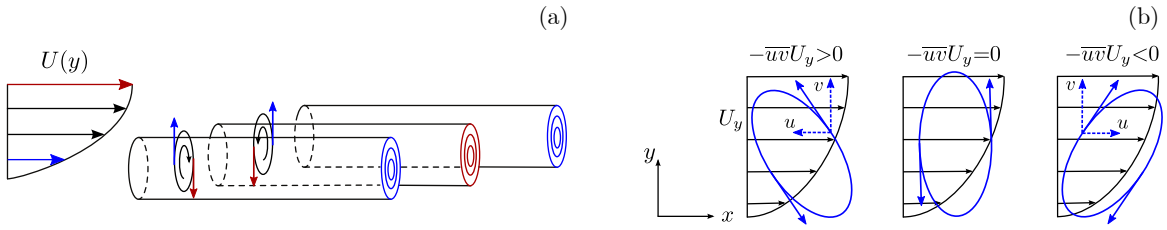

Figure 1.16: Physical mechanisms for transient growth, reproduced from Lucas [68]. (a) The lift-up effect and the (b) The Orr mechanism.

Low-momentum fluid close to the wall is lifted up away from it and high-momentum fluid at the edge of the BL is advected downward, toward the wall. The displaced fluid particles initially retain their streamwise momentum and manifest as perturbations in the streamwise BL velocity component. This process is referred to as the *lift-up* effect and is illustrated in Figure 1.16a. Numerous experiments by Klebanoff et. al [57, 55] report the presence of velocity streaks in Blasius boundary layers influenced by freestream turbulence, and highlight their significance in the occurrence of non-modal disturbance growth. Kendall [53] labels these streaks *Klebanoff modes* and shows that they are created as a result of the BL entraining freestream fluctuations and filtering out the high-frequency components.

An additional physical mechanism for transient growth was highlighted by Butler & Farrell [15] in shear flows, where a disturbance could extract energy from the baseflow through the action of a perturbation Reynolds stress. This is known as the *Orr mechanism* [82], depicted in Figure 1.16b. Disturbances tilted against the mean shear of the baseflow can borrow energy via the Reynolds stress production term $\int -\overline{uv}U_y \mathrm{d}y$, where $\overline{uv}$ is the Reynolds shear stress produced by the streamwise and wall-normal perturbations and U_y is the wall-normal gradient of the streamwise baseflow velocity component. The tilted disturbances first grow while being rotated towards an upright position, and then begin to lose energy to the baseflow as they align with the mean shear. Growth due to the Orr mechanism is weak in Blasius boundary layers when compared to the lift-up effect [120], but Åkervik et. al [140] note that it is responsible in optimally exciting TS waves. However, these two effects are often concurrent in 3D BLs [25, 13].

1.5.3. Numerical Non-Modal Stability

A popular approach to computing transient disturbance growth in shear flows has been through solving the linearised NS equations as an optimization problem. This allows for the definition of initial conditions that lead to the maximum amplification of disturbance kinetic energy within a given mathematical framework, labelled *optimal perturbations* by Farrell [36]. Non-modal growth associated to these disturbances is then defined as *optimal growth*.

Preliminary work on optimal growth in 3-D boundary layers was carried out by Breuer & Kuraishi [13], who used the temporal approach and showed that these boundary layers significantly support transient growth for various combinations of Re, spanwise wavenumber, sweep angle and pressure gradient. This was followed by investigations by Corbett & Bottaro [25], also using the temporal approach, who computed the characteristic of optimal perturbations in FSC boundary layers. They found that both modally and non-modally amplified disturbances are of similar structure, and that the optimal perturbations are initially vortices closely aligned with the external streamline that evolve into streaks further downstream. This is in contrast to non-modal growth in 2-D boundary layers, where the main modal instability mechanism (TS waves) bears no resemblance to the non-modal Klebanoff modes. Based on comparisons between the algebraic growth exhibited by the optimal perturbations and exponential growth of the LST-predicted, unstable crossflow modes, the authors conclude that the former complements the latter and acts to provide the initial conditions for modal amplification.

Pralits et. al [86] propose the use of a spatial approach to compute optimal perturbations in quasi 3-D boundary layers. Their approach allows for transiently growing disturbances to develop between regions sub-critical and super-critical to modal instability, which could not be predicted within the temporal framework. They describe a single-mode spatial approach, and one using the Parabolized Stability Equations, with the latter being comprehensively investigated by Byström [16].

The PSE are derived using alternative scaling arguments for its terms, proposed by Levin & Henningson [65], such that they are able to capture algebraic disturbance growth. Byström [16] then makes

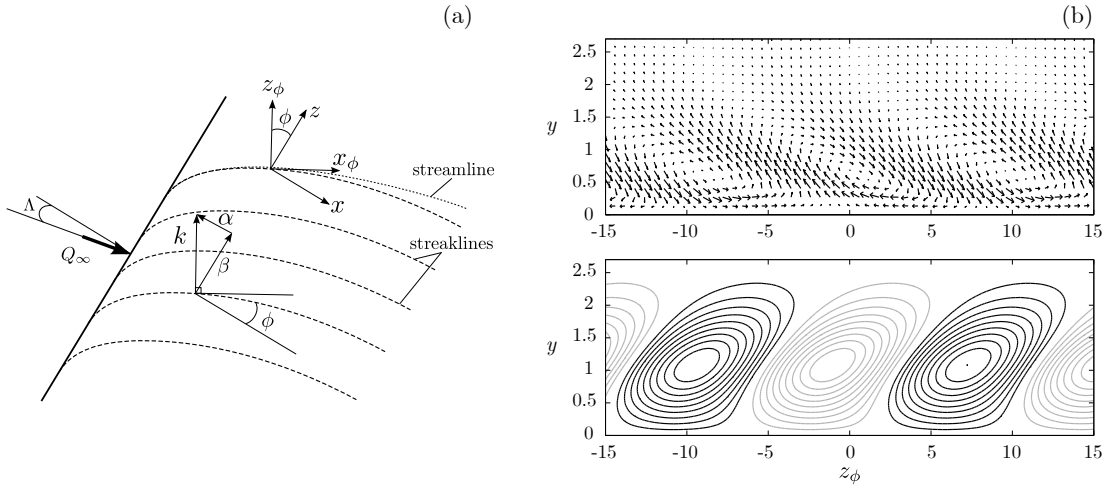

Figure 1.17: (a) Flow over an infinite flat plate with sweep angle Λ representing the PSE coordinate system (x_ϕ, z_ϕ) used by Byström [16]. The wave vector $(\alpha, \beta)^T$ is also shown. Reproduced from Lucas [68]. (b) Vectors of the optimal perturbation (upper) and contours of its downstream development (lower), projected onto the crossflow plane. Dark and light contour lines represent positive and negative streamwise disturbance velocities respectively. From Byström [16].

the assumption that the spatial evolution of the disturbances follows the external streamline, and formulates the problem in a non-orthogonal coordinate system aligned with them. This leads to a zero streamwise wavenumber α and reduces the problem to a two-dimensional flow in the streamwise coordinate. However, this assumption is seen to introduce cumulative integration errors into the disturbance growth computation, as the disturbance path deviates slightly from the external streamline. Byström [16] defines a *streakline* that follows the trajectory of the maximum of the disturbance velocity through space, determined through an iterative process. A direct/adjoint optimisation technique is used to compute the optimal disturbance growth, which is in turn used to update the streakline. The process is re-iterated until both the growth and the streakline converge. This methodology is applied to a FSC BL with a 45° sweep, for Hartree acceleration parameters of $\beta_H = 0.1$ (accelerated flow) and $\beta_H = -0.05$ (decelerated flow), depicted in Figure 1.17. The optimal perturbations are seen to be asymmetrical, counter-rotating vortices that are tilted against the mean crossflow shear, and are noted to evolve into exponential CFI modes at some downstream location. Similar to the temporal findings by Corbett & Bottaro [25], the conclusion is made that both modal and non-modal growth in swept BL flows produce disturbances of similar structure.

Tempelmann et. al [120] adapt the PSE framework described by Byström [16] for use in a Cartesian coordinate system. They modify the PSE ansatz (equation 1.9) to enforce a real streamwise wave number α, such that all growth is absorbed by the shape function $\tilde{\mathbf{q}}(x, y)$. This is important, as the decoupling of growth for the individual disturbance velocity components is a key feature of non-modal disturbance evolution. The wavenumber α is iteratively determined through the lines of constant phase of the velocity component containing the maximum disturbance energy, similar to the streakline concept proposed by Byström [16]. The authors note that the modified framework is limited to perturbations exhibiting only moderate streamwise amplification, due to the slow-varying assumption required for parabolization of the disturbance equations. Spatial optimal growth in accelerated and decelerated FSC boundary layers is computed for a wide range of parameters, once again through a direct/adjoint optimization technique. The physical mechanism for non-modal growth in swept boundary layers was determined to be a combination of both the lift-up effect and the Orr mechanism, with the initial vortices smoothly evolving into stationary CFI at downstream locations. The initial transient amplification of modal instabilities was seen to be larger for smaller sweep angles, and for disturbances initiated close to the region of neutral stability. A method for global optimization is also developed, by combining the adjoint-based technique with a Newton search line algorithm, to find the maximally amplified disturbances for all β and ω. As opposed to 2-D boundary layers, the global optimal disturbances are non-stationary and are 2-3 orders of magnitude more amplified than super-critical modal disturbances[13].

[13] In the context of accelerated FSC boundary layers. For negative Hartree parameters β_H, the TS wave is the globally optimal disturbance but is unable to be predicted by the proposed spatial framework.

The results presented in these numerical studies highlight the large extent to which non-modal growth can occur in swept boundary layers, effectively conditioning the onset and downstream development of CFI or leading to transitional scenarios. The optimal perturbations computed are expected to be similar in shape to disturbances introduced by roughness or freestream turbulence [120, 133], implying that non-modal growth in the vicinity of roughness elements [62, 136] can be modelled within a numerical framework.

1.6. Discussion & Research Gap

It is evident that DRE are effective initiators of stationary CFI in swept wing boundary layers [92, 100, 139]. However, the complex relationship between the DRE wake and the onset of BL instability is still not fully understood. Based on the literature discussed, this correlation appears to strongly depend on the physics of the near-DRE flow.

Previous investigations have shown that the DRE wake is highly non-modal and dominated by algebraic instability growth [62, 136]. However, the studies that describe these features are limited to computationally expensive DNS and wind tunnel tests involving hardly measurable scales. While more efficient numerical methods such as the PSE have been widely used to predict linear and non-linear modal instability evolution, no attempt has been made in simulating the stationary DRE wake structure within a comparably efficient, non-modal stability framework. Studies by Byström [16] and Tempelmann et. al [120] modify the classical, modal PSE to account for transient growth, but employ their methodology in the context of computing the optimal perturbations for swept boundary layers.

Additionally, Zoppini et. al [136] note that the behaviour of the steady wake features provides only a partial description of the initial stages of the DRE-receptivity process. Unsteady fluctuations also play a key role in the evolution of total and modal disturbance energy for high-amplitude DRE arrays, interacting with the steady structures to initiate either the modal crossflow instability or turbulent breakdown [34, 138, 139]. These mechanisms have been characterized in 2-D BL flows featuring DRE [34]; however a detailed experimental description of the unsteady near-element flowfield in swept wing boundary layers is absent.

1.7. Research Questions & Outline

A review of the latest advancements in swept wing boundary layer transition has been presented in the previous sections, along with the identification of gaps in the state-of-the-art. Based on the outlined considerations, the research questions that define this thesis work can be formulated:

How does the wake of an array of discrete roughness elements condition the onset of instability in a swept wing boundary layer dominated by crossflow instability?

1. **How accurately can the growth of stationary instabilities in the near-element flowfield be represented in a linear, parabolized stability framework?**
   (a) How can a linearised parabolic non-modal framework be derived from the NS equations to describe the evolution of DRE wakes?
   (b) To what extent do the assumptions of this framework limit the modelling of non-modal growth in the DRE wake?
2. **How can the structure of an experimentally measured DRE wake be used to initialize a numerical, linear, non-modal stability solution?**
   (a) How well do the predicted stability characteristics compare with experimental findings in literature?
   (b) How robust is the numerical solution to variations in the initial condition?
   (c) How well do analytic approximations model perturbations induced by the DRE wake?
3. **What role do unsteady fluctuations developing in the DRE wake play in the onset of BL instability?**
   (a) How are unsteady fluctuations in the DRE wake spatially organized? Can their spatial and spectral characteristics be associated to those of known instability types?
   (b) How do unsteady DRE-wake fluctuations affect the main mechanisms driving CFI receptivity to critical DRE configurations?
   (c) Through what mechanism can unsteady DRE-wake fluctuations lead to turbulent breakdown for super-critical DRE forcing?

The first and second sub-questions are directed toward the development of an efficient numerical framework capable of simulating disturbance growth in the vicinity of the DRE array, and its use in further understanding stationary CFI receptivity in swept wing boundary layers. The third sub-question addresses the experimental characterization of unsteady disturbances not represented in the numerical framework, and aims to identify their role in the DRE-receptivity process through HWA measurements conducted at the TU Delft low-speed facility.

In order to answer these questions, the remainder of this work is structured as follows: Chapter 2 discusses the governing equations used in the modelling of non-modal growth and their implementation into a numerical framework. A validation study for the developed tools is also presented. This is followed by a description of the experimental facility and test matrix, as well as the various measurement and post-processing techniques employed (Chapter 3). The stationary flow topology of the DRE wake is discussed in Chapter 4, and the results of simulations with initial conditions derived from it are presented. Chapter 5 outlines the experimental measurements of DRE-wake disturbances and details their spatial and temporal organisation, as well as the evolution of disturbance energy for critical and super-critical forcing configurations. Finally, Chapter 6 closes this thesis with a summary of its main findings, the conclusions drawn from them and recommendations for future work.

2

Numerical Methodology

2.1. Boundary Layer Baseflow

The study of fluid stability most commonly involves the decomposition represented by equation 1.3, where the solution to the NS equations is split into a baseflow, $\mathbf{Q}$, and disturbance field, $\mathbf{q}'$. If both $\mathbf{Q}$ and $\mathbf{q}'$ are themselves solutions to the NS equations, the equations can also be split into two separate sets governing $\mathbf{Q}$ and $\mathbf{q}'$ respectively (see Section 1.3.2). The equations for the baseflow can be independently solved for its velocity components and pressure, which then comprise the laminar reference state upon which the disturbance equations 1.4 are solved. The advantage here is that the baseflow and disturbance equations can be independently treated with simplifications, based on the specific flow configuration and type of analysis employed. This reduces the complexity in their numerical solution, in turn reducing the computational effort required as compared to conducting DNS of the full NS equations.

With regard to the baseflow, one such instance of this is in the analysis of high Reynolds number, wall-bounded flows. The NS equations in these cases can be simplified into Prandtl's BLE [87], through the use of scaling arguments to eliminate its higher-order terms. Although solutions of the BLE are approximations of solutions to the steady NS equations, they remain valid representations of the flowfield for non-separated boundary layers. For incompressible, 3-D, Newtonian flows, the BLE can be written as follows:

$$\frac{\partial U}{\partial x} + \frac{\partial V}{\partial y} + \frac{\partial W}{\partial z} = 0 \,, \tag{2.1a}$$

$$U\frac{\partial U}{\partial x} + V\frac{\partial U}{\partial y} + W\frac{\partial U}{\partial z} = U_\infty \frac{\partial U_\infty}{\partial x} + W_\infty \frac{\partial U_\infty}{\partial z} + \nu \frac{\partial^2 U}{\partial y^2} \,, \tag{2.1b}$$

$$U\frac{\partial W}{\partial x} + V\frac{\partial W}{\partial y} + W\frac{\partial W}{\partial z} = U_\infty \frac{\partial W_\infty}{\partial x} + W_\infty \frac{\partial W_\infty}{\partial z} + \nu \frac{\partial^2 W}{\partial y^2} \,, \tag{2.1c}$$

subject to the boundary conditions (BC):

$$U = V = W = 0, \quad y = 0 \,, \tag{2.2a}$$

$$U \to U_\infty, \quad W \to W_\infty, \quad y \to \infty \,, \tag{2.2b}$$

where U, V, W are the baseflow velocity components in a body-fitted coordinate system with x, y, z as the streamwise, wall-normal and spanwise coordinates respectively. The velocity components U_∞ and W_∞ correspond to the external, inviscid flowfield and are representative of the external pressure gradient. A feature of the BLE is the elimination of the static pressure as an unknown from the system of equations. Instead, the external pressure distribution is *impinged* onto the BL through the $y-$momentum equation, $\partial p/\partial y = 0$ [134]. Thus, the static pressure is constant within the BL in the wall-normal direction, equal to its corresponding magnitude in the freestream. Additionally, the BLE do not feature second-order spatial derivatives in the streamwise and spanwise coordinates, making them parabolic i.e. information propagation is one-way with the solution locally dependant on only its upstream state. This allows for them to be numerically solved using a more computationally-efficient spatial marching scheme.

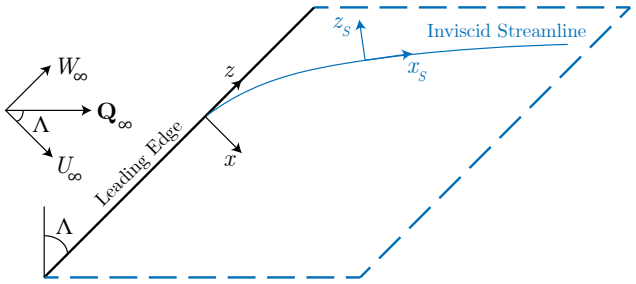

Figure 2.1: Schematic of an infinite swept flat-plate with coordinate systems aligned with the leading edge (x, z) and inviscid streamline (x_S, z_S). The sweep angle is denoted by Λ.

It is also of interest to mathematically define the BL displacement thickness, δ^*, and momentum thickness, δ_θ. The former physically represents the vertical displacement of the inviscid external streamlines due to the presence of the viscous BL, and is defined through mass conservation. The latter is representative of the shear stress exerted by the BL fluid flow on the wall and is defined through momentum conservation. Both δ^* and δ_θ will be used as a quantities for non-dimensionalization and comparison later in this work and are defined as:

$$\delta^* = \int_0^\infty \left(1 - \frac{U}{U_\infty}\right) \mathrm{d}y \,, \tag{2.3a}$$

$$\delta_\theta = \int_0^\infty \frac{U}{U_\infty}\left(1 - \frac{U}{U_\infty}\right) \mathrm{d}y \,. \tag{2.3b}$$

Falkner-Skan-Cooke BL

Given an arbitrary external flow configuration, the equations 2.1 can be numerically solved for the corresponding BL velocity components. However, there exists a class of external flows for which the spatially developing BL is self-similar i.e. its velocity profiles at various streamwise stations can be related to each other through a fixed scaling.

Consider the Cartesian coordinate system in equation 2.1 to be representative of an infinite, swept flat-plate (Figure 2.1). The chordwise coordinate, x, is oriented orthogonal to the leading edge of the plate, while the spanwise coordinate is parallel to it. The vertical coordinate, y, is normal to the surface of the flat-plate. The spanwise invariant nature of the flowfield implies that W_∞ is constant and also allows for the spanwise derivatives in 2.1 to be eliminated, reducing the equations to:

$$\frac{\partial U}{\partial x} + \frac{\partial V}{\partial y} = 0 \,, \tag{2.4a}$$

$$U\frac{\partial U}{\partial x} + V\frac{\partial U}{\partial y} = U_\infty \frac{\partial U_\infty}{\partial x} + \nu \frac{\partial^2 U}{\partial y^2} \,, \tag{2.4b}$$

$$U\frac{\partial W}{\partial x} + V\frac{\partial W}{\partial y} = \nu \frac{\partial^2 W}{\partial y^2} \,, \tag{2.4c}$$

where it is interesting to note that spanwise invariance results in a de-coupling of the $z-$momentum equation from the system. This makes the problem *quasi* 3-D as the equations 2.4a and 2.4b can be solved independently from equation 2.4c, which itself is now linear. Falkner & Skan [35] show that self-similar solutions to the equations 2.4 exist for external flows that follow a power law in the chordwise direction:

$$U_\infty(x) = U_{\mathrm{ref}} \left(\frac{x}{x_{\mathrm{ref}}}\right)^m \,, \tag{2.5}$$

with U_{ref} and x_{ref} as reference scales for velocity and length respectively, and m being the Falkner-Skan (FS) acceleration parameter. Introducing the similarity coordinate η:

$$\eta = y\sqrt{\frac{m+1}{2}\frac{U_\infty}{\nu x}} \,, \tag{2.6}$$

and the stream function ψ:

$$\psi = f(\eta)\sqrt{\frac{2}{m+1}U_\infty \nu x}\,, \tag{2.7}$$

such that $U = \partial\psi/\partial y$ and $V = -\partial\psi/\partial x$, with f being some function of η. Furthermore, making the assumption that $W = W_\infty g(\eta)$ for some other function $g(\eta)$, the spanwise invariant BLE in equation 2.4 can be transformed such that they are solely dependent on the similarity coordinate η. This reduces the system of PDE into a set of two de-coupled, ordinary differential equations (ODE):

$$\frac{\mathrm{d}^3 f}{\mathrm{d}\eta^3} + f\frac{\mathrm{d}^2 f}{\mathrm{d}\eta^2} + \beta_H\left(1 - \left(\frac{\mathrm{d}f}{\mathrm{d}\eta}\right)^2\right) = 0\,, \tag{2.8a}$$

$$\frac{\mathrm{d}^2 g}{\mathrm{d}\eta^2} + f\frac{\mathrm{d}g}{\mathrm{d}\eta} = 0\,, \tag{2.8b}$$

subject to transformed boundary conditions:

$$f = \frac{\mathrm{d}f}{\mathrm{d}\eta} = g = 0, \quad \eta = 0\,, \tag{2.9a}$$

$$\frac{\mathrm{d}f}{\mathrm{d}\eta} \to 1, \quad g \to 1, \quad \eta \to \infty\,. \tag{2.9b}$$

The equations 2.8 and 2.9 are known as the Falkner-Skan-Cooke equations [24] and describe a self-similar, spanwise invariant BL. The Hartree parameter $\beta_H = 2m/(m+1)$ in equation 2.8 represents the influence of the external pressure gradient. Positive and negative values of β_H are indicative of accelerating and decelerating BLs respectively, while 3-D Blasius flow is retrieved for $\beta_H = 0$. The BL velocity components can be obtained from the self-similar FSC solution as follows:

$$U = U_\infty \frac{\mathrm{d}f}{\mathrm{d}\eta}\,, \tag{2.10a}$$

$$V = -\frac{1}{2}\sqrt{\frac{2}{m+1}\frac{U_\infty \nu}{x}}\left((m+1)f + (m-1)\eta\frac{\mathrm{d}f}{\mathrm{d}\eta}\right)\,. \tag{2.10b}$$

$$W = W_\infty g \tag{2.10c}$$

The displacement thickness in equation 2.3a can be computed for a FSC BL through:

$$\delta^* = \sqrt{\frac{2\nu x}{(m+1)U_\infty}}\int_0^\infty \left(1 - \frac{\mathrm{d}f}{\mathrm{d}\eta}\right)\mathrm{d}\eta\,. \tag{2.11}$$

Baseflow Computation

The FSC equations are used to generate baseflows that act as prototype swept wing BLs for 3-D stability analyses. Their characteristics are largely determined by β_H and may be easily manipulated for use in parametric studies. General conclusions on 3-D BL stability can be drawn from analyses on FSC baseflows and have been featured in work by Högberg & Henningson [50], Schrader et. al [106] and Tempelmann et. al [120] among others. The advantage with solving the FSC equations as opposed to the BLE in equation 2.4 is that they are ODE, where the BL baseflow profiles are only a function of η. The numerical problem is reduced to only one spatial dimension i.e. the wall-normal coordinate, and the self-similar solution can then be analytically scaled as per equations 2.10 for the chordwise development of the BL. For BL baseflows that do exhibit self-similarity, this semi-analytic nature offered by the FSC equations is rather convenient. In addition to allowing for exact computation of the BL parameters and growth, the chordwise discretization errors encountered when solving the BLE are eliminated.

The equations 2.8 are solved for f and $\mathrm{d}f/\mathrm{d}\eta$ using an in-house solver, based on a second-order, finite difference approach. The baseflow velocity components are then computed according to equation 2.10 on a highly-refined grid within a given computational domain, and interpolated onto the numerical grid used for stability analyses. A sample computation of the FSC BL profiles is presented in Figure

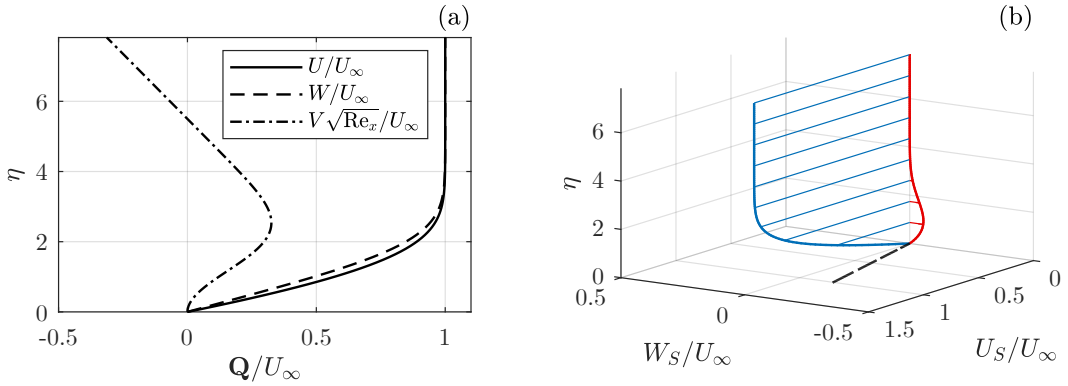

FIGURE 2.2: FSC BL velocity profiles for $m = 0.1$ with a sweep angle of 45°, at $x = x_{\mathrm{ref}}$. Coordinate system aligned with (a) the leading edge of the flat-plate and (b) the external streamline. Streamwise (red) and crossflow (blue) velocity profiles with the wall-shear line (- - -).

2.2a. The wall-tangential profiles can be projected onto a plane aligned with the external streamline through:

$$\begin{pmatrix} U_S \\ W_S \end{pmatrix} = \begin{pmatrix} \cos\phi_S & \sin\phi_S \\ -\sin\phi_S & \cos\phi_S \end{pmatrix} \begin{pmatrix} U \\ W \end{pmatrix} , \tag{2.12}$$

where U_S and W_S are the streamwise and crossflow velocity components respectively, and ϕ_S is the angle between the streamwise and chordwise coordinates. Figure 2.2b depicts the streamwise and crossflow profiles in the projected coordinate system.

2.2. Non-Modal Parabolized Stability Equations

2.2.1. Governing Equations

A starting point for the derivation of a non-modal, parabolized stability framework is with the non-linear disturbance equations 1.4 in Section 1.3.2. These were obtained by introducing the decomposition 1.3 into the incompressible NS equations and subtracting the equations for the baseflow. As the mechanisms for transient growth are linear in nature [104], a linearization of the equations 1.4 can be carried out. This is done through the assumption that disturbances are of infinitesimally small amplitudes, such that:

$$\mathbf{q}' \ll \mathbf{Q} , \tag{2.13a}$$
$$p' \ll P . \tag{2.13b}$$

The multiplication of small quantities of $\mathcal{O}(\epsilon)$, where $\epsilon \ll 1$, results in products of an even lower order of magnitude, namely $\mathcal{O}(\epsilon^2)$. For the equations 1.4, this means that the non-linear, multiplicative terms for the disturbance velocities can be neglected. The resulting linear system is then given by:

$$\boldsymbol{\nabla} \cdot \mathbf{q}' = 0 , \tag{2.14a}$$
$$\frac{\partial \mathbf{q}'}{\partial t} + (\mathbf{Q} \cdot \boldsymbol{\nabla})\mathbf{q}' + (\mathbf{q}' \cdot \boldsymbol{\nabla})\mathbf{Q} = -\frac{1}{\rho}\boldsymbol{\nabla} p' + \nu \nabla^2 \mathbf{q}' . \tag{2.14b}$$

We now introduce the Fourier ansatz 1.9, used in formulating the classical PSE [7, 49], into the linearized disturbance equations 2.14. The disturbances are thus assumed to exhibit wave-like behavior and are represented by the product of a shape function $\tilde{\mathbf{q}}(x, y)$ and phase function $\Theta(x, z, t)$. Inserting this

ansatz into equations 2.14 and assuming a spanwise invariant baseflow, we obtain:

$$0 = i\alpha\tilde{u} + \frac{\partial\tilde{u}}{\partial x} + \frac{\partial\tilde{v}}{\partial y} + i\beta\tilde{w}\,, \tag{2.15a}$$

$$\begin{aligned} 0 = {} & -i\omega\tilde{u} + Ui\alpha\tilde{u} + U\frac{\partial\tilde{u}}{\partial x} + \tilde{u}\frac{\partial U}{\partial x} + V\frac{\partial\tilde{u}}{\partial y} + \tilde{v}\frac{\partial U}{\partial y} + i\beta W\tilde{u} \\ & + \frac{i\alpha}{\rho}\tilde{p} + \frac{1}{\rho}\frac{\partial\tilde{p}}{\partial x} - \nu\left(2i\alpha\frac{\partial\tilde{u}}{\partial x} + i\tilde{u}\frac{\partial\alpha}{\partial x} + \frac{\partial^2\tilde{u}}{\partial y^2} - (\alpha^2+\beta^2)\tilde{u} + \frac{\partial^2\tilde{u}}{\partial x^2}\right)\,, \end{aligned} \tag{2.15b}$$

$$\begin{aligned} 0 = {} & -i\omega\tilde{v} + Ui\alpha\tilde{v} + U\frac{\partial\tilde{v}}{\partial x} + \tilde{u}\frac{\partial V}{\partial x} + V\frac{\partial\tilde{v}}{\partial y} + \tilde{v}\frac{\partial V}{\partial y} + i\beta W\tilde{v} \\ & + \frac{1}{\rho}\frac{\partial\tilde{p}}{\partial y} - \nu\left(2i\alpha\frac{\partial\tilde{v}}{\partial x} + i\tilde{v}\frac{\partial\alpha}{\partial x} + \frac{\partial^2\tilde{v}}{\partial y^2} - (\alpha^2+\beta^2)\tilde{v} + \frac{\partial^2\tilde{v}}{\partial x^2}\right)\,, \end{aligned} \tag{2.15c}$$

$$\begin{aligned} 0 = {} & -i\omega\tilde{w} + Ui\alpha\tilde{w} + U\frac{\partial\tilde{w}}{\partial x} + \tilde{u}\frac{\partial W}{\partial x} + V\frac{\partial\tilde{w}}{\partial y} + \tilde{v}\frac{\partial W}{\partial y} + i\beta W\tilde{w} \\ & + \frac{i\beta}{\rho}\tilde{p} - \nu\left(2i\alpha\frac{\partial\tilde{w}}{\partial x} + i\tilde{w}\frac{\partial\alpha}{\partial x} + \frac{\partial^2\tilde{w}}{\partial y^2} - (\alpha^2+\beta^2)\tilde{w} + \frac{\partial^2\tilde{w}}{\partial x^2}\right)\,. \end{aligned} \tag{2.15d}$$

Order of Magnitude Analysis

The classical PSE makes the assumption of a slowly varying shape function $\tilde{\mathbf{q}}(x,y)$, ensuring that disturbance growth and oscillation are mainly absorbed by the complex exponent $\alpha(x)$ in the phase function $\Theta(x,z,t)$. This is enforced through the normalization condition in equation 1.10. The combination of this strategy with using a local OS eigenmode as the initial condition has primarily been why the classical PSE is limited to the prediction of modal (exponential) growth. A re-evaluation of these assumptions is required for the development of a non-modal framework. To allow for independent growth of the disturbance velocity components, the classical normalization condition 1.10 is omitted. Thus, all disturbance growth is now absorbed by the shape function, while the oscillatory behaviour is retained by the phase function [120]. The result of this is that the chordwise wavenumber $\alpha(x)$ is now real, and must be determined through an alternative procedure[1]. However it is of importance to note that even with all disturbance growth absorbed by the shape functions, the slow-variance assumption of the classical PSE must still hold. This is crucial in ensuring that a parabolization the disturbance equations 2.15 can be carried out. As such, the derived framework may not be entirely valid for disturbances experiencing strong algebraic or exponential growth.

Following this, an evaluation of the relative orders of the terms in equation 2.15 is required. This will allow for an elimination of the lower-order terms in the system. Two characteristic length scales can be identified for BL flows, through which the terms of the PSE may be scaled: the chordwise length scale L and the wall-normal Blasius scale $\delta = \sqrt{\nu L/U_\infty}$. The characteristic velocity scale is taken to be the freestream velocity at the BL edge U_∞. Andersson [1] and Luchnini [69] study the non-modal growth of streaks in flat-plate BL through employing a scaling based on the BL approximation. This was extended to 3-D FSC boundary layers by Levin & Henningson [65], who attempt to appropriately scale the PSE for non-modal growth. They use two scalings, based on the BL as well as the classical PSE, and include terms relevant for both non-modal and exponential growth. This was further employed by Bagheri & Hanifi [6], Byström [16] and Tempelmann et. al [120] in their respective works on non-modal growth.

The scaling used by Tempelmann et. al [120], based on that proposed by Levin & Henningson [65] is used in the order of magnitude analysis present here. The BL approximation assumes that the wall-normal velocity component for both, baseflow and disturbance field is of $\mathcal{O}(\delta/L) = \mathcal{O}(\mathrm{Re}_\delta{}^{-1})$. The PSE scaling has the relative orders of the U, W and $\tilde{\mathbf{q}}$ as $\mathcal{O}(1)$ while the BL component V is assumed to be $\mathcal{O}(\mathrm{Re}_\delta{}^{-1})$. These two scalings are presented in Table 2.1, with both inherently featuring slow variation in the chordwise direction.

If only those terms in equations 2.15 of $\mathcal{O}(\mathrm{Re}_\delta{}^{-2})$ or lower with respect to both the BL and PSE

[1] A methodology tested in current work involved employing the classical normalization condition only for the real part of the chordwise wavenumber, $\Re(\alpha)$. However a converged solution could not be obtained, necessitating the use of an alternative procedure to determine α.

Table 2.1: Scales assumed for the quantities in equation 2.14, based on the BL as well as PSE approximation.

	x	y	U, W	V	u, w	v	p	α	β	ω
BL Scaling	L	δ	U_∞	$U_\infty\delta/L$	U_∞	$U_\infty\delta/L$	$\rho{U_\infty}^2\delta/L$	$1/\delta$	$1/\delta$	U_∞/L
PSE Scaling	L	δ	U_∞	$U_\infty\delta/L$	U_∞	U_∞	$\rho{U_\infty}^2$	$1/\delta$	$1/\delta$	U_∞/δ

scaling are retained, the system is reduced to the following:

$$0 = i\alpha\tilde{u} + \frac{\partial\tilde{u}}{\partial x} + \frac{\partial\tilde{v}}{\partial y} + i\beta\tilde{w}\,, \tag{2.16a}$$

$$\begin{aligned} 0 = {} & -i\omega\tilde{u} + Ui\alpha\tilde{u} + U\frac{\partial\tilde{u}}{\partial x} + \tilde{u}\frac{\partial U}{\partial x} + V\frac{\partial\tilde{u}}{\partial y} + \tilde{v}\frac{\partial U}{\partial y} + i\beta W\tilde{u} \\ & + \frac{i\alpha}{\rho}\tilde{p} + \frac{1}{\rho}\frac{\partial\tilde{p}}{\partial x} - \nu\left(2i\alpha\frac{\partial\tilde{u}}{\partial x} + i\tilde{u}\frac{\partial\alpha}{\partial x} + \frac{\partial^2\tilde{u}}{\partial y^2} - (\alpha^2+\beta^2)\tilde{u}\right)\,, \end{aligned} \tag{2.16b}$$

$$\begin{aligned} 0 = {} & -i\omega\tilde{v} + Ui\alpha\tilde{v} + U\frac{\partial\tilde{v}}{\partial x} + \tilde{u}\frac{\partial V}{\partial x} + V\frac{\partial\tilde{v}}{\partial y} + \tilde{v}\frac{\partial V}{\partial y} + i\beta W\tilde{v} \\ & + \frac{1}{\rho}\frac{\partial\tilde{p}}{\partial y} - \nu\left(2i\alpha\frac{\partial\tilde{v}}{\partial x} + i\tilde{v}\frac{\partial\alpha}{\partial x} + \frac{\partial^2\tilde{v}}{\partial y^2} - (\alpha^2+\beta^2)\tilde{v}\right)\,, \end{aligned} \tag{2.16c}$$

$$\begin{aligned} 0 = {} & -i\omega\tilde{w} + Ui\alpha\tilde{w} + U\frac{\partial\tilde{w}}{\partial x} + \tilde{u}\frac{\partial W}{\partial x} + V\frac{\partial\tilde{w}}{\partial y} + \tilde{v}\frac{\partial W}{\partial y} + i\beta W\tilde{w} \\ & + \frac{i\beta}{\rho}\tilde{p} - \nu\left(2i\alpha\frac{\partial\tilde{w}}{\partial x} + i\tilde{w}\frac{\partial\alpha}{\partial x} + \frac{\partial^2\tilde{w}}{\partial y^2} - (\alpha^2+\beta^2)\tilde{w}\right)\,. \end{aligned} \tag{2.16d}$$

The second-order chordwise derivatives of the shape function $\tilde{\mathbf{q}}$ are of $\mathcal{O}({\mathrm{Re}_\delta}^{-3})$ with respect to both scalings and are eliminated from the system. Although these derivatives are the main source of ellipticity in the disturbance equations 2.15, the equations 2.16 remain only quasi-parabolic. Li & Malik [66], Andersson et. al [2] show the PSE exhibit residual ellipticity through the chordwise disturbance pressure gradient $\partial\tilde{p}/\partial x$, with numerical instability manifesting for small marching steps. The solution to this problem has been to omit this term from the $x-$momentum equation 2.16b. However, this is not justified by the current order of magnitude arguments, as $\partial\tilde{p}/\partial x$ is $\mathcal{O}({\mathrm{Re}_\delta}^{-1})$ with respect to the PSE scaling. Tempelmann et. al [120] show that non-modal computations within FSC BLs are negligibly affected by the presence of the pressure gradient term, when compared with results from DNS. It is thus omitted from the current framework as well, to relax the requirements on the numerical grid and allow for higher levels of refinement.

Another quantity of interest is the term $\tilde{u}\,\partial V/\partial x$, which is absent from the classical PSE formulation. This term is $\mathcal{O}({\mathrm{Re}_\delta}^{-1})$ with respect to the BL scaling and was concluded to be important for non-modal growth by Bagheri & Hanifi [6]. The system of equations 2.16 is thus a composite, parabolized[2] approximation valid for both modal and non-modal spatial disturbance evolution. This framework will be referred to as the Non-Modal Parabolized Stability Equations (NmPSE) for the remainder of this work.

Determination of Chordwise Wavenumber

The parabolized equations 2.16 can be solved using a spatial marching scheme for the shape functions $\tilde{\mathbf{q}}$ and chordwise wavenumber α, given a baseflow and with β and ω as inputs. With the classical PSE, the normalization condition 1.10 is used to iteratively determine α at each marching station. However, the non-modal framework omits the use of this condition and instead assumes α to be real function of x.

The objective is to determine $\alpha(x)$ such that the largest periodic variations in the disturbance quantities are captured by their respective phase functions. This is done to ensure that the second-order chordwise derivatives of the shape functions remain negligible with respect to the other terms in 2.16. Tempelmann et. al [120] propose a methodology based on the *lines of constant phase* of a disturbance quantitiy. This is illustrated in Figure 1.17a, where the streaklines represent the disturbance trajectory.

[2]Excluding the pressure gradient term $\partial\tilde{p}/\partial x$

The chordwise wavenumber α can then be determined through the wavenumber vector $\mathbf{k} = (\alpha, \beta)^T$ as:

$$\alpha = -\beta \tan(\phi(x)) \ . \tag{2.17}$$

However $\mathbf{k}$, and subsequently $\phi(x)$ are unknowns and must also be computed as part of the solution procedure. Tempelmann et. al [120] determine these according to the velocity component containing the maximum disturbance energy, $\mathbf{u}_\phi$, when computing the optimal perturbations for FSC BLs. This is done as the optimal perturbations take the form of velocity streaks, and contain most of their distrubance energy in the direction perpendicular to $\mathbf{k}$. The lines of constant phase are then determined according to:

$$\phi(x) = \tan^{-1}\left(\frac{\tilde{w}(x,y)}{\tilde{u}_(x,y)}\right), \quad y = \max_y(|\mathbf{u}_\phi(x,y)|) \ . \tag{2.18}$$

An iterative procedure is used to globally determine $\alpha(x)$. The PSE are initially solved up to the end of the marching domain using the external streamline as a first estimate. The chordwise wavenumber is then computed globally according to equations 2.17 and 2.18 and the PSE are re-solved with the new estimate for α. The process is repeated until convergence is attained. It should be noted that the use of the lines of constant phase for the determination of α is only valid for disturbances closely aligned with the external streamline, as is the case with CFI.

The current work employs a modified form the methodology in Tempelmann et. al [120], as proposed by Lucas [68]. This involves determining $\alpha(x)$ locally at each marching station, rather than through global iterations. The shape functions $\tilde{\mathbf{q}}$ can be scaled using a complex amplitude function $A(x)$, such that:

$$\tilde{\mathbf{q}} = A(x)\widehat{\mathbf{q}}(x,y) \ , \tag{2.19}$$

where $\widehat{\mathbf{q}}$ is the normalized shape function vector. As per its definition, $\alpha = (1/i\mathbf{q}')\ \partial\mathbf{q}'/\partial x$ [3]. Evaluating this using the normalized shape function in equation 2.19 at $y(\widehat{\mathbf{q}} = 1)$, and with the consideration that α is real:

$$\Re\left(\frac{1}{i\mathbf{q}'}\frac{\partial \mathbf{q}'}{\partial x}\right) = \alpha(x) + \Re\left(\frac{1}{iA}\frac{\partial A}{\partial x}\right) \ . \tag{2.20}$$

The first term in equation 2.20 represents oscillatory behaviour captured by the phase function $\Theta(x,z,t)$, while the second term encompasses oscillations in the shape function. Expanding the complex amplitude as $A = |A|\exp(i\theta)$, the second term can be written as follows:

$$\Re\left(\frac{1}{iA}\frac{\partial A}{\partial x}\right) = \Re\left(\frac{1}{i|A|}\frac{\partial |A|}{\partial x} + \frac{\partial \theta}{\partial x}\right) = \frac{\partial \theta}{\partial x} \ . \tag{2.21}$$

To ensure that most of the oscillatory behaviour is captured by the phase function, we redirect the contribution from the second term in 2.20 into the exponent $\alpha(x)$. This bears some resemblance to the normalization condition for the classical PSE shape functions, adapted for use in a non-modal context:

$$\Re\left(\frac{1}{iA}\frac{\partial A}{\partial x}\right) = 0 \implies \frac{\partial \theta}{\partial x} = 0 \ . \tag{2.22}$$

The condition that $\partial\theta/\partial x = 0$ implies that the complex phase of the disturbance quantities, at a $y-$location determined by A, is held constant i.e. the complex wavenumber α is computed based on the lines of constant phase. This is a stronger form of the methodology proposed by Tempelmann et. al [120] and also allows for α to be determined locally.

The complex amplitude $A(x)$ used to normalize the shape functions in 2.19 is taken to be the maximum of the chordwise disturbance velocity, $\max_y(\tilde{u}(x,y))$. At each marching station, an initial estimate for $\alpha(x)$ is made using the external streamline, as per equation 2.17, and a solution to the NmPSE is computed. The shape function $\tilde{u}(x,y)$ is then used to compute $\partial\theta/\partial x$ and the normalization condition 2.22 is enforced iteratively as:

$$\alpha^{k+1} = \alpha^k + \left(\frac{\partial \theta}{\partial x}\right)^k \ , \tag{2.23}$$

where k here denotes the current iteration. Convergence is attained when the following criterion is satisfied:

$$(\alpha^k - \alpha^{k-1})\mathrm{Re}_{\delta_0^*} < 10^{-9} \ . \tag{2.24}$$

2.2.2. Non-Dimensionalization

The NmPSE discussed in the previous section are derived in a dimensional fashion, and are here non-dimensionalized for use in the numerical solution procedure. This is carried out using the freestream velocity at the inflow, U_0, and the BL inflow displacement thickness, δ_0^*, as the respective reference velocity and length scales. The relevant quantities in the equations 2.16 are then non-dimensionalized as follows:

$$\begin{aligned} \bar{u} &= \frac{\tilde{u}}{U_0}, \quad \bar{v} = \frac{\tilde{v}}{U_0}, \quad \bar{w} = \frac{\tilde{w}}{U_0}, \quad \bar{U} = \frac{U}{U_0}, \quad \bar{V} = \frac{V}{U_0}, \quad \bar{W} = \frac{W}{U_0}, \\ \bar{p} &= \frac{\tilde{p}}{\rho U_0^2}, \quad \bar{x} = \frac{x}{\delta_0^*}, \quad \bar{y} = \frac{y}{\delta_0^*}, \quad \bar{\alpha} = \alpha\delta_0^*, \quad \bar{\beta} = \beta\delta_0^*, \quad \bar{\omega} = \frac{\omega\delta_0^*}{U_0} . \end{aligned} \tag{2.25}$$

Substituting the dimensional quantities in equations 2.16 for those in 2.25 leads to:

$$0 = \frac{U_0}{\delta_0^*}\left(i\bar{\alpha}\bar{u} + \frac{\partial\bar{u}}{\partial\bar{x}} + \frac{\partial\bar{v}}{\partial\bar{y}} + i\bar{\beta}\bar{w} \right) , \tag{2.26a}$$

$$\begin{aligned} 0 = {} & \frac{U_0^2}{\delta_0^*}\left(-i\bar{\omega}\bar{u} + \bar{U}i\bar{\alpha}\bar{u} + \bar{U}\frac{\partial\bar{u}}{\partial\bar{x}} + \bar{u}\frac{\partial\bar{U}}{\partial\bar{x}} + \bar{V}\frac{\partial\bar{u}}{\partial\bar{y}} + \bar{v}\frac{\partial\bar{U}}{\partial\bar{y}} + i\bar{\beta}\bar{W}\bar{u} + i\bar{\alpha}\bar{p} \right) \\ & - \frac{\nu U_0}{{\delta_0^*}^2}\left(2i\bar{\alpha}\frac{\partial\bar{u}}{\partial\bar{x}} + i\bar{u}\frac{\partial\bar{\alpha}}{\partial\bar{x}} + \frac{\partial^2\bar{u}}{\partial\bar{y}^2} - (\bar{\alpha}^2 + \bar{\beta}^2)\bar{u} \right) , \end{aligned} \tag{2.26b}$$

$$\begin{aligned} 0 = {} & \frac{U_0^2}{\delta_0^*}\left(-i\bar{\omega}\bar{v} + \bar{U}i\bar{\alpha}\bar{v} + \bar{U}\frac{\partial\bar{v}}{\partial\bar{x}} + \bar{u}\frac{\partial\bar{V}}{\partial\bar{x}} + \bar{V}\frac{\partial\bar{v}}{\partial\bar{y}} + \bar{v}\frac{\partial\bar{V}}{\partial\bar{y}} + i\bar{\beta}\bar{W}\bar{v} + \frac{\partial\bar{p}}{\partial\bar{y}} \right) \\ & - \frac{\nu U_0}{{\delta_0^*}^2}\left(2i\bar{\alpha}\frac{\partial\bar{v}}{\partial\bar{x}} + i\bar{v}\frac{\partial\bar{\alpha}}{\partial\bar{x}} + \frac{\partial^2\bar{v}}{\partial\bar{y}^2} - (\bar{\alpha}^2 + \bar{\beta}^2)\bar{v} \right) , \end{aligned} \tag{2.26c}$$

$$\begin{aligned} 0 = {} & \frac{U_0^2}{\delta_0^*}\left(-i\bar{\omega}\bar{w} + \bar{U}i\bar{\alpha}\bar{w} + \bar{U}\frac{\partial\bar{w}}{\partial\bar{x}} + \bar{u}\frac{\partial\bar{W}}{\partial\bar{x}} + \bar{V}\frac{\partial\bar{w}}{\partial\bar{y}} + \bar{v}\frac{\partial\bar{W}}{\partial\bar{y}} + i\bar{\beta}\bar{W}\bar{w} + i\bar{\beta}\bar{p} \right) \\ & - \frac{\nu U_0}{{\delta_0^*}^2}\left(2i\bar{\alpha}\frac{\partial\bar{w}}{\partial\bar{x}} + i\bar{w}\frac{\partial\bar{\alpha}}{\partial\bar{x}} + \frac{\partial^2\bar{w}}{\partial\bar{y}^2} - (\bar{\alpha}^2 + \bar{\beta}^2)\bar{w} \right) . \end{aligned} \tag{2.26d}$$

Multiplying these equations by δ_0^*/U_0^2 and recognizing the Reynolds number $\mathrm{Re}_{\delta_0^*} = U_0\delta_0^*/\nu$, the equations 2.26 become:

$$0 = i\bar{\alpha}\bar{u} + \frac{\partial\bar{u}}{\partial\bar{x}} + \frac{\partial\bar{v}}{\partial\bar{y}} + i\bar{\beta}\bar{w} , \tag{2.27a}$$

$$\begin{aligned} 0 = {} & -i\bar{\omega}\bar{u} + \bar{U}i\bar{\alpha}\bar{u} + \bar{U}\frac{\partial\bar{u}}{\partial\bar{x}} + \bar{u}\frac{\partial\bar{U}}{\partial\bar{x}} + \bar{V}\frac{\partial\bar{u}}{\partial\bar{y}} + \bar{v}\frac{\partial\bar{U}}{\partial\bar{y}} + i\bar{\beta}\bar{W}\bar{u} + i\bar{\alpha}\bar{p} \\ & - \frac{1}{\mathrm{Re}_{\delta_0^*}}\left(2i\bar{\alpha}\frac{\partial\bar{u}}{\partial\bar{x}} + i\bar{u}\frac{\partial\bar{\alpha}}{\partial\bar{x}} + \frac{\partial^2\bar{u}}{\partial\bar{y}^2} - (\bar{\alpha}^2 + \bar{\beta}^2)\bar{u} \right) , \end{aligned} \tag{2.27b}$$

$$\begin{aligned} 0 = {} & -i\bar{\omega}\bar{v} + \bar{U}i\bar{\alpha}\bar{v} + \bar{U}\frac{\partial\bar{v}}{\partial\bar{x}} + \bar{u}\frac{\partial\bar{V}}{\partial\bar{x}} + \bar{V}\frac{\partial\bar{v}}{\partial\bar{y}} + \bar{v}\frac{\partial\bar{V}}{\partial\bar{y}} + i\bar{\beta}\bar{W}\bar{v} + \frac{\partial\bar{p}}{\partial\bar{y}} \\ & - \frac{1}{\mathrm{Re}_{\delta_0^*}}\left(2i\bar{\alpha}\frac{\partial\bar{v}}{\partial\bar{x}} + i\bar{v}\frac{\partial\bar{\alpha}}{\partial\bar{x}} + \frac{\partial^2\bar{v}}{\partial\bar{y}^2} - (\bar{\alpha}^2 + \bar{\beta}^2)\bar{v} \right) , \end{aligned} \tag{2.27c}$$

$$\begin{aligned} 0 = {} & -i\bar{\omega}\bar{w} + \bar{U}i\bar{\alpha}\bar{w} + \bar{U}\frac{\partial\bar{w}}{\partial\bar{x}} + \bar{u}\frac{\partial\bar{W}}{\partial\bar{x}} + \bar{V}\frac{\partial\bar{w}}{\partial\bar{y}} + \bar{v}\frac{\partial\bar{W}}{\partial\bar{y}} + i\bar{\beta}\bar{W}\bar{w} + i\bar{\beta}\bar{p} \\ & - \frac{1}{\mathrm{Re}_{\delta_0^*}}\left(2i\bar{\alpha}\frac{\partial\bar{w}}{\partial\bar{x}} + i\bar{w}\frac{\partial\bar{\alpha}}{\partial\bar{x}} + \frac{\partial^2\bar{w}}{\partial\bar{y}^2} - (\bar{\alpha}^2 + \bar{\beta}^2)\bar{w} \right) . \end{aligned} \tag{2.27d}$$

These equations 2.27 comprise the non-dimensionalized, non-modal PSE, accompanied by homogeneous boundary conditions:

$$\bar{u} = \bar{v} = \bar{w} = 0, \quad \bar{y} = 0, \tag{2.28a}$$

$$\bar{u} \to 0, \ \bar{v} \to 0, \ \bar{w} \to 0, \quad \bar{y} \to \infty . \tag{2.28b}$$

As will be discussed in the following section, the BC 2.28b is not prescribed at infinity but rather at some finite distance H sufficiently away from the wall. If the terms are grouped based on multiplications with $\bar{\mathbf{q}}$, $\partial\bar{\mathbf{q}}/\partial\bar{y}$, $\partial^2\bar{\mathbf{q}}/\partial\bar{y}^2$ and $\partial\bar{\mathbf{q}}/\partial\bar{x}$, the system of equations 2.27 can be written in matrix form:

$$\mathbb{A}\bar{\mathbf{q}} + \mathbb{B}\frac{\partial\bar{\mathbf{q}}}{\partial\bar{y}} + \mathbb{C}\frac{\partial^2\bar{\mathbf{q}}}{\partial\bar{y}^2} + \mathbb{D}\frac{\partial\bar{\mathbf{q}}}{\partial\bar{x}} = 0\,. \tag{2.29}$$

Additionally, the momentum equations in the matrix $\mathbb{A}$ contain a set of common convective-diffusive terms. These are hereafter represented by C and written as:

$$C = -i\bar{\omega} + i\bar{\alpha}\bar{U} + i\bar{\beta}\bar{W} + \frac{1}{\mathrm{Re}_{\delta_0^*}}\left(\bar{\alpha}^2 + \bar{\beta}^2 - i\frac{\partial\bar{\alpha}}{\partial\bar{x}}\right). \tag{2.30}$$

The contents of the matrices $\mathbb{A}$, $\mathbb{B}$, $\mathbb{C}$, $\mathbb{D}$, are presented in Appendix A.1.

2.2.3. Numerical Solution

Spatial Discretization

The NmPSE 2.16 and its boundary conditions 2.28 constitute a spatial initial-boundary value problem, and are solved using a numerically using a marching scheme. The computational domain is constructed over a swept, flat-plate, with the coordinate axes oriented parallel and normal to the leading edge of the plate. The BL baseflow for stability computations is computed as a FSC BL, discussed in Section 2.1. The stability domain, however, does not begin at the leading edge of the plate. Instead, it starts at a point downstream of the leading edge, where the BL has attained a finite thickness. The vertical extent of the domain, H, is constant, and prescribed to be at least five times that of the inflow BL height. This is done to account for the chordwise development of the BL and disturbance shape functions, allowing for sufficient distance away from the wall at which the external BCs can be imposed. The BL and disturbance profiles asymptotically attain their freestream values and so the selection of a larger vertical extent of the domain reduces numerical errors at the freestream boundary.

The BL baseflow and shape function solutions are computed at discrete points in the computational domain, depicted in Figure 2.3. As the problem is spanwise invariant, the discrete grid only extends in the chordwise, x, and wall-normal, y, directions. A Chebyshev pseudo-spectral collocation method is employed for discretization in the wall-normal direction. Here, the discrete collocation points are generated as the roots of the n^{th}-order Chebyshev polynomial of the first kind. The order is determined by the number of nodes in the $y-$direction, n_y. A transformation is then applied such that the Chebyshev median node is brought to some location near the wall, y_i. As the number of nodes on either side of the median node are equal, this transformation results in a biasing of the $y-$grid such that there is a concentration of nodes within the BL. The advantage to this is that shears close to the wall can be more precisely represented by the finer grid there. Additionally, this reduces the total number of nodes required and improves computational efficiency. However as the $y-$discretization is fixed with respect to the chordwise direction, the value for the parameter y_i must be tuned according to the expected downstream development of the baseflow/disturbances.

The discrete $y-$derivatives are represented by the Chebyshev pseudo-spectral differentiation matrices (PSDM). These are full matrices, denoted by $\mathcal{D}_1$ and $\mathcal{D}_2$ for the first- and second-order derivatives respectively. The $y-$discretized PDE system in equation 2.29 is thus written as:

$$(\mathbb{A} + \mathbb{B}\mathcal{D}_1 + \mathbb{C}\mathcal{D}_2)\bar{\mathbf{q}} + \mathbb{D}\frac{\partial\bar{\mathbf{q}}}{\partial\bar{x}} = 0\,. \tag{2.31}$$

The numerical grid in the chordwise direction is selected to be of constant spacing, determined by the number of chordwise points n_x. An estimate for n_x is derived from the value α, where the grid spacing is selected so as to sufficiently represent oscillatory behaviour in the chordwise direction. The derivatives $\partial\bar{\mathbf{q}}/\partial\bar{x}$ are discretized based on the marching scheme employed. This work examines two viable marching schemes: The first-order, implicit backward Euler scheme and the second-order, implicit trapezoidal scheme. The two schemes are defined as follows:

$$\bar{\mathbf{q}}^{j+1} - \bar{\mathbf{q}}^{j} = \Delta\bar{x}\mathcal{F}(\bar{x},\bar{\mathbf{q}})^{j+1}\,, \tag{2.32a}$$

$$\bar{\mathbf{q}}^{j+1} - \bar{\mathbf{q}}^{j} = \frac{\Delta\bar{x}}{2}(\mathcal{F}(\bar{x},\bar{\mathbf{q}})^{j+1} + \mathcal{F}(\bar{x},\bar{\mathbf{q}})^{j})\,, \tag{2.32b}$$

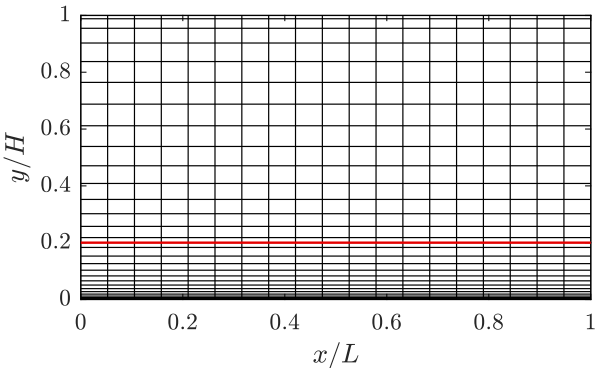

Figure 2.3: Schematic of the numerical grid used for stability computations, with $n_x = 20$ and $n_y = 30$ in the current figure. The location of the Chebyshev median y_i is indicated by the red line.

where 2.32a is the backward Euler scheme and 2.32b is the trapezoidal scheme, given $\partial\bar{\mathbf{q}}/\partial\bar{x} = \mathcal{F}(\bar{x}, \bar{\mathbf{q}})$. The superscript j denotes quantities at the current marching station and $\Delta\bar{x}$ is the non-dimensional chordwise grid spacing. The implicit nature of both methods promotes numerical stability in the marching procedure. The trapezoidal scheme is considered because of its higher order, and hence faster numerical convergence with refinement in x. The application of both methods to 2.31 allows for the solution at the $x-$station $j+1$ to be determined as:

$$\bar{\mathbf{q}}^{j+1} = \left[\mathbb{A}^{j+1} + \mathbb{B}^{j+1}\mathcal{D}_1 + \mathbb{C}^{j+1}\mathcal{D}_2 + \frac{1}{\Delta\bar{x}}\mathbb{D}^{j+1}\right]^{-1}\left[\frac{1}{\Delta\bar{x}}\mathbb{D}^{j+1}\bar{\mathbf{q}}^{j}\right], \tag{2.33a}$$

$$\bar{\mathbf{q}}^{j+1} = \left[\frac{1}{2}(\mathbb{A}^{j+1} + \mathbb{B}^{j+1}\mathcal{D}_1 + \mathbb{C}^{j+1}\mathcal{D}_2) + \frac{1}{\Delta\bar{x}}\mathbb{D}^{j+1}\right]^{-1}\left[\left(\frac{1}{\Delta\bar{x}}\mathbb{D}^{j+1} - \frac{1}{2}(\mathbb{A}^{j+1} + \mathbb{B}^{j+1}\mathcal{D}_1 + \mathbb{C}^{j+1}\mathcal{D}_2)\right)\bar{\mathbf{q}}^{j}\right]. \tag{2.33b}$$

The scheme used for solutions of the NmPSE in this work is the backward Euler method 2.33a. This is due to spurious oscillations that arise in the shape functions when using the trapezoidal scheme, further elaborated on in Chapter 4. Additionally, the matrix $\mathbb{A}$ contains the term $i\,\partial\bar{\alpha}/\partial\bar{x}$. The chordwise derivative here is discretized using first-order finite differences and is updated iteratively at each $x-$station, as part of the procedure to determine $\bar{\alpha}$.

Initial Conditions

In order for the NmPSE to be marched downstream, initial conditions for the shape functions $\bar{\mathbf{q}}$ and chordwise wavenumber $\bar{\alpha}$ must be provided. The initial conditions used in this work fall under two broad categories: modal and non-modal.

The former are generated through a solution of the local stability eigenvalue problem. The parallel flow assumptions used to derive the Orr-Sommerfeld and Squire system in 1.6 are employed; however rather than formulating the problem in terms of the wall-normal disturbance velocity and vorticity, the governing equations are instead re-written directly for $\tilde{\mathbf{q}}$ and $\tilde{p}$:

$$i\alpha\tilde{u} + \frac{\partial\tilde{v}}{\partial y} + i\beta\tilde{w} = 0\,, \tag{2.34a}$$

$$-i\omega\tilde{u} + Ui\alpha\tilde{u} + \tilde{v}\frac{\partial U}{\partial y} + i\beta W\tilde{u} = -\frac{i\alpha}{\rho}\tilde{p} + \nu\left(\frac{\partial^2\tilde{u}}{\partial y^2} - (\alpha^2+\beta^2)\tilde{u}\right), \tag{2.34b}$$

$$-i\omega\tilde{v} + Ui\alpha\tilde{v} + i\beta W\tilde{v} = -\frac{1}{\rho}\frac{\partial\tilde{p}}{\partial y} + \nu\left(\frac{\partial^2\tilde{v}}{\partial y^2} - (\alpha^2+\beta^2)\tilde{v}\right), \tag{2.34c}$$

$$-i\omega\tilde{w} + Ui\alpha\tilde{w} + \tilde{v}\frac{\partial W}{\partial y} + i\beta W\tilde{w} = -\frac{i\beta}{\rho}\tilde{p} + \nu\left(\frac{\partial^2\tilde{w}}{\partial y^2} - (\alpha^2+\beta^2)\tilde{w}\right), \tag{2.34d}$$

where the equations 2.34 are referred to as Incompressible Local Stability Theory (ILST). For a prescribed β and ω, these constitute a quadratic eigenvalue problem for α and the corresponding shape functions. A modal initial condition can thus be generated by solving 2.34 at the start of the stability

Table 2.2: Initial conditions for the NmPSE.

Type	β, ω	α	$\bar{\mathbf{q}}$
Modal	User input	ILST	ILST
Non-Modal	User input	PTV/User input	PTV/Analytic

domain. This is done numerically on the same Chebyshev $y-$grid as the NmPSE, using a companion matrix method to find the the roots of the characteristic polynomial containing all powers of α [27]. The eigenfunction and corresponding eigenvalue used as the initial condition are selected from the computed spectrum through a filter, see Boersma [11]. The filter selects the solution based on whether the shape functions decay exponentially into the freestream, at a rate that depends on the mode specifications.

The non-modal initial conditions are generated from the structure of the DRE wake. These are obtained either directly from PTV measurements by Zoppini et. al [136], or modelled using analytical functions that resemble the disturbance field in the near-wake region. The generation and use of the non-modal initial conditions are discussed in detail in Chapter 4. An important point to note is that initial disturbance amplitudes are irrelevant in a linear framework, due to the assumption of infinitesimally small disturbances. Normalized shape functions of identical initial structure will grow at the same rate for a given baseflow and parameter set. A summary of the initialization procedure is presented in Table 2.2.

Solver Algorithm and Limitations

The high-level architecture of the NmPSE solver is presented in Appendix A.2, implemented in MATLAB. This provides an overview of the code structure and its dependencies, and is briefly described here.

The baseflow velocity components and their derivatives are taken as inputs to the solver, along with the initial conditions and disturbance frequencies $\bar{\omega}$ and $\bar{\beta}$. The Chebyshev $y-$grid is generated as defined by the user, and a uniform spacing in the $x-$direction is assumed. Prescribed non-modal ICs are interpolated onto the first marching station of the stability grid, while modal ICs are locally generated at this station using ILST. The solver then enters the outer *marching* loop, where the local baseflow quantities are interpolated onto the stability grid. A first estimate for $\bar{\alpha}$ is made based on the external streamline after which the inner *wavenumber* loop is entered. Here, the coupled NmPSE system is solved using the backward Euler scheme 2.33a for the first iteration of the shape functions $\bar{\mathbf{q}}$. A new estimate for $\bar{\alpha}$ is then computed according to equations 2.22 and 2.23, and the NmPSE are re-solved. The inner loop is exited when the convergence criterion 2.24 is met. This process is repeated at each marching station within the outer loop. Once the solution has been computed at the final marching station, the function executes a global normalization routine. The condition 2.22 is enforced globally on the shape functions to re-direct residual growth into the real exponent $\bar{\alpha}$, and the shape functions themselves are normalized by the local maximum of $\bar{u}$.

The NmPSE framework is derived on the basis of certain assumptions and is thus not without limitations. It becomes important to identify these so as to prevent improper use of the tool in the study of spatial, non-modally growing disturbances. The assumptions employed in the derivation of the NmPSE are thus summarized as follows:

1. The baseflow is steady and known.
2. The disturbance quantities are effectively infinitesimal i.e. $\mathbf{q}' \ll \mathbf{Q}$, such that problem is linear.
3. The disturbance shape functions are slowly-varying in the chordwise direction, allowing for a parabolization of the governing equations.
4. The baseflow is spanwise invariant and disturbances do not undergo spanwise amplification.
5. The instabilities in question are of the convective type.
6. Compressibility and temperature effects are negligible.
7. Surface curvature effects are negligible.

Haynes & Reed [46] have shown that curvature effects on modal instability development are, in general, non-negligible when comparisons with experimental swept wing data are drawn. The region of interest on the swept wing in the current work features minimal surface curvature, such that the

swept flat-plate approximation remains valid for modal CFI. However no research has been conducted on the same for non-modally growing disturbances, such as those found in the DRE wake. It is thus not possible to quantify how sensitive the DRE wake is to curvature, and whether the use of the flat-plate approximation is truly justified in this scenario.

The slow-variance assumption used for the shape functions is also a point of ambiguity as unlike the classical PSE, growth is completely captured by the shape functions. However, transient growth has typically been characterized as occurring over short temporal or spatial scales. It is thus important to quantify the extent to which the slow-variance assumption may limit its modelling in the NmPSE framework, which will be addressed in Chapter 4 of this work.

Finally, it is important to make a distinction between the *baseflow* and *mean-flow*. The former is the basic fluid state upon which the disturbance equations may be solved, here computed as a steady laminar solution to the BLEs. The latter is a spatial average of the steady, total (disturbance plus perturbation) velocity field along the spanwise coordinate axis, at each chordwise location. In a linear framework, the two are indistinguishable. The distinction arises when disturbances begin to exhibit non-linear behaviour; the baseflow is independent of this and remains unchanged, however the mean-flow is distorted as a result of non-linear interactions between modes. The NmPSE is a linear framework and is thus unable to describe non-linearly growing disturbances. It should be noted that the finite-amplitude disturbance structure extracted from the DRE wake will be treated as infinitesimal, and that interactions between the dominant mode and its harmonics, if any, are not modelled i.e. the DRE wake structure is assumed to contain no mean-flow distortion.

2.3. Solver Verification

2.3.1. Harmonic Linearized Navier-Stokes

The parabolization of equations 2.15 rests on the slowly-varying assumption made for the disturbance shape functions $\tilde{\mathbf{q}}$. However, recent work by Sumariva & Hein [119] review and propose extensions to the PSE methodology, that eliminate the need for this. In particular, Choudhari & Streett [22], Mughal & Ashworth [78] consider an alternative ansatz for disturbances in quasi 3-D BL flows, in which the Fourier decomposition 1.9 does not feature a chordwise wavenumber α in the phase function:

$$\mathbf{q}'(x,y,z,t) = \tilde{\mathbf{q}}(x,y)e^{i\Theta(z,t)} \,, \tag{2.35a}$$

$$\Theta(z,t) = \beta z - \omega t \,. \tag{2.35b}$$

This implies that fast, oscillatory disturbance behaviour in the chordwise direction is captured by the shape function rather that the phase function. As a result, the higher-order chordwise derivatives of $\tilde{\mathbf{q}}$ in the PSE are significant and cannot be eliminated from the system 2.15. Instead, the problem is solved in elliptic form similar to DNS. Sumariva & Hein [119] label this framework the Harmonic Linearised Navier Stokes (HLNS). If the ansatz 2.36 is inserted into the linearised disturbance equations 2.14 for a spanwise invariant baseflow, we have:

$$0 = \frac{\partial \tilde{u}}{\partial x} + \frac{\partial \tilde{v}}{\partial y} + i\beta\tilde{w} \,, \tag{2.36a}$$

$$\begin{aligned} 0 = &-i\omega\tilde{u} + U\frac{\partial \tilde{u}}{\partial x} + \tilde{u}\frac{\partial U}{\partial x} + V\frac{\partial \tilde{u}}{\partial y} + \tilde{v}\frac{\partial U}{\partial y} + i\beta W\tilde{u} \\ &+ \frac{1}{\rho}\frac{\partial \tilde{p}}{\partial x} - \nu\left(\frac{\partial^2 \tilde{u}}{\partial y^2} - \beta^2\tilde{u} + \frac{\partial^2 \tilde{u}}{\partial x^2}\right) \,, \end{aligned} \tag{2.36b}$$

$$\begin{aligned} 0 = &-i\omega\tilde{v} + U\frac{\partial \tilde{v}}{\partial x} + \tilde{u}\frac{\partial V}{\partial x} + V\frac{\partial \tilde{v}}{\partial y} + \tilde{v}\frac{\partial V}{\partial y} + i\beta W\tilde{v} \\ &+ \frac{1}{\rho}\frac{\partial \tilde{p}}{\partial y} - \nu\left(\frac{\partial^2 \tilde{v}}{\partial y^2} - \beta^2\tilde{v} + \frac{\partial^2 \tilde{v}}{\partial x^2}\right) \,, \end{aligned} \tag{2.36c}$$

$$\begin{aligned} 0 = &-i\omega\tilde{w} + U\frac{\partial \tilde{w}}{\partial x} + \tilde{u}\frac{\partial W}{\partial x} + V\frac{\partial \tilde{w}}{\partial y} + \tilde{v}\frac{\partial W}{\partial y} + i\beta W\tilde{w} \\ &+ \frac{i\beta}{\rho}\tilde{p} - \nu\left(\frac{\partial^2 \tilde{w}}{\partial y^2} - \beta^2\tilde{w} + \frac{\partial^2 \tilde{w}}{\partial x^2}\right) \,. \end{aligned} \tag{2.36d}$$

The HLNS equations 2.36 do not feature α nor the normalization condition 1.10 present in the PSE framework, making them inherently capable of representing both modal and non-modal disturbance

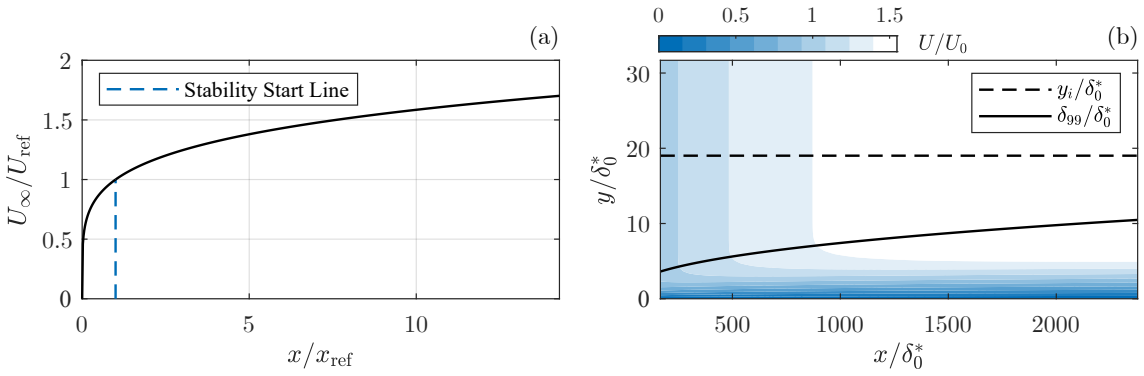

Figure 2.4: (a) Chordwise variation of the external flow component U_∞ (b) Contours of the baseflow velocity component $\bar{U}$ within the stability domain. Only one-third of the $y-$extent of the domain is shown.

growth. They are thus employed as a verification tool for results computed with the NmPSE, allowing for an identification of its limitations. Despite the increased robustness that the HLNS offers in BL stability analyses, the re-introduction of ellipticity into the problem leads to the familiar computational drawbacks associated with standard CFD methods: a more resource-intensive solution procedure and longer computational times.

The equations 2.36 are non-dimensionalized as per Section 2.25 and solved in this form. A Chebyshev $y-$discretization scheme identical to that used for NmPSE computations is also used to discretize the HLNS equations, with homogenous BCs at the wall and freestream. The $x-$grid is also retained, with a constant spacing determined by n_x. The elliptical nature of the problem indicates that the use of a marching scheme in x is no longer appropriate. A fourth-order, finite-difference scheme is instead employed to discretize the chordwise derivatives. Both chordwise BCs must also be prescribed in the elliptical framework. At the domain inflow this is selected to be the initial conditions for the shape function, listed in Table 2.2, with the exception of α. The outflow boundary condition is slightly more complex, as the final state of the evolving disturbances is not typically known.

The ellipticity of the NS equations arises from two sources, the viscous terms and the pressure field. The outflow BC can interact with incoming velocity perturbations to produce a pressure pulse felt throughout the domain, possibly negatively affecting the stability results in the interior domain to a varying degree. This is tackled by smoothly reducing the u' and w' disturbance velocity amplitudes to zero within a *buffer region*, similar to that proposed by Joslin [51]. This buffer is located at the end of the computational domain and is represented by the function:

$$F_{\text{buff}} = \frac{1}{2}\left(1 + \tanh\left\{K_{\text{buff}}\left[1 - 2\frac{\bar{x} - \bar{x}_{\text{buff}}}{\bar{x}_{\text{out}} - \bar{x}_{\text{buff}}}\right]\right\}\right), \tag{2.37}$$

where $\bar{x}_{\text{out}}$ and $\bar{x}_{\text{buff}}$ are the non-dimensional outflow and buffer start locations respectively. The parameter K_{buff} can be varied to control the strength of the amplitude damping. The outflow BC for the disturbances is thus prescribed to be homogenous, and the extent of the buffer region is selected such that the upstream influence of the boundary is adequately nullified.

2.3.2. Test Case

As a preliminary verification strategy, the NmPSE is used to compute modal disturbance growth. The results are compared with simulations using the classical LPSE as well as the HLNS, for the FSC BL case presented by Tempelmann et. al [120] and Schrader et. al [106].

Schrader et. al [106] select the FSC baseflow such that it resembles the BL in the ASU swept wing experiments by Reibert et. al [92]. The best match was obtained for an inflow Reynolds number of $\text{Re}_{\delta_0^*} = 220$, prescribed at the inflow station $\bar{x} = 167$, and for the Hartree parameter set to $\beta_H = 0.333$. The fluid in consideration is air with a kinematic viscosity of 1.458×10^{-6}. The flat-plate is swept at $\Lambda = 45°$, which leads to the external velocity components being equal at the inflow station. The FSC equations 2.8 are solved with these parameters and the baseflow velocity components are computed on the stability grid through 2.10. This is presented in Figure 2.4.

Table 2.3: Baseflow and NmPSE stability parameters used for the verification test case.

FSC Baseflow					Stability						
x_{ref}	$\lvert\mathbf{Q}_\infty\rvert$	Λ	m	β_H	H	y_i	n_y	n_x	$\bar{\alpha}_r\Delta\bar{x}$	$\bar{\beta}$	$\bar{\omega}$
0.07 m	10.98 m/s	45°	0.2	0.333	0.04 m	0.008 m	100	800	0.463	-0.19	0

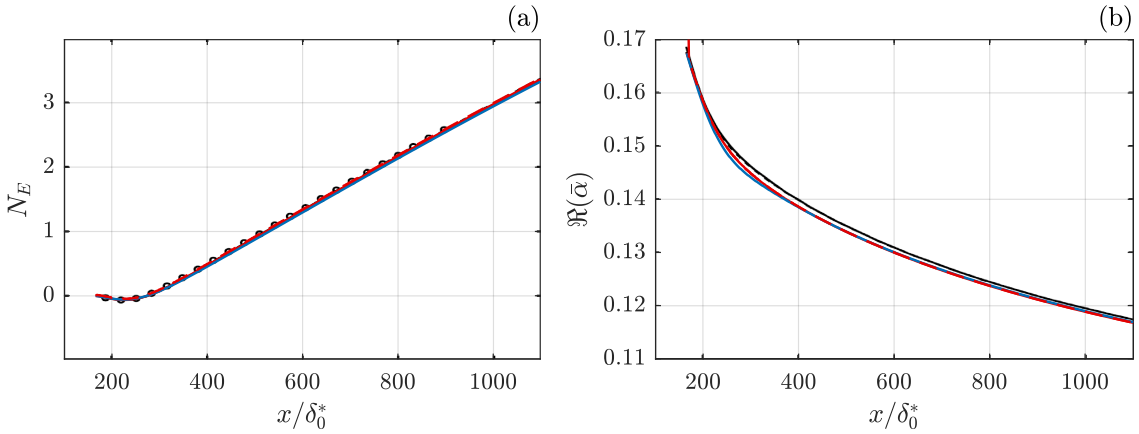

Figure 2.5: Stationary crossflow mode evolution, compared with DNS by Schrader et. al [106](○) and NmPSE simulations by Tempelmann et. al [120](—). Solid and dashed red lines correspond to the NmPSE and HLNS respectively, solid blue line represents the classical LPSE. Evolution of (a) disturbance energy and (b) real part of the chordwise wavenumber.

The stability grid extends up to a height of 40mm to sufficiently remove the domain cut-off error. The Chebyshev $y-$points are biased such that half of them are located below $y_i = 8$mm, for improved precision within the BL. Owing to the rapid convergence of pseudo-spectral methods, a y-grid density of $n_y = 100$ was deemed adequate. The $x-$spacing was selected such that there exists a sufficient number of grid points per chordwise wavelength $1/\alpha_r$[3]. Tempelmann et. al [120] analyse a stationary crossflow mode of wavenumber $\bar{\beta} = -0.19$ corresponding to the $\lambda = 12$mm dominant mode in the experiments by Reibert et. al [92]. The minus sign in the wavenumber is a result of the positive convention for $\bar{\alpha}$ and W_∞. A modal initial condition is generated through ILST using the local baseflow state at the inflow station. A summary of the selected baseflow and stability parameters for the test case are presented in Table 2.3. Additionally, computations using the HLNS define the buffer region to start at 85% of the domain length.

To quantitatively describe non-modal disturbance growth, an N-factor N_E based on disturbance energy is defined [120]:

$$\bar{E}^{\text{int}}(x) = \int_0^\infty |\tilde{u}|^2 + |\tilde{v}|^2 + |\tilde{w}|^2 \mathrm{d}y \,, \tag{2.38a}$$

$$N_E = 0.5 \log\left(\frac{\bar{E}^{\text{int}}}{\bar{E}_0^{\text{int}}}\right) , \tag{2.38b}$$

where E_0 is the integrated disturbance energy at the inflow station. Computing the N-factor using disturbance energy rather than velocity leads to it being multiplied by a factor of 2, due to energy being equal to the square of the velocity. In order to maintain consistency in using the N-factor, this is removed by including the factor 0.5 in the definition of N_E.

The chordwise evolution of disturbance energy and α are presented in Figure 2.5. As the initial condition provided is modal, the growth represented by the N_E curves is purely exponential. The disturbance energy initially decays up to the point of neutral stability at $\bar{x} \approx 230$, after which amplification occurs. It is evident from Figure 2.5a that the derived NmPSE framework is capable of predicting modal growth, and agrees well with computations using the LPSE. The N_E curve computed using the HLNS also matches very well with that of the NMPSE and LPSE. All three growth curves are also in excellent agreement with the DNS and PSE results by Schrader et. al [106] and Tempelmann et. al [120] respectively. The proposed method to determine α adequately captures the largest disturbance

[3]Real part of the chordwise wavenumber, shortened for convenience ($\alpha_r = \Re(\alpha)$)

oscillations, and compares well with α determined through the classical normalization condition for the LPSE (Figure 2.5b). The HLNS does not determine α as a distinct quantity as the requirement for slow variation of the shape functions is omitted. It is extracted from the solution for $\tilde{\mathbf{q}}$ as per the definition 2.21, where A is selected to be the same as that in the NmPSE. The α computed from the HLNS solution coincides with that determined by the NmPSE, as seen in Figure 2.5b. The results for α exhibit minor differences with the reference computations by Tempelmann et. al [120], although they capture the overall trend very well. This mismatch could be amounted to differences in the numerical set-up and solver implementation with respect to the reference case. For example, Tempelmann et. al [120] retain only the first-order terms in equations 2.15 in their derivation of a non-modal, parabolized framework, whereas the current work retains the second-order terms as well. Additionally, the specifications of the numerical grid employed are not discussed and so the discretization used here cannot be perfectly matched to that of the reference case.

Notwithstanding these deviations, the test case simulations show that both the NmPSE and HLNS produce verifiable results for modal initial conditions, and are further examined in a non-modal setting in Chapter 4.

3

Experimental Configuration

3.1. Wind Tunnel Facility & Swept Wing Model

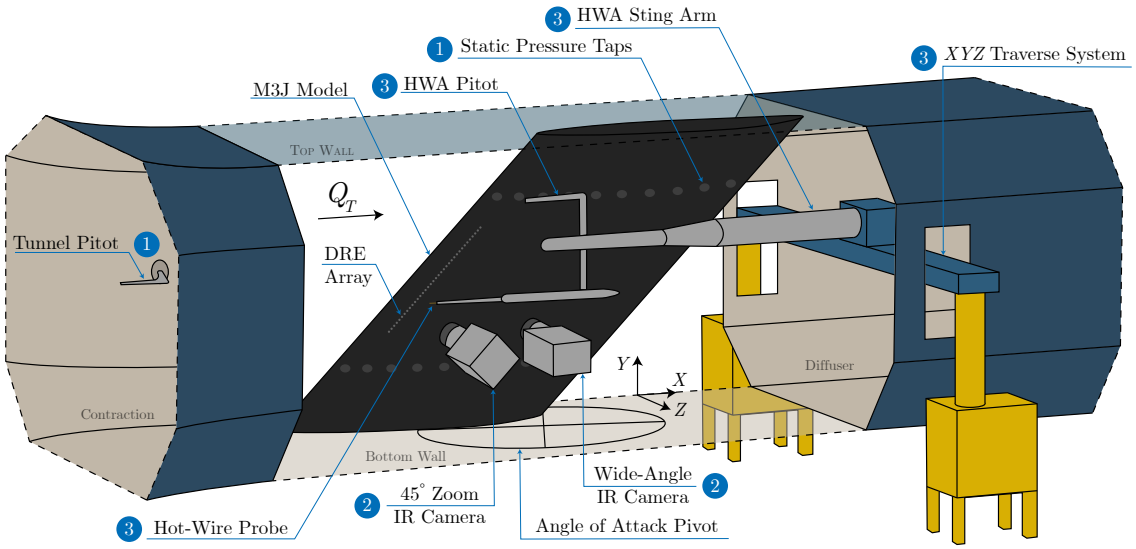

Figure 3.1: Sketch of the wind tunnel test section and employed set-up. The side walls are not drawn for visualization clarity. Components corresponding to the various measurements systems are grouped and labelled as follows: (1) Pressure measurement system. (2) Infrared thermography system. (3) Hot-wire anemometry system.

The steady-state simulations carried out with the numerical tools in Chapter 2 are complemented by experimental measurements of the unsteady flow phenomena. The measurement campaign is conducted in the low turbulence tunnel (LTT), an atmospheric, closed return wind tunnel, situated at the Delft University of Technology.

The LTT facility is constructed over two stories, with the airflow driven by a six-bladed fan located on the lower floor. The upper floor consists of the contraction, test section, and part of the diffuser. Turning vanes ensure a smooth redirection of the airflow between the vertical and horizontal tunnel segments. The wind tunnel is subsonic and can reach a maximum speed of 117 m/s within the test section. A defining feature is the low turbulence level characterizing the test section flow, which is an important parameter in ensuring that stationary CFI dominate the transition scenario [80, 28]. Low turbulence is achieved thanks to the combined presence of a series of purposedly designed anti-turbulence screens, located in the wind tunnel settling chamber, and a high convergent contraction ratio driving the flow field in the test section. The current work utilizes all seven available screens, restricting T_u to less than 0.03% for all measurements [109].

The test section is an octagonal, inter-changeable chamber of length 2.60 m, width 1.80 m and height 1.25 m. Its vertical walls diverge slightly in the downstream direction, accounting for blockage caused

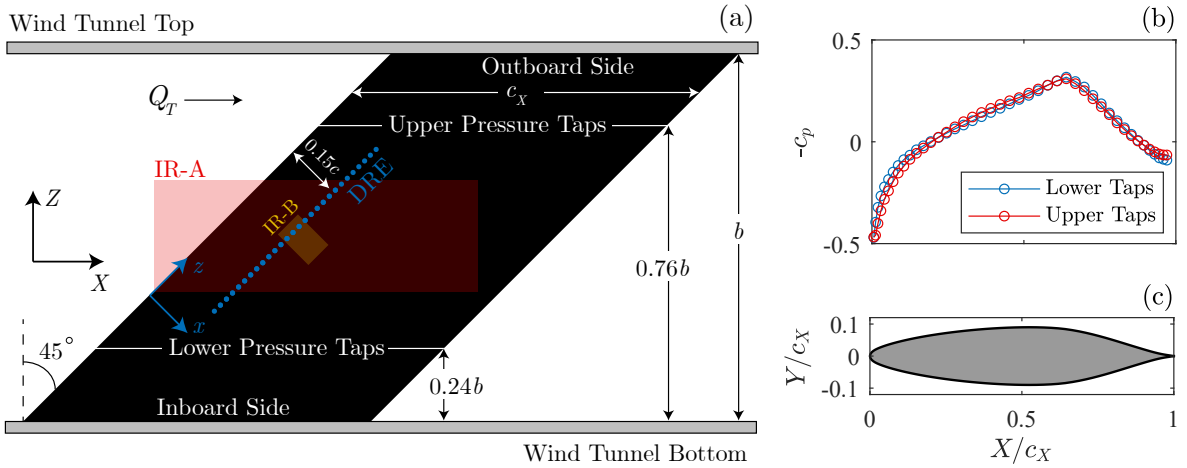

Figure 3.2: (a) Cross-sectional schematic of the wind tunnel test section, with the M3J swept wing model and DRE array. Shaded regions indicate the domains imaged by the full and zoomed IR camera configurations, labelled IR-A and IR-B respectively. (b) Pressure coefficient distribution measured on the wing pressure side, for Re= 2.17×10^6. (c) 66018M3J airfoil section.

by the tunnel-wall BL that develops within the measurement region. The freestream reference velocity and pressure in the test section are measured by a pitot-static tube located at the end of the contraction, connected to a Mensor DPG2101 digital pressure gauge. The reference temperature is monitored within the contraction, using a Pt100 Resistance Temperature Detector. These measured reference quantities are used to calculate the fluid density ρ_∞ and kinematic viscosity ν. Figure 3.1 depicts the test section and organization of the main measurement systems used in the experimental campaign.

A constant-chord, swept wing model known as the M3J, designed in-house [110], is used as the test section model in the current work (Figure 3.2a). The wing features a leading-edge sweep of 45°, streamwise chord $c_X = 1.27$ m and span $b = 1.25$ m, and has been used for various swept wing transition studies at the Delft University of Technology [111, 139, 136]. Two coordinate reference systems are used to describe quantities measured over the model: one is integral with the wind tunnel floor, with spatial components X, Y, Z; the second one is integral to the wing model, with z-axis and x-axis respectively aligned and orthogonal to the leading edge, and spatial components x, y, z.

The M3J airfoil section is a modified NACA 6-series symmetric foil (66018), which features a leading edge radius of approximately 1%, preventing attachment line instabilities [84, 99] (Figure 3.2c). The airfoil is designed to promote accelerated flow for up to 70% of the chord length at zero incidence angle, where the pressure minimum is then encountered. This region of acceleration features minimum surface curvature, to avoid the amplification of TS waves and Görtler vortices. Additionally, the wing ensures spanwise invariant conditions in the measurement region, which extends across its midspan. The measurements in the current work are conducted on the *pressure side* of the wing, at an incidence angle $\alpha = -3.36°$ and a chord Reynolds number $\mathrm{Re}_{c_X} = 2.17 \times 10^6$. This configuration, in combination with the design features of the model, enable exclusive amplification of CFI within the pressure side BL. The BL on the *suction side* of the wing is forced to turbulence using a strip of turbulator tape, for experimental repeatability. Finally, the model itself is constructed out of a glass-fiber reinforced epoxy resin and polished to a surface roughness level of 0.2 μm rms. This is crucial as the background roughness level must be sufficient lower in amplitude than the DRE array utilized, to prevent it influencing the development of stationary CFI in forced configurations.

A series of 92 pressure taps are installed on the pressure side of the model surface, divided equally between the inboard and outboard sides of the wing. They are represented by the grey circles in Figure 3.1, with their exact positioning shown in Figure 3.2. These are used to measure the static pressure distribution on the wing pressure side in the streamwise $X-$direction, through a DTC-Initium digital pressure scanner. The static pressure measurements $p_s(X)$ are converted into the pressure coefficient c_p through:

$$c_p = \frac{p_s(X) - p_\infty}{\frac{1}{2}\rho_\infty Q_T^2}\,, \tag{3.1}$$

Table 3.1: Geometric parameters of the DRE arrays.

Case	λ (mm)	λ/λ_1	d_D (mm)	k_D (mm)	k_D/d_D
k_3	8	1	1.767 ± 0.004	0.3292 ± 0.0009	0.186
k_4	8	1	1.721 ± 0.009	0.4374 ± 0.0035	0.261

where ρ_∞ and Q_T are the freestream density and velocity determined from the tunnel pitot-static tube system (Figure 3.2b).

Discrete Roughness Elements

The cylindrical DRE arrays used in the experimental studies are selected to emulate the configuration of Zoppini et. al [136], which acts as reference case for the numerical investigations in Chapter 4. Comparably to previous research efforts [92, 100], DRE arrays are applied on the wing surface to focus CFI development into a single monochromatic mode. The inter-element spacing (i.e. the forced mode) was chosen to coincide with the wavelength of the most amplified CFI mode $\lambda_1 = 8$ mm for the current set-up, as predicted by LST [73, 109].

The manufacturing of the DRE arrays was done in-house, through CNC laser-cutting of adhesive transfer vinyl film. The height of the elements could be controlled through appropriate layering of the film. The arrays were applied at a fixed chord location of $x/c = 0.15$ [139], where the unperturbed experimental BL thickness is $\delta_{99} \simeq 1.3$ mm. Owing to the increased BL thickness and minimal surface curvature at this chord location, near-element measurements are more accessible as compared to upstream locations. Two forcing configurations are investigated in this work, featuring DRE of nominal height $k_D = 0.3$ mm or $k_D = 0.4$ mm. These two cases are labelled k_3 and k_4 respectively for the remainder of this work. The forcing configurations can be described using the roughness Reynolds number previously defined, which for the considered cases are computed to be $\mathrm{Re}_{k_D} = 192$ and $\mathrm{Re}_{k_D} = 330$ respectively. The former falls within the critical-forcing regime, where the DRE array leads to the onset of stationary CFI. The latter configuration behaves super-critically and introduces near-wake instabilities that rapidly grow and breakdown, causing transition in the element vicinity [139, 136]. These scenarios were discussed in Section 1.4.3. Both configurations feature cylindrical elements of nominal diameter $d_D = 2$ mm. However their geometry entails mild deviations due to the manufacturing process. A statistic investigation has been performed, characterizing the elements shape and height by means of a laser scanner profilometer, and the resulting geometrical parameters are reported in Table 3.1.

3.2. Measurement Techniques

3.2.1. Infrared Thermography

IR thermography is a non-intrusive measurement technique[1] allowing for rapid determination of the near-wall heat transfer characteristics of the flowfield. Surfaces at ambient temperature emit electromagnetic radiation primarily within the infrared spectrum, according to Wien's law. Infrared sensors are used to detect energy within this wavelength band, from which temperature estimates are made. The relation between the radiated energy flux and surface temperature is given by the Stefan-Boltzmann law:

$$q_r = \epsilon_r \sigma T^4 \,, \tag{3.2}$$

where σ is the Stefan-Boltzmann constant. The coefficient ϵ_r stems from the grey-body hypothesis, relating the emissivity of a real emitter to that of a black body, and is dependent on direction and the temperature itself. Astarita and Carlomagno [17] provide an extensive description of radiation theory and IR sensors used in IR thermography measurements.

The radiative heat-transfer mechanics are exploited in fluid dynamics applications through the Reynolds analogy, which relates the surface shear stress to the surface heat transfer in wall-bounded flow:

$$\frac{\mathrm{St}}{c_f} = \frac{1}{2}\mathrm{Pr}^{-\frac{2}{3}} \,, \tag{3.3}$$

[1] IR thermography is non-intrusive only when temperature differences between the flowfield and surface are low [64].

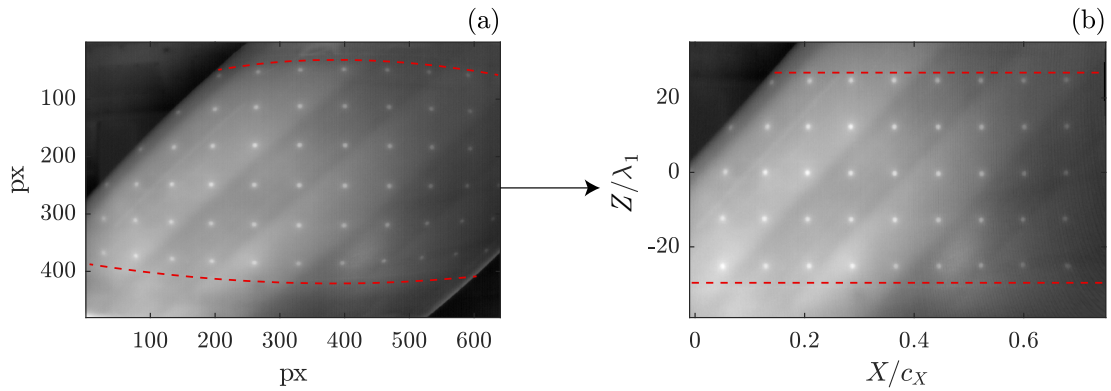

Figure 3.3: De-warping of the IR thermography images. (a) Raw calibration target image. (b) De-warped image in the XYZ wind tunnel coordinate system.

where St, Pr and c_f are the Stanton number, Prandtl number and skin-friction coefficient respectively. The surface shear stress is dependant on the gradient of the velocity profile at the wall, following equation 1.1. Turbulent BLs feature larger velocity gradients close to the wall when compared to laminar BLs, as a result of momentum redistribution due to turbulent mixing. The implication of this in the context of the Reynolds analogy (3.3) is that convective heat transfer at the wall is higher for turbulent BLs. This results in thermal contrast between laminar and turbulent flow regions. Active heating of the surface may be used to improve this thermal contrast for flows in the incompressible regime, where temperature variations are small. Thus, the technique can be used for detection and characterization of the transition front, and of the transitional BL modulation due to stationary CFI development.

Experimental Set-Up

In the current work, IR thermography is employed to gain an overview of the perturbed BL flow in the wake of the DRE. Stationary vortical structures can induce regions of locally high and low shear, which manifest as regions of low and high relative temperature respectively as per 3.3. This allows for the observation of velocity streaks and the imprint of stationary crossflow vortices. The IR acquisitions are performed with two Optris PI640 IR cameras: one camera is equipped with a wide angle lens, $f = 10.5$ mm, and images the whole wing chord length with resolution 0.85 mm/px; the second camera features a zoomed-in lens, $f = 18.7$ mm, and captures a small domain aligned with the leading edge and centred at $x/c = 0.20$ with resolution 0.43 mm/px. The wide-lens configuration provides a global overview of the developing BL flow, indicating whether laminar-turbulent transition occurs in the element vicinity. The zoomed-in configuration allows for the preliminary characterization of the near-element flow features. The positioning of these two cameras and the extent of the regions imaged by them are indicated in Figure 3.1 and Figure 3.2a respectively.

During the acquisition, five external halogen lamps (3 × 400W and 2 × 500W) actively heat the model surface, improving the thermal contrast between the high and low shear regions. Acquisitions are performed collecting 80 images at a frequency of 4 Hz, averaging them to increase the signal-to-noise ratio. The averaged images are then geometrically mapped to the X, Y, Z Cartesian framework by applying an in-house calibration procedure [95].

Calibration Procedure

The raw thermal maps acquired using IR thermography are distorted by the surface curvature of the airfoil, as well as by the positioning of the IR cameras. To correct for this and determine the spatial location of the images in the XYZ wind tunnel coordinate system, a calibration procedure is conducted. First, a reference calibration target is applied to the surface of the wing, as shown in Figure 3.3, and is irradiated by the halogen lamp array. The target consists of a rectangular grid of black dots printed on a flexible white background, creating points of thermal contrast due to the higher emissivity of black paint. The captured IR images of the target are averaged and processed using a custom MATLAB script, where a numerical grid is constructed to correspond to the physical black dots. A polynomial distortion correction is then applied to de-warp the image [40], after which its pixels are scaled to physical coordinates. The script returns an object containing the details of the calibration process,

which is then used to correct subsequent IR measurements. Additionally, a smaller target is used for calibration of the zoomed-in images, although the correction procedure remains the same.

3.2.2. Hot-Wire Anemometry

Hot-wire anemometry is a well-established technique which allows for point-wise measurements of the fluid velocity. A heated wire-sensor probe is inserted into the flowfield and used to measure a representative velocity signal, exploiting the convective heat transfer mechanisms between the wire and the flow. The dimensions of the wire are typically micron size, to improve the spatial resolution of the technique and to reduce the thermal inertia of the wire. This also allows for velocity fluctuations much smaller than the mean flow to be detected, with excellent temporal resolution. The high frequency response of HWA makes it ideal for the measurement of unsteadiness in the flowfield, such as in turbulent BLs.

HWA is based on a Wheatstone bridge circuit, illustrated in Figure 3.4 . In its simplest form the circuit consists of four arms, each containing a resistor, with the hot-wire sensor constituting one of the arms. When the ratio of resistances (a) and (b) is the same as the ratio of (c) and (d), the bridge is said to be *balanced*. Throughout this work, the bridge is operated as a Constant Temperature Anemometer (CTA). With a CTA configuration, the current flowing through the hot-wire probe is adjusted so that its temperature remains at a prescribed setting. As the hot-wire sensor is immersed in the flow field, the convective heat exchange modifies its temperature. Specifically, when the flow velocity increases, the probe experiences more convective cooling and its temperature drops. The resistance of the probe is a linear function of its temperature and decreases as well, causing the Wheatstone bridge to be unbalanced. A feedback amplifier in the circuit senses this and signals for an increase in current, increasing the temperature of the wire. Thus, through varying the voltage of the circuit, the feedback amplifier maintains the wire at a fixed resistance and temperature so that the bridge is balanced, i.e. no current flows through the feedback amplifier.

The variation of the voltage is correlated to changes in the flow velocity through a calibration procedure. The hot-wire is assumed to be in thermal equilibrium with the fluid, with negligible heat exchange due to conduction and radiation. The electrical heating produced by the Joule-effect is then only balanced by convection due to the surrounding fluid.

$$I_w^2 R_w = h_a A_w (T_w - T_a) \,, \tag{3.4}$$

where R_w is the wire resistance, I_w is the current through the wire, T_w is its temperature and A_w is the area of wire exposed to the fluid. The temperature of the fluid is denoted by T_a. The convective heat transfer coefficient h_a in equation 3.4 can be replaced by the Nusselt number $\mathrm{Nu} = h_a d_w / k_a$, with d_w and k_a being the wire diameter and thermal conductivity of the fluid respectively. For the forced convection regime that the wire operates in, Nu can be expressed as a function of the Reynolds number Re:

$$\frac{E_w^2}{R_w} = \frac{k_a \mathrm{Nu}}{d_w} A (T_w - T_a) = \frac{k_a A}{d_w} f(\mathrm{Re}) (T_w - T_a) \,, \tag{3.5}$$

where $E_w = I_w R_w$ is the bridge voltage. The equation 3.5 can be written in the form $E_w^2 = A + BU^n$, where A, B, n are constants and U is the flow velocity measured by the hot-wire. The constants encompass the effect of the ambient flow conditions and properties of the wire, and must be determined as part of the calibration procedure. The calibration must be performed at appropriate intervals between measurements, so as to properly account for thermal drift in the system.

Experimental Set-Up

HWA is employed to fully characterize the near-element flow topology, allowing for the local acquisition of temporally-resolved unsteady velocity signals. The HWA measurement system consists of a single-wire, ceramic body, BL probe (Dantec Dynamics 55P15). A feature of these probes is that their prongs extend under the probe mount, facilitating near-wall measurements. The wire-sensor is made out of tungsten and has a nominal length and diameter of 1.25 mm and 5 μm respectively. The system is operated using a TSI IFA-300 constant temperature bridge with automatic overheat ratio adjustment.

The hot-wire probe is mounted to a three degree-of-freedom traversing system that operates in the X, Y, Z wind tunnel coordinate system (Figure 3.1). Given an input file with the measurement coordinates, the traverse automatically positions the hot-wire probe, with a nominal spatial precision

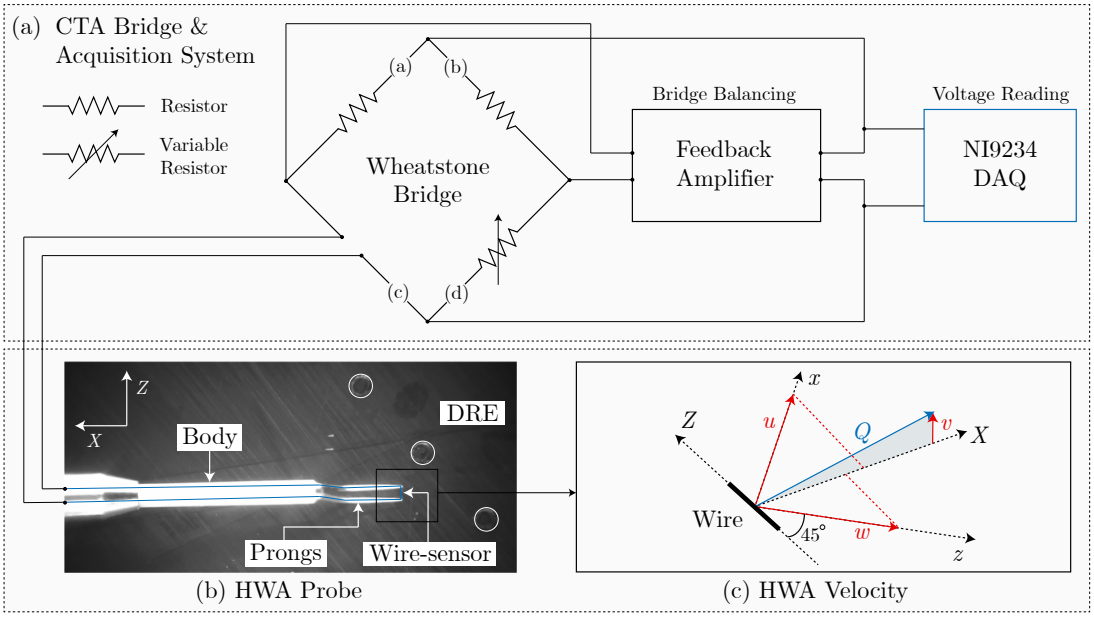

Figure 3.4: Schematic of the HWA measurement system. (a) Simplified diagram of the CTA Wheatstone bridge and digital acquisition system. (b) Boundary layer hot-wire probe, positioned aft of the DRE array. (c) Velocity component measured by the HWA sensor.

of 2.5 μm. The use of a single-wire probe allows for only one velocity component to be measured depending on the orientation of the probe, shown in Figure 3.4b. This is due to directional sensitivity of the cooling experienced by the wire, which is more responsive to flow normal to the wire than to tangential flow. For all measurements, the probe is aligned parallel to the $Z-$axis of the wind tunnel system, and orthogonal to the $X-$coordinate. As a result, the wire-sensor measures a projected velocity whose magnitude can be constructed as:

$$Q = \sqrt{(u\cos(45°) + w\sin(45°))^2 + v^2}\,, \tag{3.6}$$

where u, v, w are the velocity components in the x, y, z wing coordinate system.

The bridge voltage signal is registered by an NI9234 digital acquisition system, and is converted into the velocity component Q through the calibration process. This calibration is performed at the start of each measurement day using a pitot-static tube, connected to a Mensor DPG2101 digital pressure gauge. The probe and pitot tube are moved to a freestream position where voltage and velocity measurements are taken for various speeds in the test section. A correlation between the two is then made through a fourth-order polynomial fit, while correcting for effects due to the ambient temperature and pressure. The velocity signal sensed by the probe is sampled at a frequency $f_s = 51.2$ kHz for a sampling time of 2 s, to ensure statistical convergence of the measurements.

As a precautionary measure, toroidal magnets are fixed to the cable connecting the HWA probe to the Wheatstone bridge. This is done to minimize electromagnetic interference between the HWA system and components such as the traversing system's motors, or the wind tunnel engine.

Uncertainty Quantification

In order to verify the accuracy of the HWA measurements, it is important to estimate the inherent measurement uncertainty. Measurement errors can be grouped into two broad categories based on their origin: random or systematic. Random errors arise from spurious fluctuations in the measurement and can be minimized through statistical analysis. Systematic errors, also known as bias, originate from the measurement system itself, the experimental configuration and the wind tunnel user. Sources of these errors in the context of HWA could be from the calibration process, proximity of the sensor to the wall, vibration of the probe, misalignment of the traverse system, and ambiguity in regions of reversed flow, among others. Systematic errors cannot be tackled through statistics, but can be identified and mitigated through careful design and set-up of measurement systems.

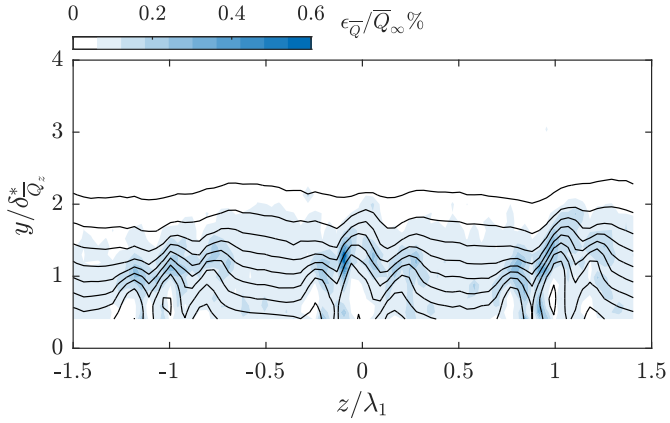

Figure 3.5: Contours of the percent uncertainty in the HWA mean velocity field. Black lines represent 10 contour levels of $\overline{Q}$, ranging from 0 to 1.

The uncertainty due to random error in the HWA velocity signals can be quantified following Sciacchitano & Wienke [108], through the equations:

$$\epsilon_{\overline{Q}} = \pm \frac{\langle Q \rangle}{\sqrt{N_{s_{\text{eff}}}}} , \tag{3.7a}$$

$$\epsilon_{\langle Q \rangle} = \pm \frac{\langle Q \rangle}{\sqrt{2(N_{s_{\text{eff}}} - 1)}} , \tag{3.7b}$$

where $\overline{Q}$ and $\langle Q \rangle$ are the temporal mean and standard deviation of the velocity signal respectively. $N_{s_{\text{eff}}}$ is the effective number of samples in the measurement. For samples that are uncorrelated in time, this is equal to the total number of samples measured i.e. $N_{s_{\text{eff}}} = N_s$. For correlated samples, Smith et. al [116] determine $N_{s_{\text{eff}}}$ based on the integral time scale T_i of the velocity signal, using the autocorrelation coefficient $\rho_s(\tau)$:

$$N_{s_{\text{eff}}} = \frac{N_s}{2T_i/\Delta t} , \tag{3.8a}$$

$$T_i = \lim_{T \to \infty} \int_0^T \rho_s(\tau) \mathrm{d}\tau , \tag{3.8b}$$

with $\Delta t = 1/f_s$. In most practical scenarios, the integral 3.8b is not evaluated over the full limit and in instead computed up to the point at which the autocorrelation coefficient first falls to zero [108]. This approach is valid when the measurement time is greater than $10T_i$ [116]. It is apparent from equations 3.7 and 3.8 that uncertainty is high when the ratio $2T_i/\Delta t \gg 1$. HWA measurements typically feature high sampling rates and as such lead to the velocity signals being highly correlated. For BL measurements the largest integral times scales are found in the freestream, although $\langle Q \rangle$ is usually low. An estimate for local uncertainty due to random errors is presented in Figure 3.5, for a measurement plane in the vicinity of the DRE array. The uncertainty increases closer to the wall, being the largest aft of the roughness elements where spanwise gradients are large.

3.3. Experimental Test Matrix

The measurement campaign was designed to complement the results by Zoppini et. al [136], who employed 3-D dual pulse PTV to resolve the steady-state features of the DRE wake. As discussed in Section 3.1, two DRE configurations are investigated: a critical forcing array of height $k_D = 0.3$ mm and a super-critical forcing array of height $k_D = 0.4$ mm. Both arrays are spaced at $\lambda_1 = 8$ mm corresponding to the dominant stationary crossflow mode predicted by LST and previous works [139, 136].

HWA is the primary technique used to measure velocity fluctuations in the near-element flow field. This is done through an ensemble of hot-wire scans, conducted at successive chord locations from $x/c = 0.15$ to $x/c = 0.17$ (Figure 3.6). These scans map out the BL in a wall-normal $y - z$ plane

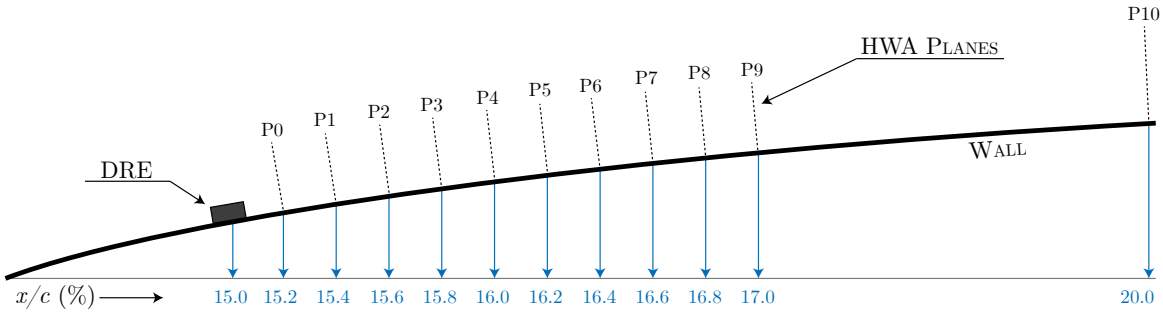

Figure 3.6: Chordwise location of the HWA measurement planes aft of the DRE array. Schematic is not to scale.

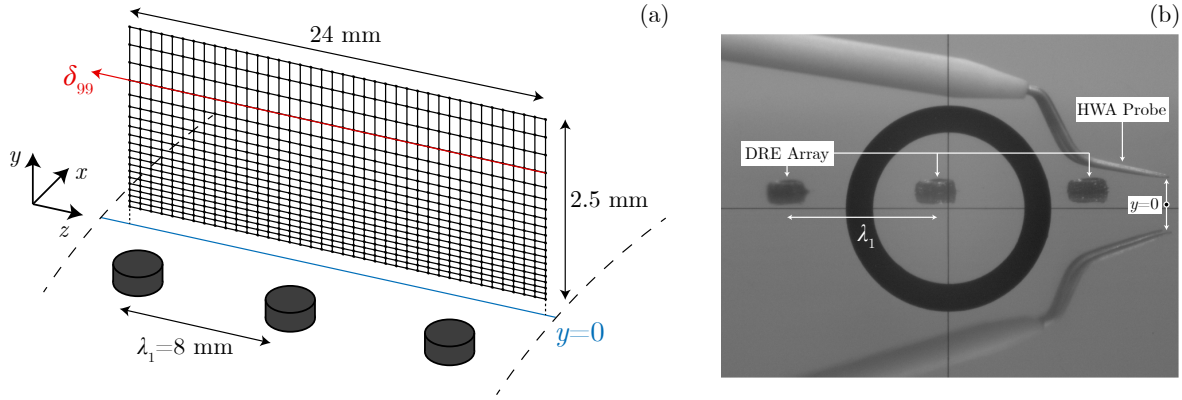

Figure 3.7: (a) A schematic of the $y-z$ HWA measurement planes. Blue line indicates the local location of the wall. Red line is an estimate of the average BL thickness, used to appropriately select the $y-$distribution of measurement points. (b) Image captured using the micro-alignment telescope system. Black cross hairs are built-in guides used to assist positioning of the telescope. The black dot on the far right is the mid-point of the line connecting the HWA probe to its reflection, providing a visual estimate for the wall location.

at each x/c station, by measuring individual BL velocity profiles over a range of spanwise locations (Figure 3.7a). The $y-z$ planes consist of 32 measurement points in the y-direction, whose spacing is progressively increased when moving from the wall toward the freestream. This allows for better resolution of the near-wall BL features with a lower number of wall-normal points, reducing the overall measurement time. The vertical extent of the plane is adjusted based on the chordwise development of the BL thickness, starting from a height of 2.5 mm in the element vicinity. The extent in the spanwise direction is selected to be 24 mm ($3\lambda_1$) to include three roughness elements for statistical and spatial spectral analysis. The spacing between spanwise points is uniform, with a resolution of 0.3 mm. Additionally, a coarser hot-wire scan is conducted at $x/c = 0.2$ to characterize downstream instability development. This plane consists of 27 and 50 points in the $y-$ and $z-$directions respectively and extends up to a nominal height of 3.3 mm.

The BL profile scans are scripted to begin at the wall and end in the freestream. However, the hot-wire probe must be manually positioned at the first measurement point, which corresponds to the lower bound of the domain. There is a limit to this, due to the physical size of the probe as well as a thermal *wall-effect* [97]. At positions very close to the wall, the measurements are affected by spurious heat transfer between the probe and the wall, and result in *tails* in the velocity profiles. This is addressed in Section 3.4.1, where the wall location is determined through linear extrapolation. Considering these factors, the closest measurement point is selected to be at a location where the BL mean velocity is 15% of the local freestream velocity. A micro-alignment telescope is used to assist and monitor the near-wall positioning of the probe, to verify that collisions with the wall are averted (Figure 3.7b). Preliminary examination of the flow field performed using the IR images also enables precise positioning of each measurement plane. Three roughness elements from the DRE array are selected to be included in the measurement domain, located at the mid-span of the swept wing model. The traverse is shifted between chordwise stations such that successive $y-z$ planes follow the stationary flow features initiated by the same three elements.

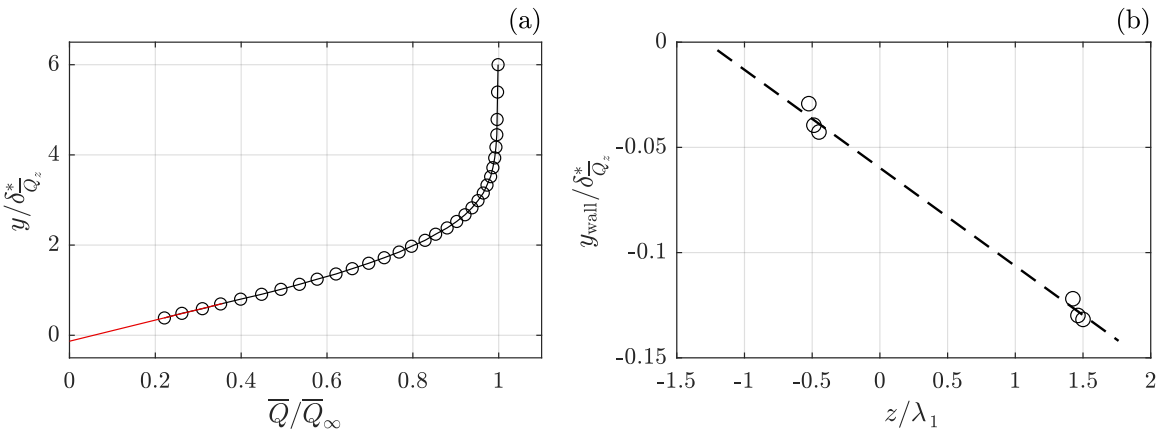

FIGURE 3.8: Wall-finding procedure applied to a HWA plane at $x/c = 0.156$. (a) Linear extrapolation (red line) of the mean velocity profile (∘-) at $z/\lambda_1 = 1.5$ toward the wall. (b) Least-squares fit of the wall location (- - -). The three roughness element centres are located at $z/\lambda_1 = -1, 0, 1$. Markers (∘) indicate estimations of y_{wall} at locations in-between the roughness elements where the BL is unperturbed.

3.4. HWA Processing Techniques

3.4.1. Wall-Finding

As discussed in Section 3.3, the lower limit of the HWA measurement planes is the $y-$location at which the unperturbed BL velocity is 15% of its local freestream magnitude. Measurement points closer to the wall suffer from heat transfer between the wire and wall, disrupting the velocity measurements [97]. This leads to the formation of a *tail* in the local mean velocity profiles, where the velocity magnitude retains almost constant values.

The result of this is that the actual location of the wall in the acquired velocity fields is unknown and must be determined in a post-processing procedure. For 2-D BLs, this has typically been done through a least-squares approach, where the local velocity profile is linearly extrapolated toward the wall [130]. The wall location, y_{wall}, is determined as the point at which the extrapolated velocity goes to zero i.e. the profile satisfies the no-slip condition. The zero external pressure gradient for Blasius flow implies that the curvature of the velocity profile at the wall, $\partial^2\overline{Q}/\partial y^2\,|_{y=0}$, is also zero. Thus, linearly extrapolating the profile is a valid approach and is done using points at which the mean BL velocity falls below 35% of the local freestream velocity. The velocity profiles tails are omitted from the linear fit.

The current work features an accelerated, 3-D BL with roughness elements, and linearly extrapolating the local HWA velocity profiles leads to systematic errors in determining the location of the wall. As such, the *Dice* approach proposed by White & Ergin [130] is adopted to minimize this error (Figure 3.8). The approach involves processing the measurement plane as a whole, rather than the local velocity profiles at each spanwise measurement station. A series of velocity profiles are selectively extracted from the unperturbed BL region in between roughness elements. Only these profiles are subjected to the least-squares velocity fit and a representative wall location is determined at each of these spanwise locations. A second linear fit is then performed to interpolate the obtained wall locations and determine the effective y_{wall} as a function of the spanwise coordinate z. The local velocity profiles are then each shifted by an amount determined by the y_{wall} local fit value. This also corrects for misalignment between the traverse system and the wing surface in the spanwise direction. The advantage to using only the unperturbed inter-element velocity profiles is that the strongly decelerated regions in the wake of the DRE are excluded from the wall-finding procedure. This minimizes the error in estimating y_{wall}. However, it should be noted that this error is not completely eliminated as the unperturbed BL flow is still mildly accelerated within the measurement domain. As this acceleration is only mild, the linear least-squares approach can still very well approximate the location of the wall.

3.4.2. Spatial Analysis

An overview of the spatial organization of the DRE wake can be obtained through the temporal mean and standard deviation of the HWA velocity fields, $\overline{Q}$ and $\langle Q \rangle$ respectively. Contours of $\overline{Q}$ allow for a

characterization of the stationary flow features within each $y-z$ plane, while $\langle Q \rangle$ is representative of unsteadiness in the flowfield. The mean velocity field is spanwise-averaged along the $z-$coordinate to obtain the mean BL profile, $\overline{Q}_z = \text{mean}(\overline{Q})_z$. This mean profile is computed for each chordwise plane and subtracted from the corresponding $\overline{Q}$ field to obtain the stationary disturbance velocity field, $\overline{Q}_d = \overline{Q} - \overline{Q}_z$. The wall-normal disturbance profile is computed as the spanwise standard deviation of the mean velocity field, $\langle \overline{Q} \rangle_z$, and can be used to gain an insight into the overall stationary disturbance amplitude evolution. Additionally, a spatial Fast Fourier Transform (FFT) is applied to $\overline{Q}_d$ to investigate the spanwise spectral content of the disturbances. In this manner, the evolution of the shape function amplitudes of individual Fourier modes can be tracked. All quantities are non-dimensionalized by the local freestream velocity in the corresponding $y-z$ plane, $\overline{Q}_\infty$, estimated as the average of $\overline{Q}_z$ for $y > \delta_{99}$. Spanwise lengths are non-dimensionalized by the DRE forcing wavelength, $\lambda_1 = 8$ mm, and wall-normal lengths by the displacement thickness at $x/c = 0.165$, computed to be $\overline{\delta^*} \approx 0.46$ mm.

In the context of the current work, the stationary disturbance amplitudes are estimated through an integration of the disturbance profiles along y, from the wall up to δ_{99} [92, 29]. The profile used is that of the mean disturbance energy, for which the amplitude is then computed as:

$$\overline{E} = \frac{1}{\delta_{99}} \int_0^{\delta_{99}} \langle \overline{Q} \rangle_z^2 \mathrm{d}y \ . \tag{3.9}$$

The effective N-factor, $N_{\overline{E}}$ [102], is computed as per equation 2.38b where the $\bar{E}_0^{\text{int}}$ is taken to be the mean disturbance energy amplitude estimated at the first HWA plane.

3.4.3. Welch's Modified Periodogram

For an analysis of the unsteady fluctuations in the DRE vicinity, it is of interest to investigate the frequency content of the HWA velocity signals. At each measurement point, the mean velocity is subtracted from the total signal to isolate the fluctuating component i.e. $Q' = Q - \overline{Q}$, which is then non-dimensionalized by the freestream velocity of the first measurement plane. An estimate of the power spectral density (PSD) of Q' at each point is then made using Welch's method [129]. The method involves splitting the entire signal into a finite number of overlapping segments. A windowing function is applied to each signal segment to enforce periodicity at its extremes, after which a FFT is carried out. The output of the FFT is squared and then averaged over all segments to obtain an estimate for the signal PSD. Welch's method offers reduced noise in the PSD estimate in exchange for frequency bin resolution. Thus, a trade-off solution to this must be determined based on the type of application involved. Additionally, the use of overlapping segments is to compensate for the loss in signal power due to the windowing of each segment. The frequency resolution for temporal analysis was selected to be 25 Hz, with the corresponding segment length computed to be $N_s/25 = 2048$ samples. The segment overlap was set to be 50% of the segment length and a Hamming window was employed as the windowing function. An estimate for the unsteady disturbance energy contained within a HWA measurement plane is computed by first spatially integrating the PSD over the plane, followed by multiplication with the frequency bin size:

$$E'(x,f) = \Delta f \iint_{yz} \text{PSD}(x,y,z,f) \mathrm{d}z\mathrm{d}y \ . \tag{3.10}$$

Similarly, the energy contained within selected frequency bands can be obtained through integration of the PSD over the plane, as well as within the band:

$$E'_{f_1-f_2}(x) = \int_{f_1}^{f_2} \iint_{yz} \text{PSD}(x,y,z,f) \mathrm{d}z\mathrm{d}y\mathrm{d}f \ . \tag{3.11}$$

4

Stationary DRE Wake Analysis

The following chapter discusses the strategies undertaken and results relating to modelling of the stationary DRE wake features within a non-modal stability framework, the NmPSE. The reference baseflow configuration considered was acquired in a previous experimental campaign by Zoppini et. al [136], providing the structure of the DRE wake. This is used as the basis from which initial conditions for the NmPSE solver are extracted. Growth of the primary, stationary wake mode is numerically solved for, and a series of parametric studies are conducted to check the robustness of the NmPSE framework. This is followed by a full numerical reconstruction of the DRE wake, provided by the analysis of the harmonic modes. As an alternative to experimental ICs, analytical approximations of the wake structure are formulated and their validity is investigated for the primary wake mode. Lastly, a convergence study is performed to quantify the effect of the discretization on the non-modal stability simulations.

4.1. Baseflow Matching

The experimental 3-D dual-pulse PTV investigation conducted by Zoppini et. al [136] forms the basis for the non-modal stability simulations carried out in this work. Their research involved near-DRE measurements within the M3J swept wing BL, at a chord Reynolds number of 2.17×10^6. The baseflow employed throughout this thesis is thus constructed to match the reference experimental BL.

The external velocity components, U_∞ and W_∞, needed to generate the numerical BL flow were obtained from the experimental data set of Zoppini et. al [136] through two sources: 3-D dual-pulse PTV measurements, and the pressure coefficient (c_p) distribution. With the former, the BL profiles were obtained by spanwise averaging the velocity fields at successive chordwise locations. The chordwise development of the external flow was then computed as the respective averages of the U and W profiles in the freestream. The c_p distribution allows for the local BL freestream velocity magnitude, Q_∞, to be determined according to:

$$Q_\infty = Q_T \sqrt{1 - c_p}\,, \tag{4.1}$$

where Q_T is the freestream velocity in the wind tunnel test section. For a spanwise invariant flowfield and constant $W_\infty = Q_T \cos(\Lambda)$, the chordwise external velocity distribution can then be obtained through Pythagoras theorem, $U_\infty = \sqrt{Q_\infty^2 - W_\infty^2}$. This approach neglects mild blockage in W_∞ due to the wind tunnel walls. The experimental external velocity components are depicted in Figure 4.1a, within a domain of interest located in the vicinity of the DRE array (placed at $x/c = 0.15$). Additionally, the chordwise external velocity is computed using the FSC power law in equation 2.5, and presented alongside the experimental distributions. The parameters U_{ref}, x_{ref} and m were determined according to a least-squares fit between the experimental data and the power law. It is seen that the experimental U_∞ closely follows a FSC-type external flow within the region of interest, implying that the BL is self-similar here. Thus, a solution of the FSC equations 2.8 would be nearly identical to that of the spanwise invariant BLE 2.4. As per the discussion in Section 2.1, the baseflows for all stability simulations in this chapter was hence generated through solving the FSC equations.

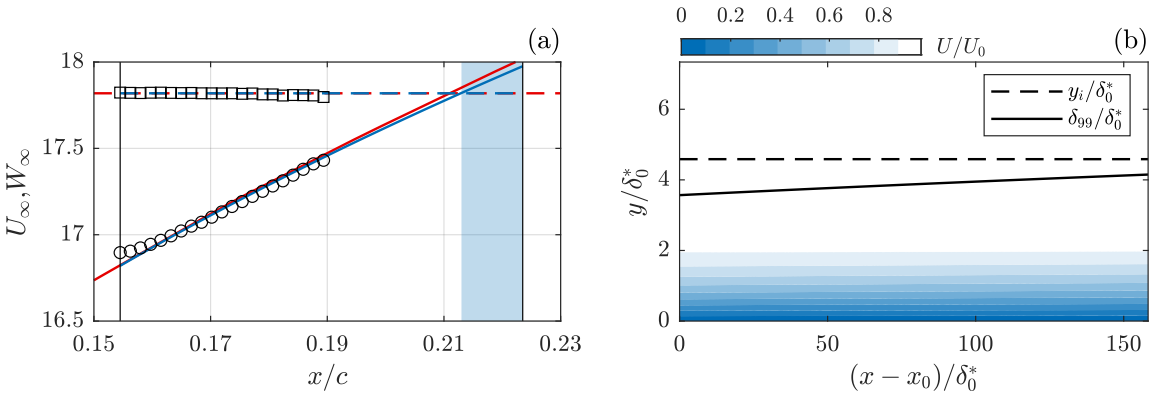

Figure 4.1: (a) External flow matching within the stability domain (black vertical lines). U_∞, W_∞ obtained from PTV measurements [136] (○, □), experimental c_p distribution (solid, dashed red line), FSC power law (solid, dashed blue line). Blue shaded region represents the extent of the HLNS buffer. (b) Contours of the baseflow velocity component $\bar{U}$ within the stability domain. The $y-$extent of the domain shown is $0.06H$.

Table 4.1: Baseflow and stability domain parameters used for the non-modal simulations.

FSC Baseflow					Stability				
x_{ref}	U_{ref}	W_∞	m	β_H	H	y_i	n_y	x_{in}/c	x_{out}/c
0.154 m	16.82 m/s	17.81 m/s	0.18	0.305	0.05 m	0.002 m	100	0.154	0.223

Table 4.1 lists the FSC BL and stability domain parameters used to simulate the experimental set-up of Zoppini et. al [136]. The inflow displacement thickness, δ_0^*, was computed to be 0.433 mm, corresponding to an inflow Reynolds number of $\text{Re}_{\delta_0^*} = 496$, in accordance with the experiment. These are used to non-dimensionalize the baseflow quantities as well as the stability computations. The stability domain is selected such that it begins at the chordwise location where the experimental initial conditions are sampled, being $x/c = 0.154$ for all simulations. The outflow station is chosen to be at $x/c = 0.223$, which lies further downstream than the last station for which experimental data is available. This is done to allow for a sufficient domain length over which stationary CFI may emerge in the far-wake, and also to account for the buffer region used with the HLNS.

Similar to the test case set-up in Section 2.3.2, the vertical extent of the stability domain, H, is set to 50 mm such that the domain cut-off error is negligible. The pseudo-spectral wall-normal discretization is biased so that half of the Chebyshev collocation points lie below $y_i = 2$ mm, which is approximately the maximum thickness of the experimental BL in the measurement region. The density of grid points in the wall-normal direction is $n_y = 100$ for all simulations, considered adequate based on the rapid convergence of the Chebyshev discretization with refinement. The chordwise grid density, n_x, is selected on the basis of the parameter $\bar{\alpha_r}\Delta\bar{x}$, where $\bar{\alpha_r}$ is roughly estimated from a modal LPSE analysis under the same conditions. This is adjusted depending on the harmonic in question. The results are noted to be sensitive to the choice of n_x, as evidenced by a convergence study presented at the end of this chapter. Finally, the buffer region was selected to start at 85% of the domain length for all computations involving the HLNS. Figure 4.1b depicts the chordwise development of the BL baseflow, within the defined stability domain.

4.2. Experimental Initial Conditions

4.2.1. DRE Wake Structure

The DRE forcing configuration selected for use in numerical stability analyses was that of k_3, defined in Section 3.1, and also investigated by Zoppini et. al [136]. The configuration is characterized by a roughness Reynolds number of $\text{Re}_k = 192$ and lies within the critical regime, where the stationary DRE-wake features are expected to develop into stationary CFI at downstream locations [62, 136].

Figure 4.2a presents a wall-normal slice of the stationary chordwise velocity disturbance field, u', measured using 3-D dual-pulse PTV [136]. This was obtained in a manner similar to that defined for the spatial analysis of the HWA fields in Section 3.4.2. The key flow features within the DRE-wake

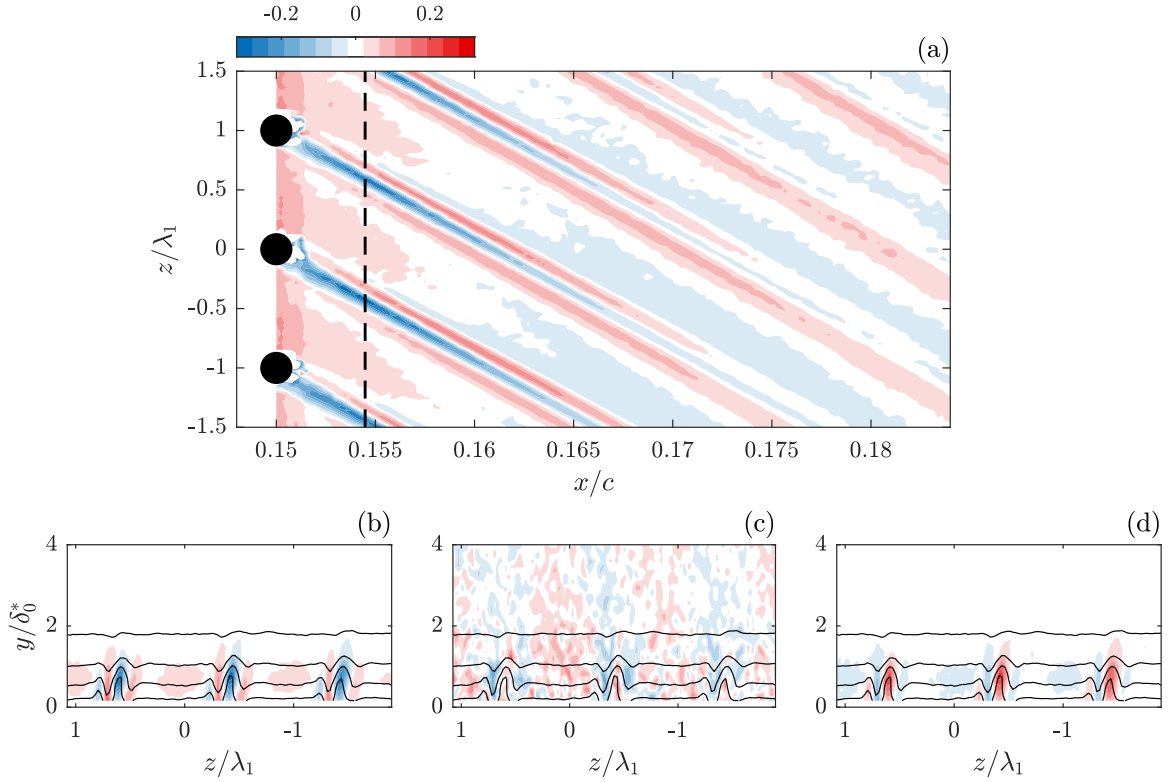

Figure 4.2: (a) Wall-normal slice of the experimental u'/U_0 disturbance field aft of the DRE array at $y/\delta_0^* = 0.55$. Black dashed line is the location at which the initial conditions are sampled. Contours of (a) u'/U_0 (b) $10v'/U_0$ (c) w'/U_0 disturbance fields at the sampling location.

are apparent, as discussed in section 1.4.3 and reported by previous investigations [14, 62, 136]. A set of low and high-speed velocity streaks induced by the HSV system develops aft of each roughness element. The strength of the central low speed streak increases rapidly up to $x/c = 0.153$, after which it undergoes gradual decay. The high-speed streaks begin to increase in strength shortly after the low-speed maximum. The outboard high-speed streak peaks in amplitude at $x/c = 0.16$ after which it decays, while the inboard streak is sustained to the end of the measurement region. At $x/c = 0.18$, the disturbance field begins to resemble that induced by stationary CFI. The asymmetry between the outboard and inboard streaks can be attributed to the 3-D nature of the flowfield, with structures co-rotating with the crossflow velocity profile being sustained [62].

The initial plane from which the ICs for the NmPSE are extracted was selected to be at $x/c = 0.154$. This is located at approximately where the low-speed streak is at its maximum amplitude, and where the high-speed streaks begin to amplify. The u', v' and w'disturbance fields at the initial plane are presented in Figure 4.2b-d. Contour lines of the local, steady BL velocity u are superimposed on the disturbance fields. The central low-speed region aft of each roughness element attains its maximum at $y/\delta_0^* \approx 0.55$, after which it decays into the freestream. The DRE-wake is also noted to be highly localized, with the regions between elements featuring largely unperturbed flow. This is in agreement with findings by Ergin & White [34], wherein the wake of each element in the DRE array resembles that of an isolated roughness element for $\lambda_1 > 3d_D$.

4.2.2. Extraction of ICs

Fourier Analysis of Initial Plane

A spanwise FFT is performed on the chordwise disturbance field, $\overline{u}_d$, at the initial plane (4.2b), in order to determine its spatial spectral content. Figure 4.3a presents the distribution of Fourier amplitudes among spanwise modes of wavelength λ. The largest wavelength at which spectral energy is concentrated is that of the DRE forcing, i.e. $\lambda_1 = 8$ mm. However, spectral peaks are identified over a wide range of super-harmonics (smaller wavelengths) of the forced mode. This is a consequence of the highly

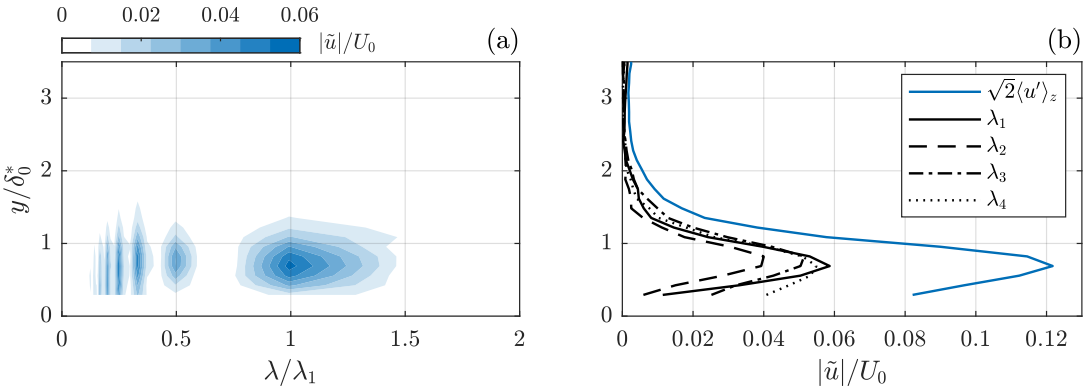

Figure 4.3: (a) Spanwise FFT of the u' field at the initial plane ($x/c = 0.154$). (b) $\tilde{u}$ shape function amplitudes of the forced mode and first three harmonics, compared with the experimental velocity standard deviation profile.

localized nature of the near-element flowfield, resulting from the finite diameter, d_D, and inter-element spacing, λ_1, of the DRE array [139]. The velocity perturbations aft of the element can thus be considered pseudo-pulses, containing a wide spectrum of spanwise frequencies. These frequencies do not necessarily correspond to natural modal instabilities, i.e. eigensolutions of the Orr-Sommerfeld and Squire system 1.6, but are representative of the DRE wake features in Fourier space. It is seen from Figure 4.3a that spectral energy is nearly equally distributed among the primary mode and its first four harmonics, which altogether comprise up to 56% of the total disturbance energy in the DRE wake.

The shape function amplitudes corresponding to the first three modes are extracted and shown in Figure 4.3b, along with the spanwise standard deviation profile, $\langle u' \rangle_z$. The primary mode is labelled as λ_1 and higher harmonics are subscripted to follow this. The amplitude of the λ_1 mode falls significantly below the total disturbance amplitude represented by $\langle u' \rangle_z$, further highlighting the contribution of the super-harmonics in the elements vicinity. This also implies that their inclusion is necessary in numerically reconstructing the DRE wake within a non-modal framework. All modes are spatially well-contained within the BL, peaking in amplitude at a wall-normal distance comparable to the element height.

Interpolation onto Numerical Stability Grid

The Fourier modes extracted from the DRE wake were each subjected to a pre-processing routine in order to ensure compatibility with the numerical solvers (Figure 4.4). The complex shape functions, $\tilde{u}, \tilde{v}, \tilde{w}$, were first forced to a value of zero at and beyond a height corresponding to the local BL thickness. This was done to avoid artefacts in the interpolation of these shape functions onto the stability grid outside of the BL, as the disturbances are expected to exponentially decay into the freestream. A value of zero was also prescribed at the wall, to satisfy the no-slip condition. The real and imaginary components of each shape function were then separately interpolated onto the Chebyshev $y-$grid at the initial marching station, using Piecewise Cubic Hermite Interpolating Polynomials (PCHIP) (see Fritsch & Carlson [38]). The use of PCHIP proved to be more robust to the disturbances affecting the experimental data set and better interpolated flat regions, as compared to using cubic splines.

The interpolated shape functions were treated with a smoothing filter, in an effort to remove residual noise that was carried over from the PTV shape functions during interpolation. The smoothing filter operated by dividing the discrete shape function vectors into windows, over which a linear regression was performed. The windows were selected to be ten grid elements in length, to best preserve the original shape of the ICs after smoothing. While the smoothing filter eliminates discontinues arising from the PCHIP interpolation, allowing for more compatibility with the numerical solvers, it can possibly affect the results of the non-modal stability analyses. Thus, its effect on the growth of the primary mode, λ_1, is investigated in Section 4.2.3.

4.2.3. Primary Mode Analysis

As the monochromatic CFI mode that emerges downstream of the DRE wake has a wavelength equal to the inter-element spacing [92, 111, 139], it is of foremost interest to simulate the non-modal evolution of the primary Fourier mode, $\lambda_1 = 8$ mm, within the wake.

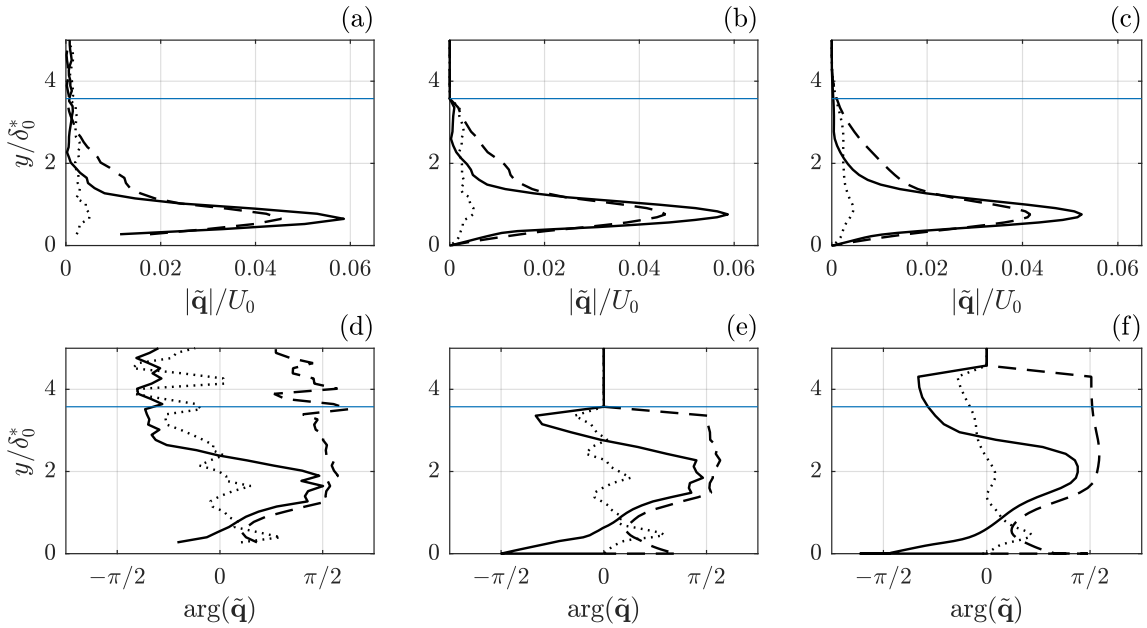

Figure 4.4: (a,d) Experimental shape functions extracted from PTV data. (b,e) Shape functions interpolated onto the stability grid. (c,f) Interpolated shape functions with additional smoothing. Solid, dotted and dashed lines correspond to $\tilde{u}$, $\tilde{v}$ and $\tilde{w}$ respectively. Blue line indicates the local δ_{99}.

The disturbance velocity ICs for the primary mode were extracted as per the preceding discussion, and interpolated onto the stability grid at the inflow of the domain (Figure 4.4). The baseflow and stability grid parameters employed for these simulations were listed in Table 4.1. The chordwise grid density n_x was selected to be 300 points based on LPSE estimates for $\bar{\alpha}_r$, such that the parameter $\bar{\alpha}_r \Delta\bar{x} = 0.146$. Further inputs to the NmPSE and HLNS are the non-dimensional spanwise wavenumber, $\bar{\beta} = 2\pi\delta_0^*/\lambda_1 = -0.316$, and the non-dimensional frequency, $\bar{\omega} = 0$, corresponding to the stationary, primary CFI mode. Once again, the minus sign in $\bar{\beta}$ arises from the positive convention for W_∞ and $\bar{\alpha}$. Figure 4.5a depicts the disturbance velocities at the initial plane, for the λ_1 Fourier mode in the DRE wake.

To complete the system of experimental ICs prescribed at the inflow station, the shape function for the disturbance pressure, $\bar{p}$, must also be specified along with the disturbance velocity components. This however, is not readily available from the PTV data set. As a test, the disturbance pressure was prescribed in two ways: it was either set to zero at the inflow station or computed as a modal ILST solution. It was seen that either choice of the initial disturbance pressure did not affect the growth of the velocity perturbations for both the NmPSE and HLNS. Thus, for the sake of simplicity, the IC for $\bar{p}$ was set to zero for all numerical computations.

The NmPSE requires an additional input in the form of the chordwise wavenumber, $\bar{\alpha}$, which is omitted from the HLNS framework. This is obtained as an approximation from the PTV data using the chordwise disturbance velocity, u'. The classical definition $\alpha = \Re((1/iu')\,\partial u'/\partial x)$ [3] is employed, evaluated at the wall-normal location where the PTV shape functions for u' attain their maximum. This ensures consistency with the computation method for $\bar{\alpha}$ used by the NmPSE (Section 2.2.1). The experimental $\bar{\alpha}$ estimates for the λ_1 mode are shown as a scatter plot in Figure 4.5b. The estimates are rather noisy in the element vicinity, but start to converge at further downstream locations where the wake begins to take on a modal nature. The initial $\bar{\alpha}$ value for the NmPSE is approximated as the median of the scatter, with the assumption that its variation is low within the DRE wake. For the λ_1 mode, this results in $\bar{\alpha}_0 \approx 0.29$.

The evolution of disturbance energy for the λ_1 mode is presented in Figure 4.6a. This is quantified using the N-factor, N_E, defined as per equation 2.38. As predicted by the NmPSE, the disturbance energy first begins to decay strongly, reaching its minima approximately $20\delta_0^*$ lengths downstream of the initial plane. This is followed by a similarly rapid phase of energy growth up to around $60\delta_0^*$ downstream lengths, after which the growth rate begins to decrease, resembling that of exponential disturbance

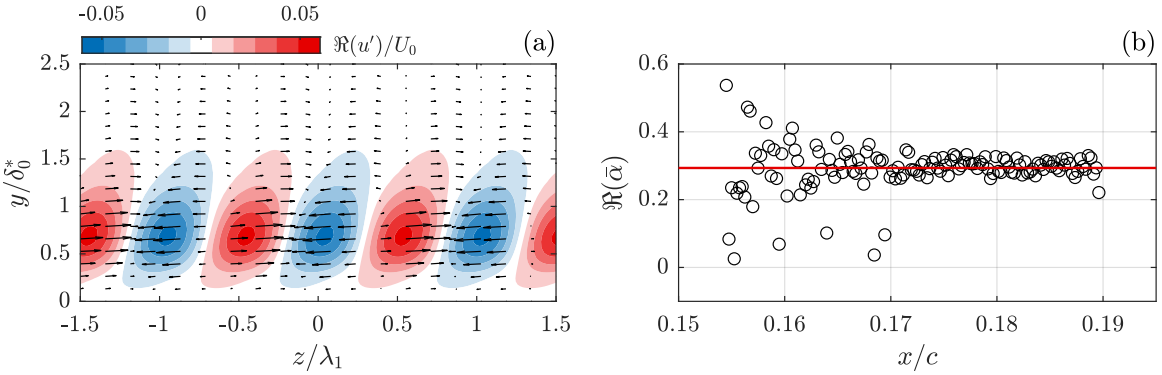

Figure 4.5: (a) Contours of the disturbance velocity u' for the primary Fourier mode, at the initial plane. Vectors represent the vectorial sum of the v' and w' components. (b) Experimental estimates for the wavenumber $\bar{\alpha}$ (∘) in the DRE wake region. Solid red line represents the median value of the scatter.

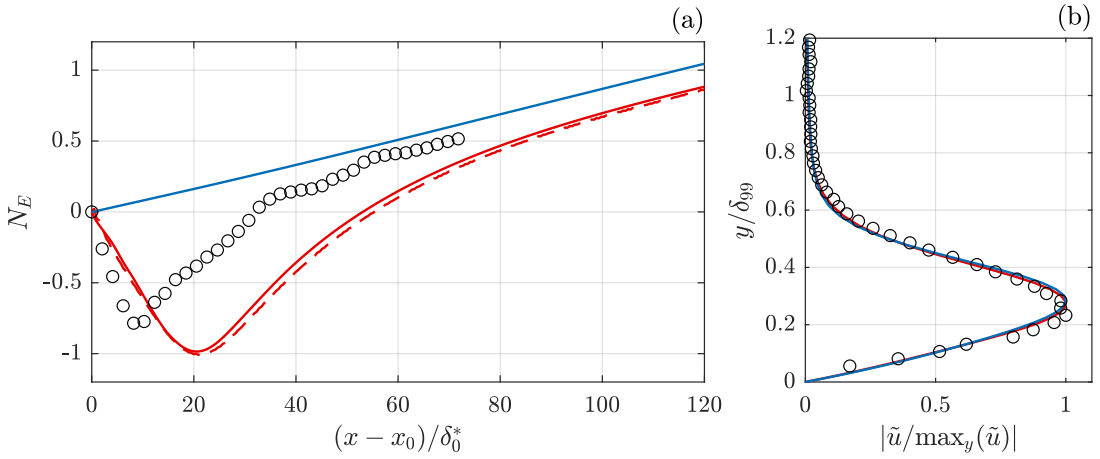

Figure 4.6: (a) Evolution of the λ_1 DRE wake mode with the NmPSE (solid red line), HLNS (dashed red line) and from PTV data [136] (∘). Solid blue line represents a modal LPSE computation. (b) Normalized $\tilde{u}$ shape functions for the NmPSE (solid red line), LPSE (solid blue line) at the outflow station. PTV data (∘) at the last available $x-$station is superimposed.

amplification. This behaviour is reproduced by the HLNS, agreeing very well with predictions by the NmPSE. However, mild deviations between the two are observed during the phases of rapid decay and growth in the element vicinity. The NmPSE is seen to under-predict the decay phase, while over-predicting non-modal amplification downstream of the minima. The energy minima itself is slightly over-predicted by the NmPSE. This could be a result of violation of the slow variance condition for the NmPSE in these regions of strong growth/decay, which is not the case for the HLNS. A modal computation using the LPSE is also shown for comparison purposes, initialized with an ILST solution at the inflow. The pure CFI mode is unstable within the stability domain and undergoes monotonic, exponential energy growth. Beyond $100\delta_0^*$ downstream lengths, the N_E curves for the NmPSE, HLNS and LPSE are parallel, and energy growth rates are equal. This indicates that the non-modal solvers correctly predict the emergence and exponential amplification of the stationary CFI mode outside of the DRE wake. It is also of interest to note the lower outflow N-factor predicted by the non-modal as compared to the LPSE, aligning with the hypothesis by Zoppini et. al [139] that transient growth/decay in the DRE wake acts to lower the effective amplitude of the induced CFI.

While the non-modal solvers agree well with each other, there is a distinction between the experimental PTV growth curves and numerical predictions. The PTV disturbance energy decays more rapidly downstream of the inflow plane and attains its minima at about half the N-factor predicted by the non-modal solvers. The minima is also reached at half the distance, located at approximately $10\delta_0^*$ lengths downstream of the inflow plane. The energy recovery rate after the minima is close to that of the non-modal solvers, although still slightly over-predicted numerically. The disturbance is ampli-

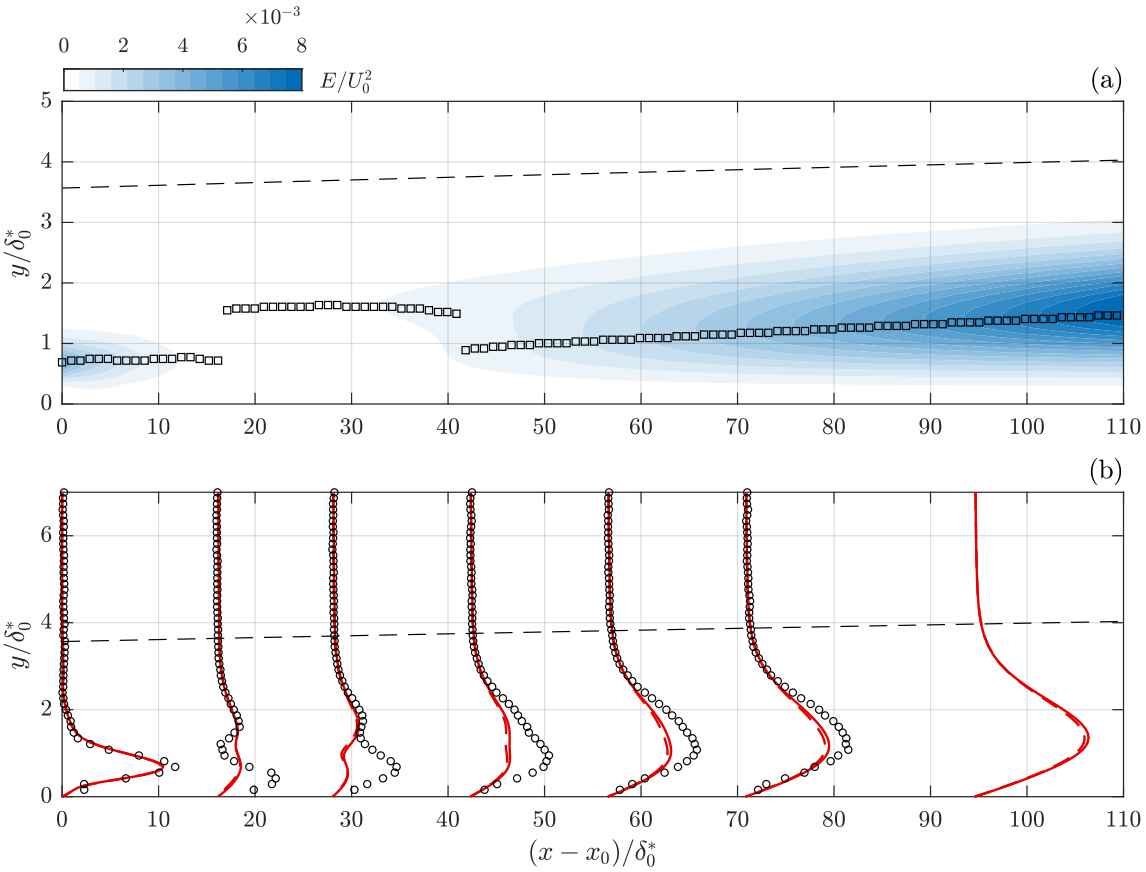

Figure 4.7: (a) Contours of disturbance energy for the λ_1 mode. Markers (□) indicate local energy maxima. (b) Shape functions of the chordwise disturbance velocity, $\tilde{u}$, for the NmPSE (solid red lines), HLNS (dashed red lines) and from PTV [136] (○). Dashed black line represents BL δ_{99}.

fied exponentially beyond $50\delta_0^*$ downstream lengths, aligning with the modal LPSE curve at a slightly lower outflow N-factor. As a result of the lower minima, this slightly larger than the outflow N-factor predicted by the non-modal solvers. Although the non-modal evolution phase for the experimental λ_1 mode occurs over a shorter chordwise scale, the overall trend is well captured by both the NmPSE and the HLNS. This is in contrast to the LPSE, which is limited to predicting modal growth as per the ansatz 1.9, where all three velocity components are constrained to grow according to a single $\bar{\alpha}$ in the phase function. Thus, it does not capture the region of transient energy decay/amplification in the DRE wake.

The shape function amplitudes of the chordwise disturbance velocity component at the outflow station are presented in Figure 4.6b. The shape functions are normalized by their maxima and the wall-normal coordinate by the local boundary layer thickness, δ_{99}. The respective predictions by the LPSE and NmPSE are seen to be nearly identical. This further validates that the NmPSE correctly evolves the λ_1 Fourier mode extracted from the DRE wake into the OS eigenfunction corresponding to modal CFI. This is also reflected by the experimental PTV data, which is in good agreement with the numerical shape functions. The mild mismatch could be amounted to the difference in sampling location between experiment and computations, as the last available experimental station is upstream of the final marching station.

A deeper insight into non-modal development predicted by the NmPSE can be gained by characterizing the development of the λ_1 shape functions throughout the stability domain. Figure 4.7a presents the evolution of disturbance energy additionally as a function of the wall-normal coordinate. Here, $\bar{E}(\bar{x}, \bar{y})$ is evaluated as per equation 2.38a although the wall-normal integration is not performed. The markers (○) follow the maxima of the disturbance energy profile through its downstream evolution. At and near the inflow, disturbance energy is largely concentrated around the peak in the non-modal ICs, but starts to diffuse during the decay phase. The energy peak itself does not vary much as the mode

decays. However, just upstream of the energy minima at $x - x_0 = 20\delta_0^*$, a jump in the disturbance energy peak is observed. The new maxima is located at $y/\delta_0^* \approx 1.7$, nearly half of the local BL thickness, and is remains here during the initial phase of disturbance energy recover. At $x - x_0 = 40\delta_0^*$, energy is seen to spread lower into the BL and the peak experiences a second jump, moving closer to the wall. Downstream of this location, the disturbance energy profile begins to undergo exponential amplification while diffusing in the wall-normal direction. The location of the energy peak remains fairly constant relative to the local BL thickness, shifting in the wall-normal direction as per the BL development.

The *peak switching* behaviour seen in the disturbance energy profiles is further revealed through the $\tilde{u}$ disturbance shape function evolution in Figure 4.7b. For the NmPSE, the initial peak in the shape function rapidly decays, resulting the initial non-modal energy decay as seen in Figures 4.7a and 4.6a. As the energy minima is approached, the secondary upper peak begins to emerge and overtakes the lower peak in amplitude. The switch in the energy peak is observed around this location. Both peaks undergo amplification during the transient energy growth phase, although the amplification experienced by the lower peak is larger. At around $40\delta_0^*$ downstream lengths, the two peaks are of equal amplitude and merge into a single structure further downstream. The shape function then grows exponentially and begins to resemble that of the stationary CFI mode. The evolution of $\tilde{u}$ predicted by the NmPSE qualitatively resembles that of the experimental λ_1 mode, although there exist some key differences. In addition to evolving over a short chordwise distance, peak switching does not occur in the experimental shape function. Although the initial velocity streak undergoes rapid decay and a secondary upper peak emerges, the lower peak remains dominant. Downstream of the energy minima, the upper peak amplifies and merges with the lower peak close to $x - x_0 = 60\delta_0^*$. The disturbance then evolves as a modal CFI.

The effect of peak-switching is rather crucial with the NmPSE framework, as $\bar{\alpha}$ is updated based on the maxima in the $\tilde{u}$ shape function. The locations at where a jump in the energy peak is observed features a discontinuous change in $\bar{\alpha}$, and a subsequently large $\partial\bar{\alpha}/\partial\bar{x}$. This could possibly result in some level of error being introduced into the solution at these marching stations. Figure 4.7b also presents the evolution of $\tilde{u}$ predicted by the HLNS for comparison, as $\bar{\alpha}$ does not influence its solution. The shape functions of the non-modal solvers generally agree very well, although mild deviations exist around their local maxima. It is also noted that these deviations become more apparent at locations downstream of a jump in the energy peak. However, as previously discussed, the deviations may also be related to the slow variance assumption for the NmPSE shape functions.

Effect of Marching Scheme

As discussed in section 2.2.3, the NmPSE is marched in the chordwise direction using the first-order backward Euler scheme 2.33a. In addition to this, a test case was run with the trapezoidal scheme as shown in 2.33b, to investigate if the use of a higher-order $x-$discretization might prove beneficial for the NmPSE. The λ_1 mode was simulated, using a setup identical to that in the previous section. However, a solution could not be obtained using the trapezoidal scheme with the parameter $\bar{\alpha_r}\Delta\bar{x} = 0.146$. In particular, the inner wavenumber loop for $\bar{\alpha}$ was seen unable to converge immediately downstream of the inflow station. The inability of the trapezoidal NmPSE to converge persisted with refinement of the $x-$grid, although a solution could be obtained for a coarser grid with $\bar{\alpha_r}\Delta\bar{x} = 0.292$. To facilitate comparison with the backward Euler NmPSE, the test was instead performed at this level of refinement.

Figure 4.8a presents the evolution of N_E for the backward Euler and trapezoidal NmPSE solvers. It is seen that two curves disagree significantly, with trapezoidal scheme predicting lower growth rates as well as a much lower energy minima. The region of exponential growth close to the outflow also features a lower growth rate as compared to the backward Euler solution, indicating that modal evolution may be erroneously predicted. While the trapezoidal solution does lie closer to the experimental data set, this is assumed to be purely coincidental. A standout feature is the appearance of oscillations in the trapezoidal NmPSE growth curves, which are most prominent in the region of non-modal disturbance evolution between the inflow and $60\delta_0^*$ lengths downstream. These appear to originate as a result of spurious oscillations in the λ_1 shape function, as can be seen in the the comparison between Figure 4.8b and Figure 4.8c. With $\tilde{u}$ for example, the magnitude of the shape function itself exhibits oscillatory behaviour, contrary to oscillations typically being represented by the shape function phase, $\arg(\tilde{u})$. Figure 4.8c also reveals that the oscillations are rather uniform throughout the stability domain, with a wavenumber estimated to be approximately 0.62. It is interesting to note that this is nearly equal to the first harmonic of the modal $\bar{\alpha}$ extracted at the outflow station, as predicted by the NmPSE, HLNS as well as the LPSE.

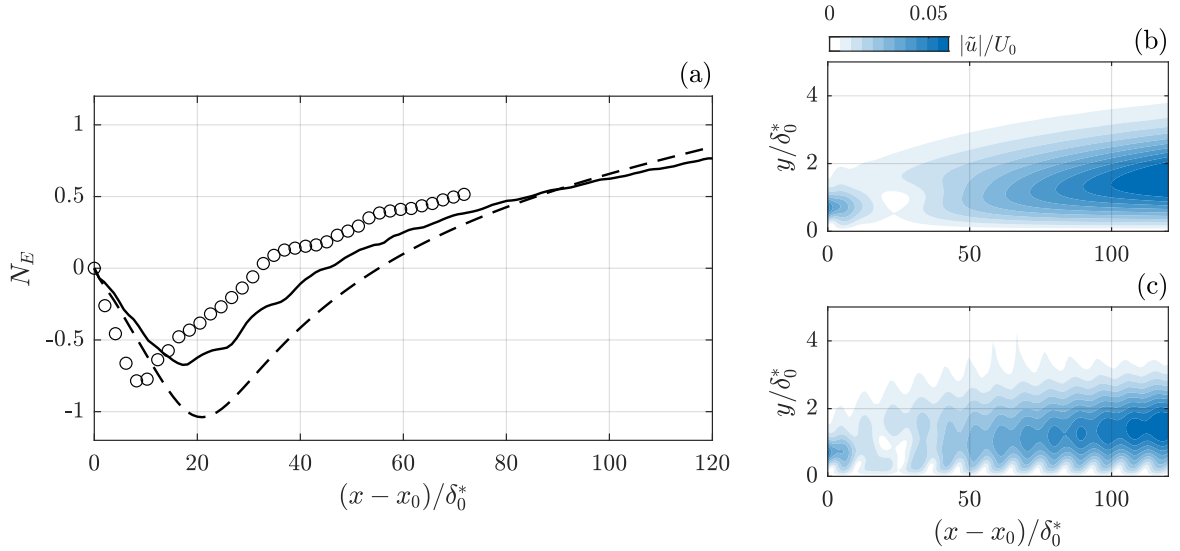

Figure 4.8: (a) Growth of λ_1 predicted by the backward Euler NmPSE (dashed red line), trapezoidal NmPSE (solid red line) and from PTV data [136] (○). Contours of the $\tilde{u}$ shape function amplitude shown for (b) backward Euler NmPSE and (c) trapezoidal NmPSE.

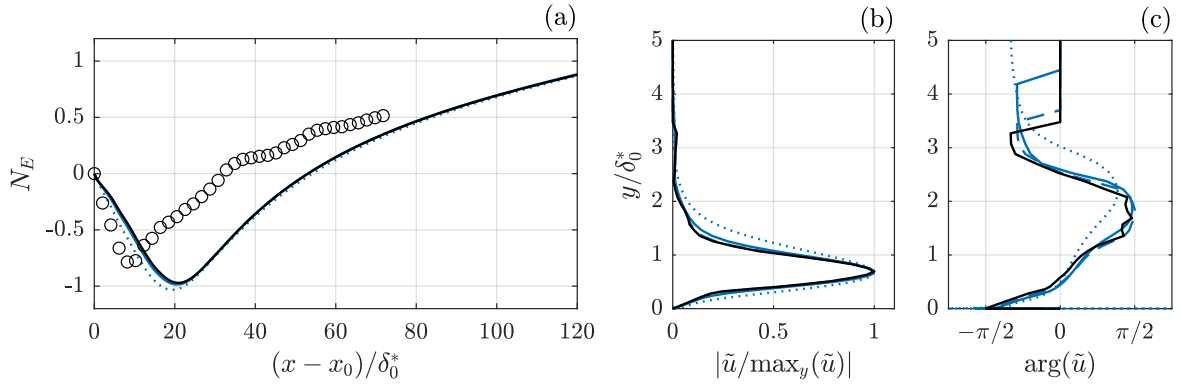

Figure 4.9: (a) Growth of λ_1 computed with the NmPSE for varying IC smoothing. Non-smoothed (solid black line), smoothing windows of 5 (dashed red line), 10 (solid red line) and 20 grid elements (dotted red line), and PTV data [136] (○). (b) Shape function magnitude and (c) phase for the various smoothing windows.

The close agreement between the backward Euler NmPSE and the HLNS in Figure 4.6a implies that the use of a trapezoidal marching scheme results in erroneous predictions for the non-modal growth curves. This combined with the presence of spurious oscillations in $|\tilde{\mathbf{q}}|$ motivated the use of the backward Euler scheme for all further non-modal computations with the NmPSE.

Effect of IC Smoothing

Noise in the PTV ICs supplied to the NmPSE and HLNS is reduced using the smoothing procedure described in Section 4.2.2. It is however important to determine whether this smoothing actually affects the results of the non-modal computations, and if so, quantify by how it does so. The strength of the smoothing filter is based on the window length selected for the linear regression. Tests with the NmPSE for the λ_1 Fourier mode were run for window lengths of five, ten and twenty $y-$grid elements, as well as with no smoothing applied.

From Figure 4.9a it can be seen that the energy N-Factor curves are practically unaffected for the smoothing windows of five and ten grid elements, as compared to the case with no additional smoothing. The strongest smooth applied does however cause a noticeable change in the initial, non-modal growth phase of the mode. The growth rate downstream of the inflow is larger for this case, and a lower energy minima is attained at a slightly earlier location than with the non-smoothed IC. The cause for this is possibly revealed in Figures 4.9b and 4.9c. It is seen that the largest smoothing window causes non-

Table 4.2: Stability parameters for the DRE-wake Fourier harmonics.

Harmonic	λ (mm)	β	n_x	$\bar{\alpha_r}\Delta\bar{x}$
λ_2	4	-0.69	600	0.139
λ_3	2.667	-1.035	900	0.136
λ_4	2	-1.38	1200	0.142
λ_5	1.6	-1.725	1500	0.149

negligible alterations in the $\tilde{u}$ shape function, which now deviates from what was originally extracted in the DRE wake. These deviations are sufficient enough such that λ_1 mode is no longer correctly represented in the NmPSE framework and evolves differently as a result. The five and ten grid element windows retain the mode shape to a much better extent, leading to a match in growth curves for these cases. It is thus evident that the NmPSE is sensitive to the shape of the IC, and that the smoothed shape functions must closely follow the mean profile of the raw, interpolated shape functions in order to ensure repeatable non-modal growth computations. This concept is further explored in Section 4.3, where the use of analytic approximations of the λ_1 shape functions are investigated.

4.2.4. Analysis of Higher Harmonics

Figure 4.3a reveals that spectral energy is not solely concentrated within the primary Fourier mode at the initial plane, with the first four harmonics of λ_1 also being significant contributors. Although these harmonics are expected to decay downstream of the DRE-wake region as stationary CFI corresponding to λ_1 begin to emerge [62, 136] (Figure 4.2a), it is still of interest to simulate their evolution within the non-modal framework. The linearisation employed within the NmPSE and HLNS implies that each spanwise harmonic can be simulated independently, after which the resulting disturbances fields may simply be subjected to an inverse FFT to numerically reconstruct the DRE wake.

The ICs for the harmonic Fourier modes are extracted from the experimental PTV data [136] through the procedure discussed in Section 4.2.2, for the λ_1 mode, using a PCHIP interpolation with additional smoothing. The initial valued for $\bar{\alpha}$ is also extracted as previously discussed, as the median of its PTV estimates. All modes are stationary ($\bar{\omega} = 0$), and their corresponding non-dimensionalized spanwise wavenumbers are presented in Table 4.2. While the baseflow and wall-normal discretization are not changed for the stability calculations, the chordwise discretization is adjusted for each harmonic so as to maintain a similar $\bar{\alpha_r}\Delta\bar{x}$ parameter through all computations. This ensures that a sufficient number of chordwise wavelengths are still represented by the stability grid for higher harmonics.

The chordwise evolution of each wake harmonic is presented in Figure 4.10, for both experimentally-derived and ILST ICs, quantified through N_E. Close to the initial plane, both the NmPSE and the HLNS are in good agreement with each other for all harmonic modes. In fact, this agreement remains fairly good for the second and third harmonics right up to the outflow station for the analysis. Downstream of $x - x_0 = 20\delta_0^*$, disagreement between the two non-modal solvers is evident for the first and fourth harmonics. This rather inconsistent mismatch among harmonics seems unlikely to stem from rapid mode decay and violation of slow-variance for the NmPSE, as the third harmonic decays faster than the first and similarly to the fourth.

The general growth trend for second, third and fourth harmonics is seen to agree well with the experimental data shortly downstream of the initial plane, with the modes experiencing mild transient growth followed by strong transient decay. While the decay phase compares well with experiment initially, the non-modal solvers predict a short stretch of rapid decay beyond $x - x_0 \approx 40\delta_0^*$. This decay slows as the outflow is approached and begins to resemble that from LPSE predictions. As a result, the numerically predicted outflow N-factors are significantly lower than those of the experimental dataset. The situation is largely different for the λ_2 harmonic. From Figure 4.10a it is evident that the numerically predicted growth trend deviates significantly from the experiment, with the mode transiently growing downstream of the inflow versus the monotonic decay seen in the experimental data. The experimental energy decays up to approximately $30\delta_0^*$ downstream lengths after which it begins to slowly recover. This is not predicted by the non-modal solvers, for which the λ_2 mode is seen to undergo continuous decay up to the outflow. The outflow decay rates are seen to closely resemble the exponential decay predicted by the LPSE, although slightly over-predicted by the NmPSE.

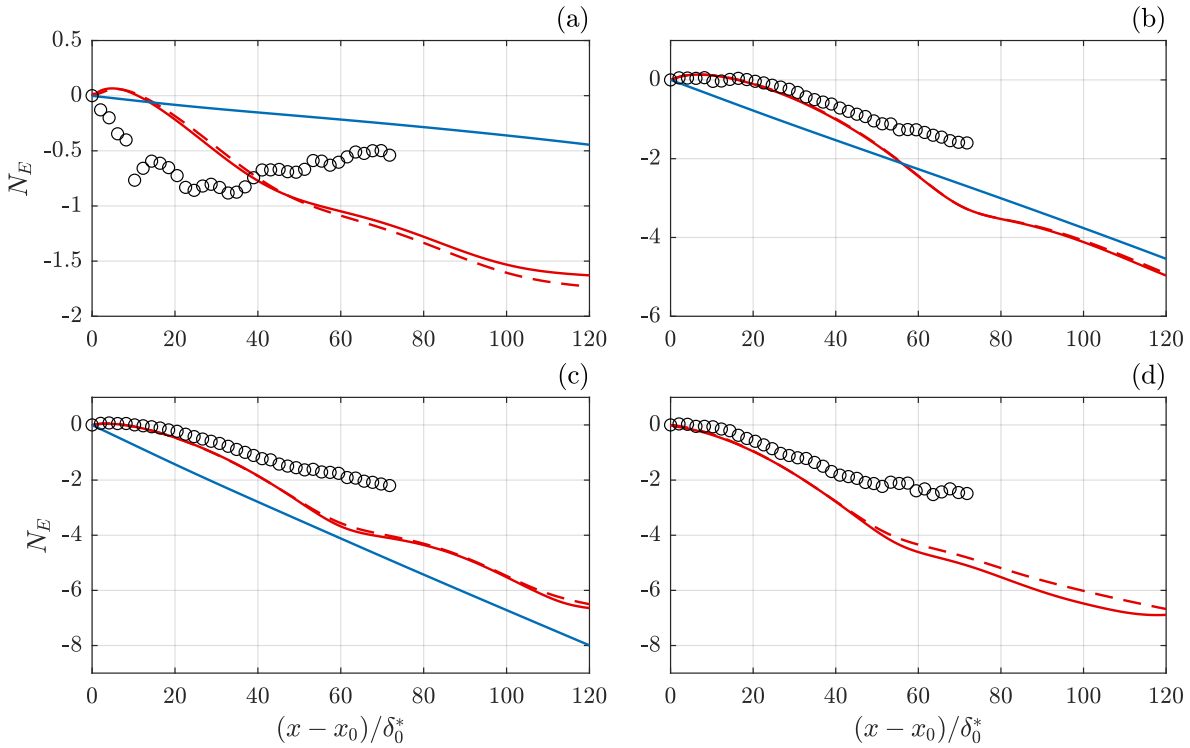

Figure 4.10: Non-modal growth of the (a) λ_2, (b) λ_3, (c) λ_4 and (d) λ_5 DRE wake modes, computed with the NmPSE (solid red line), HLNS (dashed red line) and from PTV data [136] (○). Solid blue line represents a modal LPSE computation (unavailable for λ_5).

Numerical Reconstruction of the DRE Wake

The disturbance fields corresponding to the λ_1 Fourier mode and its harmonics, computed with the NmPSE and HLNS, can be superposed to numerically reconstruct the evolution of the DRE wake. This allows for the overall behaviour of the DRE wake to be compared with the similarly reconstructed experimental PTV dataset [136]. This reconstruction is performed using an inverse FFT, including the contributions of the first five Fourier wake modes. As the harmonic disturbance fields were computed on a finer chordwise grid, these are sub-sampled onto the coarsest grid level (corresponding to λ_1) in order to enable reconstruction.

The evolution of total[1] disturbance energy in the DRE wake is computed from the spanwise standard deviation profiles, $\langle \mathbf{q}' \rangle_z$. These profiles are then used to evaluate the total N_E through equation 2.38. Figure 4.11a shows that the initial evolution of total disturbance energy compares quite well between non-modal solvers and experiment, although this agreement is short-lived. Downstream of $x - x_0 = 10\delta_0^*$, the numerical energy decays at a higher predicted rate, and attains a lower minimum as compared to the PTV trend. However, it is noted that both the numerical and experimental N-factor attain their energy minimum at a similar chordwise station, namely $x - x_0 = 40\delta_0^*$. The total energy recovers downstream of this station and begins to exhibit exponential growth toward the outflow, as compared with the representative modal LPSE computation. The NmPSE and HLNS curves are largely in agreement with each other, although slight discrepancies are seen beyond the energy minima.

The reconstructed chordwise disturbance velocity fields allow for a topological characterization of DRE wake flow as predicted by the NmPSE and HLNS (Figures 4.11b and 4.11c). Qualitatively, both the NmPSE and HLNS reproduce the evolution of the wake reported by Zoppini et. al [136] quite well. The central low-speed streak and the accompanying inboard and out-board streaks are predicted as seen in Figure 4.2a, although distinctions can be made between both non-modal solvers. In particular, the emergence of stationary CFI from the streaky structures downstream of $x - x_0 = 40\delta_0^*$ is in better agreement with experiment for the HLNS. As seen in Figure 4.2a, the inboard streak develops into the corresponding high-speed region for stationary CFI, while the outboard high- and low-speed streaks have

[1]The use of *total* in this context implies that the flowfield is reconstructed using the fundamental Fourier mode and its first four harmonics (λ_{1-5}). This terminology is maintained for further discussions.

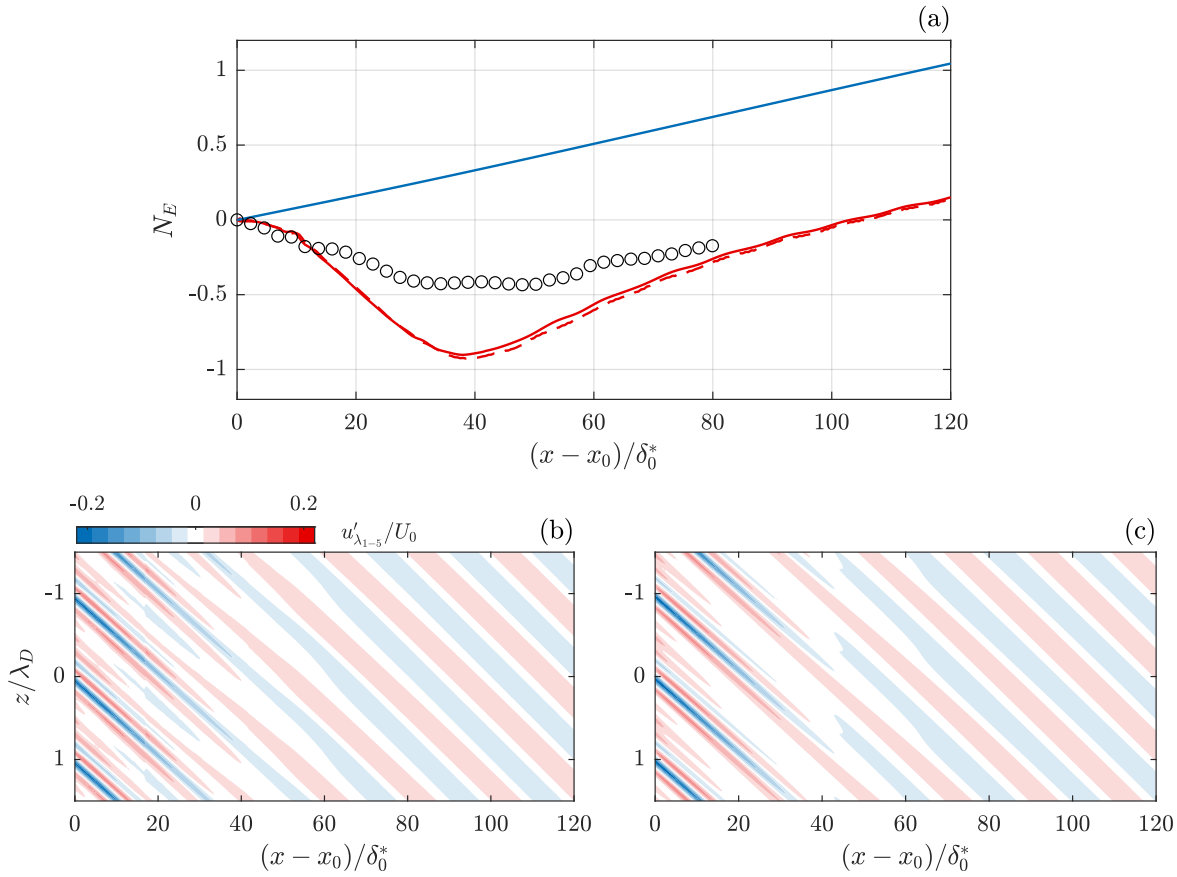

Figure 4.11: (a) Total energy N-factor for the λ_{1-5} reconstructed disturbance field computed with the NmPSE (solid red line), HLNS (dashed red line) and from experiment [136] (○). Solid blue line is an LPSE computation for the CFI mode corresponding to λ_1. Contours of the chordwise disturbance velocity field reconstructed with the (b) NmPSE and the (c) HLNS at $y/\delta_0^* = 0.55$.

decayed by $x - x_0 = 40\delta_0^*$. The low-speed CFI region then develops from the decaying low-speed streak expanding into the inter-element flowfield. The NmPSE does predict a similar behaviour, although this appears to be spanwise phase-shifted beyond the $x - x_0 = 40\delta_0^*$ point. This is evident on inspection of the stationary CFI for the NmPSE at the outflow, which are phase-shifted with respect to the HLNS. The reconstruction of the NmPSE disturbance fields involves the use of $\bar{\alpha}(\bar{x})$, which is absent in the HLNS framework. The peak-switching described in section 4.2.3 induces a discontinuous change in $\bar{\alpha}$, which in turn manifests as the phase change seen in 4.11b. This effect seems to be primarily qualitative, although it is noted that the NmPSE and HLNS N-factors in 4.2a exhibit slight differences after the switch in the energy peak. This could be due to the same $\partial\bar{\alpha}/\partial\bar{x}$ errors hypothesised to occur in section 4.2.3.

Further quantification of the evolution of the total disturbance field is done through the $\langle u' \rangle_z$ profiles, presented in Figure 4.12a. As with the disturbance energy N-factors in Figure 4.11a, the non-modal solvers and experiment are in good initial agreement. However the numerical $\langle u' \rangle_z$ profiles experience a large decrease in peak amplitude leading up to and downstream of $x - x_0 = 40\delta^*$, in correspondence with the lower energy minima seen in Figure 4.11a. Notwithstanding the amplitude discrepancy, the predicted overall change in profile shape does resemble the experimental data. The initial peak undergoes decay, followed by the appearance of a secondary *hump* at $y/\delta_0^* \approx 2$. The lower peak and the secondary hump eventually merge during the energy recover phase, resulting in a profile corresponding to stationary CFI as the outflow is approached. It is also seen that the profiles corresponding to both the NmPSE and HLNS are effectively identical throughout the domain. Contours of the reconstructed u' disturbance velocity component at the inflow and outflow are shown in Figures 4.12b and 4.12c, computed with the NmPSE. The outflow features a disturbance pattern characteristic of stationary CFI, having evolved from the highly localized disturbance field in the DRE wake. The high-speed peaks in the inter-element

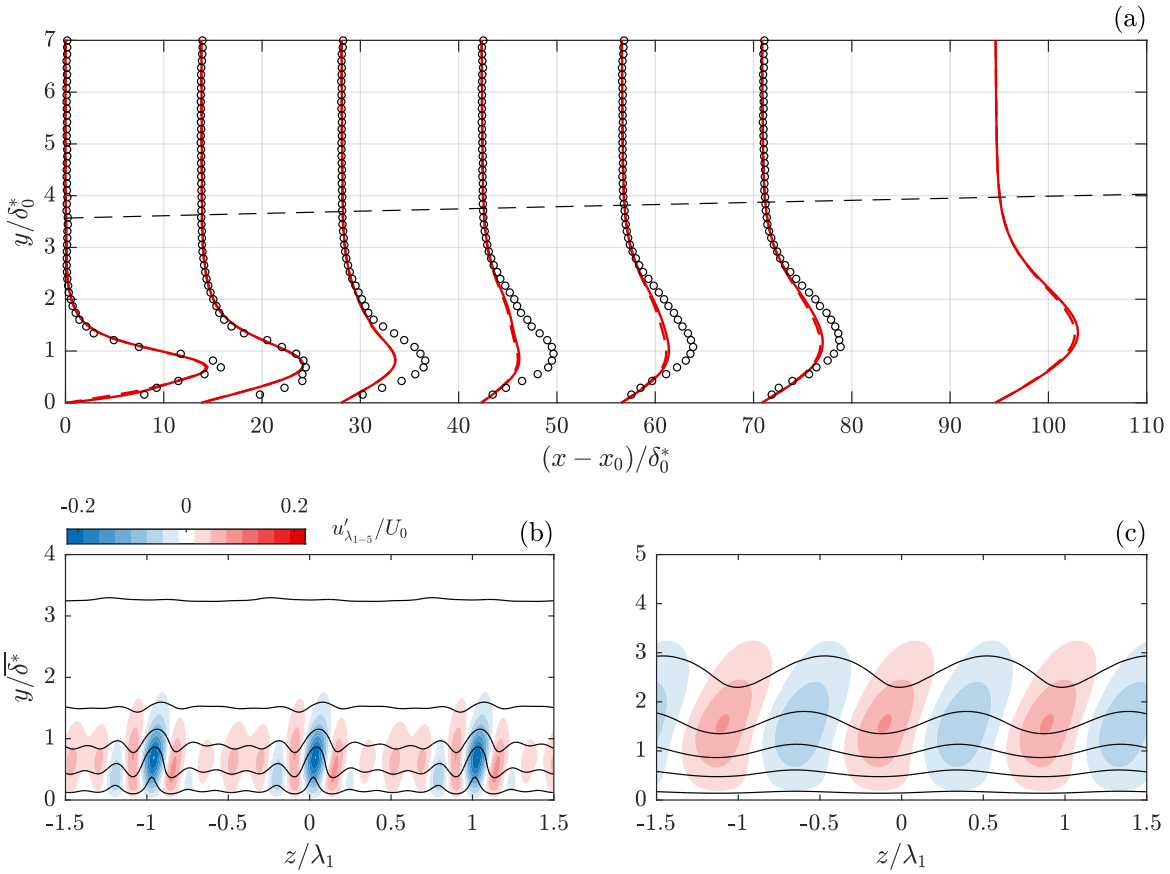

Figure 4.12: (a) Spanwise standard deviation profiles of the chordwise disturbance velocity, $\langle u' \rangle_z$, from the NmPSE (solid red line), HLNS (dashed red line), and PTV [136] (○). Black dashed line represents BL δ_{99}. Reconstructed chordwise disturbance velocity at (b) the initial plane and (c) $x - x_0 = 120\delta^*$. Black contour lines of u/U_0 are superimposed.

region at the inflow are the result of using a finite number of discrete spanwise modes to reconstruct the wake.

4.2.5. Intermediate Discussion

The numerical analysis of all contributing Fourier wake modes reveals pertinent differences in the total and modal disturbance energy between simulation and experiment. Figures 4.11 and 4.12a show that the non-modal solvers over-predict the decay of total energy in the DRE wake, while the topological features are well represented numerically. The largest qualitative difference is seen in the evolution of the first Fourier harmonic in Figure 4.10a, for which predicted behaviour is in opposition to experimental observations by Zoppini et. al [136]. As the NmPSE and HLNS have largely predict similar disturbance evolution, it is difficult to pinpoint the exact reason for the discrepancy with experiment at this stage. Henningson [47] notes that the evolution of total disturbance energy is through purely linear mechanisms, given the decomposition 1.3. In this light it could be argued that the disagreement seen in Figure 4.12a is not related to unaccounted-for non-linearity, but possibly due to an imperfect translation of the experimental ICs into a numerical stability framework. Non-linear behaviour in the individual modes however could possibly be significant. The ICs extracted from the DRE wake are of finite amplitude, yet are treated as infinitesimal in a linearised framework. This discrepancy could be the source of the behaviour exhibited by the first harmonic, and the decay mismatch seen with λ_1. The decomposition 1.3 itself is rather questionable in the experimental framework, as there exists large ambiguity in separating the baseflow and disturbance field given the experimental DRE wake. The assumption of spanwise invariance for the baseflow thus comes into question. However the qualitative agreement seen with the numerical predictions, particularly with Figures 4.11b and 4.12b, is more inclined with the baseflow being spanwise invariant, at least within the stability domain considered.

Table 4.3: Parameters for the Gaussian analytic shape functions.

Component	$\mathbf{A_q}$	$\mathbf{H_q}$	$\Phi_{q_{99}}$
$\bar{u}$	0.06	4.1055×10^{-4}	$\pi/2$
$\bar{v}$	0.045	7.6978×10^{-4}	0
$\bar{w}$	0.005	4.1055×10^{-4}	$\pi/2$

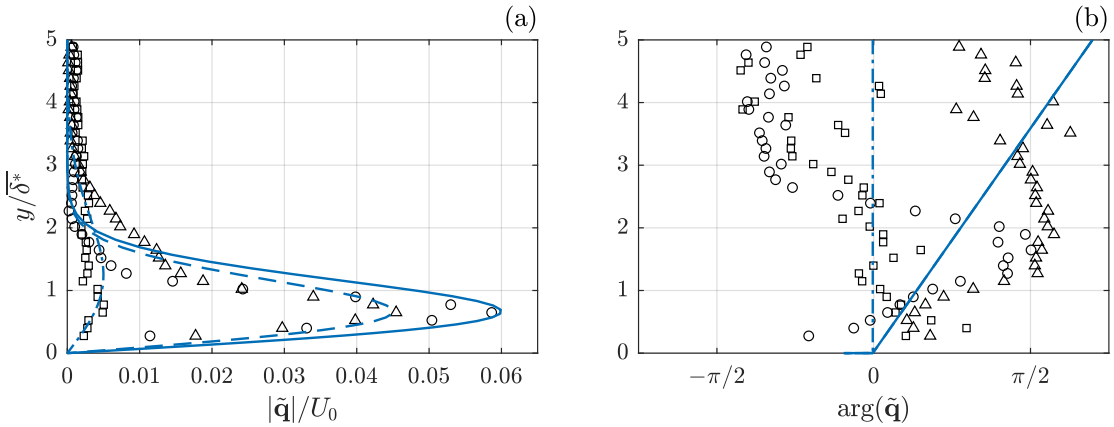

Figure 4.13: (a) Amplitude and (b) phase of the λ_1 shape functions. Blue lines correspond to analytic $\tilde{u}$ (—), $\tilde{v}$ (-.-), and $\tilde{w}$ (- - -) while markers correspond to experimental $\tilde{u}$ (○), $\tilde{v}$ (□), and $\tilde{w}$ (△).

4.3. Analytic Initial Conditions

4.3.1. Approximation of the Experimental Wake

The DRE-wake shape functions for the primary mode, λ_1, and its harmonics (Figures 4.3b and 4.4) can be characterized as resembling 3-D velocity streaks, featuring a distinct peak in amplitude close to the wall for the u' and w' disturbance velocities. As these streaks are rather regular in their structure, it is of interest to instead approximate the PTV-extracted ICs with generalized, analytical functions.

The effect that an analytic approximation of the PTV ICs has on non-modal growth is investigated for the λ_1 Fourier mode. The analytic functions themselves are selected to be linearly-weighted Gaussian functions, of the form:

$$\bar{\mathbf{q}} = \sqrt{2}\frac{\mathbf{A_q}}{\mathbf{H_q}}\bar{y}e^{(0.5-\frac{\bar{y}^2}{\mathbf{H_q}}+i\Phi_q)}\ , \tag{4.2}$$

where $\mathbf{A_q} = (A_u, A_v, A_w)^T$ is an amplitude parameter, $\mathbf{H_q} = (H_u, H_v, H_w)^T$ is a height parameter, and $\Phi_q = (\Phi_u, \Phi_v, \Phi_w)^T$ is used to control the shape function phase. Φ_q is a function of $\bar{y}$ that linearly varies the shape function phase from zero at the wall to a prescribed angle $\Phi_{q_{99}}$ at the BL edge. The linear variation was selected to investigate whether the use of a first-order phase approximation would be able to sufficiently reproduce the experimental IC results. The values of these parameters were selected so as to best approximate the PTV shape functions for the λ_1 Fourier mode and are listed in Table 4.3, with the shape functions depicted in Figure 4.13. The BL baseflow, stability grid, and inputs $\bar{\omega}$ and $\bar{\beta}$ were defined identically to Section 4.2.3, and the initial value for $\bar{\alpha}$ was also extracted from the PTV data as previously discussed.

Figure 4.14a compares the evolution of λ_1 disturbance energy for the experimental ICs and their analytic approximations, computed with both non-modal solvers. For a rather basic approximation of the experimental ICs, the growth curves are seen to compare generally well. The initial energy decay and recovery is predicted with the analytic ICs, as well as the downstream exponential growth. However while these trends are predicted similar between solvers and IC types, the match between them is not exact. This is expected to an extent, based on the results shown in Figure 4.9a where the non-modal growth computations were seen to be affected by noticeable changes in the shape function. The NmPSE curves for both ICs in Figure 4.14a match well during the initial decay phase, although the energy minima is over-predicted with the analytic ICs. Subsequent energy recovery is under-predicted, with the outflow N-factor being slight lower for the analytic case. Similar behaviour is observed with the

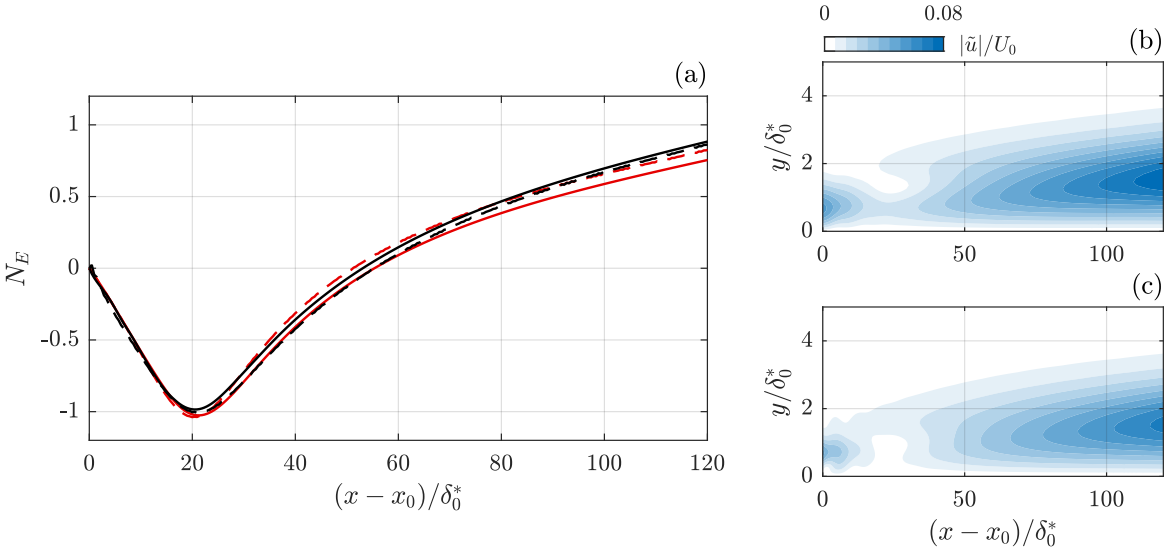

Figure 4.14: (a) Non-modal growth of λ_1 with analytic (red) and experimental (black) ICs, computed with the NmPSE (solid lines) and HLNS (dashed lines). Contours of the $\tilde{u}$ shape function amplitude shown for (b) analytic and (c) experimental ICs computed with the NmPSE.

HLNS, although the outflow N-factor recovers such that both the experimental and analytic IC scenarios match. While the analytic IC growth curves differ slightly from their experimental IC counterparts, the NmPSE and HLNS appear to be in better agreement for the former scenario than with the latter.

An examination of the $\tilde{u}$ shape function evolution is also carried out with Figures 4.14b and c, being similarly predicted for both experimental and analytic ICs. However unlike with the experimental ICs, peak-switching is not observed for the analytic approximation. This is seen close to $x - x_0 = 20\delta_0^*$, where the lower peak in Figure 4.14b is consistently higher in amplitude than the upper peak.

4.3.2. Parametric Studies

From Figure 4.14, it appears that the use of approximate analytic ICs results in fairly good predictions for non-modal growth computed with PTV-extracted ICs. However, it is of interest to understand how sensitive the NmPSE and HLNS are to the structure of these analytic ICs, particularly in the selection of the shape function amplitude peak and the linearly-varying phase approximation. These parameters are investigated in the following section for the λ_1 Fourier mode, employing the baseflow and stability grid defined in Table 4.1.

Location of Maximum Disturbance Amplitude

The wall-normal location of the disturbance amplitude peak for the analytic shape functions can be controlled through the parameter set $\mathbf{H_q}$. For this series of tests, non-modal growth is computed for $0.5\mathbf{H_q}$, $\mathbf{H_q}$ and $2\mathbf{H_q}$. The parameter Φ_q is set as per Table 4.3 for the three cases, as is $\mathbf{A_q}$ which in any case has no effect in a linearised framework. Figures 4.15b-d depict the analytic IC for the chordwise disturbance velocity, for the three $\mathbf{H_q}$ cases investigated.

The non-modal evolution of disturbance energy is presented in Figure 4.15a, represented by the energy N-factor. It is evident that the location of the disturbance amplitude peak quite significantly affects the extent to which the λ_1 mode grows non-modally. The energy corresponding to the disturbance located closest to the wall undergoes strong decay immediately downstream of the initial plane, followed by rapid energy recovery beyond $x - x_0 = 10\delta_0^*$. The energy growth rate appears to gradually relax into an exponential trend as the outflow is reached. The opposite is seen for the disturbance located furthest from the wall, where growth and decay rates are lower as compared to the originally positioned disturbance peak. All three cases exhibit exponential growth at the outflow, although the experimental IC growth curve is best represented using the original $\mathbf{H_q}$ analytic IC. It is also noted that the NmPSE and HLNS predictions are not in perfect agreement, with discrepancies similar to those seen in the previous sections of this chapter. The two non-modal solvers generally agree well immediately downstream of the inflow up to the energy minima, after which the disagreement begins

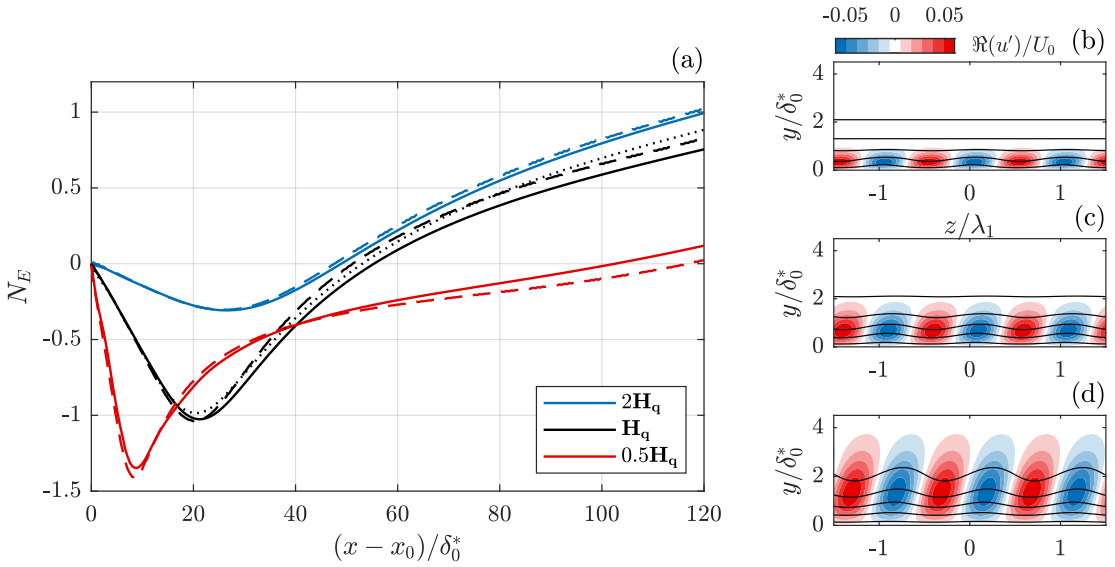

Figure 4.15: (a) Analytic IC energy growth with the NmPSE (solid lines) and HLNS (dashed lines) for varying $\mathbf{H_q}$. Black dotted is an NmPSE computation with experimental ICs. Contours of the analytic chordwise disturbance velocity IC for λ_1, for (b) $0.5\mathbf{H_q}$ (c) $\mathbf{H_q}$ and (d) $2\mathbf{H_q}$. Black contour lines represent 5 levels of the chordwise BL velocity.

to manifest. Possible origins for this could be amounted to either the parabolization in the NmPSE, errors introduced due to discontinuous changes in $\bar{\alpha}(\bar{x})$, or a combination of both.

Effect of Shape Function Phase

The experimental shape function phase is approximated through the linearly varying function Φ_q, with a value of zero at the wall to $\Phi_{q_{99}}$ at the BL edge. As seen from Figure 4.13 the PTV-extracted shape function phases can be rather ambiguous, and hence the linear approximation may not be accurately representative of the experimental trends. Setting the $\tilde{u}$ and $\tilde{w}$ phases to vary from zero at the wall to $\pi/2$ at δ_{99}, and the phase for $\tilde{v}$ as zeros leads to a fairly good analytical estimate of non-modal growth for λ_1, previously shown in Figure 4.14. However, it is important to quantify the effect variations in the prescribed phase may have on predicted non-modal growth, to gauge the validity of employing such an approximation. Three tests are conducted for $\Phi_{q_{99}} = -pi/2, 0, \pi/2$, for the original $\mathbf{H_q}$ using the same baseflow and stability grid as the previous disturbance amplitude peak tests. The analytic ICs for the chordwise disturbance velocity corresponding to these three cases are shown in Figures 4.16b-d.

It is observed from Figure 4.16a that the selected shape function phase does indeed significantly affect the extent to which the λ_1 mode grows non-modally. Selecting Φ_q to vary to $-pi/2$ at the BL edge instead of the original approximation leads to a lower energy minima and downstream recovery rate. Additionally, the disturbance energy amplifies at a relatively lower exponential rate toward the outflow. The $\Phi_{q_{99}} = 0$ case appears to lie in the middle in terms of the predicted energy minima, although all three cases are seen to decay at the same rate immediately downstream of the inflow plane. Notable discrepancy is observed when comparing the curves corresponding to the NmPSE and HLNS, with the HLNS predicting slightly larger decay and growth rates during the initial transient phase. This in turn leads to the corresponding outflow N-factors being larger than NmPSE estimates. While the effect that an incorrectly-approximated shape function phase has on the λ_1 growth is prominent, the non-modal solvers are seen to be more sensitive to the wall-normal location of the disturbance amplitude peak (Figure 4.15a). The initial growth trends exhibit large differences between successive values of $\mathbf{H_q}$, translating into large deviations in the outflow N-factor. This is not as extreme with the range of $\Phi_{q_{99}}$.

The high sensitivity of the non-modal solvers to these changes in the initial conditions is expected, as the modified IC may be associated to a completely different set of non-normal eigenmodes of the OS/Squire system. It is thus difficult to parametrize the predicted non-modal growth, as this would require an unfeasibly large parameter set. This is in agreement with approaches seen in the state-of-the-art, where the maximally amplified non-modal disturbances are instead obtained through the solution of an optimization problem [120, 16, 25].

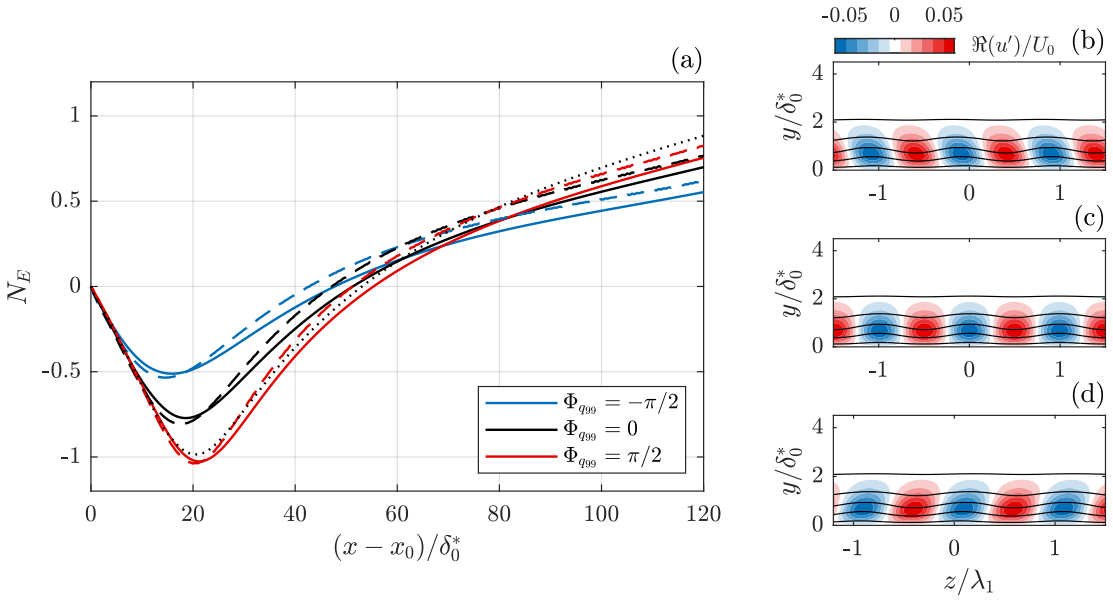

Figure 4.16: (a) Analytic IC energy growth with the NmPSE (solid lines) and HLNS (dashed lines) for varying Φ_{q99}. Black dotted is an NmPSE computation with experimental ICs. Contours of the analytic chordwise disturbance velocity IC for λ_1, for (b) $\Phi_{q99} = -\pi/2$ (c) $\Phi_{q99} = 0$ and (d) $\Phi_{q99} = \pi/2$. Black contour lines represent 5 levels of the chordwise BL velocity.

4.4. Convergence Study

The non-modal computations carried out in this chapter were performed on a consistent stability grid, such that the effects of discretization were eliminated from the analyses. However, an investigation of these effects is crucial as quantities of varying orders of magnitude and associated length scales are represented on the same numerical grid. The baseflow is computed on a highly-resolved grid and interpolated onto that used for stability. The refinement level was selected such that the stability computations attained convergence with regard to the baseflow discretization. As such, the convergence study performed can be solely associated to the convergence of the stability characteristics, given a consistent baseflow configuration. Furthermore, the wall-normal and chordwise discretization are independent of each other and are investigated separately within this section.

4.4.1. Wall-Normal Discretization

The wall-normal discretization is a critical parameter, as an accurate representation of the BL and disturbance profiles, and their associated gradients, is dependent on the number of nodes utilized. This is particularly important close to the wall, where gradients are large and the disturbance profiles peak in amplitude. As discussed in Section 2.2.3, a pseudo-spectral differentiation is employed in the wall-normal direction using a Chebyshev polynomial basis. The collocation points for this are clustered near the wall via a cosine spacing algorithm [72]. The effect of the number of Chebyshev nodes, n_y, on non-modal growth of the λ_1 Fourier mode is investigated in this study, using the smoothed experimental ICs. The baseflow and stability domain are defined as per Table 4.1, with n_y varied between a series of values.

Figure 4.17 presents the growth curves and outflow shape functions computed for n_y equal to 25, 50, 75 and 100, with an $x-$discretization of $n_x = 300$. It is seen that beyond 50 collocation points in y the results rapidly converge for both the NmPSE and HLNS, with the N_E curves being essentially identical between 75 and 100 collocation points. The NmPSE outflow shape functions however exhibit a mild difference in peak amplitude between these two n_y levels. This does not appear to influence the non-modal disturbance growth, as evidenced by Figure 4.17a.

4.4.2. Chordwise Discretization

The chordwise grid features uniform spacing and employs a marching scheme with first-order derivatives being approximated via a backward Euler approach (Section 2.2.3). For all non-modal computations, the

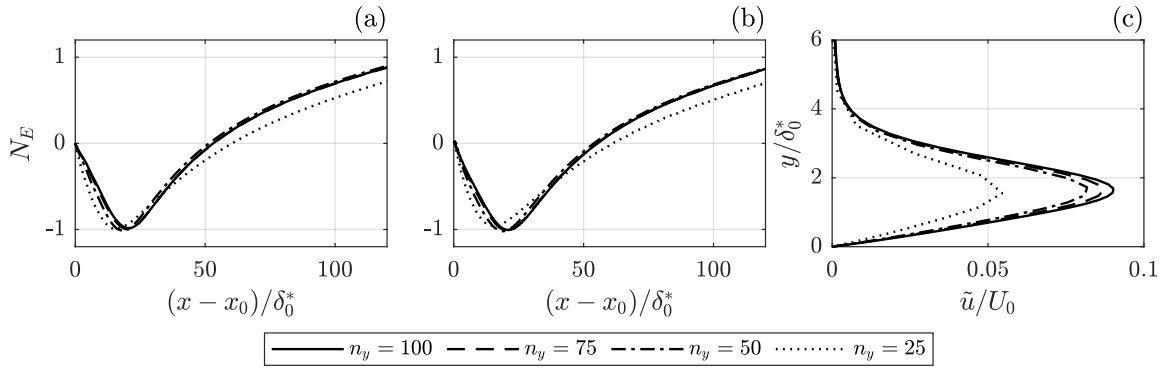

Figure 4.17: Convergence study for the $y-$discretization. Energy N-factors for the (a) NmPSE and (b) HLNS. (c) NmPSE Chordwise disturbance velocity shape function amplitude at $x - x_0 = 120\delta_0^*$.

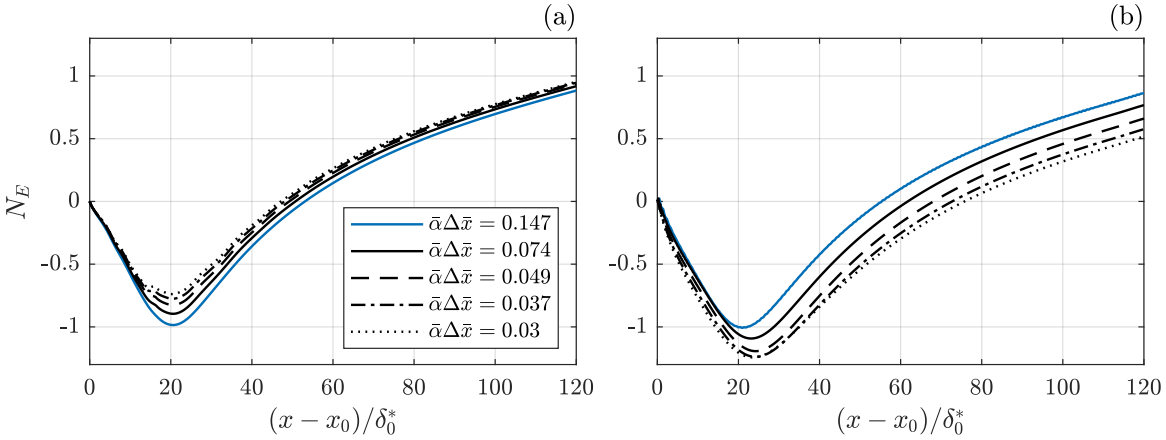

Figure 4.18: Convergence study for the $x-$discretization. Energy N-factors for the (a) NmPSE and (b) HLNS.

$x-$grid was selected based on the parameter $\bar{\alpha}_r\Delta\bar{x}$, so as to be able to sufficiently represent disturbance oscillatory behaviour. The omission of the $\partial\bar{p}/\partial\bar{x}$ term from the NmPSE relaxes its limit for the minimum step size [66, 120], and allows for finer $x-$grids to be employed.

The effect of the chordwise discretization on non-modal growth predicted by the NmPSE and HLNS is studied for n_x equal to 300, 600, 900, 1200 and 1500, for the λ_1 Fourier mode. This is done with the baseflow and stability parameters once more selected as per Table 4.1, with $n_y = 100$. Figures 4.18a and 4.18b present rather interesting results. It is seen that the energy N-factors exhibit visible changes in their growth trends with $x-$grid refinement for both non-modal solvers. However both solvers appear to converge in opposing directions, with their best agreement with each other being at the $n_x = 300$ level. Overall change between levels is not overly large for the NmPSE, although the energy minima increases to higher N-factors with refinement. Additionally, subtle spurious oscillations begin to become apparent at the finest level, almost similar to those seen with the trapezoidal marching scheme in Section 4.2.3. This could stem from a violation of the assumptions inherent to the parabolic NmPSE, seeing that finer grid levels introduce larger error into the domain. The HLNS on the other hand does not appear to attain convergence in N_E with refinement. The growth trends appear to remain relatively unchanged between n_x levels, although a decrease toward lower N-factors is seen in the energy minima. The location of the minima also shifts slightly downstream with refinement, thought it is not quite evident why the HLNS exhibits such large variations in its solution for progressively smaller $\Delta\bar{x}$ values.

5

Non-Stationary DRE Wake Measurements

This chapter discusses the results of the experimental measurements performed to characterize unsteady phenomena pertinent to the DRE wake region. A qualitative analysis of the global flowfield is first presented, using IR thermography, followed by the investigation of the local boundary layer baseflow through hot-wire measurements. The steady features of the HWA-measured DRE wake are then discussed for critical and super-critical forcing configurations, and the evolution of stationary disturbances is characterized. Finally, a comprehensive description of the unsteady flow phenomena is provided for both configurations, identifying the dominant spatial structures, temporal spectra and behaviour of unsteady fluctuation energy in the DRE wake.

5.1. Baseflow Topology & Transitional Behaviour

IR Thermography Characterization

A qualitative overview of the flowfield can be gained from the images captured using IR thermography, presented in Figure 5.1 for the wing pressure-side. The wide-angle lens configuration (Figures 5.1a and 5.1c) allows for a global characterization of the BL state, particularly the location and nature of the transition front. For the critical DRE forcing with $\mathrm{Re}_{k_D} = 192$, the BL is largely laminar. The temperature profile varies uniformly from the leading edge up to $X/c_X \approx 0.39$, as a result of the surface-to-flow heat transfer varying with natural BL development. Between $X/c_X = 0.4 - 0.45$, the emergence of sawtooth-like patches of low temperature (dark regions) is observed, characteristic of stationary CFI-induced breakdown into turbulence. Faint, alternating light and dark steaks can be observed in the bright region upstream of the transition front. These spanwise variations in temperature correspond to the modulation of the mean-flow due to the presence of non-linear growth of the stationary CFI [92, 111]. The BL is fully turbulent aft of the mid-chord region, much before the pressure minima is reached.

The super-critical DRE forcing with $\mathrm{Re}_{k_D} = 330$ presents a distinctly different transition scenario. Here, the modal CFI growth phase is bypassed and transition is seen to occur in the vicinity of the DRE array. This is attributed to the excessive amplitudes of disturbances induced by the super-critical DREs, leading to breakdown to turbulence as per path D in Figure 1.3 [76, 34].

The zoomed-lens configuration in Figures 5.1b and 5.1d allows for a description of the near-element flow topology pertaining to the two transition scenarios. The DRE arrays in the images are seen as low temperature spots, owing to the higher thermal conductivity of the manufacturing material. The wake of the $\mathrm{Re}_{k_D} = 192$ forcing configuration features a series of faint high and low temperature streaks, alternating in the spanwise direction. These are indicative of the HSV system developing around and aft of the elements [14, 62, 136]. The HSV system induces a series of high and low velocity streaks, perturbing the BL flow by respectively increasing and decreasing the local wall shear stress (as further discussed in Section 5.2.1). This manifests as variations in the spanwise temperature profile through the Reynolds analogy (Section 3.2.1). The reduction in contrast toward $x/c = 0.18$ is indicative of reducing

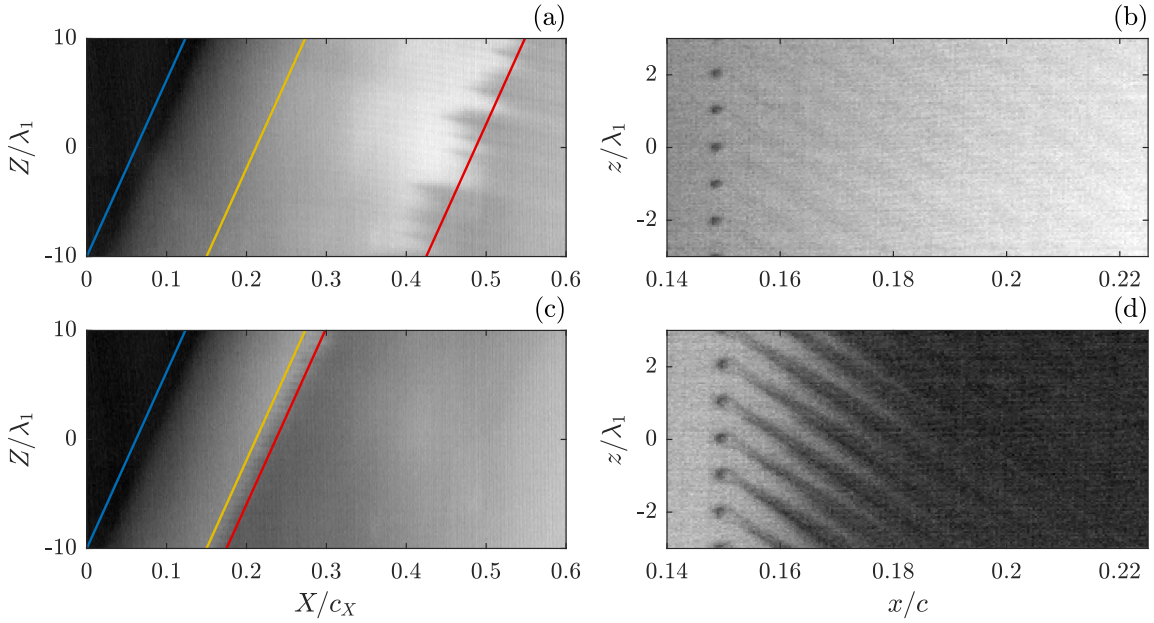

Figure 5.1: IR thermography fields acquired using the following configurations: Wide-angle lens for (a) $\mathrm{Re}_{k_D} = 192$ and (c) $\mathrm{Re}_{k_D} = 300$, and zoom lens for (b) $\mathrm{Re}_{k_D} = 192$ and (d) $\mathrm{Re}_{k_D} = 300$. The flow enters from the left with the blue, yellow and red lines representing the leading edge, DRE location and approximate transition front respectively.

streak amplitude, with the wall-shear modulation being of low enough amplitude to not be sensed by the IR camera.

Stronger thermal modulation, however, is seen with IR images of the the $\mathrm{Re}_{k_D} = 330$ forcing configuration. The imprint of the HSV system is more clearly seen in this scenario, manifesting as fork-like structures originating from each element in the array. The higher thermal contrast can be attributed once more to the stronger stationary disturbances induced by the HSV system, resulting in a more prominent modulation of the local wall shear stress. At $x/c \approx 0.155$, the two velocity streaks originating from each side of the element merge into a single streak, which then locally evolves into a turbulent wedge after a short distance downstream. The wedge progressively expands in the spanwise direction and by $x/c = 0.18$, merges with neighbouring turbulent wedges. The flow is completely turbulent by $x/c = 0.2$, as indicated by Figure 5.1c.

Baseflow Velocity Profiles

The stationary near-element flow topology is characterized later in this chapter, through the ensemble of hot-wire scans carried out within the BL. However, to ensure that the experimental findings in this work are comparable with existing literature for the cases investigated, a characterization of the steady BL baseflow is conducted.

Figure 5.2a presents contours of the time-averaged HWA velocity component $\overline{Q}$, measured within the BL, for the k_3 ($\mathrm{Re}_{k_D} = 192$) forcing configuration. Immediately aft of the DRE array, perturbations in the BL are highly localized and centred at integer multiples of the forcing wavelength. The inter-element flowfield pertaining to k_3 is seen to be largely unperturbed, and is representative of the laminar baseflow defined in stability analyses. These regions are indicated by the dashed vertical lines in Figure 5.2a. The $\overline{Q}$ fields are spanwise averaged, resulting in a single representative BL profile for each chordwise measurement station. These HWA BL profiles are compared with a numerical solution of the laminar, spanwise-invariant BLEs (equations 2.4), computed using an in-house solver. The external flow conditions for the BLE solver were set to match those of the experimental setup, and the computed numerical BL components were projected onto the HWA measurement frame through equation 3.6. Figure 5.2c presents a comparison between the numerical BL profile and that extracted from the HWA measurements for k_3, at $x/c = 0.152$. The good match confirms that the spanwise-averaged BL profiles are also representative of the laminar basic state in the element vicinity, enabling comparison of the BL stability characteristics in the current work with previous findings in literature. This match is seen to hold for k_3 at further downstream locations as well, as shown for $x/c = 0.17$ in Figure 5.2d.

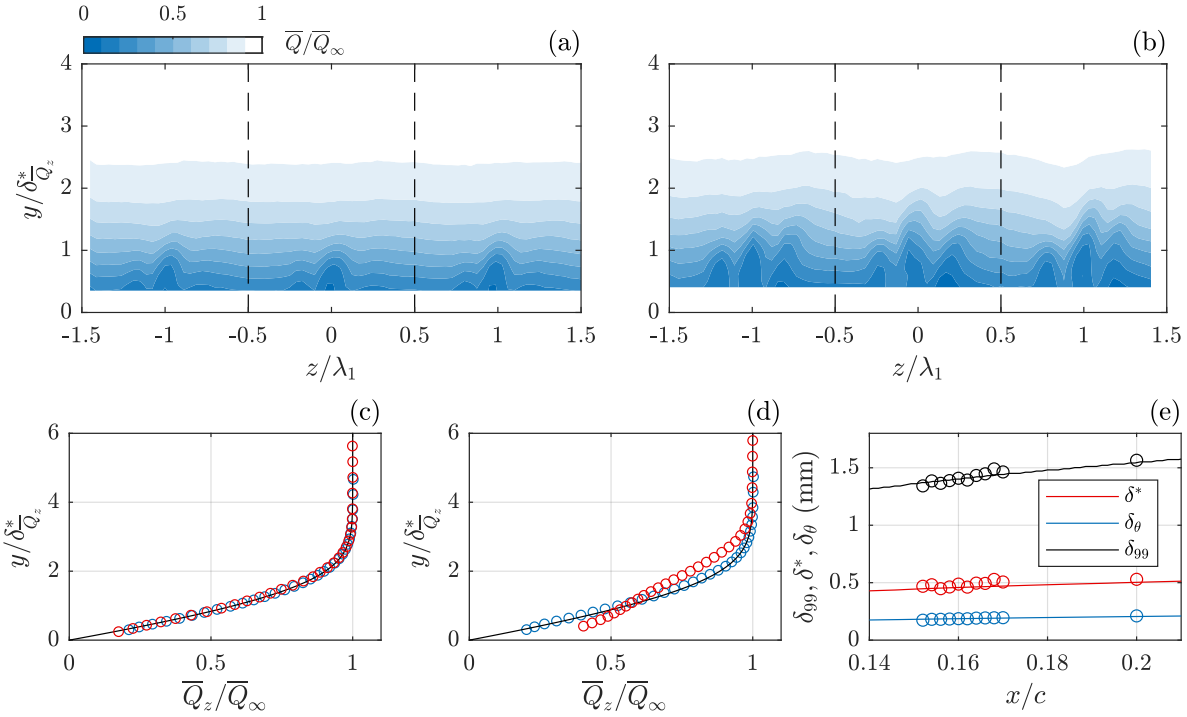

FIGURE 5.2: HWA-measured BL velocity contours for the (a) k_3 and (b) k_4 forcing configurations, at $x/c = 0.152$. Numerical (—) and HWA baseflow profiles for k_3 (red ∘) and k_4 (blue ∘) at (c) $x/c = 0.152$ and (d) $x/c = 0.17$. (e) BL parameters.

The $\overline{Q}$ field measured in the element vicinity for the k_4 configuration is presented in Figure 5.2b, and also indicates a localized perturbation field. However, the BL perturbations are of higher amplitude as compared to the k_3 forcing case, and extend further into the unperturbed inter-element region. Comparison between the spanwise-averaged BL profile from HWA and the numerical BLE solution in the element vicinity (Figure 5.2c) shows good agreement between the two, indicating that the spanwise-averaged BL profile here is representative of the laminar basic state for the k_4 configuration as well. However Figure 5.2d shows that spanwise-averaged BL profile for k_4 at $x/c = 0.17$ is instead resemblant of a turbulent BL profile, thus deviating from the laminar numerical profile. This is expected based on the preliminary IR diagnostics reported in Figure 5.1d. Velocity disturbances are widespread as the flowfield has taken on a largely turbulent nature, with merging turbulent wedges expanding in the spanwise direction.

Finally, Figure 5.1e compares the evolution of the integral parameters, δ^* and δ_θ, and the BL thickness, δ_{99}, for the numerical and HWA-extracted BL profiles. The quantities agree well with numerical computations, further validating the experimental measurements.

5.2. Steady Near-Element Flow Topology

An analysis of the time-averaged velocity fields acquired using HWA is first carried out, so as to quantify the development of stationary instabilities in the DRE wake. This is done using the steady disturbance velocity, $\overline{Q}_d$, defined in Section 3.4.2, extracted for each wall-normal measurement plane.

5.2.1. Critical Forcing

The near-element disturbance field induced by the critical DRE forcing configuration k_3 is characterized in this section, with contours of $\overline{Q}_d$ presented in Figure 5.3. The first measurement plane at $x/c = 0.152$ reveals a highly localized disturbance field, with a low-speed wake located at integer multiples of the DRE forcing wavelength, λ_1. These strong regions of decelerated flow correspond to the recirculation regions aft of each element in the DRE array. The central low-speed wakes are each flanked by a high-speed streak on either side, and a low-speed streak on their outboard sides. These are induced by the HSV system pertaining to each element in the DRE array, as seen in Figure 5.1b and reported by Kurz

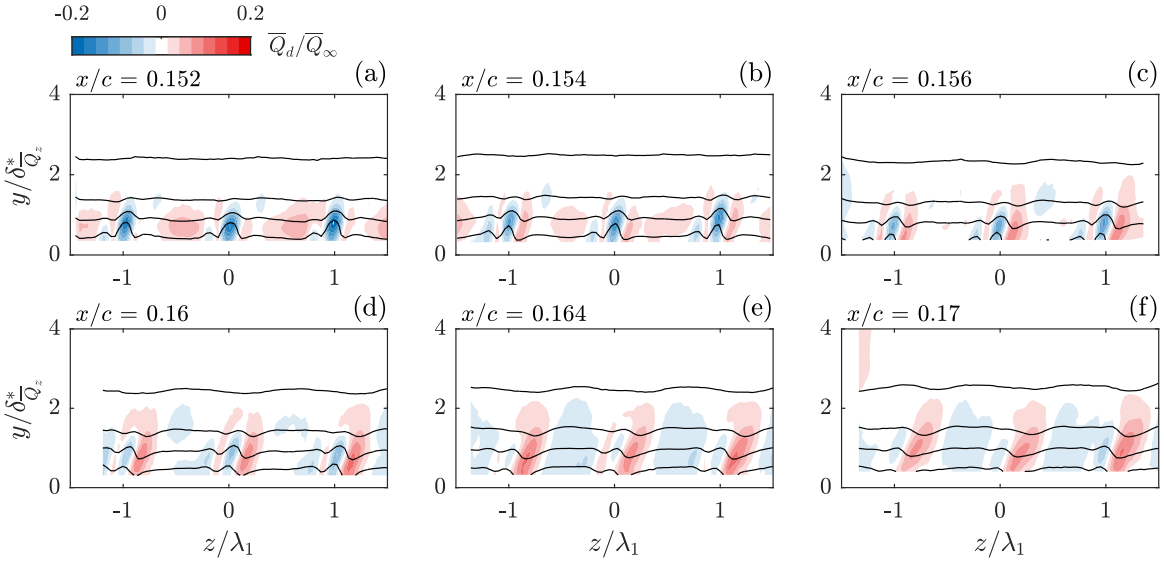

Figure 5.3: Contours of the steady disturbance velocity measured using HWA, at successive chordwise locations, for $\mathrm{Re}_{k_D} = 192$. Black isolines of the steady BL velocity are superimposed.

& Kloker [62] and Zoppini et. al [136]. The local flow topology aft of each element is similar to that of an isolated roughness element in a swept BL [14, 138], owing to the inter-element spacing being larger than $3\lambda_1$ [34].

Moving downstream, the high-speed streak is seen to rapidly amplify while both the central low-speed speed region and outboard streak experience gradual decay. As $x/c = 0.16$ is reached, a clear asymmetry in the flowfield is observed. The outboard low-speed streak is damped, while the central region and the inboard high-speed streak attain comparable amplitudes. This behaviour has been distinctly reported in previous works [62, 14, 136], where DRE wake structures co-rotating with the crossflow velocity component are preferentially sustained. Between $x/c = 0.16 - 0.164$, the central low-speed streaks have decayed, while the high-speed streak continues to persist, albeit slowing in its growth. The disturbance field is also seen to be less localized, as structures begin to resemble those pertaining to modal CFI. This is apparent at $x/c = 0.17$, where the entire spanwise extent of the BL is affected by spanwise-alternating velocity (and hence momentum) modulations, typically associated to the modal development of stationary CFI.

The observed stationary disturbance evolution is largely in agreement with the 3-D dual-pulse PTV findings of Zoppini et. al [136], who characterized the flowfield into two regions based on disturbance structure: the near-wake, between $x/c = 0.152 - 0.16$, where highly localized velocity streaks are prevalent, and the far-wake region downstream of $x/c = 0.164$, where disturbance begin to take on a modal nature. The authors also report the rapid growth and decay of the outboard high-speed streak in the near-wake region, extending further downstream and dominated by the modal CFI development (seen in Figures 4.2a and 4.2b). This however is not clearly seen in the HWA measurements, possibly due to the insufficient spanwise resolution.

Spectral Analysis and Steady Energy Growth

A spanwise FFT is performed at each HWA measurement plane, to characterize the spectral content of the stationary disturbances induced by the k_3 forcing configuration. From Figure 5.4a it is seen that most of the disturbance energy is concentrated within the λ_1 mode at $x/c = 0.152$, although spectral peaks are also identified at the higher harmonics of λ_1. This corresponds to observations by Zoppini et. al [136], and is a result of the highly localized nature of the near-wake flow. The wake of each element effectively acts as a pseudo-pulse, containing all spanwise frequencies. Far downstream at $x/c = 0.2$, the harmonic peaks vanish and energy is solely concentrated within the λ_1 mode. This is indicative of modal stationary CFI emerging downstream of the far-wake region.

The wall-normal disturbance profiles in Figure 5.4b also provide an insight into the structure and evolution of the stationary disturbances. The noticeable contribution of the higher harmonics to the near-wake disturbance energy is seen in the mismatch between the λ_1 and total standard deviation

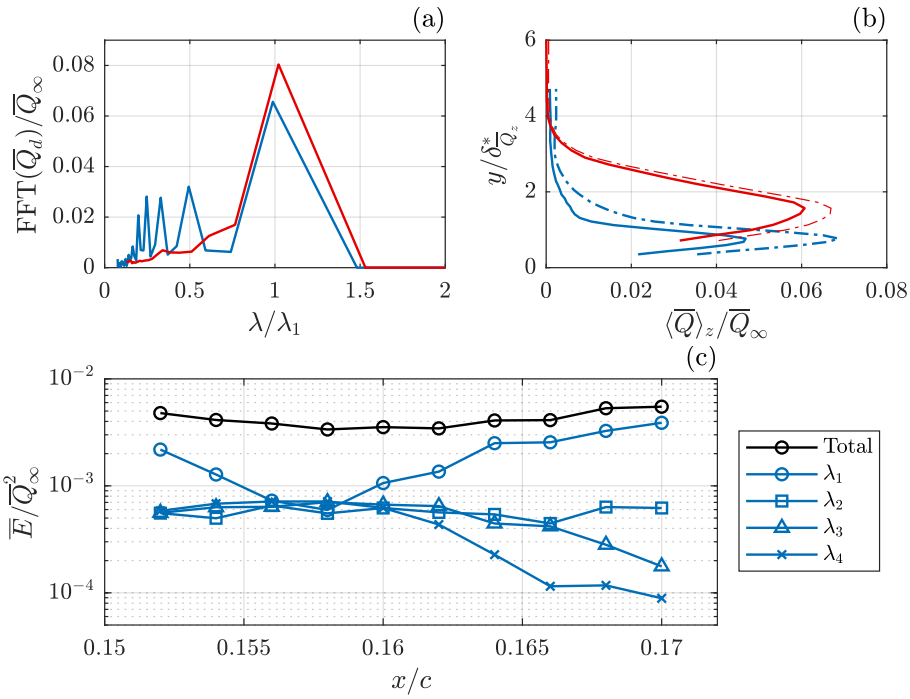

Figure 5.4: Spanwise FFT analysis for $\mathrm{Re}_{k_D} = 192$ at $x/c = 0.152$ (blue lines) and $x/c = 0.2$ (red lines). (a) Spanwise spectra at the wall-normal location of maximum disturbance amplitude. (b) Standard deviation (-.-) and λ_1 (—) disturbance profiles. (c) Stationary disturbance energy evolution.

profiles at $x/c = 0.152$. The amplitude peak is also located in correspondence with the element height, indicating the presence of strong shear generated by low-speed recirculation region. At $x/c = 0.2$, the two disturbances profiles are strongly comparable in wall-normal evolution and amplitude values, further indicating the onset of modal behaviour. The upward-shift of the disturbance amplitude peak occurs as a result of the changeover between the streak instability (located close to the wall) in the near-wake and CFI in the far wake.

The amplitude evolution of the stationary DRE wake features is tracked through the integrated steady disturbance energy, defined as per equation 3.9. This was computed for the total standard deviation profiles as well as for the first four Fourier modes, and is presented in Figure 5.4. It is seen that the total disturbance energy remains nearly constant within the DRE wake, although mild decay and energy recovery is observed between $x/c = 0.156 - 0.164$. The λ_1 mode however, is seen to undergo significant transient decay downstream of the elements, attaining its energy minima at $x/c \approx 0.156$. The energy begins to recover beyond this point and comprises nearly all of the steady disturbance energy by $x/c = 0.17$. This corresponds once more to the emergence of naturally unstable CFI in the far-wake. Disturbance energy in the second and third harmonics appear to undergo mild initial amplification, followed by decay beyond $x/c = 0.16$, while the first harmonic is seen to remain at a largely invariant energy level throughout the measurement region. The behaviour of disturbance energy is in good agreement with observations by Zoppini et. al [136], who also report transient growth dominating the stationary near-wake flow development.

5.2.2. Super-critical Forcing

The critical DRE forcing configuration incurs stationary near-element features that evolve into modal CFI downstream, with transient growth identified as the fundamental disturbance evolution mechanism [136]. However, the transition scenario for the super-critical k_4 configuration involves a bypass of modal instability growth, with breakdown into turbulence occurring in the vicinity of the DRE array (Figure 5.1d). This behaviour is associated to flow-tripping, and the stationary disturbance topology pertaining to the DRE wake in this scenario is characterized through the HWA measurements presented in Figure 5.2.2.

Similarly to k_3, the disturbance field in the vicinity of the elements ($x/c = 0.152$) is highly localized,

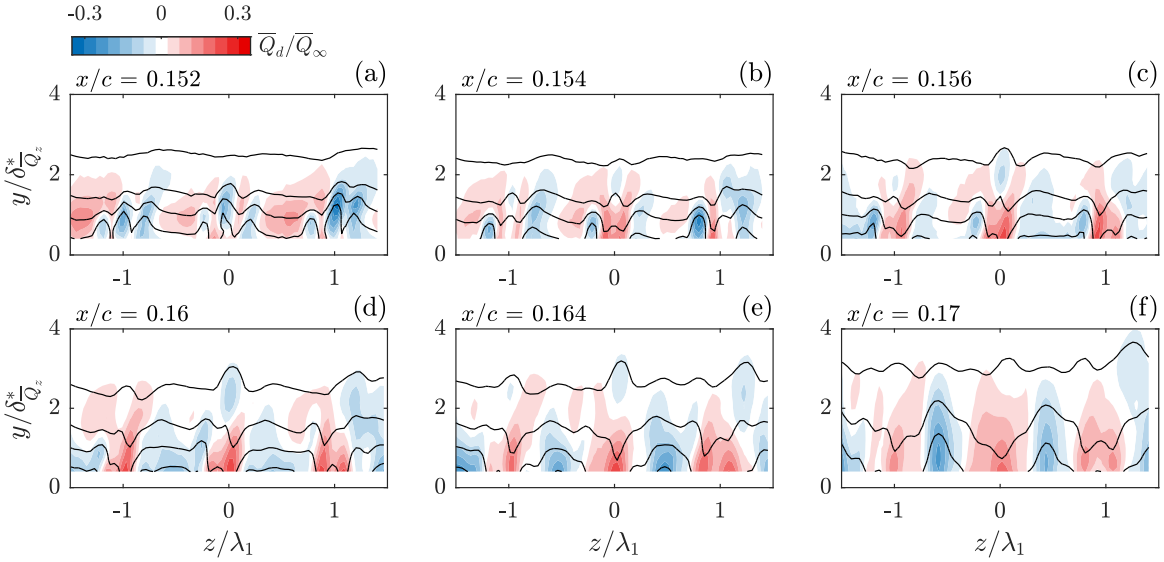

Figure 5.5: Contours of the steady disturbance velocity measured using HWA, at successive chordwise locations, for $\mathrm{Re}_{k_D} = 330$. Black isolines of the steady BL velocity are superimposed.

although larger in amplitude. A central low-speed region develops aft of the elements, corresponding to their recirculation regions, and is flanked by high-speed streaks on either side. The high-speed streaks themselves are each neighboured by a low-speed streak of magnitude almost comparable to the central low-speed region. These structures can once more be attributed to the strong HSV system developing around the high-amplitude elements of the DRE array. In the chordwise extent between $x/c = 0.152 - 0.156$, a rapid change in the disturbance topology is observed. The central low-speed region decays, and is replaced by a merger of the flanking high-speed streaks. Amplification of the outboard low-speed streak is also observed to occur. This merging of the high-speed streaks was also seen in preliminary IR characterization of the flowfield (Figure 5.1d), and marks the onset of a turbulent wedge. Downstream of $x/c = 0.16$, the central, merged high-speed streak gradually grows in the spanwise and wall-normal direction, while the outboard low-speed streak expands into the inter-element region, amplifying mildly. Breakdown is already evident at $x/c = 0.17$ and the disturbance field is dominated by the presence of localized turbulent wedges. As with k_3, the asymmetry in the disturbance field is evident, with only the outboard low-speed streak persisting at downstream locations.

The evolution of the stationary disturbance field for k_4 reported here corresponds well with observations by Zoppini et. al [136], who also identify a merging of the two high-speed streaks. They additionally demarcate the near- and far-wake regions as before and after this merger respectively. Similar streak behaviour is also reported for an isolated, super-critical roughness element in 2-D and 3-D BLs [56, 67, 62, 138].

Spectral Analysis and Steady Energy Growth

In a similar manner to the analysis performed for the critical forcing case, a spanwise FFT is also performed for each HWA measurement plane for k_4. As seen in Figure 5.6a, spectral energy in the vicinity of the elements at $x/c = 0.152$ is largely concentrated within the λ_1 mode, although spectral peaks are also evident at the λ_3 and λ_4 harmonics. These harmonic peaks are still evident at $x/c = 0.17$ along with a larger peak at the λ_2 harmonic. This suggests that the velocity streaks are milder, yet still identifiable in the far-wake flow, comparable to observations for super-critical, isolated roughness elements [62, 138]. The disturbance profiles at $x/c = 0.152$ once again attain their maximum amplitude in correspondence within the elements height (Figure 5.6b). The amplitudes themselves are larger than k_3, representative of the stronger recirculation region and shears induced by the k_4 configuration. At $x/c = 0.17$, the streak-like structure of the disturbance profile is retained, with the disturbance maxima moving closer to the wall, as opposed to the onset of CFI with the critical forcing configuration.

Figure 5.6c depicts the amplitude evolution of the steady disturbance energy, computed for the whole field and for the first four Fourier modes. Energy in the element vicinity is largely concentrated within the λ_1 mode, which undergoes rapid decay downstream of the elements. This is accompanied

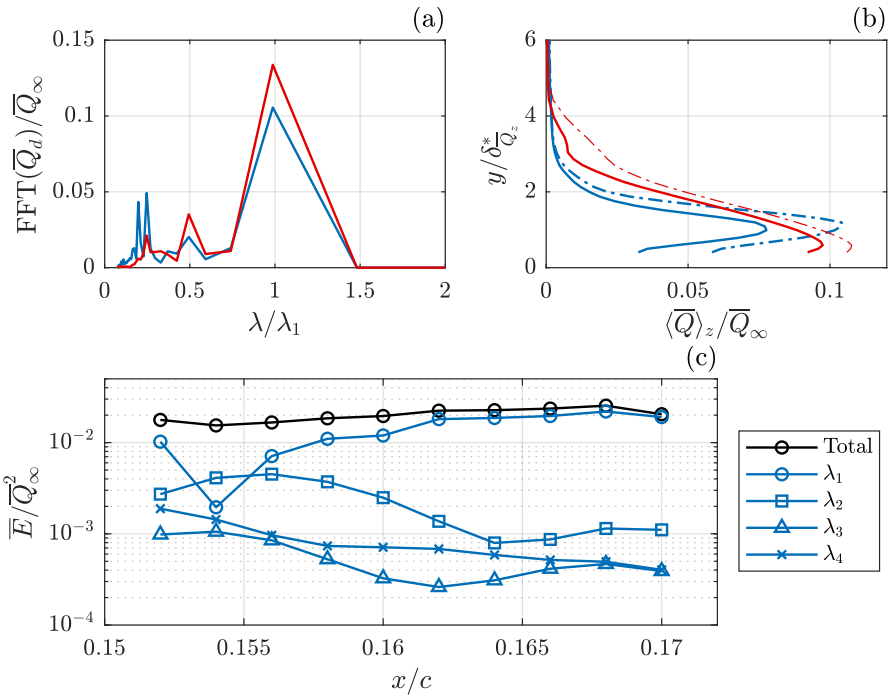

Figure 5.6: Spanwise FFT analysis for $\mathrm{Re}_{k_D} = 330$ at $x/c = 0.152$ (blue lines) and $x/c = 0.17$ (red lines). (a) Spanwise spectra at the wall-normal location of maximum disturbance amplitude. (b) Standard deviation (-.-) and λ_1 (—) disturbance profiles. (c) Stationary disturbance energy evolution.

by transient amplification of the first harmonic, which attains its maxima close to $x/c = 0.156$, corresponding to the merging of the stationary high-speed streaks in Figure . The first harmonic decays downstream of this point while the λ_1 mode is amplified, saturating in amplitude towards the end of the far-wake region. The third harmonic is seen to evolve similarly to the first, although at lower energy level, while the second harmonic exhibits a monotonic decay in energy.

It is evident from Figure 5.6 that transient growth drives the evolution of the stationary flow features for the super-critical DRE wake, which is characterised by a series of laminar velocity streaks. Transient growth in super-critical scenarios typically features the rapid amplification of steady disturbance energy in the near-wake disturbances, initiating the breakdown of the laminar streak structures into turbulence [34, 136]. However, as seen in 5.6c, the total steady disturbance energy varies minimally within the DRE wake. This implies that the stationary transient disturbances are not strong enough to initiate an explosive growth in steady disturbance energy that results in breakdown into turbulence, as such only present partial into the transition scenario.

5.3. Unsteady Disturbance Behaviour

The analysis of the stationary disturbance fields presented in the previous section highlights the highly non-modal nature of the DRE wake for both DRE forcing configurations. While stationary disturbances are the primary drivers of wake flow evolution for the critical forcing configuration, the strong recirculation regions and streak-induced shears imply that unsteadiness in the DRE wake may play a role in the emergence of CFI. This role would be significantly larger for the super-critical forcing configuration due to the higher amplitudes involved, with the flow-tripping mechanisms pertinent to it having largely been associated to unsteady disturbance energy growth in previous work [34, 138, 136]. Thus, in order to fully characterize the evolution of disturbances in the DRE wake, an investigation of the unsteady velocity fluctuations measured within each HWA plane is carried out.

5.3.1. Critical Forcing

The spatial organisation of unsteadiness in the DRE wake region for the k_3 configuration is quantified through the velocity standard deviation fields, $\langle Q\rangle$, in Figure 5.7. Aft of the DRE array, at $x/c = 0.152$, the standard deviation peaks are located on top of each element, at $y/\delta^*_{\overline{Q}_z} \approx 0.8$. This locally

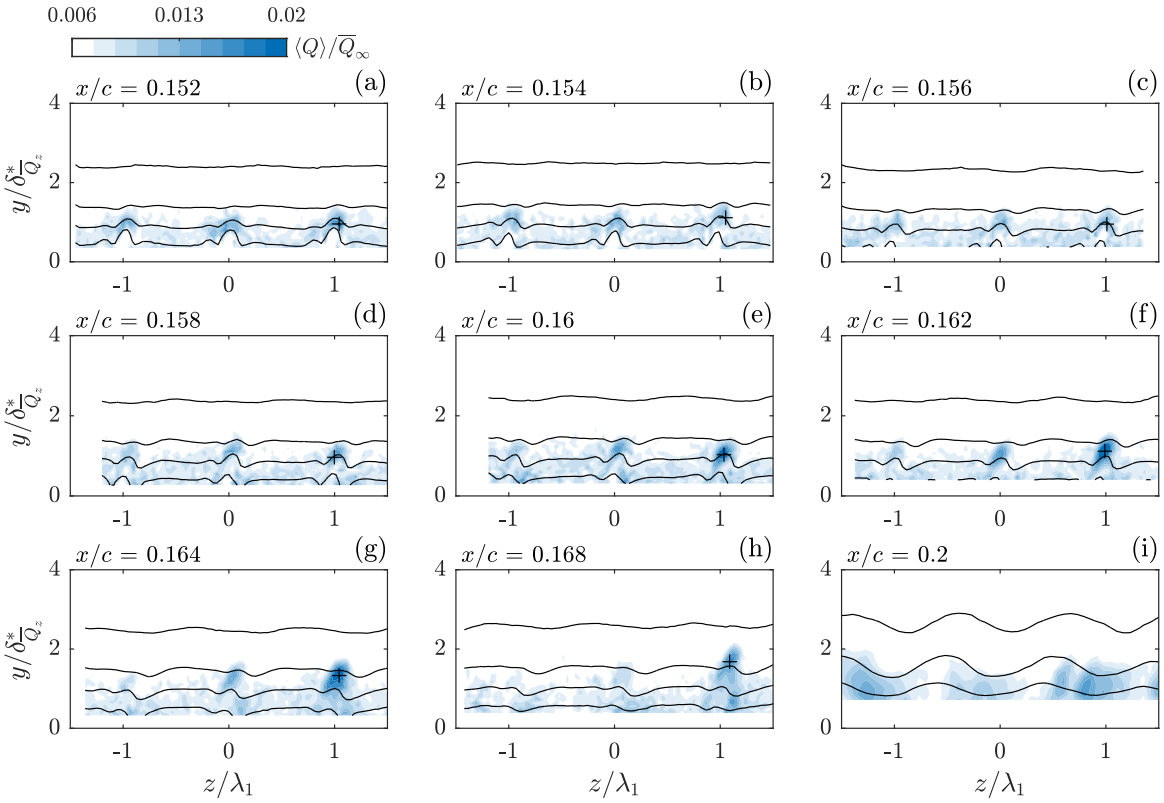

Figure 5.7: Standard deviation fields of the HWA velocity signal at successive chordwise locations, for $\mathrm{Re}_{k_D} = 192$. Black isolines of the steady BL velocity are superimposed. The black (+) symbols denote the locations at which spectra are extracted.

corresponds to the strong low-speed recirculation region in the DRE wake, which is accompanied by locally increased spanwise and wall-normal shear. This topology is resemblant to that observed with DRE in a 2-D BL [34], further implying that the onset and evolution of unsteady fluctuation regions is strongly correlated to the shear layers induced by the stationary wake disturbances.

The high fluctuation regions decay downstream of the initial plane, in correspondence with the decay of the central, low-speed recirculation wake (Figure 5.3). However, beyond $x/c = 0.158$ it is observed that these regions begin to amplify, particularly strongly for that associated to the inboard element. From Figure 5.3, this is seen to occur simultaneously with the rapid amplification of the inboard high-speed streak. A strong spanwise shear originates between the central low-speed region and inboard high-speed streak, suggesting that the amplification of the unsteady peaks is enhanced by the development of this shear layer. Following this rise in local fluctuation intensity, the unsteady peaks gradually decay toward the end of the domain alongside the emergence of modal CFI. This decay in local fluctuation intensity could possibly be due to a relaxation of spanwise shears as the stationary disturbances become less localized. The transition scenario is thus governed by the evolution of modal CFI downstream of $x/c = 0.168$, as evidenced by the IR characterization in Figure 5.1a. The plane at $x/c = 0.2$ presents a BL perturbed by stationary CFI, with unsteady fluctuations localized around the downwelling region associated to the crossflow vortices. This locally corresponds to the region of development of the type III secondary instability, that originates as a result of interaction between stationary and travelling CFI [50, 12, 111]. However, an investigation of its spectral characteristics is needed to confirm this. It is also noted from Figure 5.3 that the fluctuation regions corresponding to the inboard element amplify more strongly as compared to those around the middle and outboard elements. This could be due to irregularities arising from the DRE manufacturing procedure.

Spectral Characteristics

The high-fluctuation regions in Figure 5.7 can be further characterized through an investigation of their spectral content. Frequency spectra are extracted at locations marked by the black (+) symbols,

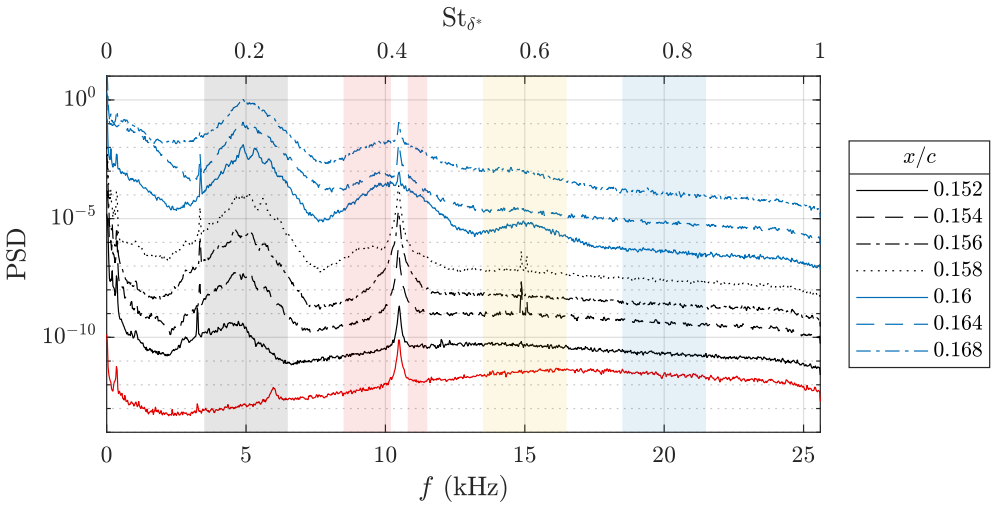

Figure 5.8: Velocity signal spectra for $\mathrm{Re}_{k_D} = 192$, extracted at the points of maximum fluctuation intensity in the $\langle Q \rangle$ fields, at successive chordwise locations. The red line is a representative velocity spectrum extracted in the freestream. Each spectrum is offset by a decade for visual clarity. Frequency bands of interest are shown as shaded regions: f_1 (grey), f_2 (red), f_3 (yellow) and f_4 (blue).

corresponding to the local maxima of the high-fluctuation regions. Owing to the flow periodicity, the unsteady spectra extracted at these locations for the inboard element are considered to be representative of unsteady disturbance behaviour in corresponding regions for the middle and outboard elements.

Figure 5.8 presents the evolution of the unsteady disturbance spectra for the critical k_3 forcing configuration, quantified using the signal PSD. The high-fluctuation region immediately aft of the DRE array at $x/c = 0.152$ features a distinct *hump* centred around approximately 5 kHz. Energy is nearly evenly distributed over frequencies larger than this 5 kHz hump, with the exemption of a tonal peak close to 11 kHz. This peak however is seen to persist in all velocity spectra extracted, and can be attributed to electronic noise in the HWA bridge rather than physical fluctuations in the flowfield [109, 98]. A representative spectrum extracted in the freestream is presented in Figure 5.8 to highlight the persistence of this peak. Between $x/c = 0.152 - 0.158$, the 5 kHz energy hump amplifies and a secondary hump is seen to emerge, centred around its first harmonic at 10 kHz. The PSD at the first harmonic however is affected by the presence of the electronic noise peak at 11 kHz. At $x/c = 0.16$, a third energy hump appears at the second harmonic, centred around 15 kHz. As per Figures 5.3 and 5.4c, this location also corresponds to beginning of the region of modal growth. The spectral energy humps at 5 kHz and its harmonics persist downstream of $x/c = 0.16$, although they are observed to widen and merge with each other toward the end of the far-wake.

To allow universal comparison of the frequency spectra associated to k_3 with established findings in literature, a local Strouhal number, $\mathrm{St}_{\delta^*} = f\delta^*/|\mathbf{Q}(k_D)|$ is defined [56, 138]. Here δ^* is the unperturbed BL displacement thickness at the DRE location and $|\mathbf{Q}(k_D)|$ is the unperturbed BL velocity magnitude extracted at the element height, k_D. These are obtained from a corresponding numerical BL solution, which was previously validated in Section 5.1. From Figure 5.8 it can be seen that the fundamental energy hump is centred at $\mathrm{St}_{\delta^*} = 0.2$, with the harmonics humps located at a corresponding $\mathrm{St}_{\delta^*} = 0.4$ and $\mathrm{St}_{\delta^*} = 0.6$. This corresponds very well to the shedding range of a circular cylinder ($\mathrm{St}_{\delta^*} = 0.18 - 0.25$), as reported by Klebanoff et. al [56] and Kuester & White [60]. While clear tonal behaviour in the flowfield is not present in Figure 5.8, the existence of the spectral humps and their associated St_{δ^*} suggest that the unsteady instability mechanism can be attributed to cylinder shedding. This is localized around the top of each element, where the fluctuation intensity attains its maximum.

Disturbance Energy Growth

The evolution of unsteady disturbance energy in the DRE wake can be tracked through a spatial integration of the velocity spectra within each HWA measurement plane. This is computed as per equation 3.10 and is shown for the k_3 forcing configuration in Figure 5.9a. Furthermore, a second integration is performed within selected frequency bands, to quantify growth pertaining to unsteady disturbances within these bands. For k_3, these are selected to be 3 kHz wide and centred around the

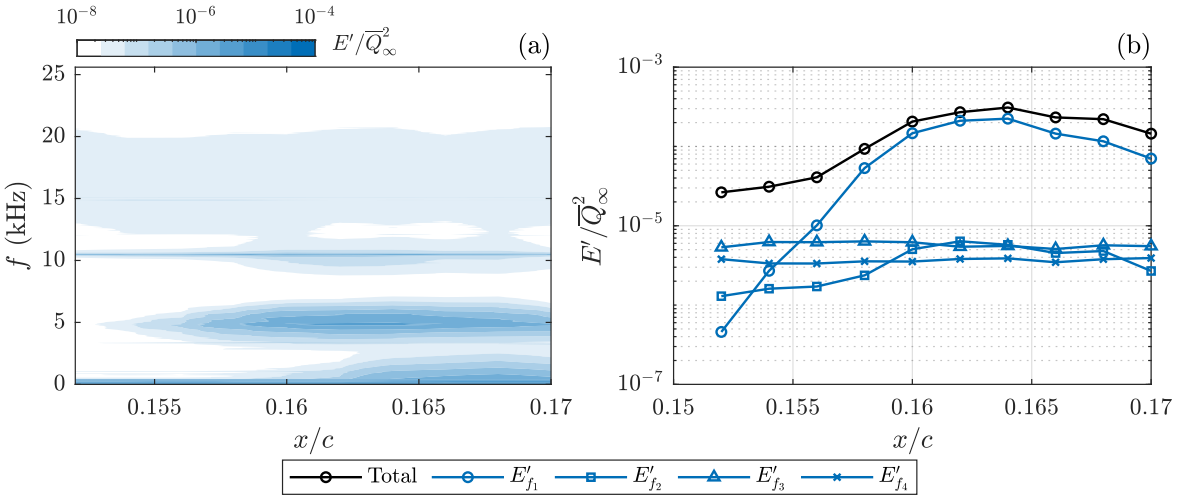

Figure 5.9: Chordwise evolution of (a) the spatially integrated energy spectra and (b) the energy integrated within selected frequency bands, for $\mathrm{Re}_{k_D} = 192$.

fundamental frequency, $f_1 = 5$ kHz, and its first three harmonics, $f_2 = 10$ kHz, $f_3 = 15$ kHz and $f_2 = 20$ kHz. The bands were depicted as shaded regions in Figure 5.8, and the energy growth corresponding to them is shown in Figure 5.9b. To ensure meaningful quantitative comparisons, the electronic peak at 11 kHz is removed from the f_2 frequency band. Additionally, Figure 5.9a indicates a consistent band of high fluctuation energy, extending up to approximately 500 Hz. The nature of this band implies that it is very likely due to vibration of the hot-wire probe within the BL, and it is filtered out of the computation of total energy.

It is seen that the total unsteady disturbance energy, E'_{tot}, is transiently amplified downstream of the DRE array, driven by shedding within the E'_{f_1} frequency band. In the vicinity of the DRE array, the energy component E'_{f_1} is observed to experience rapid exponential growth from being the lowest contributor to E'_{tot}, to becoming the dominant energy band by $x/c = 0.158$. This is reflected by the energy contours in Figure 5.9a, which show that the amplification of E'_{f_1} is additionally accompanied by a widening of the f_1 energy band. The amplification of E'_{f_1} continues up to $x/c = 0.164$ where it attains is maxima, after which it begins to gradually decay. As the energy peak in E'_{f_1} is approached, the energy in band f_2 also begins to mildly amplify. Unlike E'_{f_1}, the growth of E'_{f_2} is far less extreme, with energy plateauing at $x/c = 0.16$ At the end of the measurement domain, the f_1 band is still dominant although a pile-up of spectral energy is observed to occur at frequencies lower than 5 kHz. The energy contained within the f_3 and f_4 bands is not seen to notably vary within the DRE wake. A tonal accumulation of energy is also present close to 10 kHz, which can be amounted to contamination due to the electronic bridge noise previously discussed.

The growth and decay of E'_{f_1} and E'_{f_2} is in good correlation with observations by Ergin & White [34] for a 2-D BL. This was also shown in Figure 1.12b, where unsteady energy for a critical forcing configuration is seen to rapidly grow in the immediate vicinity of the DRE array before gradually decaying downstream. The peak in E'_{f_1} is attained shortly after the stationary high-speed streak is amplified to its maximum (Figure 5.3), but still remains relatively low in its amplitude. As the stationary streaks evolve into modal CFI, the strong shears of the highly-localized near-wake region are relaxed, which provides a less unstable state for the amplification of unsteady disturbance energy 1.12. This would correlate with the observed decay in E'_{f_1} and E'_{f_2} toward the end of the domain. Although the unsteady disturbances are seen to undergo large initial transient amplification, the low unsteady energy levels and stabilization in the far-wake result in the stationary structures largely driving the evolution of the DRE wake flow for the critical forcing configuration.

5.3.2. Super-critical Forcing

The analysis of unsteady fluctuations in the wake of the super-critical forcing configuration is crucial to fully characterizing disturbance behaviour in the flowfield. This is due to the fundamentally different transition scenario encountered with k_4, where breakdown into turbulence occurs in the vicinity of the

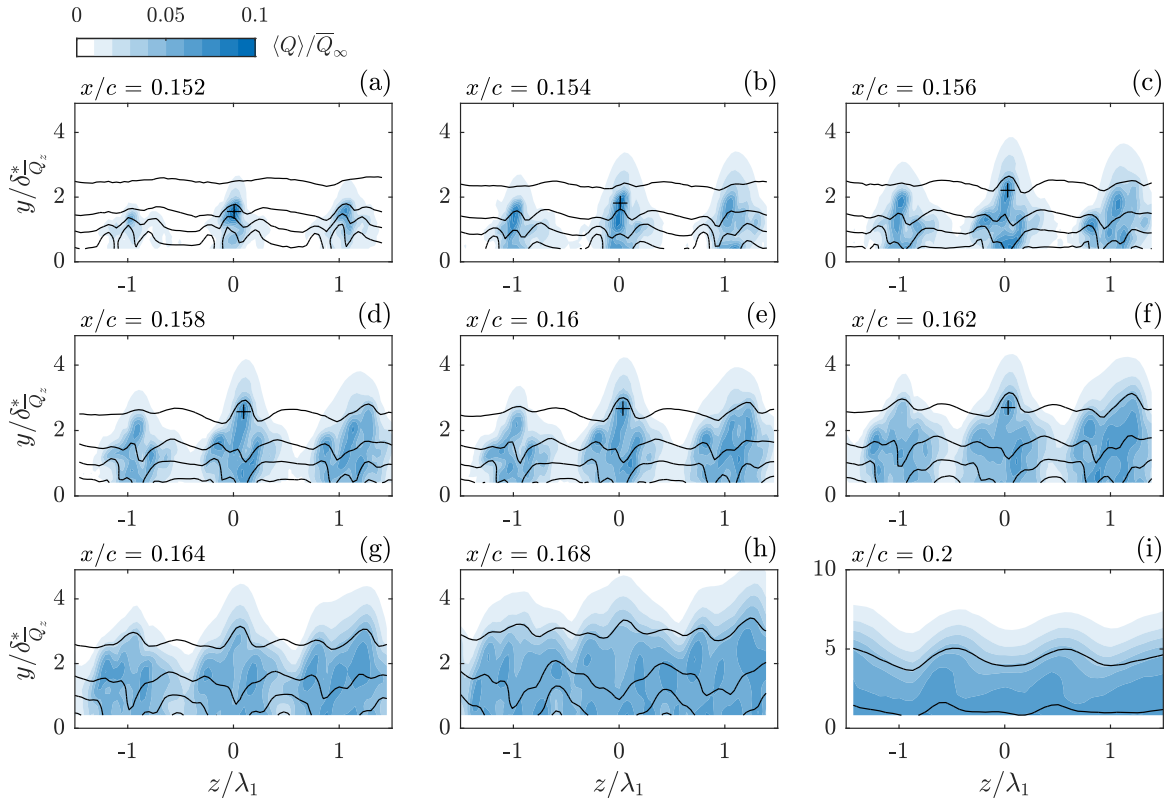

Figure 5.10: Standard deviation fields of the HWA velocity signal at successive chordwise locations, for $\mathrm{Re}_{k_D} = 330$. Black isolines of the steady BL velocity are superimposed. The black (+) symbols denote the locations at which spectra are extracted.

DRE array, preventing the development of modal CFI. This scenario was observed in the initial IR characterization presented in Figure 5.1a.

Comparably to the critical forcing configuration presented beforehand, the spatial organisation of the unsteady disturbances is investigated through the velocity standard deviation fields, $\langle Q \rangle$, shown in Figure 5.10. Fluctuations immediately aft of the DRE array at $x/c = 0.152$ are highly localized, with a high intensity fluctuation region located on top of each element. These locally correspond to the stationary, low-speed recirculation region developing here, as seen in Figure 5.2.2. Additionally, lower-intensity fluctuation regions also appear on either side of each element, in the spanwise shear layer between the pair of stationary high- and low-speed streaks induced by the HSV system [62, 136]. The fluctuation amplitudes for the k_4 configuration are noted to be nearly an order of magnitude larger than those corresponding to k_3. This is expected as the higher-amplitude elements in the array induce stronger stationary disturbances into the flowfield, which in turn lead to larger spanwise and wall-normal shears [34, 136, 138].

At further downstream locations, the high fluctuation intensity regions on top of the elements begin to rapidly grow in the spanwise and wall-normal direction, agglomerating with the lower-intensity regions on the sides of the elements. By $x/c = 0.16$ a rise in unsteady disturbance amplitude is also seen close to the wall, directly under the central high-fluctuation region. This can be associated to the merging of the stationary high-speed streaks into a single, central streak. Unsteadiness in the flowfield is enhanced aft of this phenomenon, which has been seen to be associated with laminar breakdown and the onset of turbulent flow within the DRE wake [54, 56]. The localized unsteady fluctuation regions further expand in the spanwise and wall-normal direction up to $x/c = 0.16$ where a series of local turbulent wedges begin to form. The expansion of the wedges induced by the individual elements is limited by flow periodicity, and they begin to merge into each other by the end of the measurement domain. A further downstream plane at $x/c = 0.2$ reveals an unsteady disturbance field resembling that of a turbulent BL, albeit modulated by residual periodicity induced by the stationary streaks (Figure 5.2.2).

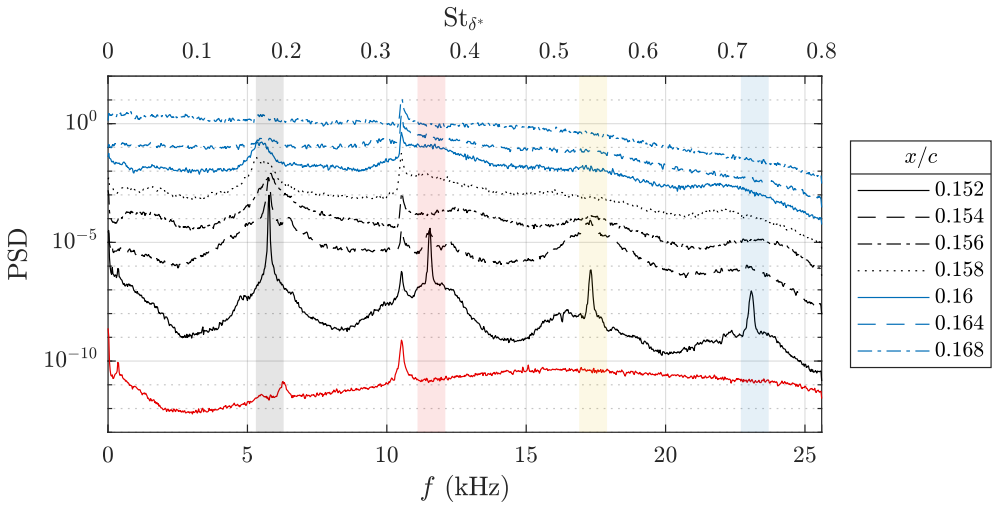

Figure 5.11: Velocity signal spectra for $\mathrm{Re}_{k_D} = 330$, extracted at the points of maximum fluctuation intensity in the $\langle Q \rangle$ fields, at successive chordwise locations. The red line is a representative velocity spectrum extracted in the freestream. Each spectrum is offset by a decade for visual clarity. Frequency bands of interest are shown as shaded regions: f_1 (grey), f_2 (red), f_3 (yellow) and f_4 (blue).

Spectral Characteristics

As with k_3, velocity spectra are extracted at the maximum fluctuation intensity region identified in each chordwise HWA plane, denoted by the black (+) symbols in Figure 5.2.2. In contrast to the critical case, the extracted spectra show strongly tonal behaviour in the vicinity of the elements, at $x/c = 0.152$. The fundamental tone is located at around 5.8 kHz, with its harmonics at 11.6 kHz, 17.4 kHz and 23.2 kHz also distinctly present. It is also noted that each of these tones is centred at a spectral hump, similar to that seen in the velocity spectra of k_3. A fifth tone is identified close to 10 kHz, but this is attributed once more to electronic noise in the HWA bridge, as this tone is ubiquitous in all critical and super-critical measurements [109, 98].

The spectral peaks quickly vanish when moving downstream, although the humps are still prominent as spectral energy is re-distributed over a wider range of frequencies. By $x/c = 0.6$, in correspondence to the merging of the stationary high-speed streaks, the velocity spectrum acquires a more broadband character. This can be correlated to enhanced flow unsteadiness and the emergence of the localized turbulent wedges, which rapidly develop aft of $x/c = 0.16$. At further downstream locations the spectra are mainly broadband, indicating that the flowfield is primarily turbulent in these regions.

If the velocity spectra are once again represented by the local Strouhal number, St_{δ^*}, comparisons can be made with the forcing configurations established in literature. The dominant tone is seen to lie in the $\mathrm{St}_{\delta^*} = 0.17 - 0.18$ range, close to the $\mathrm{St}_{\delta^*} = 0.2$ hump for the critical forcing scenario and at the edge of the cylinder shedding range reported by Klebanoff et. al [56] and Kuester & White [60] ($\mathrm{St}_{\delta^*} = 0.18 - 0.25$). Thus the unsteady instability mechanism in the DRE wake is seen to be consistent between the k_3 and k_4 cases, associated to cylinder shedding. However, the super-critical forcing configuration strongly concentrates spectral energy into distinct tones that manifest on top of each element in the DRE array. At further downstream locations, St_{δ^*} loses its significance as the broadband turbulent spectrum becomes more prevalent.

Disturbance Energy Growth

The unsteady disturbance energy spectra are spatially integrated as per the equations 3.10 and 3.11, to obtain the integrated fluctuation energy (Figure 5.12a) within each HWA plane, as well as the energy contained within discrete frequency bands. The selected frequency bands are depicted in Figure 5.11 as shaded regions. These are 1 kHz in width and centred around the fundamental frequency, $f_1 = 5.8$ kHz, and its first three harmonics, $f_2 = 11.6$ kHz, $f_3 = 17.4$ kHz and $f_2 = 23.2$ kHz. The evolution of integrated disturbance energy energy within these bands is presented in Figure 5.12b.

It can be seen that the total unsteady energy, E'_{tot}, is over an order of magnitude larger for the super-critical forcing configuration as compared to the critical case. Additionally, E'_{tot} experiences exponential growth throughout the domain, with a slight decrease in its growth rate at the domain

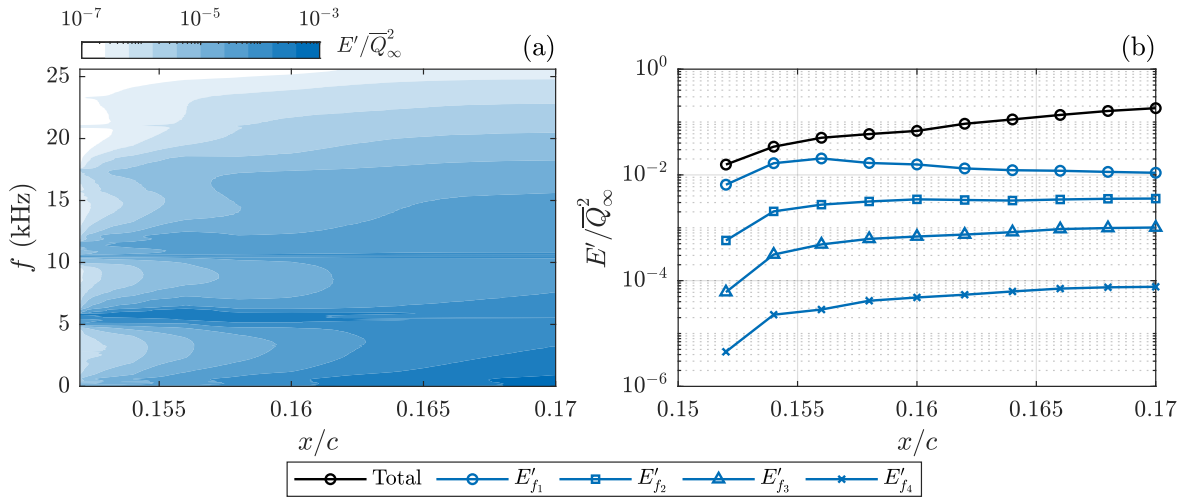

Figure 5.12: Chordwise evolution of (a) the spatially integrated energy spectra and (b) the energy integrated within selected frequency bands, for $\mathrm{Re}_{k_D} = 330$.

end ($x/c = 0.17$). In the vicinity of the DRE array the dominant frequency, f_1, is seen to be nearly comparable to E'_{tot}, implying that most of the unsteady disturbance energy is contained within this band. A rapid spread of energy from the tonal peaks into neighbouring frequency bands is observed when moving downstream, as shown in Figure 5.12a. A shallow peak can be seen in the E'_{f_1} growth curve, correlating with the merging of the high speed streaks at $x/c = 0.156$, before the energy decays to a saturation level. The harmonic band energies E'_{f_2} - E'_{f_4} undergo monotonic growth throughout the domain before saturating along with E'_{f_1} by $x/c = 0.17$.

The observed unsteady disturbance energy growth is in good agreement with the findings reported by Ergin & White [34] for super-critical DRE in 2-D BLs, who also report the rapid amplification and saturation of the energy levels. The larger element induces initial instabilities with higher (excessive) initial amplitudes, which rapidly increase the overall level of E' in the near-wake region. These initiated near-wake instabilities are subsequently amplified by through cylinder shedding in the presence of the strong recirculation region forming in the element wake, accompanied by the development of significant shears. The sustained high fluctuations levels grow to non-linear amplitudes and inhibit the relaxation of the steady disturbance energy, causing turbulent breakdown in the far-wake region [34].

6

Conclusion & Recommendations

6.1. Conclusions

A series of research questions were defined at the start of this thesis (Section 1.6), in an effort to further understand how the flow topology of a DRE wake conditions the onset of insatiabilities in a swept wing BL. The results of the numerical and experimental investigations discussed in the preceding chapters provide conclusive answers to these questions, which are presented here.

How accurately can the growth of stationary instabilities in the near-element flowfield be represented in a linear, parabolized stability framework?

Stationary disturbances in the DRE wake have been observed to undergo significant non-modal growth, as seen in previous studies on swept BL flow [14, 62, 137]. In order to be able to numerically simulate these stationary disturbances, a parabolized non-modal stability framework was derived in Chapter 2. The Fourier ansatz for the classical PSE was redefined, such that all disturbance growth was represented by the mode shape functions. This ansatz was inserted into the linearised disturbance equations, and an order of magnitude analysis was conducted similarly to Levin & Henningson [65], Tempelmann et. al [120], using non-modal scaling arguments. The scaling allowed for an elimination of the second-order streamwise derivatives, which were of $\mathcal{O}(\mathrm{Re}_{\delta_0^*}^{-3})$ relative to the other terms. By additionally neglecting the streamwise disturbance pressure gradient, as per Li & Malik [66], the system of equations was made fully parabolic and solved using a spatial marching scheme.

The NmPSE framework successfully predicted modal disturbance growth, when initialized with CFI eigenmodes computed through ILST. Its accuracy in predicting non-modal growth was quantified through the numerical investigations carried out in Chapter 4. The effect that the assumptions pertinent to NmPSE might have on non-modal growth predictions was assessed through comparisons with the elliptic HLNS framework. The NmPSE and HLNS are seen to generally agree well for all initial conditions studied, predicting nearly identical shape functions and disturbance energy evolution trends. It could thus be concluded that the slow-variance assumption, and hence the parabolization of the NmPSE, is not a major detriment in the prediction of stationary wake evolution, given the physical scales involved. Rather, the slight mismatch between the NmPSE and HLNS can be amounted to the need for a chordwise wavenumber for the NmPSE. The determination of this chordwise wavenumber in a non-modal framework was seen to be ambiguous, and possibly introduces errors into the NmPSE solution through discontinuous variations. Both the NmPSE and HLNS are also seen to be sensitive to the choice of streamwise discretization, which is a limiting factor in the accurate quantitative prediction of stationary DRE wake disturbances.

How can the structure of an experimentally measured DRE wake be used to initialize a numerical, linear, non-modal stability solution?

The stationary topology of the DRE wake was obtained from the experimental, 3-D dual-pulse PTV measurements of Zoppini et. al [136]. An initial plane was selected in the vicinity of the elements,

and a spanwise Fourier analysis was employed to identify the dominant spectral components of the disturbance velocity field at this location. The complex shape functions corresponding to the dominant Fourier mode and its higher harmonics were extracted and interpolated onto the inflow station of the numerical stability grid. A smoothing filter was then applied to the interpolated shape functions, to remove residual noise carried over from the experimental data.

A series of simulations were run with the NmPSE using experimental ICs extracted for a critical DRE forcing configuration, for the primary Fourier mode, λ_1. Qualitatively, the numerical computations agree quite well with experiment, with the NmPSE predicting a strong initial phase of transient decay and growth, followed by exponential amplification. This is in contrast to the classical LPSE, which predicted only modal amplification. The qualitative agreement is also seen for the evolution of the harmonic modes and total disturbance energy in the DRE wake, with the exception of the first harmonic. The DRE wake structure obtained through reconstruction of the NmPSE disturbance velocity fields is also seen to compare well with experiment, although discrepancies are introduced by discontinuous variations in the chordwise wavenumber. Nonetheless, the NmPSE correctly predicts the emergence of stationary CFI downstream of the wake region. Quantitatively, the NmPSE over-predicts the initial transient decay phase experienced by the primary Fourier mode. The mode also appears to evolve over a longer chordwise length as compared to experiment, although exhibiting similar shape function evolution. Growth of the second, third and fourth harmonics initially matches experiment but deviates significantly at downstream locations, where the harmonics undergo strong decay. The NmPSE also over-predicts the minima of total energy growth for the reconstructed disturbance velocity fields, though the spanwise standard deviation profiles are seen to closely resemble those of the experiment.

The robustness of the NmPSE to alterations of the experimental ICs was studied, such as with the additional smoothing procedure applied to the interpolated shape functions. No noticeable change is observed in the growth curves of the primary Fourier mode, so long as the smoothed shape functions closely follow the mean wall-normal profile of the interpolated ICs. The use of heavy smoothing, such that the ICs are drastically altered, leads to deviations in the computed growth curves. This concept was further investigated through the use of analytic ICs to approximate the experimental DRE wake shape functions. Linearly-weighted Gaussian functions were employed, defined such that they could be parametrically controlled to fit experimental shape function data corresponding to the primary Fourier mode. The energy growth curves corresponding to the experimental ICs are nearly matched by those computed with the analytic approximations. However, the NmPSE predicts a slightly lower outflow N-factor when using analytic ICs. As ambiguity can exist in approximating the experimental ICs, a parametric study was conducted, varying the wall-normal extent and phase of the analytic shape functions. The growth curves were seen to be significantly altered by the variation of these parameters, implying that an analytic approximation must be carefully chosen such as to avoid large differences with respect to the experimental ICs.

What role do unsteady fluctuations developing in the DRE wake play in the onset of BL instability?

An experimental measurement campaign was conducted at the TU Delft low turbulence wind tunnel facility using HWA, to characterize the structure and evolution of unsteady DRE wake fluctuations. Two DRE forcing configurations were investigated, with preliminary qualitative analysis of the respective flowfields carried out using IR thermography. While the critical DRE forcing is seen to introduce stationary CFI into the BL, the super-critical forcing configuration leads to rapid turbulent breakdown in the vicinity of the DRE.

Time-averaged HWA measurements of the critical DRE wake reveals a localized system of stationary velocity streaks developing aft of each element. These evolve into modal CFI in the far-wake region, in agreement with observations by Zoppini et. al [136] for an identical critical forcing configuration. Non-stationary measurements show that unsteadiness in DRE wake is largely localized around each element in the array, with peaks in the unsteady fluctuation level located on top of each element. Temporal point spectra, extracted at the locations of maximum fluctuation intensity, reveal the concentration of spectral energy within a series of broadband humps. The fundamental hump is observed to be centred around a locally-defined Strouhal number of $\mathrm{St}_{\delta^*} = 0.2$, corresponding to the shedding range reported for a circular cylinder [60, 57]. Unsteady disturbance energy in near-wake undergoes strong transient amplification, driven by cylinder shedding within the fundamental frequency band, before decaying into

the far-wake. This is correlated with the emergence of stationary CFI and the de-localization of the DRE wake features, which provides a less unstable state for the amplification of unsteady disturbances. Unsteady instabilities thus appear to play only a minor role in the evolution of the critical DRE wake, as it is seen to be largely driven by the stationary flow features.

The super-critical forcing configuration is seen to introduce stronger disturbances into the DRE wake, as a result of its higher element amplitudes. The flowfield in the element vicinity is also seen to be localized, with stationary disturbances taking the form of streaky structures. These disturbances undergo rapid, transient amplification in the near-wake region, downstream of which the laminar streaks locally break down into turbulent wedges. The stronger shear layers induced by the super-critical DREs also introduce high-amplitude, unsteady fluctuations into the DRE wake. Regions of high fluctuation intensity are localized around the top as well as the sides of the elements and merge as the wake evolves, eventually coalescing into local turbulent wedges. An analysis of temporal spectra extracted at the fluctuation intensity maxima reveals that the unsteady disturbances are strongly tonal in the immediate vicinity of the DRE. These tonal peaks are associated once more to cylinder shedding, through the Strouhal number of the fundamental energy band [60, 57] and undergo rapid decay. Spectral energy is redistributed among frequencies as the flow evolves, and takes on a broadband character in the far wake with the onset of turbulent breakdown. The total unsteady disturbance energy, and that contained within the fundamental frequency band and its harmonics, amplify exponentially and saturate in the far-wake. Mild transient amplification is also seen in the E'_{f_1} energy band. Thus, unsteady disturbances introduced by the super-critical DRE array are initially amplified through cylinder shedding in the element vicinity. However unlike with the critical forcing configuration, the high unsteadiness level is sustained by the stronger stationary disturbances and further amplifies to non-linear levels. This prevents the relaxation of the steady flow features, and transition occurs shortly downstream of the DRE location.

6.2. Recommendations

While the NmPSE framework used in this thesis was capable of qualitatively simulating DRE wake evolution, given an experimental set of initial conditions, there is still much left to be desired in terms of its quantitative performance. To this extent, various improvements could be implemented in future research, advancing toward an accurate, robust, and computationally efficient method.

- The need for a chordwise wavenumber is a critical disadvantage that the NmPSE faces in non-modal growth computations, with the error associated to it clearly seen to be non-negligible. The immediate solution to this is its elimination from the problem, which effectively gravitates the state-the-art toward the elliptic HLNS. However, the elimination of α comes at the cost of parabolization and its associated computational benefits. Future research could involve the investigation of alternative methods to deal with α, should computational efficiency of the non-modal solver be the main priority. The HLNS too however, is not without its drawbacks, as seen with its high sensitivity to the numerical grid, and its reliance on a properly defined buffer region for the outflow boundary conditions. These problems must be addressed in future research, should working with the HLNS be the preferred direction.
- While the NmPSE and HLNS were not able to quntitatively predict the experimental evolution of the DRE wake, their results were in close agreement with each other. This could indicate that there is either a large sensitivity of the non-modal framework to experimentally-derived ICs, or that an essential part of the flow physics was not modelled. The effect of surface curvature, for example, might be an important parameter to consider in a non-modal stability solution. Haynes & Reed [46] show that curvature effects are significant for modal computations with the PSE, although this has not as of yet been quantified in a non-modal framework (to the author's knowledge). While surface curvature of the swept wing within the domain of interest in this work was low, it is not completely flat. Hence, the validity of the flat plate assumption for non-modal computations of the DRE wake could be investigated in future work, through derivation of the equations in a curvilinear coordinate system.
- Only a single DRE forcing configuration was numerically studied in this work. It would be of interest to quantify how the NmPSE and HLNS perform for ICs associated to other Re_{k_D} configurations. This would allows for a better understanding of how the non-modal solvers respond

to physical variations in the ICs. Research into this could possibly be extended to investigate more accurate analytic approximations of the DRE wake for use with the non-modal solvers.

In addition to the few suggestions provided for future numerical work, the experimental measurements carried out in this thesis may be extended or improved upon.

- The standard deviation fields obtained for the critical forcing configuration (5.7) indicate aperiodicity in the flowfield, where high-fluctuation intensity regions are more prominent on the inboard element. This was attributed to manufacturing defects as a result of the laser-cutting process. To mitigate this in future experiments, an alternative manufacturing method can be investigated, such as using glass-cutters. This would eliminate deformities arising as a result of laser burns. The flowfield induced by the glass-cut DRE array would have to first be characterized, before a dedicated measurement campaign is conducted.

Bibliography

[1] Andersson, P., Berggren, M., and Henningson, D. Optimal disturbances and bypass transition in boundary layers. *Physics of Fluids 11*, 1 (1999), 134–150.

[2] Andersson, P., Henningson, D. S., and Hanifi, A. On a stabilization procedure for the parabolic stability equations. *Journal of Engineering Mathematics 33* (1998), 311–332.

[3] Arnal, D. Boundary layer transition: Predictions based on linear theory. *AGARD Report 793* (1994).

[4] Arnal, D., and Archambaud, J. Laminar-turbulent transition control: NLF, LFC, HLFC. *Advances in Laminar-Turbulent Transition Modeling* (2008).

[5] Arnal, D., and Casalis, G. Laminar-turbulent transition prediction in three-dimensional flows. *Progress in Aerospace Sciences 36*, 2 (2000), 173–191.

[6] Bagheri, S., and Hanifi, A. The stabilizing effect of streaks on tollmien-schlichting and oblique waves: A parametric study. *Physics of Fluids 19*, 7 (2007), 078103.

[7] Bertolotti, F., Herbert, T., and Spalart, P. Linear and nonlinear stability of the blasius boundary layer. *Journal of Fluid Mechanics 242* (sep 1992), 441–474.

[8] Bertolotti, F. P. Receptivity of three-dimensional boundary-layers to localized wall roughness and suction. *Physics of Fluids 12*, 7 (2000), 1799–1809.

[9] Bippes, H. Instability features appearing on swept wing configurations. In *Laminar-Turbulent Transition* (Berlin, Heidelberg, 1990), D. Arnal and R. Michel, Eds., Springer Berlin Heidelberg, pp. 419–430.

[10] Bippes, H. Basic experiments on transition in three-dimensional boundary layers dominated by crossflow instability. *Progress in Aerospace Sciences*, 35 (1999), 363–412.

[11] Boersma, J. Business jet design using laminar flow. Master's thesis, Delft University of Technology, 2017.

[12] Bonfigli, G., and Kloker, M. Secondary instability of crossflow vortices: validation of the stability theory by direct numerical simulation. *Journal of Fluid Mechanics 583* (jul 2007), 229–272.

[13] Breuer, K. S., and Kuraishi, T. Transient growth in two- and three-dimensional boundary layers. *Physics of Fluids 6*, 6 (jun 1994), 1983–1993.

[14] Brynjell-Rahkola, M., Schlatter, P., Hanifi, A., and Henningson, D. Global stability analysis of a roughness wake in a falkner-skan-cooke boundary layer. *Procedia IUTAM 14* (2015), 192–200.

[15] Butler, K. M., and Farrell, B. F. Three-dimensional optimal perturbations in viscous shear flow. *Physics of Fluids A: Fluid Dynamics 4*, 8 (1992), 1637–1650.

[16] Byström, M. *Optimal disturbances in boundary layer flows.* PhD thesis, 2007.

[17] Carlomagno, G., and Astarita, T. *Infrared Thermography for Thermo-Fluid-Dynamics.* 01 2013.

[18] Carpenter, A., Saric, W., and Reed, H. Roughness receptivity in swept-wing boundary layers–experiments. *International Journal of Engineering Systems Modelling and Simulation 2*, 1-2 (2010), 128–138.

[19] CARRILLO, J. R., REIBERT, M., AND SARIC, W. Distributed-roughness effects on stability and transition in swept-wing boundary layers.

[20] CHERUBINI, S., TULLIO, M. D. D., PALMA, P. D., AND PASCAZIO, G. Transient growth in the flow past a three-dimensional smooth roughness element. *Journal of Fluid Mechanics 724* (may 2013), 642–670.

[21] CHOUDHARI, M. Roughness-induced generation of crossflow vortices in three-dimensional boundary layers. *Theoretical and Computational Fluid Dynamics 6*, 1 (Feb 1994), 1–30.

[22] CHOUDHARI, M., AND STREETT, C. *Theoretical prediction of boundary-layer receptivity.*

[23] COLLIS, S. S., AND LELE, S. K. Receptivity to surface roughness near a swept leading edge. *Journal of Fluid Mechanics 380* (1999), 141–168.

[24] COOKE, J. C. The boundary layer of a class of infinite yawed cylinders. *Mathematical Proceedings of the Cambridge Philosophical Society 46*, 4 (1950), 645–648.

[25] CORBETT, P., AND BOTTARO, A. Optimal linear growth in swept boundary layers. *Journal of Fluid Mechanics 435* (2001), 1.

[26] CROUCH, J. *Theoretical studies on the receptivity of boundary layers.*

[27] DANABASOGLU, G., AND BIRINGEN, S. A chebyshev matrix method for spatial modes of the orr-sommerfeld equation. Contractor Report 19890016814, National Aeronautics and Space Administration, aug 1989.

[28] DEYHLE, H., AND BIPPES, H. Disturbance growth in an unstable three-dimensional boundary layer and its dependence on environmental conditions. *Journal of Fluid Mechanics 316* (jun 1996), 73–113.

[29] DOWNS, R., AND WHITE, E. Free-stream turbulence and the development of cross-flow disturbances. *Journal of Fluid Mechanics 735* (2013), 347–380.

[30] DOWNS, R., WHITE, E., AND DENISSEN, N. Transient growth and transition induced by random distributed roughness. *AIAA Journal 46* (2008), 451–462.

[31] DRELA, M. *Flight vehicle aerodynamics.* The MIT Press„ Cambridge, Massachusetts :, 2014.

[32] DREWS, S., DOWNS, R., DOOLITTLE, C.AND GOLDSTEIN, D., AND WHITE, E. Direct numerical simulations of flow past random distributed roughness. In *49th AIAA Aerospace Sciences Meeting including the New Horizons Forum and Aerospace Exposition* (jan 2011), American Institute of Aeronautics and Astronautics.

[33] ELLINGSEN, T., AND PALM, E. Stability of linear flow. *The Physics of Fluids 18*, 4 (1975), 487–488.

[34] ERGIN, F., AND WHITE, E. Unsteady and transitional flows behind roughness elements. *AIAA Journal 44*, 11 (2006), 2504–2514.

[35] FALKNER, V., AND SKAN, S. Some approximate solutions of the boundary layer equations. *The London, Edinburgh, and Dublin Philosophical Magazine and Journal of Science 12*, 80 (1931), 865–896.

[36] FARRELL, B. F. Optimal excitation of perturbations in viscous shear flow. *The Physics of Fluids 31*, 8 (1988), 2093–2102.

[37] FISCHER, P., AND CHOUDHARI, M. Numerical simulation of roughness-induced transient growth in a laminar boundary layer. In *34th AIAA Fluid Dynamics Conference and Exhibit* (jun 2004), American Institute of Aeronautics and Astronautics.

[38] FRITSCH, F. N., AND CARLSON, R. E. Monotone piecewise cubic interpolation. *SIAM Journal on Numerical Analysis 17*, 2 (1980), 238–246.

[39] GASTER, M. A note on the relation between temporally-increasing and spatially-increasing disturbances in hydrodynamic stability. *Journal of Fluid Mechanics 14*, 2 (1962), 222–224.

[40] GONZALEZ, R. C., AND WOODS, R. E. *Digital image processing*. Prentice Hall, Upper Saddle River, N.J., 2008.

[41] GRAVER, B., ZHANG, K., AND RUTHERFORD, D. Co2 emissions from commerical aviation, 2018. Working Paper 2019-16, The International Council on Clean Transportation, sep 2019.

[42] GREGORY, N., AND WALKER, W. *The effect on transition of isolated surface excrescences in the boundary layer*. HM Stationery Office, 1956.

[43] GÖRTLER, H. Instabilität laminarer grenzschichten an konkaven wänden gegenüber gewissen dreidimensionalen störungen. *ZAMM - Journal of Applied Mathematics and Mechanics / Zeitschrift für Angewandte Mathematik und Mechanik 21*, 4 (1941), 250–252.

[44] HALL, P., MALIK, M. R., AND POLL, D. I. A. On the stability of an infinite swept attachment line boundary layer. *Proceedings of the Royal Society of London. Series A, Mathematical and Physical Sciences 395*, 1809 (1984), 229–245.

[45] HAYNES, T., AND REED, H. *Computations in nonlinear saturation of stationary crossflow vortices in a swept-wing boundary layer*.

[46] HAYNES, T., AND REED, H. Simulation of swept-wing vortices using nonlinear parabolized stability equations. *Journal of Fluid Mechanics 405* (feb 2000), 325–349.

[47] HENNINGSON, D. Comment on ''transition in shear flows. nonlinear normality versus non-normal linearity'' [phys. fluids 7, 3060 (1995)]. *Physics of Fluids 8*, 8 (1996), 2257–2258.

[48] HERBERT, T. Parabolized stability equations. *AGARD: Special Course on Progress in Transition Modelling, AGARD-R-d793* (1993).

[49] HERBERT, T. Parabolized stability equations. *Annual Review of Fluid Mechanics 29*, 1 (1997), 245–283.

[50] HÖGBERG, M., AND HENNINGSON, D. Secondary instability of cross-flow vortices in falkner–skan–cooke boundary layers. *Journal of Fluid Mechanics 368* (aug 1998), 339–357.

[51] JOSLIN, R. D., STREETT, C. L., AND CHANG, C.-L. Validation of three-dimensional incompressible spatial direct numerical simulation code: A comparison with linear stability and parabolic stability equation theories for boundary-layer transition on a flat plate. Technical Publication 19920021052, National Aeronautics and Space Administration, jul 1992.

[52] KAWAKAMI, M., KOHAMA, Y., AND OKUTSU, M. Stability characteristics of stationary crossflow vortices in three-dimensional boundary layer. In *37th Aerospace Sciences Meeting and Exhibit* (Reno,NV,U.S.A., Jan. 1999), American Institute of Aeronautics and Astronautics.

[53] KENDALL, J. *Experimental study of disturbances produced in a pre-transitional laminar boundary layer by weak freestream turbulence*.

[54] KENDALL, J. Laminar boundary layer velocity distortion by surface roughness: Effect upon stability. *AIAA paper 195* (1981), 1981.

[55] KLEBANOFF, P. Effect of free-stream turbulence on a laminar boundary layer. In *Bulletin of the American Physical Society* (1971), vol. 16, American Institute of Physics, 1305 Walt Whit RD, STE 300, Melville, NY 11747-4501 USA, pp. 1323–+.

[56] KLEBANOFF, P. S., CLEVELAND, W. G., AND TIDSTROM, K. D. On the evolution of a turbulent boundary layer induced by a three-dimensional roughness element. *Journal of Fluid Mechanics 237* (apr 1992), 101–187.

[57] KLEBANOFF, P. S., TIDSTROM, K. D., AND SARGENT, L. M. The three-dimensional nature of boundary-layer instability. *Journal of Fluid Mechanics 12*, 1 (1962), 1–34.

[58] KOCH, W. On the spatio-temporal stability of primary and secondary crossflow vortices in a three-dimensional boundary layer. *Journal of Fluid Mechanics 456* (2002), 85–111.

[59] KOHAMA, Y., SARIC, W., AND HOOS, J. A. A high frequency, secondary instability of crossflow vortices that leads to transition. *Proc. Boundary Layer Transition and Control. London: Royal Aeron. Soc* (1991), 4–1.

[60] KUESTER, M., AND WHITE, E. Structure of turbulent wedges created by isolated surface roughness. *Experiment in Fluids 57* (2016).

[61] KUESTER, M. S., AND WHITE, E. B. Roughness receptivity and shielding in a flat plate boundary layer. *Journal of Fluid Mechanics 777* (jul 2015), 430–460.

[62] KURZ, H., AND KLOKER, M. Mechanisms of flow tripping by discrete roughness elements in a swept-wing boundary layer. *Journal of Fluid Mechanics 796* (2016), 158–194.

[63] LANDAHL, M. A note on an algebraic instability of inviscid parallel shear flows. *Journal of Fluid Mechanics 98*, 2 (1980), 243–251.

[64] LEMARECHAL, J., COSTANTINI, M., KLEIN, C., KLOKER, M. J., WÜRZ, W., KURZ, H. B., STREIT, T., AND SCHABER, S. Investigation of stationary-crossflow-instability induced transition with the temperature-sensitive paint method. *Experimental Thermal and Fluid Science 109* (dec 2019), 109848.

[65] LEVIN, O., AND HENNINGSON, D. S. Exponential vs algebraic growth and transition prediction in boundary layer flow. *Flow, Turbulence and Combustion 70*, 1 (Jan 2003), 183–210.

[66] LI, F., AND MALIK, M. R. On the nature of pse approximation. *Theoretical and Computational Fluid Dynamics 8* (1996), 253–273.

[67] LOISEAU, J., ROBINET, J., CHERUBINI, S., AND LERICHE, E. Investigation of the roughness-induced transition: global stability analyses and direct numerical simulations. *Journal of Fluid Mechanics 760* (2014), 175–211.

[68] LUCAS, J. *Spatial optimal perturbations for transient growth analysis in three-dimensional boundary layers*. PhD thesis, Universite de Toulouse, 2014.

[69] LUCHINI, P. Reynolds-number-independent instability of the boundary layer over a flat surface: optimal perturbations. *Journal of Fluid Mechanics 404* (2000), 289–309.

[70] MACK, L. Boundary-layer linear stability theory. Tech. rep., California Inst of Tech Pasadena Jet Propulsion Lab, 1984.

[71] MACK, L. Stability of three-dimensional boundary layers on swept wings at transonic speeds. In *Symposium Transsonicum III: IUTAM Symposium Göttingen* (may 1988), Springer.

[72] MALIK, M. Numerical methods for hypersonic boundary layer stability. *Journal of Computational Physics 86*, 2 (1990), 376–413.

[73] MALIK, M., LI, F., CHOUDARI, M., AND CHANG, C. Secondary instability of crossflow vortices and swept-wing boundary-layer transition. *Journal of Fluid Mechanics 399* (nov 1999), 85–115.

[74] MESSING, R., AND KLOKER, M. J. Investigation of suction for laminar flow control of three-dimensional boundary layers. *Journal of Fluid Mechanics 658* (jun 2010), 117–147.

[75] MICHELIS, T. *Boundary Layer Separation: Diagnostics and Control*. PhD thesis, 2017.

[76] MORKOVIN, M. On the many faces of transition. In *Viscous drag reduction*. Springer, 1969, pp. 1–31.

[77] MORKOVIN, M. Transition in open flow systems-a reassessment. *Bull. Am. Phys. Soc. 39* (1994), 1882.

[78] MUGHAL, M. S., AND ASHWORTH, R. Uncertainty quantification based receptivity modelling of crossflow instabilities induced by distributed surface roughness in swept wing boundary layers.

[79] MÜLLER, B. Experimentelle untersuchung der querströmungsinstabilität im linearen und nichtlinearen bereich des transitionsgebietes. Tech. rep., 1990. LIDO-Berichtsjahr=1990,.

[80] MÜLLER, B., AND BIPPES, H. Experimental study of instability modes in a three-dimensional boundary layer. *AGARD CP, NATO AGARD* (1989).

[81] NG, L. L., AND CROUCH, J. D. Roughness-induced receptivity to crossflow vortices on a swept wing. *Physics of Fluids 11*, 2 (1999), 432–438.

[82] ORR, W. M. The stability or instability of the steady motions of a perfect liquid and of a viscous liquid. part ii: A viscous liquid. *Proceedings of the Royal Irish Academy. Section A: Mathematical and Physical Sciences 27* (1907), 69–138.

[83] OXLEY, D., AND JAIN, C. Global Air Passenger Markets: Riding Out Periods of Turbulence.

[84] PFENNINGER, W. Flow phenomena at the leading edge of swept wings. In *Special course on drag reduction* (1977), AGARD Report 654.

[85] POLL, D. I. A. Some observations of the transition process on the windward face of a long yawed cylinder. *Journal of Fluid Mechanics 150* (1985), 329–356.

[86] PRALITS, J., BYSTRÒM, M., HANIFI, A., HENNINGSON, D., AND LUCHINI, P. Optimal disturbances in three-dimensional boundary-layer flows. *ERCOFTAC Bulletin 74* (01 2007), 23–31.

[87] PRANDLT, L. In *Verhandlungen des dritten internationalen Mathematiker-Kongresses in Heidelberg* (1904).

[88] RADEZTSKY, R., REIBERT, M., AND SARIC, W. Effect of isolated micron-sized roughness on transition in swept-wing flows. *AIAA Journal 37*, 11 (nov 1999), 1370–1377.

[89] RAYLEIGH, L. On the dynamics of revolving fluids. *Proceedings of the Royal Society of London. Series A, Containing Papers of a Mathematical and Physical Character 93*, 648 (1917), 148–154.

[90] REED, H., AND SARIC, W. Stability of three-dimensional boundary layers. *Annual Review of Fluid Mechanics 21*, 1 (1989), 235–284.

[91] REED, H., SARIC, W., AND ARNAL, D. Linear stability theory applied to boundary layers. *Annual review of fluid mechanics 28*, 1 (1996), 389–428.

[92] REIBERT, M., SARIC, W., CARRILLO, J., AND CHAPMAN, K. Experiments in nonlinear saturation of stationary crossflow vortices in a swept-wing boundary layer. In *34th Aerospace Sciences Meeting and Exhibit* (jan 1996), American Institute of Aeronautics and Astronautics.

[93] RESHOTKO, E. Transient growth: a factor in bypass transition. *Physics of Fluids 13*, 5 (2001), 1067–1075.

[94] RESHOTKO, E., AND TUMIN, A. Application of transient growth theory to bypass transition. In *IUTAM Symposium on One Hundred Years of Boundary Layer Research* (Dordrecht, 2006), G. E. A. Meier and H.-J. Sreenivasan, K. R.and Heinemann, Eds., Springer Netherlands, pp. 83–93.

[95] RIUS-VIDALES, A., KOTSONIS, M., ANTUNES, A., AND COSIN, R. Effect of two-dimensional surface irregularities on swept wing transition: Forward facing steps. In *2018 Fluid Dynamics Conference* (jun 2018), American Institute of Aeronautics and Astronautics.

[96] RIZZETTA, D., VISBAL, M., REED, H., AND SARIC, W. Direct numerical simulation of discrete roughness on a swept-wing leading edge. *AIAA journal 48*, 11 (2010), 2660–2673.

[97] RUIS-VIDALES, A. *Influence of a forward-facing step on crossflow instability and transition: An experimental study in a swept wing boundary-layer*. PhD thesis, Technische Universiteit Delft, 2022.

[98] SADDOUGHI, S. G., AND VEERAVALLI, S. V. Hot-wire anemometry behaviour at very high frequencies. *Measurement Science and Technology 7* (1996), 1297–1300.

[99] SARIC, W., CARPENTER, A., AND REED, H. Passive control of transition in three-dimensional boundary layers, with emphasis on discrete roughness elements. *Philosophical Transactions of the Royal Society A: Mathematical, Physical and Engineering Sciences 369*, 1940 (2011), 1352–1364.

[100] SARIC, W., CARRILLO, R., AND REIBERT, M. Leading-edge roughness as a transition control mechanism, 1998.

[101] SARIC, W., REED, H., AND WHITE, E. Stability and transition of three dimensional boundary layers. *Annual Review of Fluid Mechanics 35*, 1 (2003), 413–440.

[102] SARIC, W., WEST, D., TUFTS, M., AND REED, H. Experiments on discrete roughness element technology for swept-wing laminar flow control. *AIAA Journal 57*, 2 (2019), 641–654.

[103] SARIC, W. S. Görtler vortices. *Annual Review of Fluid Mechanics 26*, 1 (1994), 379–409.

[104] SCHMID, P., AND HENNINGSON, D. Applied mathematical sciences, 2001.

[105] SCHMID, P. J. Nonmodal stability theory. *Annual Review of Fluid Mechanics 39*, 1 (2007), 129–162.

[106] SCHRADER, L., BRANDT, L., AND HENNINGSON, D. Receptivity mechanisms in three-dimensional boundary-layer flows. *Journal of Fluid Mechanics 618* (2009), 209–241.

[107] SCHUBAUER, G. B., AND SKRAMSTAD, H. K. Laminar boundary-layer oscillations and transition on. *Journal of research of the National Bureau of Standards 38* (1947), 251.

[108] SCIACCHITANO, A., AND WIENEKE, B. PIV uncertainty propagation. *Measurement Science and Technology 27*, 8 (jun 2016), 084006.

[109] SERPIERI, J. *Cross-Flow Instability*. PhD thesis, Technische Universiteit Delft, 2018.

[110] SERPIERI, J., AND KOTSONIS, M. Design of a swept wing wind tunnel model for study of cross-flow instability. In *33rd AIAA Applied Aerodynamics Conference* (jun 2015), American Institute of Aeronautics and Astronautics.

[111] SERPIERI, J., AND KOTSONIS, M. Three-dimensional organisation of primary and secondary crossflow instability. *Journal of Fluid Mechanics 799* (2016), 200–245.

[112] SHARMA, A., DREWS, S., KUESTER, M. S., GOLDSTEIN, D. B., AND WHITE, E. B. Evolution of disturbances due to distributed surface roughness in laminar boundary layers. In *52nd Aerospace Sciences Meeting* (jan 2014), American Institute of Aeronautics and Astronautics.

[113] SIMEN, M. Local and non-local stability theory of spatially varying flows. In *Instability, Transition, and Turbulence*. Springer, 1992, pp. 181–201.

[114] SMAN, E. V. D. Towards a sustainable air transport system. Tech. rep., TU Delft, NLR, 2021.

[115] SMITH, A., AND GAMBERONI, N. *Transition, Pressure Gradient and Stability Theory*. ARC-19322. Douglas Aircraft Company, El Segundo Division, 1956.

[116] SMITH, B. L., NEAL, D. R., FEERO, M. A., AND RICHARDS, G. Assessing the limitations of effective number of samples for finding the uncertainty of the mean of correlated data. *Measurement Science and Technology 29*, 12 (nov 2018), 125304.

[117] SOMMERFELD, A. Ein beitrag zur hydrodynamischen erklärung der turbulenten flüssigkeitsbewegung. g. castelnuovo, ed. In *Atti del IV Congresso internazionale dei matematici*, pp. 116–124.

[118] SQUIRE, H. B. On the stability for three-dimensional disturbances of viscous fluid flow between parallel walls. *Proceedings of the Royal Society of London. Series A, Containing Papers of a Mathematical and Physical Character 142*, 847 (1933), 621–628.

[119] SUMARIVA, J. A. F., AND HEIN, S. J. *Adaptive Harmonic Linearized Navier-Stokes equations used for boundary layer instability analysis in the presence of large streamwise gradients.*

[120] TEMPELMANN, D., HANIFI, A., AND HENNINGSON, D. S. Spatial optimal growth in three-dimensional boundary layers. *Journal of Fluid Mechanics 646* (2010), 5–37.

[121] TEMPELMANN, D., SCHRADER, L., HANIFI, A., BRANDT, L., AND HENNINGSON, D. Numerical study of boundary-layer receptivity on a swept wing. In *6th AIAA Theoretical Fluid Mechanics Conference* (2011), American Institute of Aeronautics and Astronautics.

[122] TEMPELMANN, D., SCHRADER, L., HANIFI, A., BRANDT, L., AND HENNINGSON, D. Swept wing boundary-layer receptivity to localized surface roughness. *Journal of Fluid Mechanics 711* (sep 2012), 516–544.

[123] TREFETHEN, L., AND EMBREE, M. *Spectra and Pseudospectra.* 01 2005.

[124] TREFETHEN, L. N. Pseudospectra of linear operators. *SIAM Rev. 39*, 3 (sep 1997), 383–406.

[125] TREFETHEN, L. N., TREFETHEN, A. E., REDDY, S. C., AND DRISCOLL, T. A. Hydrodynamic stability without eigenvalues. *Science 261*, 5121 (1993), 578–584.

[126] VAN INGEN, J. L. A suggested semi-empirical method for the calculation of the boundary layer transition region. *Technische Hogeschool Delft, Vliegtuigbouwkunde, Rapport VTH-74* (1956). Publisher: Delft University of Technology.

[127] WASSERMANN, P., AND KLOKER, M. Mechanisms and passive control of crossflow-vortex-induced transition in a three-dimensional boundary layer. *Journal of Fluid Mechanics 456* (2002), 49–84.

[128] WASSERMANN, P., AND KLOKER, M. Transition mechanisms in a three-dimensional boundary-layer flow with pressure-gradient changeover. *Journal of Fluid Mechanics 530* (may 2005), 265–293.

[129] WELCH, P. The use of fast fourier transform for the estimation of power spectra: A method based on time averaging over short, modified periodograms. *IEEE Transactions on Audio and Electroacoustics 15*, 2 (jun 1967), 70–73.

[130] WHITE, E., AND ERGIN, G. Using laminar-flow velocity profiles to locate the wall behind roughness elements. *Experiments in Fluids 36* (01 2004), 805–812.

[131] WHITE, E., AND SARIC, W. *Application of variable leading-edge roughness for transition control on swept wings.*

[132] WHITE, E., AND SARIC, W. Secondary instability of crossflow vortices. *Journal of Fluid Mechanics 525* (2005), 275–308.

[133] WHITE, E. B., RICE, J. M., AND GÖKHAN ERGIN, F. Receptivity of stationary transient disturbances to surface roughness. *Physics of Fluids 17*, 6 (2005), 064109.

[134] WHITE, F. M. F. M. *Viscous fluid flow: Frank M. White.* McGraw-Hill Medical, New York (N.Y.), 1991. OCLC: 817763693.

[135] ZOPPINI, G., MICHELIS, T., RAGNI, D., AND KOTSONIS, M. Swept Wing Boundary Layer Transition Control by Multiple DRE Forcing. unpublished, 2021.

[136] ZOPPINI, G., MICHELIS, T., RAGNI, D., AND KOTSONIS, M. The near-wake of discrete roughness elements on swept wings: tomographic ptv measurements. In *Submitted to: 12th International Symposium on Turbulence and Shear Flow Phenomena (TSFP12)* (2022).

[137] ZOPPINI, G., RAGNI, D., AND KOTSONIS, M. Experimental investigation on receptivity of crossflow instability to discrete roughness amplitude and location. In *AIAA Scitech 2021 Forum* (jan 2021), American Institute of Aeronautics and Astronautics.

[138] ZOPPINI, G., RAGNI, D., AND KOTSONIS, M. Experimental investigation of isolated roughness induced transition in a swept wing boundary layer. In *AIAA SCITECH 2022 Forum* (jan 2022), American Institute of Aeronautics and Astronautics.

[139] ZOPPINI, G., WESTERBEEK, S., RAGNI, D., AND KOTSONIS, M. Receptivity of crossflow instability to discrete roughness amplitude and location. *Journal of Fluid Mechanics 939* (2022), A33.

[140] ÅKERVIK, E., EHRENSTEIN, U., GALLAIRE, F., AND HENNINGSON, D. S. Global two-dimensional stability measures of the flat plate boundary-layer flow. *European Journal of Mechanics - B/Fluids 27*, 5 (2008), 501–513.

A

Appendix

A.1. Non-Modal PSE System of Equations

The system of equations 2.27 can be written in matrix form:

$$\mathbb{A}\bar{\mathbf{q}} + \mathbb{B}\frac{\partial \bar{\mathbf{q}}}{\partial \bar{y}} + \mathbb{C}\frac{\partial^2 \bar{\mathbf{q}}}{\partial \bar{y}^2} + \mathbb{D}\frac{\partial \bar{\mathbf{q}}}{\partial \bar{x}} = 0 \tag{A.1}$$

The vector $\bar{\mathbf{q}}$ here includes the shape function for the pressure as well, such that $\bar{\mathbf{q}} = (\bar{u}, \bar{v}, \bar{w}, \bar{p})^T$. The contents of the coefficient matrices $\mathbb{A}$, $\mathbb{B}$, $\mathbb{C}$, $\mathbb{D}$ are as follows:

$$\mathbb{A} = \begin{pmatrix} i\bar{\alpha} & 0 & i\bar{\beta} & 0 \\ C + \frac{\partial \bar{U}}{\partial \bar{x}} & \frac{\partial \bar{U}}{\partial \bar{y}} & 0 & i\bar{\alpha} \\ \frac{\partial \bar{V}}{\partial \bar{x}} & C + \frac{\partial \bar{V}}{\partial \bar{y}} & 0 & 1 \\ \frac{\partial \bar{W}}{\partial \bar{x}} & \frac{\partial \bar{W}}{\partial \bar{y}} & C & i\bar{\beta} \end{pmatrix} \tag{A.2a}$$

$$\mathbb{B} = \begin{pmatrix} 0 & 1 & 0 & 0 \\ \bar{V} & 0 & 0 & 0 \\ 0 & \bar{V} & 0 & 1 \\ 0 & 0 & \bar{V} & 0 \end{pmatrix} \tag{A.2b}$$

$$\mathbb{C} = \begin{pmatrix} 0 & 0 & 0 & 0 \\ -\frac{1}{\mathrm{Re}} & 0 & 0 & 0 \\ 0 & -\frac{1}{\mathrm{Re}} & 0 & 1 \\ 0 & 0 & -\frac{1}{\mathrm{Re}} & 0 \end{pmatrix} \tag{A.2c}$$

$$\mathbb{D} = \begin{pmatrix} 1 & 0 & 0 & 0 \\ \bar{U} - \frac{2i\bar{\alpha}}{\mathrm{Re}} & 0 & 0 & 0 \\ 0 & \bar{U} - \frac{2i\bar{\alpha}}{\mathrm{Re}} & 0 & 1 \\ 0 & 0 & \bar{U} - \frac{2i\bar{\alpha}}{\mathrm{Re}} & 0 \end{pmatrix} \tag{A.2d}$$

Where the common convection-diffusion term C is written as:

$$C = -i\bar{\omega} + i\bar{\alpha}\bar{U} + i\bar{\beta}\bar{W} + \frac{1}{\mathrm{Re}_{\delta_0^*}}\left(\bar{\alpha}^2 + \bar{\beta}^2 - i\frac{\partial \bar{\alpha}}{\partial \bar{x}}\right) \tag{A.3}$$

A.2. NmPSE High-Level Architecture

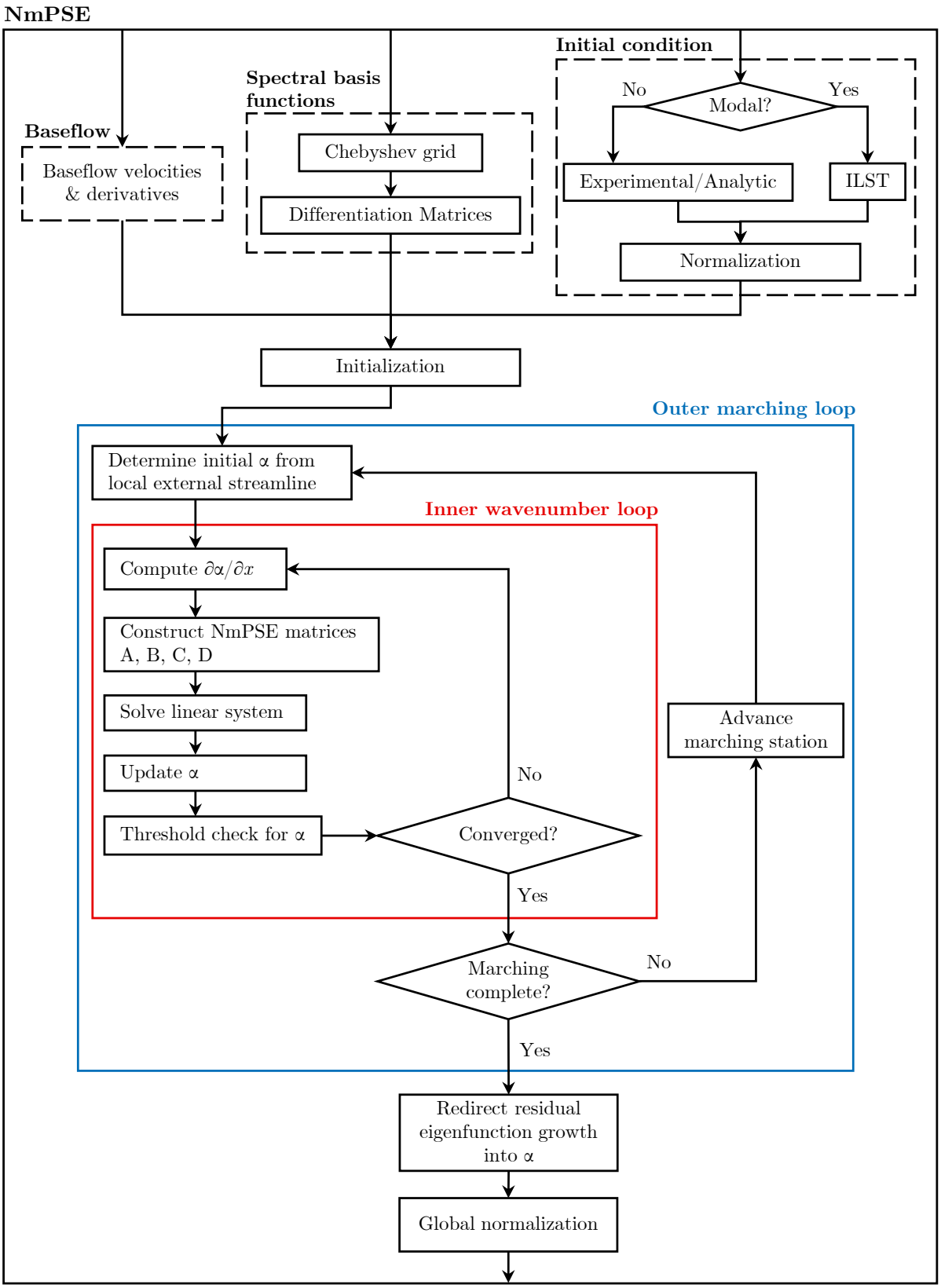

A.3. Code Listing: NmPSE_v2_5.m

```
function [u,v,w,p,alpha,Aq] = NmPSE_v2_5(Re,IC,uIC,vIC,wIC,Ur,Vr,Wr,dxUr,dxVr,dxWr,dyUr,dyVr
    ,dyWr,x_md,y_md,omega,beta,alf,N,y_max,y_i)
% Executes a Non-Modal PSE simulation from min(x_md) to max(x_md(:,M)) at each given x-
% station of the given mean flow (Ur,Vr,Wr), assuming it to be given on a
% uniform grid. The fields are to be given such as to go from the free-
% stream to the wall as the (row-)index increases. Downstream stations
% correspond to an increasing column index.

% The outputs are the complex shape functions of u, v, w and p, along with
% the chordwise wavenumber. The shape functions are normalised with the local maximum of u.

% Chordwise grid density
[ ,nx] = size(Ur);

%% Spectral Basis Functions

% Set up Chebyshev grid and associated Pseudo-Spectral Differentiation
% Matrices (PSDMs) in the computational domain: i.e. eta in [-1,1]
[eta,DM] = chebdif(N,2);

% Transform the PSDMs to the physical domain: eta |-> y
[y,D1,D2] = MappingMalik(y_max,y_i,eta',DM(:,:,1),DM(:,:,2));
clear DM eta

% The PSDMs will generally pop up with the size (N-2)x(N-2), accordingly
% define the identity and zero column and row
I  = eye(N-2);
Z  = zeros(N-2);
Zc = zeros(N-2,1);
Zr = zeros(1,N-2);

%% Initial Condition Assignment (Modal/Non-Modal Velocity, Zero Pressure)

% Initialize solution vector phi = [u v w p]'(x,y) and alpha = alpha(x)
phi   = zeros(4*(N-2)+2,nx);
alpha = zeros(1,nx);

if strcmpi(IC,'nonmod')

    % Assign non-modal initial conditions as per user input

    % Set non-modal IC at first phi station
    phi(1:3*(N-2),1) = [uIC(2:end-1);vIC(2:end-1);wIC(2:end-1)];

    % Prescribe alpha at the first station
    alpha(1) = alf;

elseif strcmpi(IC,'mod')

    % Execute ILST analysis for modal initial conditions

    tic
    fprintf('| Running ILST for inflow conditions...\n')
    [EVOS,uOS,vOS,wOS,pOS,yOS] = solver_ILST(...
        Re,Ur(:,1),Wr(:,1),dyUr(:,1),dyWr(:,1),y_md,...
        omega,beta,N,y_max,y_i);
    fprintf('\b\b\b\b, finished in %.2f seconds.\n',toc)

    % Filter eigenfunctions for correct eigenvalue
    [OSeigval,index] = EVfilter(EVOS,vOS,yOS,omega,beta,d99(1));

    % Initialize solution vector phi = [u v w p]'(x,y) and alpha = alpha(x)
    phi    = zeros(4*(N-2)+2,nx);
    alpha  = zeros(1,nx);

    %Set ILST eigenfunction in first phi station
    phi(:,1) = ([uOS(2:end-1,index);
```

```
                vOS(2:end-1,index);
                wOS(2:end-1,index);
                pOS(:,index)]);

    % Set ILST eigenvalue as alpha for first station
    alpha(1) = real(OSeigval);

else
    fprintf('Invalid initial condition input! \n')
end

%% Execute Marching Algorithm

% External velocities at the first station
Ue  = Ur(1,:);
We  = Wr(1,:);

Ph     = atan(We./Ue);             % Determine external streamline inclination
yinteg = linspace(0,max(y),4000);  % Pre-allocate array for wall-normal interpolation
iu     = sqrt(-1);

% Start progress bar
percentage = 0;
fprintf('| Starting marching method.')
fprintf('| Progress:  %.0f percent',percentage)

% Outer marching loop
for i=2:nx

    % Determine intial guess for alpha from the local external streamline
    alpha(i) = -tan(Ph(i))*beta;

    % Interpolate baseflow components and create diagonal matrix form
      U = diag(interp1(y_md,  Ur(:,i),y(2:N-1),'spline'));
    dxU = diag(interp1(y_md,dxUr(:,i),y(2:N-1),'spline'));
    dyU = diag(interp1(y_md,dyUr(:,i),y(2:N-1),'spline'));

      V = diag(interp1(y_md,  Vr(:,i),y(2:N-1),'spline'));
    dxV = diag(interp1(y_md,dxVr(:,i),y(2:N-1),'spline')); % Note: Order 1/Re^2
    dyV = diag(interp1(y_md,dyVr(:,i),y(2:N-1),'spline'));

      W = diag(interp1(y_md,  Wr(:,i),y(2:N-1),'spline'));
    dxW = diag(interp1(y_md,dxWr(:,i),y(2:N-1),'spline'));
    dyW = diag(interp1(y_md,dyWr(:,i),y(2:N-1),'spline'));

    % Reset convergence measure
    dal = 1;

    % Inner wavenumber loop
    while abs(dal)*Re >= 1e-9

        % N o n  -  m o d a l  P S E | Backward Euler
        %--------------------------------------------
        % [A + B(d/dy) + C(d2/dy2) + D(d/dx)] q = 0

        % LHS  = A + B*Dy1 + C*Dy2 + D/dx;
        % RHS  = D/dx*q_old;

        %------------M A T R I X----C O N S T R U C T I O N------------

         % Determine d(alpha)/dx
        dx  =  x_md(1,i) - x_md(1,i-1);
        dax =  (alpha(i) - alpha(i-1))/dx;

        % Define common convection-diffusion terms
        Cvd = -iu*omega*I + iu*alpha(i)*U + iu*beta*W + ... % Convective
            I*(alpha(i)^2 + beta^2)/Re - iu*dax*I/Re;       % Diffusive

        % Construct wall-normal derivative matrices (Dy1 = d/dy, Dy2 = d2/dy2)
        Dy1 = blkdiag(D1(2:end-1,2:end-1),D1(2:end-1,2:end-1),D1(2:end-1,2:end-1),D1);
        Dy2 = blkdiag(D2(2:end-1,2:end-1),D2(:,2:end-1),D2(2:end-1,2:end-1),D2);
```

```
138
139         % Construct A
140         A = [ iu*alpha(i)*I     Z     iu*beta*I    [Zc        Z          Zc]      % Continuity
141                 Cvd + dxU      dyU       Z         [Zc  iu*alpha(i)*I   Zc]      % x-Momentum
142                    dxW         dyW      Cvd        [Zc     iu*beta*I     Zc]      % z-Momentum
143                     Zr          Zr        Zr        [0         Zr         0 ]      %     |
144                    dxV      Cvd + dyV    Z         [Zc        Z          Zc]      % y-Momentum
145                     Zr          Zr        Zr        [0         Zr         0 ];     %     |
146
147         % Construct B
148         B = [ Z    I    Z  [Zc  Z  Zc]      % Continuity
149               V    Z    Z  [Zc  Z  Zc]      % x-Momentum
150               Z    Z    V  [Zc  Z  Zc]      % z-Momentum
151               Zr   Zr   Zr [1   Zr  0]      %     |
152               Z    V    Z  [Zc  I  Zc]      % y-Momentum
153               Zr   Zr   Zr [0   Zr  1] ];   %     |
154
155         % Construct C
156         C = [  Z      [Zc        Z         Zc ]      Z      [Zc  Z  Zc]      % Continuity
157              -1/Re*I  [Zc        Z         Zc ]      Z      [Zc  Z  Zc]      % x-Momentum
158                Z      [Zc        Z         Zc ]   -1/Re*I   [Zc  Z  Zc]      % z-Momentum
159                Zr     [-1/Re     Zr        0  ]      Zr     [0   Zr  0]      %     |
160                Z      [Zc     -1/Re*I      Zc ]      Z      [Zc  Z  Zc]      % y-Momentum
161                Zr     [0         Zr      -1/Re]      Zr     [0   Zr  0] ];   %     |
162
163         % Construct D
164     D_com = U - 2*iu*alpha(i)*I/Re;                 % Common Term in the D-Matrix
165         D = [   I      Z       Z      [Zc  Z  Zc]      % Continuity
166               D_com    Z       Z      [Zc  Z  Zc]      % x-Momentum
167                  Z     Z     D_com    [Zc  Z  Zc]      % z-Momentum
168                  Zr    Zr      Zr     [0   Zr  0]      %     |
169                  Z    D_com    Z      [Zc  Z  Zc]      % y-Momentum
170                  Zr    Zr      Zr     [0   Zr  0] ];   %     |
171
172         %------------S O L V E------------
173         % Define LHS and RHS
174         Ml  = A + B*Dy1 + C*Dy2 + D/dx;
175         Mr  = D/dx*phi(:,i-1);
176
177         % Solve linear problem
178         phi(:,i) = Ml\Mr;
179
180         %------------U P D A T E----A L P H A------------
181
182         % Store previous iteration for alpha
183         alphaold = alpha(i);
184
185         % Compute new alpha through the non-modal "normalization condition"
186
187         u        = phi(1:N-2,i);       % u shape function at current station
188         uold     = phi(1:N-2,i-1);     % u shape function at previous station
189         dux      = (u - uold)/dx;      % d(u)/dx
190
191         % Find the wall-normal maxima of the u shape function
192         [ ,k]    = max(abs(interp1(y(2:end-1),u,yinteg,'spline')));
193         umax     = interp1(y(2:end-1),u,yinteg(k),'spline');
194         dumax    = interp1(y(2:end-1),dux,yinteg(k),'spline');
195
196         % Compute new alpha by absorbing residual phase change in u
197         alphaphi = real((dumax/umax)/iu);
198         alpha(i) = alpha(i) + alphaphi;
199
200         % Check difference wrt previous iteration
201         dal = alpha(i) - alphaold;
202
203     end
204
205     % Notify progress
206     for j = 1:numel(num2str(percentage))+9; fprintf('\b'); end
207     percentage = round(100*i/nx);
208     fprintf('%.0f percent ',percentage)
```

```
209
210 end
211
212 %% Output/Normalization Routine
213
214 % Augment Dirichlet conditions to perturbation velocity components
215 phi = [zeros(1,nx); phi(0*(N-2)+1:1*(N-2)  ,:); zeros(1,nx);
216        zeros(1,nx); phi(1*(N-2)+1:2*(N-2)  ,:); zeros(1,nx);
217        zeros(1,nx); phi(2*(N-2)+1:3*(N-2)  ,:); zeros(1,nx);
218                     phi(3*(N-2)+1:4*(N-2)+2,:)];
219
220 % Extract the individual shape functions
221 u   = phi(0*N+1:1*N,:);
222 v   = phi(1*N+1:2*N,:);
223 w   = phi(2*N+1:3*N,:);
224 p   = phi(3*N+1:4*N,:);
225
226 % Calculate the residual growth in the eigenfunction
227 dux      = -FD1d4o(u,dx);
228 yinteg   = linspace(0,max(y),4000);
229 umax     = ones(1,nx);
230 alphaphi = zeros(1,nx);
231
232 for i = 2:nx
233     [ ,k]       = max(abs(interp1(y,u(:,i),yinteg,'spline')));
234     umax(i)     = interp1(y,u(:,i),yinteg(k),'spline');
235     dumax       = interp1(y,dux(:,i),yinteg(k),'spline');
236     alphaphi(i) = (dumax/umax(i))/iu;
237 end
238
239 alpha = alpha + alphaphi;
240
241 % Shape function normalization
242 [ ,k]   = max(abs(interp1(y,u(:,1),yinteg,'spline')));
243 umax(1) = interp1(y,u(:,1),yinteg(k),'spline');
244
245 for i = 1:nx
246     u(:,i) = u(:,i)/abs(umax(i));
247     v(:,i) = v(:,i)/abs(umax(i));
248     w(:,i) = w(:,i)/abs(umax(i));
249     p(:,i) = p(:,i)/abs(umax(i));
250 end
251
252 % Store shape function amplitudes
253 Aq = umax;
254
255 end
```